



Universiteit  
Leiden  
The Netherlands

## **Modeling vascular disease using self-assembling human induced pluripotent stem cell derivatives in 3D vessels-on-chip**

Nahon, D.M.

### **Citation**

Nahon, D. M. (2024, June 26). *Modeling vascular disease using self-assembling human induced pluripotent stem cell derivatives in 3D vessels-on-chip*. Retrieved from <https://hdl.handle.net/1887/3765789>

Version: Publisher's Version

License: [Licence agreement concerning inclusion of doctoral thesis in the Institutional Repository of the University of Leiden](#)

Downloaded from: <https://hdl.handle.net/1887/3765789>

**Note:** To cite this publication please use the final published version (if applicable).

**Modeling vascular disease using self-assembling  
human induced pluripotent stem cell derivatives  
in 3D vessels-on-chip**

**Dennis M. Nahon**

## Colophone

Modeling vascular disease using self-assembling human induced pluripotent stem cell derivatives in 3D vessels-on-chip

Dennis Martijn Nahon  
Thesis Leiden University Medical Center

ISBN: 978-94-6496-141-6  
Printing: Gildeprint, [www.gildeprint.nl](http://www.gildeprint.nl)

Cover: immunofluorescence microscopy image taken by Dennis M. Nahon, adapted and extended using Stable Diffusion by Jeroen M. Stein.

Copyright: © Dennis M. Nahon, Zoetermeer, the Netherlands  
All rights reserved. No part of this publication may be reproduced or transmitted in any form or by any means without permission of the author, or, when applicable, of the publishers of the scientific papers.

The research described in this thesis was conducted at the department of Anatomy & Embryology of the Leiden University Medical Center, the Netherlands. It was supported by the following grants: The Netherlands Organ-on-Chip Initiative (NOCI), an NWO Gravitation project funded by the Ministry of Education, Culture and Science of the government of the Netherlands (024.003.001) and The Novo Nordisk Foundation Center for Stem Cell Medicine supported by Novo Nordisk Foundation grants (NNF21CC0073729).

Publication of this thesis was financially supported by the Dutch Heart Foundation and Stichting Proefdiervrij.

# **Modeling vascular disease using self-assembling human induced pluripotent stem cell derivatives in 3D vessels-on-chip**

Proefschrift

ter verkrijging van  
de graad van doctor aan de Universiteit Leiden,  
op gezag van rector magnificus prof. dr. ir. H. Bijl,  
volgens besluit van het college voor promoties  
te verdedigen op woensdag 26 juni 2024  
klokke 15:00 uur

door

Dennis Martijn Nahon  
geboren te Voorburg  
in 1993

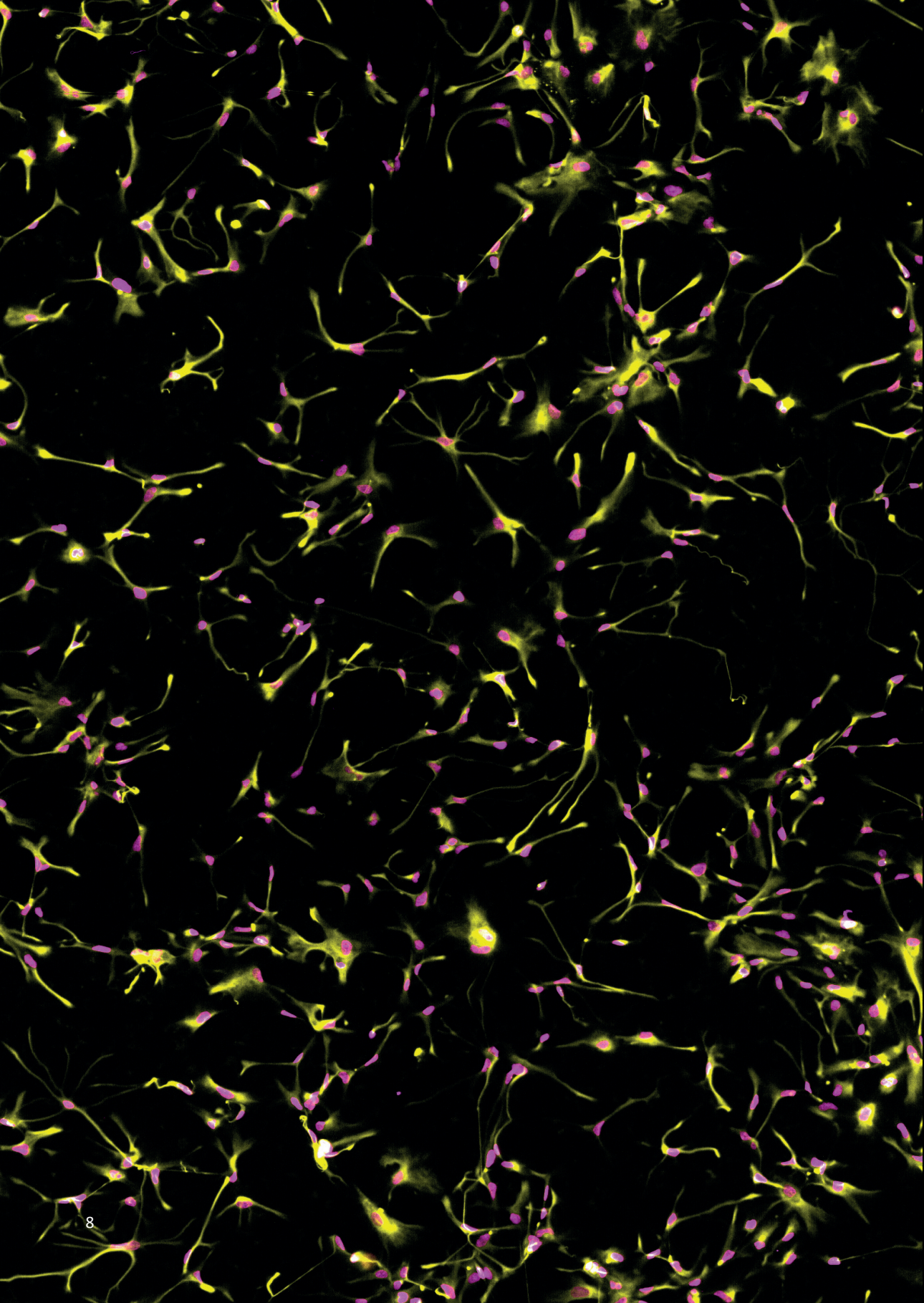
<b>Promotor</b>	Prof. dr. C.L. Mummery
<b>Co-promotor</b>	Dr. V.V. Orlova
<b>Promotiecommissie</b>	Prof. dr. M.J.T.H. Goumans Prof. dr. A.M.J.M. van den Maagdenberg Prof. dr. A.J. van Zonneveld Prof. dr. P.L. Hordijk (VU Medical Center Amsterdam) Prof. dr. A.D. van der Meer (University of Twente)

To endless exploration,



## Index

<b>Chapter 1</b>	General introduction	8
<b>Chapter 2</b>	Taking microphysiological systems to the next level: Why quantification of physiological features is essential	20
<b>Chapter 3</b>	Genetic repair of human induced pluripotent cell line from patient with Dutch-type cerebral amyloid angiopathy	86
<b>Chapter 4</b>	Characterization of endothelial cell functionality in RVCL-S using patient-derived hiPSCs	102
<b>Chapter 5</b>	Vascular defects associated with hereditary hemorrhagic telangiectasia revealed in patient-derived isogenic hiPSCs in 3D vessels on chip	128
<b>Chapter 6</b>	Self-assembling vessel-on-chip model with hiPSC-derived astrocytes	158
<b>Chapter 7</b>	Discussion and future perspectives	194
<b>Appendix</b>		
	Summary	208
	Nederlandse samenvatting	210
	Curriculum vitae	214
	List of publications	216
	Dankwoord	218



# **Chapter 1**

## **General Introduction**

## Introduction

Functional vasculature is essential for maintaining the health of every part of the human body. It delivers oxygen and nutrients, transports immune cells and removes metabolic and other waste products. It consists of connected cylindrical tubes of divergent diameters in an organized network of arteries, arterioles, capillaries, venules and veins, through which blood flows. The vessel wall is composed of a single layer of endothelial cells surrounded by either multiple layers of smooth muscle cells or single pericytes, depending on the location of the vessel within the vascular tree. The exact composition and functionality varies greatly between tissues and along the arteriovenous axis<sup>1,2</sup>. Vascular cell dysfunction plays a key role in many chronic conditions, such as ischemic heart disease and stroke and even the initiation and propagation of severe COVID-19<sup>3,4</sup>. Creating predictive pre-clinical human models to study vascular (patho)physiology is essential if cures or therapies are to be found for the many vascular diseases affecting all age groups. The overall aim of this thesis is to generate the cellular components of the vessels and introduce them into advanced (on-chip) models to improve vascular disease modeling, with a specific focus on vascular pathologies affecting the brain.

## The blood-brain barrier

The central nervous system (CNS) consists of a minimal functional entity, known as the neurovascular unit (NVU); it is composed of vascular cells, glial cells and neurons (Figure 1). This intricate assembly is responsible for inducing and maintaining the highly specialized barrier known as the blood-brain barrier (BBB), which separates the blood from the brain parenchyma.

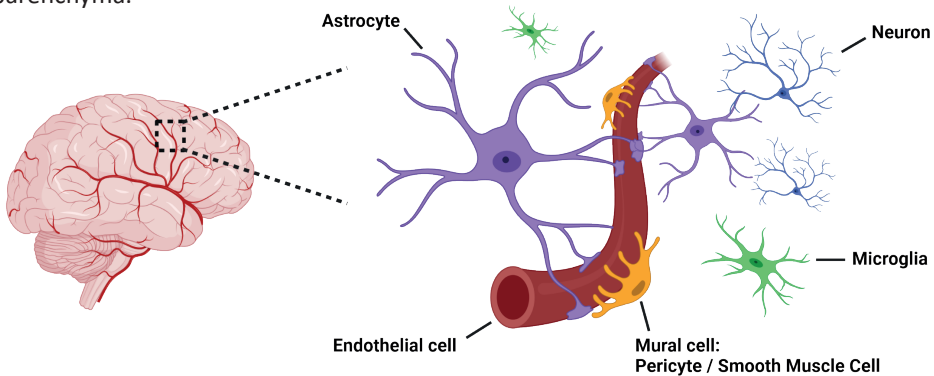


**Figure 1: Schematic representation of the composition and organization of the cell types making up the neurovascular unit.**

Formation of the BBB is initiated when mesoderm-derived blood vessels of the perineural vascular plexus penetrate the neuro-ectoderm, guided by neuronal and neural progenitor cell (NPC)-derived vascular endothelial growth factor (VEGF)<sup>5</sup>. Subsequent induction of BBB-

identity in ECs is regulated by activation of multiple pathways, with the canonical Wnt/ $\beta$ -catenin pathway being the most prominent<sup>6</sup>.

Within the BBB, the expression of specific tight junction (TJ) proteins strictly regulates the paracellular passage of molecules. Simultaneously, active inhibition of transcellular transport through the vessel wall occurs. Additionally, expression of several influx and efflux transporters tightly regulate active transport in- and out of the CNS. Moreover, (low levels of) adhesion molecules on the ECs limit the entry of immune cells into the brain. These combined characteristics not only prevent the entry of neurotoxic components and pathogens but also allow precise regulation of molecular transport, required for the high metabolic demand<sup>7</sup>. Though the primary BBB properties appear to be EC-specific, their functionality is highly dependent on the intricate interactions and crosstalk with the other cell types present in the NVU. Pericytes and astrocytes are recognized as the most significant contributors to maintaining BBB stability.

Pericytes, located in close proximity to the ECs, share the same basement membrane and play a crucial role in the BBB by regulating the inflammatory response, strengthening tight junctions and secreting laminins<sup>8</sup> and vitronectin<sup>9,10</sup>. The recruitment of pericytes to the BBB is facilitated by the binding of platelet-derived growth factor BB (PDGF-BB), secreted by ECs, to platelet derived growth receptor  $\beta$  (PDGF- $\beta$ ) in pericytes<sup>5</sup>. Activation of this pathway leads to pericyte recruitment and proliferation in a concentration-dependent manner. Disruption of this and other pathways, leading to abnormal pericyte function, has been associated with various neurological disorders<sup>11,12</sup>. These include diabetic retinopathy and multiple neurodegenerative diseases such as Alzheimer's disease<sup>13</sup>.

Astrocytes, have polarized "end-feet" that ensheath the cerebral vasculature; they serve as the essential cellular link between blood vessels and neurons. Their high density and localized expression of the water channel aquaporin 4 (AQP4) and the Kir4.1 K<sup>+</sup> channel ensures tight regulation of ion content in the perivascular space, which is crucial for neuronal function and BBB stability<sup>11,14</sup>. Moreover, astrocytes also secrete basement membrane proteins such as laminins  $\alpha$ 1 and  $\alpha$ 2<sup>15</sup> and signaling molecules such as retinoic acid (RA) and sonic hedgehog (SHH), contributing to the induction and stabilization of tight junctions<sup>16</sup>. *In vitro* studies have shown that astrocyte-secreted factors such as glial cell line-derived neurotrophic factor (GDNF)<sup>17</sup> or angiopoietin-1 (ANG-1), acting through the TIE2 EC specific receptor<sup>18</sup>, regulate the acquisition and maintenance of EC-BBB identity.

Dysregulation of any of these cellular interactions can compromise integrity of the BBB. These three cell types are thus key players in various (inherited) vascular neurodegenerative disorders, most of which are rare but collectively affect a large group of individuals who develop many pathologies often the result of hemorrhage from unstable vessels.

### **Inherited vascular disorders with cerebral pathologies**

Neurological disorders and neurodegenerative diseases are an increasing burden on society. Accumulating evidence indicates a fundamental role of the dysfunction of the brain vasculature in these pathophysiological conditions<sup>19</sup>. Known links between vascular mediated neuro-pathologies include BBB breakdown, hypoperfusion-hypoxia and EC-derived neurotoxic and inflammatory factors<sup>20</sup>. Three specific vascular disorders associated with cerebral pathologies that we have studied because of their prevalence in the Netherlands are Dutch-type cerebral amyloid angiopathy (D-CAA), also known as hereditary cerebral haemorrhage with amyloidosis-Dutch type (HCHWA-D), Retinal vasculopathy with cerebral leukoencephalopathy and systemic manifestations (RVCL-S) and Hereditary hemorrhagic telangiectasia (HHT).

These pathologies give rise to a spectrum of effects, ranging from mural cell apoptosis and aberrant mural cell-EC cross talk<sup>21</sup> to altered basement membrane composition and structure<sup>22</sup> or more severe arteriovenous malformations (AVMs)<sup>23</sup>. Overall, these phenotypic changes lead to reduced stability and integrity of cerebral blood vessels, that can result in hemorrhagic strokes.

### **Vascular disease modeling**

Our current understanding of these vascular pathologies is primarily based on studies using commercially available cell lines expressing aberrant forms of putatively causative genes, primary patient material or mutant mouse models. While commercially available cell (lines) have proven to be valuable tools in biomedical research, their prolonged culture may lead to the loss of tissue specific characteristics. Additionally, they commonly cannot be obtained from patients as disease specific models. Patient material (from which to derive vascular cells for example) is in principle more relevant to study disease, it may however be limited by its availability, especially in the case of rare diseases. In addition, invasive procedures may be required to obtain the cells and once in culture the lifespan of these cells may be limited. Mouse models by contrast allows studying how a disease might manifest in a living organism but they lack the human genetic background and may differ from human physiology. Blood flow rates or the immune component influencing the vasculature for example may be very different in mice to that in humans. As a result, even mice expressing corresponding human mutations may display different disease phenotypes than those observed in patients. An illustrative example of these differences was demonstrated in a recent study comparing single nuclei sequencing of brain vasculature in Alzheimer's patients and a commonly used Alzheimer's mouse model: this revealed only minimal overlap in the differentially expressed genes in both cases<sup>24</sup>. This further emphasizes the need for humanized models to accurately assess the pathways involved in complex diseases.

In recent years, significant progress in stem cell biology has allowed the increasing use of adult human stem cells or human induced pluripotent stem cells (hiPSCs). So far,

adult tissue sources of vascular stem or progenitor cells have not been described. hiPSCs, by contrast are pluripotent and can form all cell types of the body including vascular cells<sup>25</sup>. They are derived through reprogramming of somatic cells to a pluripotent state using just four transcription factors<sup>26</sup> and have already proven a powerful tool for disease modeling<sup>27</sup>. They can not only be generated from healthy individuals but can also be derived from patients with genetic disorders and can be genetically engineered to introduce- or remove disease-specific mutations or variants for specific types of disease modelling<sup>28</sup>. Additionally, hiPSCs can be genetically modified to incorporate cell type-specific (fluorescent) reporter constructs or phenotypic sensors allowing them to be identified in-, or selected from, mixed cell populations.

### hiPSC-derived ECs

There are multiple protocols to differentiate ECs from hiPSCs. These vary from embryoid body (aggregate)-formation, direct 2D monolayer cultures using cytokines, directed genetic modification, and most recently formation of vascular organoids. Arguably the most commonly used are the monolayer protocols, wherein developmental cues are simulated by the sequential addition of molecules and growth factors. Initially, hiPSCs are patterned towards mesoderm using either Glycogen synthase kinase 3 (GSK3) inhibitor (CHIR99021)<sup>29</sup> either alone or in combination with Bone morphogenetic protein 4 (BMP4)<sup>30</sup>. Subsequently, EC specification is achieved by using Vascular Endothelial Growth Factor (VEGF) in combination with an ALK5 inhibitor (SB431542)<sup>29</sup> or protein kinase A activation via cyclic AMP using Forskolin<sup>30</sup>. More recently, specialized protocols have been developed to differentiate tissue specific endothelial cells<sup>31</sup>.

Generation of brain endothelial cells has been of particular interest to enable study of brain pathologies and facilitate improved drug treatments through the BBB. This is important because many drugs (for example to treat neurodegenerative diseases or brain tumors) cannot cross the BBB and reach its potential cellular target within the brain. Various approaches have been taken to establish authentic 'BBB-ECs'<sup>32</sup>. One of the most well-known and widely used are hiPSC-derived brain microvascular endothelial cells (iBMECs). Differentiation of iBMECs was based on the initial protocol from<sup>33</sup> which was later adapted to enhance the yield and improve BBB properties further<sup>34,35</sup>. However, while these cells typically exhibit EC properties such as high transendothelial electrical resistance (TEER) and expression of efflux transporters, they lack proper expression of vascular lineage genes and instead express markers for the neuroectodermal epithelial lineage<sup>36,37</sup>.

An alternative approach involves co-culturing of hiPSC-ECs with tissue-specific cells. This is an approach which has previously been shown to induce an EC tissue-specific molecular identity for several organ systems<sup>38,39</sup>, including the brain<sup>40</sup>. This co-culture strategy underscores the plasticity of ECs and the significance of the environment and cellular interactions in creating more *in vivo*-like systems, essential for studying complex

diseases.

### **Organ-on-chip**

One of the more recent approaches which enables closer simulation of the native environment are microphysiological systems (MPS). MPS are distinct from conventional cell cultures in that they include features such as gas- and fluid flow; for this reason, some are referred to as microfluidic Organs-on-Chip (OoCs)<sup>41,42</sup>. These advanced models can provide mechanical cues to cells as in real tissues, creating systems with the potential to impact understanding of human physiology and disease, toxic effects of the environment or drugs and the identification of novel therapeutics. Each OoC aims to replicate one or more specific aspects of organ and tissue function *in vitro* and thus can be different in design depending on the application.

### **Vessel-on-chip**

Numerous Vessel-on-Chip (VoC) models have been developed to facilitate the study of various functional aspects of the vasculature (Figure 2)<sup>43,44</sup>. Broadly, these models can be categorized into two types: those in which vessels are engineered to have specific dimension, and those where vessels form themselves (self-organize) through vasculogenesis or angiogenesis. Engineered models with vessels of specific sizes, offer the advantage of more tightly regulated architecture, which aids in recapitulating uniform flow patterns and functional readouts influenced by local vessel dimension and flow pattern, such as permeability. On the other hand, models utilizing the self-assembling capacity of vascular cells into 3D lumens have the advantage of better mimicking the formation and dynamics of complex vascular bed, resembling what is seen *in vivo*. Moreover, the direct interaction between the different cell types incorporated in the device can be investigated more accurately as these cells are not “forced” into specific configurations. Lastly, self-assembling models tend to be easier to handle in comparison to other systems.

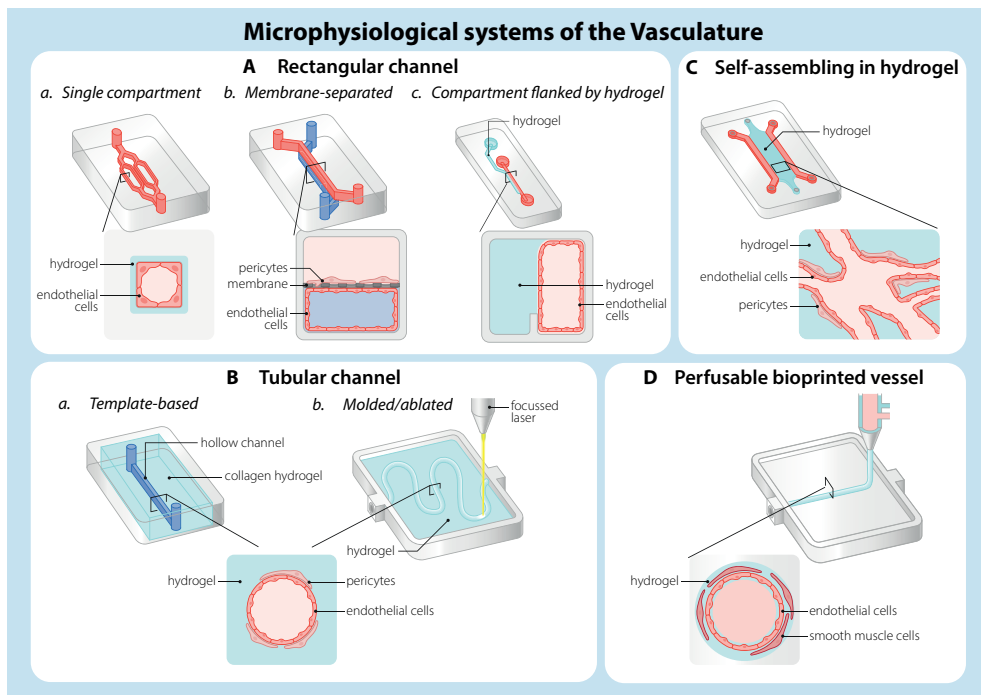


**Figure 2: Design principles of different microphysiological systems of the human vasculature (adapted from Nahon, Moerkens et al 2024, in press)**

### Aim and scope of this thesis

In the past decade, a wide range of complex models have been developed to study neuro-pathologies. However, most of these have been either technically intricate and hard to reproduce, or have only been described in proof-of-concept formats using primary cells or commercially available cell lines. In this thesis, the objective was to enhance the biological relevance of the existing models by creating modular and robust models that incorporate hiPSCs to study disease phenotypes (Figure 3).

In **chapter 2** we first discuss the current status and future prospects of MPS and emphasize the need for measurable standards that allow quantitative comparisons of MPS outcomes with physiological observations in humans so that their *in vivo* relevance and predictive value can be properly assessed as fit-for-purpose in specific applications. Moving to **chapter 3**, we describe the genetic repair of a human induced pluripotent cell line obtained from a patient with D-CAA. This provided isogenically paired hiPSC lines, as a resource for further study of the underlying disease mechanism. In **chapter 4** we use similarly generated isogenically paired disease and corrected hiPSC lines from a patient with RVCL-S to study the EC defects in these cells. Continuing to **chapter 5** we employed isogenic HHT diseased and healthy hiPSCs, to produce ECs and investigate vascular defects using both 2D assays

and a more complex 3D VoC model. Here, the significance of the more complex VoC model becomes evident, as disease phenotypes were not evident in conventional 2D assays, but were clearly revealed in the VoC model. In **chapter 6**, we further enhanced the complexity of the VoC model towards a BBB model by incorporating hiPSC-derived astrocytes into the vascular networks. Detailed characterization of the VoC was carried out, and the networks are further improved through the application of continuous flow or activation of the cyclic AMP pathway. Finally, in **chapter 7**, the work described in this thesis is discussed and the future outlook for the field of complex vascular disease modeling described based on the present state-of-the-art.

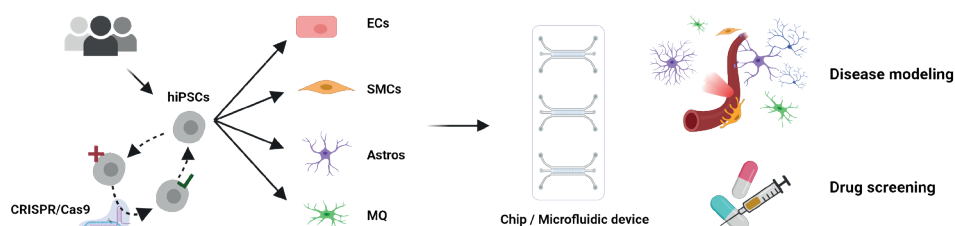


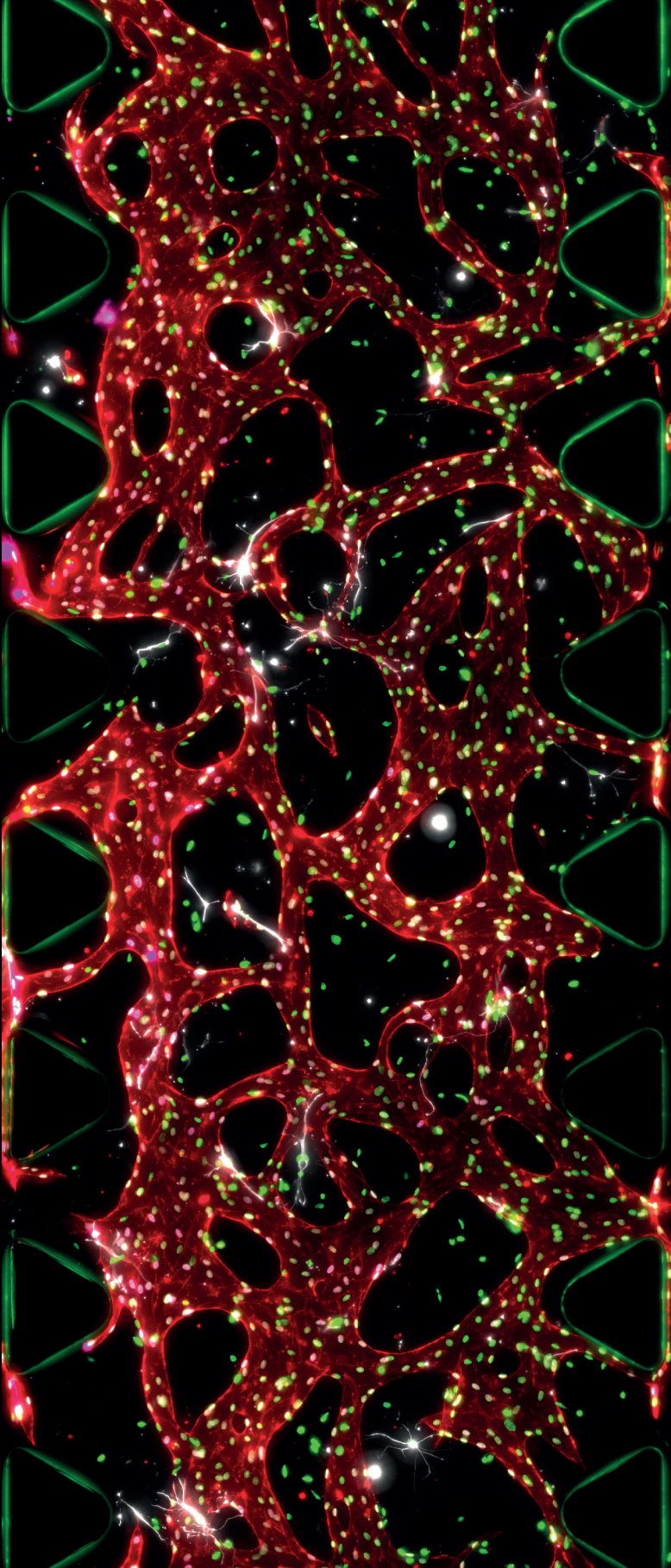
**Figure 3: The use of hiPSC-derived vascular cells inside a microfluidic device for generating robust vessel-on-chip systems to study disease modelling or drug screening.** hiPSCs of either healthy donors or patients can be used. Disease specific mutations in patient hiPSC lines can be corrected for example, using CRISPR/Cas9 technology, to create isogenically paired cells. This way creating a modular vessel-on-chip system to investigate the cell-type specific contribution of each cell type. hiPSCs = human induced pluripotent stem cells, ECs = Endothelial cells, SMCs = Smooth Muscle Cells, Astros = Astrocytes, MQ = Macrophages.

## References

1. Winkler, E. A. et al. A single-cell atlas of the normal and malformed human brain vasculature. *Science* (1979) 7377, (2022).
2. Vanlandewijck, M. et al. A molecular atlas of cell types and zonation in the brain vasculature. *Nature* 554, 475–480 (2018).
3. Trimm, E. & Red-Horse, K. Vascular endothelial cell development and diversity. *Nat Rev Cardiol* 0123456789, (2022).
4. Teuwen, L. A., Geldhof, V., Pasut, A. & Carmeliet, P. COVID-19: the vasculature unleashed. *Nat Rev Immunol* 20, 389–391 (2020).
5. Zhao, Z., Nelson, A. R., Betsholtz, C. & Zlokovic, B. V. Establishment and Dysfunction of the Blood-Brain Barrier. *Cell* 163, 1064–1078 (2015).
6. Langen, U. H., Aylloo, S. & Gu, C. Development and cell biology of the blood-brain barrier. *Annu Rev Cell Dev Biol* 35, 591–613 (2019).
7. Sweeney, M. D., Zhao, Z., Montagne, A., Nelson, A. R. & Zlokovic, B. V. Blood-brain barrier: From physiology to disease and back. *Physiol Rev* 99, 21–78 (2019).
8. Gautam, J., Cao, Y. & Yao, Y. Pericytic Laminin Maintains Blood-Brain Barrier Integrity in an Age-Dependent Manner. *Transl Stroke Res* 11, 228–242 (2020).
9. Aylloo, S. et al. Pericyte-to-endothelial cell signaling via vitronectin-integrin regulates blood-CNS barrier. *Neuron* 110, 1641-1655.e6 (2022).
10. He, L. et al. Analysis of the brain mural cell transcriptome. *Sci Rep* 6, (2016).
11. Armulik, A. et al. Pericytes regulate the blood-brain barrier. *Nature* 468, 557–561 (2010).
12. Bell, R. D. et al. Pericytes Control Key Neurovascular Functions and Neuronal Phenotype in the Adult Brain and during Brain Aging. *Neuron* 68, 409–427 (2010).
13. Winkler, E. A., Bell, R. D. & Zlokovic, B. V. Central nervous system pericytes in health and disease. *Nature Neuroscience* vol. 14 1398–1405 Preprint at <https://doi.org/10.1038/nn.2946> (2011).
14. Abbott, N. J., Rönnbäck, L. & Hansson, E. Astrocyte-endothelial interactions at the blood-brain barrier. *Nat Rev Neurosci* 7, 41–53 (2006).
15. Yao, Y., Chen, Z. L., Norris, E. H. & Strickland, S. Astrocytic laminin regulates pericyte differentiation and maintains blood brain barrier integrity. *Nat Commun* 5, 1–12 (2014).
16. Alvarez, J. I. et al. The hedgehog pathway promotes blood-brain barrier integrity and CNS immune quiescence. *Science* (1979) 334, 1727–1731 (2011).
17. Igarashi, Y. et al. Glial cell line-derived neurotrophic factor induces barrier function of endothelial cells forming the blood-brain barrier. *Biochem Biophys Res Commun* 261, 108–112 (1999).
18. Lee, S.-W. et al. SSeCKS regulates angiogenesis and tight junction formation in blood-brain barrier. *Nat Med* 9, (2003).
19. Sweeney, M. D., Kisler, K., Montagne, A., Toga, A. W. & Zlokovic, B. V. The role of brain vasculature in neurodegenerative disorders. *Nat Neurosci* 21, 1318–1331 (2018).
20. Zlokovic, B. V. Neurovascular pathways to neurodegeneration in Alzheimer’s disease and other disorders. *Nat Rev Neurosci* 12, 723–738 (2011).
21. Kamp, J. A. et al. Amyloid  $\beta$  in hereditary cerebral hemorrhage with amyloidosis-Dutch type. *Rev Neurosci* 25, 641–651 (2014).
22. Stam, A. H. et al. Retinal vasculopathy with cerebral leukoencephalopathy and systemic manifestations. *Brain* 139, 2909–2922 (2016).
23. Letteboer, T. G. W. et al. Hereditary hemorrhagic telangiectasia: ENG and ALK-1 mutations in Dutch patients. *Hum Genet* 116, 8–16 (2005).
24. Yang, A. C. et al. A human brain vascular atlas reveals diverse mediators of Alzheimer’s risk. *Nature* 603, 885–892 (2022).
25. Cochrane, A. et al. Advanced in vitro models of vascular biology: Human induced pluripotent stem cells and organ-on-chip technology. *Adv Drug Deliv Rev* (2018) doi:10.1016/j.addr.2018.06.007.
26. Takahashi, K. & Yamanaka, S. Induction of Pluripotent Stem Cells from Mouse Embryonic and Adult Fibroblast Cultures by Defined Factors. *Cell* 126, 663–676 (2006).
27. Sharma, A., Sances, S., Workman, M. J. & Svendsen, C. N. Multi-lineage Human iPSC-Derived Platforms for Disease Modeling and Drug Discovery. *Cell Stem Cell* 26, 309–329 (2020).
28. Van Den Berg, A., Mummery, C. L., Passier, R. & Van der Meer, A. D. Personalised organs-on-chips:

- functional testing for precision medicine. *Lab Chip* 19, 198–205 (2019).
29. Orlova, V. V. et al. Generation, expansion and functional analysis of endothelial cells and pericytes derived from human pluripotent stem cells. *Nat Protoc* 9, 1514–1531 (2014).
  30. Patsch, C. et al. Generation of vascular endothelial and smooth muscle cells from human pluripotent stem cells. *Nat Cell Biol* 17, 994–1003 (2015).
  31. Nguyen, J., Lin, Y.-Y. & Gerecht, S. The next generation of endothelial differentiation: Tissue-specific ECs. *Cell Stem Cell* 28, 1188–1204 (2021).
  32. Workman, M. J. & Svendsen, C. N. Recent advances in human iPSC-derived models of the blood–brain barrier. *Fluids Barriers CNS* 17, 1–10 (2020).
  33. Lippmann, E. S. et al. Derivation of blood-brain barrier endothelial cells from human pluripotent stem cells. *Nat Biotechnol* 30, 783–791 (2012).
  34. Lippmann, E. S., Al-Ahmad, A., Azarin, S. M., Palecek, S. P. & Shusta, E. V. A retinoic acid-enhanced, multicellular human blood-brain barrier model derived from stem cell sources. *Sci Rep* 4, 1–10 (2014).
  35. Qian, T. et al. Directed differentiation of human pluripotent stem cells to blood-brain barrier endothelial cells. *Sci Adv* 3, (2017).
  36. Lu, T. M. et al. Pluripotent stem cell-derived epithelium misidentified as brain microvascular endothelium requires ETS factors to acquire vascular fate. *Proc Natl Acad Sci U S A* 118, (2021).
  37. Lu, T. M. et al. Human Induced Pluripotent Stem Cell-Derived Brain Endothelial Cells: Current Controversies. *Front Physiol* 12, (2021).
  38. Cao, X. et al. Tissue microenvironment dictates the state of human induced pluripotent stem cell-derived endothelial cells of distinct developmental origin in 3D cardiac microtissues. *Biorxiv* (2022).
  39. Palikuqi, B. et al. Adaptable haemodynamic endothelial cells for organogenesis and tumorigenesis. *Nature* 585, (2020).
  40. Campisi, M. et al. 3D self-organized microvascular model of the human blood-brain barrier with endothelial cells, pericytes and astrocytes. *Biomaterials* 180, 117–129 (2018).
  41. Vunjak-Novakovic, G., Ronaldson-Bouchard, K. & Radisic, M. Organs-on-a-chip models for biological research. *Cell* 184, 4597–4611 (2021).
  42. Ingber, D. E. Human organs-on-chips for disease modelling, drug development and personalized medicine. *Nat Rev Genet* (2022) doi:10.1038/s41576-022-00466-9.
  43. Mandrycky, C. J., Howard, C. C., Rayner, S. G., Shin, Y. J. & Zheng, Y. Organ-on-a-chip systems for vascular biology. *J Mol Cell Cardiol* 159, 1–13 (2021).
  44. Pollet, A. M. A. O. & den Toonder, J. M. J. Recapitulating the vasculature using Organ-on-Chip technology. *Bioengineering* 7, 1–18 (2020).





# Chapter 2

## Taking microphysiological systems to the next level: Why quantification of physiological features is essential

### Abstract

Microphysiological systems (MPS) are cellular models that replicate aspects of organ and tissue function *in vitro* which can be used either individually or linked to each other. They are distinct from conventional cell cultures in that they include features such as gas- and fluid flow; for this reason, some are referred to as microfluidic Organs-on-Chip (OoCs). These advanced models can provide mechanical cues to cells as in real tissues, creating systems with the potential to impact understanding of human physiology and disease, toxic effects of the environment or drugs and the identification of novel therapeutics. To fulfill this potential, however, it is crucial to develop measurable standards that allow quantitative comparisons of MPS outcomes with physiological observations in humans so that their *in vivo* relevance and predictive value can be properly assessed as fit-for-purpose in specific applications. In this review we use MPS of the vascular system, intestine, brain and heart to illustrate the importance of quantifying physiological features of *in vitro* models for comparison with human *in vivo* observations and measuring variability between systems and operators. Specifically, we distinguish the quantification of ‘designed features’ that can be controlled in MPS design from ‘emergent features’ that describe cellular function within the device. We propose methods for improving MPS with read-outs and sensors that monitor complex physiology quantitatively and could lead to wider end-user adoption and regulatory acceptance.

*This chapter is adapted from:*

*Standardizing designed and emergent quantitative features in microphysiological systems. Nature Biomedical Engineering. (2024) In press*

*Dennis M. Nahon\*, Renée Moerkens\*, Hande Aydogmus, Bas Lendemeijer, Jeroen M. Stein, Adriana Martinez-Silgado, Milica Dostanić, Jean-Philippe Frimat, Cristina Gontan, Mees N.S. de Graaf, Michel Hu, Dhanesh G. Kasi, Lena S. Koch, Kieu T.T. Le, Sangho Lim, Heleen H.T. Middelkamp, Joram Mooiweer, Paul Motreuil-Ragot, Eva Niggel, Cayetano Pleguezuelos-Manzano, Jens Puschhof, Nele Revyn, José M. Rivera-Arbelaez, Jelle Slager, Laura M. Windt, Mariia Zakharova, Berend J. van Meer, Valeria V. Orlova, Femke M.S. de Vrij, Sebo Withoff, Massimo Mastrangeli, Andries van der Meer, and Christine L. Mummery*

## Introduction

Microphysiological systems (MPS) are cellular models that recapitulate aspects of (human) physiology by recreating the dynamic microenvironment to which cells are exposed in organs or tissues. They often integrate features such as gas- and fluid flow and are then referred to as microfluidic Organs-on-Chip (OoCs). Their design may also allow incorporation of mechanical stimulation (e.g. contraction, stretch and strain) into living tissue constructs. Many MPS harbor multiple compartments that enable local microenvironments to be regulated independently to support different cell types, while still allowing communication between adjacent compartments. This facilitates complex co-culture in a single system or coupling of multiple MPS to model multi-organ interactions. The first examples of how these advanced model systems can impact toxicological, pharmaceutical and biomedical science are now beginning to emerge<sup>1,2</sup>.

With increasing interest in using MPS, there is a pressing need to develop measurable standards to compare different systems and assess their *in vivo* relevance and predictive value. For this, it is essential to quantify physiological features of tissues in MPS and compare these with actual human (or animal) physiology *in vivo*. However, whilst MPS allow strict control over the culture microenvironment and are thus well-suited to quantify physiological features, most studies to date have only described their qualitative features. Realizing a shift towards quantitative outputs will require control over features such as compartment dimensions, fluid flow rates and system oxygen concentrations, as well as precision monitoring of cellular function (e.g. barrier integrity, electrophysiological properties, metabolite production, immune cell recruitment) inside the system. This will aid the development of measurable standards to qualify systems as fit-for-purpose i.e. suitable for measuring the parameter of interest, and will improve reproducibility of models between users. Qualification and standardization will take MPS technology to 'the next level' and ensure MPS become accepted options for regulatory agencies and end-users<sup>3</sup>.

In this review, we (1) define and categorize quantifiable physiological features (2) provide an overview of physiological features of the human vascular system, intestine, heart and brain that are quantified in design or as read-outs of MPS (3) demonstrate how this approach enables the comparison between MPS and human *in vivo* observations and, finally (4) identify some key technical advances which could improve quantification of physiological features in MPS in the future.

## Defining quantifiable physiological features for microphysiological systems

In essence, MPS use reverse-engineering to mimic specific organ- or tissue functions by incorporating and emulating essential cellular and biophysical components<sup>4,5</sup>. These are based on current understanding of human physiology: we define these as 'physiological features' in this review. In the context of quantitative modeling, it is helpful to categorize these features into 'designed' or 'emergent' (*Figure 1*). Importantly, features are not limited

to one of the two groups but can belong to both depending on the model and functional read-out required.

*Designed features* are physiological features directly translatable into device design or chemical or mechanical input. Examples include compartment dimensions, fluid flow dynamics and oxygen concentration. Designed features can be tightly regulated in MPS and are intended to be close mimics of *in vivo* conditions. Whether or not they are actually in a physiologically relevant range often depends on technical limitations in engineering and fabricating the device set-up.

*Emergent features* are physiological features that describe cellular function. These features cannot be completely controlled ‘upfront’ by device design or input; rather they develop in MPS as a result of intrinsic cellular properties and the microenvironment in the culture system. Examples of emergent features are barrier integrity of a cell layer, electrophysiological properties of the tissues or immune cell migration. Specialized sensors or downstream read-outs are required to monitor emergent features in MPS.

Quantifying emergent features in MPS can indicate physiological relevance and whether the particular device design is suitable for the intended application. Quantification of designed features provides insight into how design choice impacts emergent features and physiological output. In addition, quantitative control of designed features enhances the robustness of MPS and their reproducibility between users. Quantifying both designed and emergent features is essential if they are to be used, directly or indirectly, in developing measurable standards of physiological output in MPS. The selection of features relevant to integrate or monitor in any MPS depends on the specific research question. In general, ‘as simple as possible, but as complex as necessary’ is the guiding principle. This is in line with the widely accepted notion that MPS should be “fit-for-purpose” i.e. capture just one or a few features rather than having one complex device that serves all conceivable functions or applications<sup>6</sup>. This means that the designed features incorporated in an MPS should be limited to those necessary to induce the cellular organization and differentiation state required for physiologically relevant levels of the emergent features being investigated. Similarly, the sensors or read-outs should be limited to those sufficient for monitoring the emergent features of interest. Several causal relationships between designed and emergent features are well-established (e.g. oxygen concentration in an intestinal model impacts microbiome diversity). However, more often the exact implications of designed features have yet to be investigated. Quantification of both types of features in MPS will be necessary to reveal these interactions and provide insight into which designed features are required to create useful models for each goal.

The physiological relevance of any MPS depends on whether the quantified features actually reflect human physiological parameters. *In vitro* to *in vivo* translation requires critical evaluation of what kinds of data can be collected, how it is measured and normalized and which units might be used. We discuss this for the vascular system, intestine, heart and

brain in the sections below.

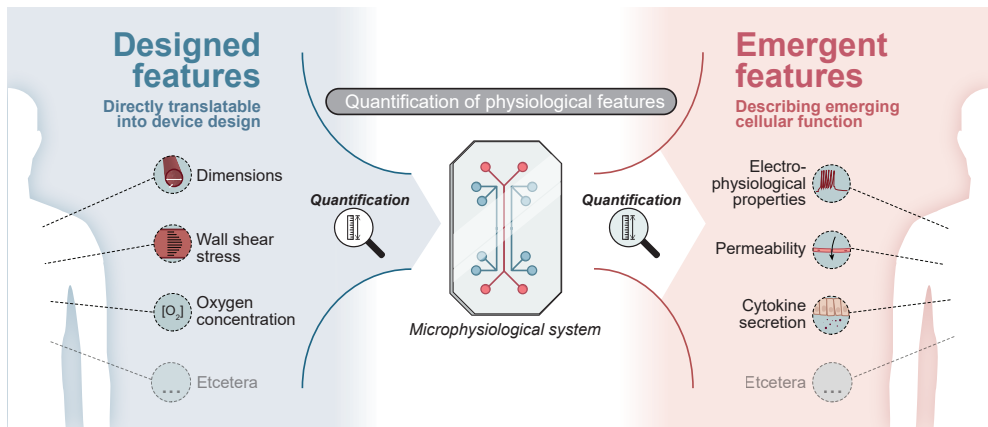


**Figure 1: Microphysiological systems (MPS) can quantitatively control and monitor physiological features.** Two types of quantifiable physiological features can be distinguished: (1) ‘Designed features’ that can be controlled by chip design (e.g. compartment dimensions) or input (e.g. wall shear stress, oxygen concentration) and (2) ‘Emergent features’ that describe cellular function (e.g. electrophysiological properties, permeability, cytokine secretion) which develops as the combined result of design and biological responses of the cells inside the system. Features may belong to either or both groups depending on the specific model and functional read-out required.

## Quantification of physiological features in microphysiological systems of the vasculature, intestine, heart and brain and their *in vivo* relevance

In this section, we provide a comprehensive overview of quantifiable physiological features of the human vasculature, intestine, heart and brain, to provide deeper understanding of the elements required to create physiologically relevant and fit-for-purpose MPS. We describe examples of quantitative modeling of designed and emergent physiological features and compare these with values measured in humans *in vivo* (Table 1). The examples were selected because the quantification methods used and/or absolute values determined are most similar *in vivo* and in MPS; they can thus be used to assess the relevance of the model and benchmark certain physiological feature in MPS. Their value, for example for drug screening, would thus become evident for researchers and regulators alike. Quantified physiological features specific to a single organ are described in SI Note 6. Descriptions and an overview of the designed and emergent physiological features of the four selected organs are shown in SI Note 2 and SI Figure 1.

We report physiological features of the healthy state, not those specifically associated with any pathology, to ensure broad relevance in fit-for-purpose MPS applications. Although the ultimate goal of MPS is often modelling disease, these models themselves usually depend on cellular processes that also occur in physiological states. Quantifying “healthy” features, as in this review, provides a baseline for pathological values, which are often

abberant values of the same physiological features. The selection of organs is based on the developmental argument to include derivatives of all three germ layers: mesoderm (heart), endoderm (intestine), ectoderm (brain) and the blood vessels that link all organs in the body. We have covered a range of MPS per organ, for which the general design principles are shown in *Figure 2*. The majority of the systems discussed include microfluidics and are thus considered OoCs and referred to as Vessel-on-Chip (VoC), Gut-on-Chip (GoC), Heart-on-Chip

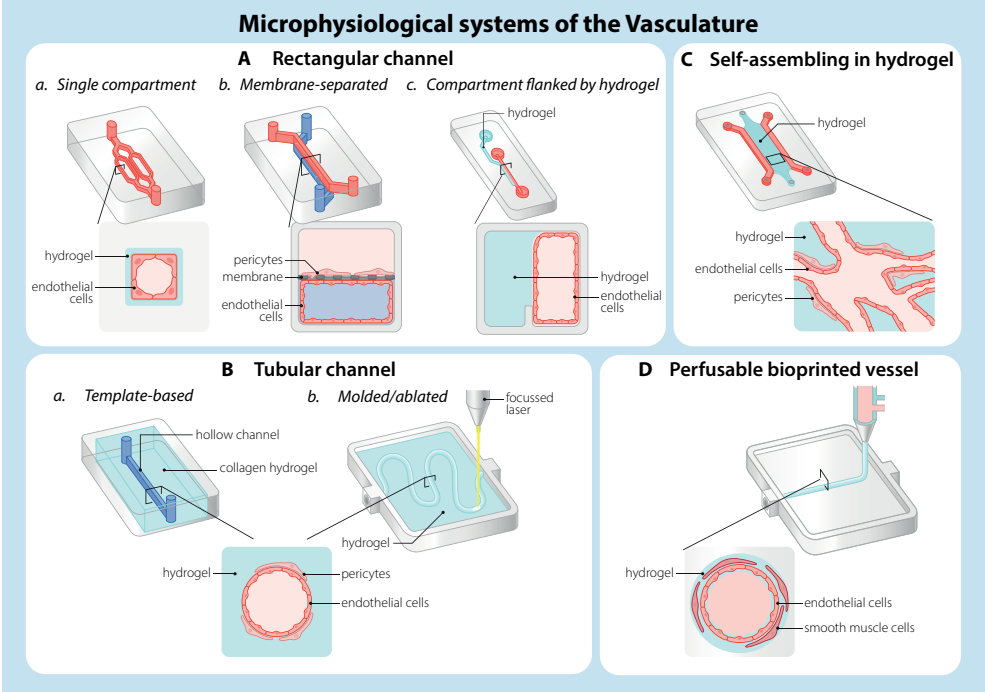


**Figure 2: Design principles of different microphysiological systems of the human vasculature**  
 Microphysiological systems of the vasculature: Aa) Single patterned channel, usually in PDMS although agarose gelatin hydrogel is also used. Widely used for mono-cultures of endothelial cells. Ab) Two aligned channels (upper and lower), separated by porous membrane. Unidirectional pressure-driven fluid flow can be introduced in both channels. The device is generated from PDMS, coated with a thin hydrogel layer. Cells can be cultured in both channels. The upper channel is usually seeded with tissue-specific cell types like astrocytes, neurons, lung- or intestinal epithelium and the lower channel with endothelial cells. Ac) Devices designed for use with gravitational bidirectional flow. Used in 2- and 3-channel formats. The side channel is used to seed endothelial cells and is flanked by a hydrogel-filled channel separated using a phase-guide. Tissue-specific cells can be seeded in the hydrogel channel. Ba) Tubular channels using templating are based on removing or replacing a structure within hydrogel. Examples include needle removal, or using differences in viscosity of fluids as in viscous finger patterning. A tubular structure remains which can be seeded with cells. Bb) Molding or laser ablation can create tubular structures within hydrogels in self-designed patterns. C) Self-assembly based systems make use of the vasculogenic capacity of endothelial cells: the ability to self-organize into vascular networks. Endothelial cells are usually mixed with mural cells, seeding in a hydrogel channel to enable development of a 3-dimensional (3D) vascular network. The hydrogel channel is usually flanked by media channels to enable network perfusion. D) Several tissue engineering approaches to bio-print vessel structures are available. One is printing cell-laden hydrogel within a predetermined structure.

Advanced 3D-printed structures are designed to connect to microfluidic set-ups after seeding. Aa) based on REF.<sup>7</sup> Ab) based on design by Emulate Inc, Boston, MA, USA and REF.<sup>8</sup> Ac) based on design by Mimetas, Oegstgeest, NL and REF.<sup>9</sup> Ba) based on REFS.<sup>10,11</sup> Bb) based on REF.<sup>12,13</sup> C) based on REF.<sup>14-16</sup> D) based on REF.<sup>17,18</sup>

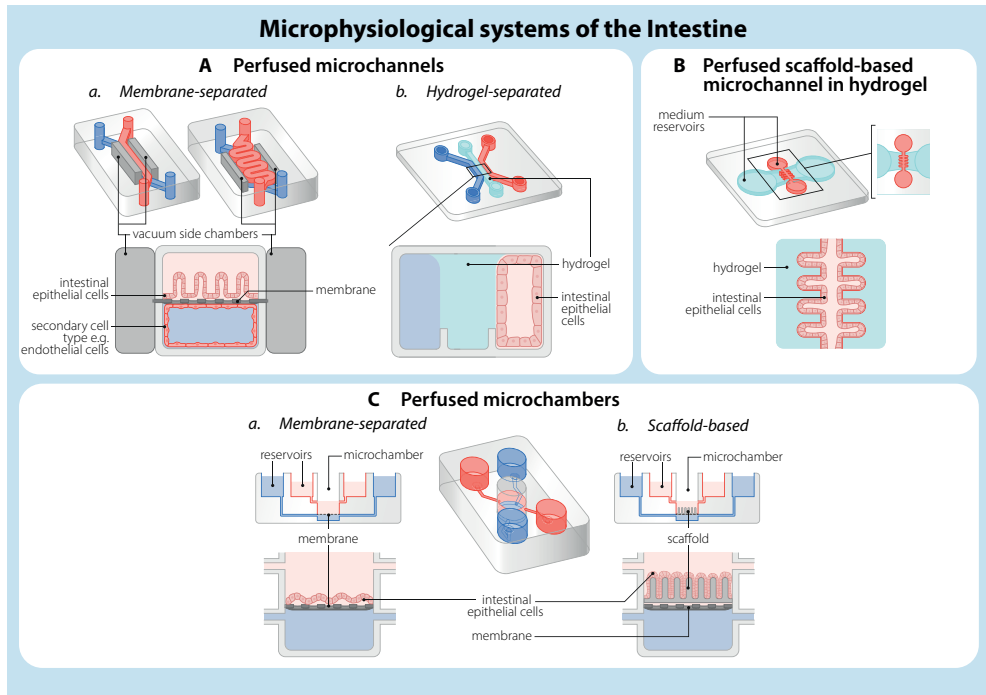


**Figure 3: Design principles of different microphysiological systems of the human intestine**  
 Microphysiological systems of the intestine: Aa) Two aligned channels (upper and lower), separated by porous membrane. Unidirectional pressure-driven fluid flow can be introduced in both channels. The device is made from PDMS, coated with a thin hydrogel layer. Cells can be cultured in both channels. The upper channel is usually seeded with intestinal epithelium and the lower channel with endothelial cells. The channel can either be linear, as on the left side, or bent, as on the right. Two smaller ‘vacuum chambers’ are parallel to the microfluidic channels and to pressurize and stretch the membrane and recapitulate peristaltic movement. Ab) Two aligned channels, separated by a hydrogel layer. Cells can be cultured in all three compartments (also within the hydrogel layer). Bidirectional gravitational fluid flow can be introduced to both channels. The device is made from plastic, coated with a thin layer of hydrogel. Ba) Two microchambers, separated by a porous membrane. Both compartments can be used for cell culture but the upper compartment is usually used. Pressure-driven unidirectional flow (peristaltic pump) can be introduced to both chambers. Bb) Two microchambers, separated by a porous membrane. A scaffold with villus-crypt architecture is located on the membrane. Both compartments can be used for cell culture but the upper compartment is usually used. Gravitational bidirectional flow can be introduced to both chambers. C) One tubular microchannel with villus-crypt architecture created in hydrogel by laser ablation. The device contains two separate media compartments (for perfusion of the microchannel lumen, from left to right, and in the hydrogel above and below the microchannel to create a gradient through the hydrogel). Cells can be grown in the microchannel or in the hydrogel. Unidirectional fluid flow (syringe pump) can be introduced to the microchannel. Aa) based on design by Emulate Inc, Boston, MA, USA and REF.<sup>19,20</sup> Ab) based on design by Mimetas, Oegstgeest, NL and REF.<sup>21,22</sup> Ba) based on REF.<sup>23</sup> Bb) based on REF.<sup>24</sup> C) based on REF.<sup>25</sup>

## Microphysiological systems of the Heart

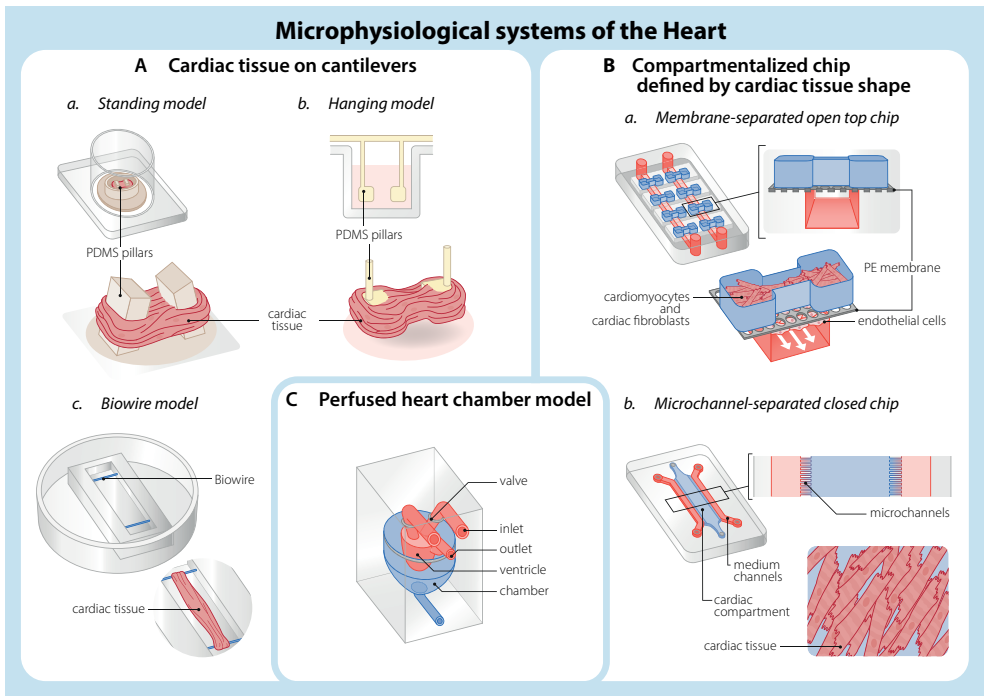


**Figure 4: Design principles of different microphysiological systems of the human heart**

Microphysiological systems of the heart: Aa) Standing rectangular micropillars made of PDMS that fit into 96-well plates. Ab) Hanging cylindrical pillars made of PDMS in a rack of 4 pairs that fit into 24-well plates. Ac) Patterned polystyrene sheets (Biowire). 3D-cardiac tissue is anchored to two horizontal wires within a chamber with two carbon electrodes that allow electrical stimulation. Ba) Open-top compartment system with “dogbone shaped” cardiac tissue on top, separated by a porous membrane. Lower channel is perfusable and can be used as an endothelial cell compartment. Bb) Cardiac tissue confined to the centre channel with side micro-channels to stimulate diffusion of nutrients from the flanking media channels. C) Polycaprolactone (PCL) / gelatin based heart chamber scaffold with input and output channels and a catheter for pressure and volume measurements.

Aa) based on REF.<sup>26,27</sup> Ab) based on REF.<sup>28</sup> Ac) based on REF.<sup>29</sup> Ba) based on REF.<sup>30</sup> Bb) based on REF.<sup>31</sup> C) based on REF.<sup>32</sup>

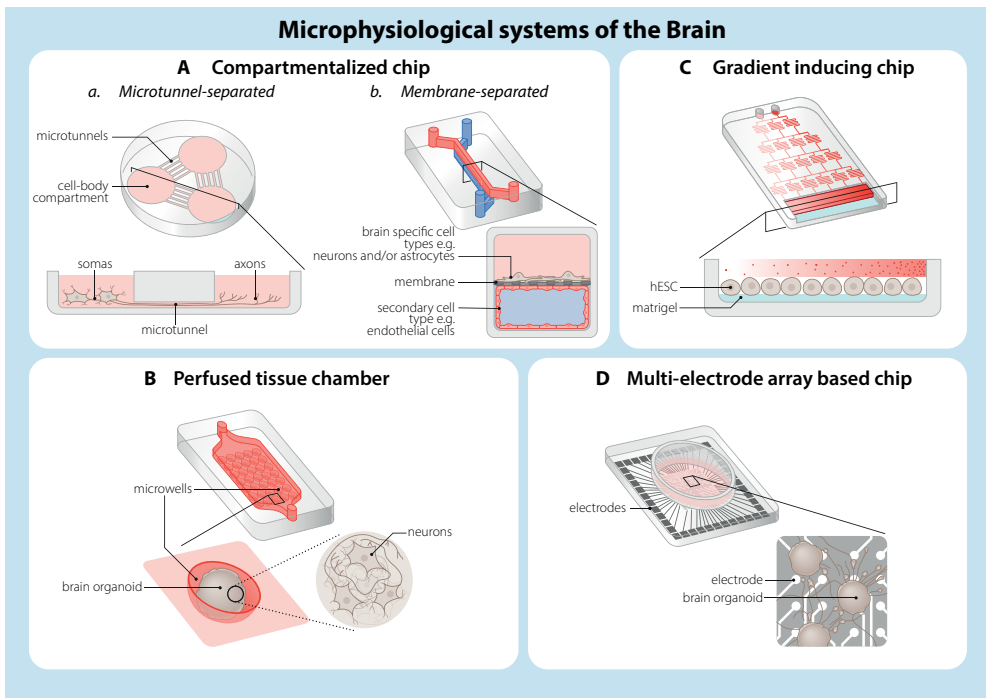


**Figure 5: Design principles of different microphysiological systems of the human brain**

Microphysiological systems of the brain: Aa) Specific cell-cell interactions in compartmentalized systems can be achieved through microtunnel or patterned devices. Here, the device has multiple culture compartments separated by microtunnels, resulting in physical separation of cell bodies of different cell types as they are unable to migrate but their protrusions can extend into a different compartment. Ab) Two aligned channels (upper and lower), separated by porous membrane. Unidirectional pressure-driven fluid flow can be introduced in both channels. The device is made from PDMS, coated with a thin hydrogel layer. Cells can be cultured in both channels. The upper channel is usually seeded with tissue-specific cell types like astrocytes or neurons and the lower channel with endothelial cells. C) Perfused tissue chambers containing microwells to enable culture of brain organoids, while creating interstitial flow. D) Gradient-inducing system created by sequential diffusive mixing of two inlet media, through which a linear growth factor gradient is established over the cell culture area. N) Multi-electrode array based systems have electrodes integrated into the device to measure the longitudinal development of electrophysiological network activity of for example neurons *in vitro* in real-time. Aa) based on REF.<sup>33-35</sup> Ab) based on design by Emulate Inc, Boston, MA, USA and REF.<sup>8</sup> B) based on REF.<sup>36</sup> C) based on REF.<sup>37</sup> D) based on REF.<sup>38</sup>

## Designed features

We first describe physiological features that can be directly implemented and controlled in device design. We focus on how these features have been modeled and measured in an exemplary way in MPS of the vasculature, intestine, heart and brain and emphasize considerations that should be taken into account in comparing *in vitro* with *in vivo* measurements.

Table 1   Quantification of designed and emergent physiological features in microphysiological systems and human in vivo								
Category	Organ	Feature	MPS		In vivo (human)		Ref In MPS	Ref In Vivo
			Method	Quantification	Quantification	Quantification		
Organ architecture	Vessel	Tube diameter	Laser ablation	10-500 $\mu\text{m}$	Arteries: 0.03-2.5 cm, arterioles: 10-300 $\mu\text{m}$ , capillaries: 5-10 $\mu\text{m}$ , venules: 8-100 $\mu\text{m}$ , veins: 0.01-2 cm		39	40
	Intestine	Tube dimensions	3D bioprinting	700-1000 $\mu\text{m}$			17,18	
			Laser ablation	Diameter: 150 $\mu\text{m}$ ; length: 1200 $\mu\text{m}$ ; DLR: 0.125	Diameter: 2.5 cm (SI), 4.8 cm (LI); length: 300 cm (SI), 110-190 cm (LI); DLR: 0.008 (SI), 0.025-0.044 (LI)		24	41
	Heart	Crypt-villus chamber volume	Laser ablation	Crypt: diameter: 50-75 $\mu\text{m}$ ; depth: 170 $\mu\text{m}$ ; DDR: 0.29-0.44	Crypt SI: diameter: 50 $\mu\text{m}$ ; depth: 132-219 $\mu\text{m}$ ; DDR: 0.23-0.38.		32	42-44
			Nanofibrous scaffold	500 $\mu\text{L}$	Villus SI: diameter: 132-165 $\mu\text{m}$ ; height: 273-720 $\mu\text{m}$ ; DHR: 0.18-0.60		33	45
Brain	Regional connections	Compartmentalized system	Connection dentate gyrus - CA3 neurons within hippocampus	Separation of functional and structural neurons between and within brain regions		34	46	
		Compartmentalized system	Two cortical layers	Six cortical layers		34	47	
Fluid flow	Vessel	Wall shear stress	Various pump systems	Arteries: 1.2-1.5 Pa, arterioles: 0.42 Pa, capillaries/venules: 0.03-0.72 Pa, veins: 1 Pa	Arteries: 2.23 Pa, arterioles: 6-14 Pa, capillaries: 1.2 Pa, venules: 0.3-1 Pa, veins: 0.1-0.6 Pa		14, 48-51	52,53
			Syringe pump	4-10%	5-10%		54	55,56
		Circumferential strain						

Designed

Category	Organ	Feature	MPS		Ref In Vivo	
			Method	Quantification		
Fluid flow	Intestine	Wall shear stress	Pressure-driven flow	0.6-6 mPa	~0.2-8 mPa	19, 20, 57, 58
	Brain	Cerebral spinal fluid flow	Syringe pump Miniature osmotic pump	2 mPa 0.15 µl/min	0.02-3 ml/min depending on brain structure	20, 59, 60
Structural deformation	Intestine	Peristalsis	Vacuum chambers lining microchannel	Deformation: 0-30%; Frequency: 0.15 Hz	Deformation: 7.2-27.4% (SI); Frequency: 0-10 Hz (SI), 0.06-0.7 mHz (5-61/day) (LI)	19, 20, 58, 61
	Heart	Afterload	External magnets	0.61-5.40 mN/mm <sup>2</sup>	8.31 mN/mm <sup>2</sup> (human modelling)	62
	Vessel	Tissue elasticity	Tunable synthetic hydrogel	1-6 kPa	Arteries: 50-150 kPa, venous: 3-50 kPa (mouse)	63, 64
	Intestine		Hydrogel	0.75 kPa	SI: 0.6-2.6 kPa, LI: 0.9 kPa	24, 65
Oxygen concentration	Heart		Chemically cross-linked hydrogel	9.64 kPa		66
	Brain		Varying acrylamide/bis composition	1, 13, 90 kPa (soft, normal, stiff)	Fetal: ~1 kPa, adult: ~13 kPa	67, 68
	Vessel	Oxygen concentration	Brain tissue-derived ECM	0.1 kPa	0.4 kPa	69, 70
			Oxygen scavenging channel	1-5%	1-13%	71, 72

Designed

Category	Organ	Feature	MPS		In vivo (human)	Ref In MPS	Ref In Vivo	
			Method	Quantification				
Designed	Oxygen concentration	Oxygen concentration	Integrated oxygen sensor	~0.3-1.5% (Gradient outlet-inlet epithelium channel)	Intestinal lumen: ~4-5% (SI), ~0.4-1.5% (LI)	73	74	
			Hypoxic incubator	1, 5, 21%	5-10%	75	76	
			Hypoxic incubator	5%	1-5%	8	77	
Emergent	Cell type diversity	Cell type diversity	scRNAseq	NA	ECs, SMCs, Pericytes, perivascular fibroblast, Mφ (heterogeneous between tissues and along arteriovenous axis)	-	78	
		Epithelial cell diversity		50% SC, 30% ent, 5-10% dividing cell, 4-5% EEC, 2-3% PC, 2% M-like, 1% gob, 0.5-1% tuft	Ileum: 70-75% ent, 10-11% prog, 5% gob, 4-5% TA, 3-4% SC, 1-2% PC, 0-1% EEC. Colon: 35% prog, 20-22% gob, 15% ent, 12-14% TA, 8-10% PC, 3-4% SC, 0-1% EEC	24	79	
		Cell type diversity		NA	30% cardiomyocyte, 24% fibroblast, 17% mural cell, 12% ECs, 10% immune cell	-	80, 81	
				NA	10 major cell types, highly heterogeneous between brain regions	-	82, 83	
	Cell type localization and interaction	Vessel	Astrocyte coverage of endothelial layer	IF co-localization	9%	100% (rat)	84	85
			Pericyte coverage of endothelial layer	IF co-localization	16%	10-70% average all tissues, 30% BBB (rat)	84	85, 86

Category	Organ	Feature	MPS		Ref In Vivo	
			Method	Quantification		
Cell type localization and interaction	Intestine	Epithelial cell type localization along crypt-villus axis	IF, fluorescence intensity along crypt-villus axis	Score from 0 (base) to 1 (top): proliferative cells 0-0.5, differentiated cells 0.5-1.	87, 88	
	Brain	Regional specification	WNT gradient via microfluidics	Regional development along rostral-caudal axis	36, 89	
		Synapse density	IF	2.2-2.6x103 synapses/ $\mu$ m2	8.6-12.9x108 synapses/mm3	90, 91
		Neurotransmitter release and uptake	In-chip Electrochemical sensors	1-minute timescale	Millisecond timescale (mouse/rat)	92, 93, 94
Inflammatory response	Vessel	Cytokine secretion	Luminex. Il-6	0.3 ng/ml	0.1 - 305 ng/ml	95, 96
	Intestine		Multiplex assay, LPS, IFN- $\gamma$ and TPCA-1 stimulated	Percentage of inhibition: Apical/Basal: IL-8 60%/70%, CCL-20 55%/70%, CXCL10 10%/50%	NA	22
Barrier integrity	Brain		Membrane based antibody array	Upregulation of inflammatory cytokines	Upregulation of inflammatory cytokines	97, 98
	Vessel	Permeability of the endothelial layer	Leakage assay 20 kDa	3x10-6 cm/s	2.4x10-7 cm/s (rat)	9, 99
			Leakage assay 70 kDa	4x10-7 cm/s	1.5x10-7 cm/s (rat)	7, 99
		Permeability of the epithelial layer	Fluorescent tracer leakage (4.4 kDa FD)	P-app: 7.12x10-6 cm/s	0.11-0.12x10 <sup>-6</sup> cm/s (SI), 0.05-0.1x10 <sup>-6</sup> cm/s (LI)	21, 100

Emergent

Category	Organ	Feature	Method	MPS	Quantification	In vivo (human)	Ref In MPS	Ref In Vivo
<b>Barriere integrity</b>	Intestine	Permeability of the epithelial layer	Rhodamine123 permeability	Influx: $5 \times 10^{-6}$ cm/s, efflux: $1 \times 10^{-6}$ cm/s	Quantification	NA	25	-
			LC-MS: caffeine and atenolol	Caffeine: $3.4 \times 10^{-4}$ cm/s, Atenolol: $3.8 \times 10^{-4}$ cm/s	Quantification	Caffeine: $2.93 \times 10^{-4}$ cm/s, Atenolol: $0.2 \times 10^{-4}$ cm/s	23	23
<b>Electrical signaling</b>	Heart	Resting membrane potential	Patch clamp	-97 mV	-90 mV		101	102
			Impaling electrode measurement	-57 mV			103	
			Impaling electrode measurement	$97 \pm 2$ mV	102-110 mV		103	102
	Brain	Conduction velocity	Voltage-sensitive dye and optical-mapping	$47.4 \pm 12.4$ cm/s	30-100 cm/s		104	102
			MEA	0.2 Hz to 3 Hz	0.05 Hz to 500 Hz oscillations		38	105
<b>Renewal</b>	Vessel	Angiogenesis	Imaging	16 $\mu\text{m}/\text{h}$	NA		106	-
			Intestine	EdU pulse-chase: 12h pulse, 10-day chase	4 days for full turnover	3.48 days (average entire GI epithelium)	24	58, 107
		Epithelial turnover rate	EdU pulse-chase: 24h pulse, 96h chase	40 $\mu\text{m}/\text{day}$	38-63 $\mu\text{m}/\text{day}$ (Si, neonatal rat), 216/143 $\mu\text{m}/\text{day}$ (Duodenum/ileum, mouse)		66	108, 109

Data was included based on the criteria as stated in Supplemental Information Note 1. Abbreviations: MPS=microphysiological system, NA=not available, ref=reference, SI=small intestine, LI=large intestine, DLR=diameter-to-length ratio, DDR=diameter-to-depth ratio, DHR=diameter-to-height ratio, ECM=extracellular matrix, GI=gastrointestinal, EC=endothelial cell, SMC=smooth muscle cell, M $\phi$ =macrophage, prog=progenitor cell, SC=stem cell, ent=enterocyte, gob=goblet cell, PC=Paneth(-like) cell, EEC=enteroendocrine cell, TA=transit-amplifying cell, BBB=blood-brain barrier, CRC=colorectal cancer, LC-MS=liquid chromatography-mass spectrometry, IF=immunofluorescence, scRNA-seq=single-cell RNA-sequencing, FD=fluorescein isothiocyanate-dextran, IL=interleukin, IFN=interferon, LPS=lipopolysaccharide, Papp=apparent permeability, m=meter, Hz=Hertz, Pa=Pascal, Hz=Hertz, V=voltage, N=Newton, h=hour, min=minute, s=second.

## Organ architecture

Organ function is highly dependent on its organization and architecture. Stem cell based 3-dimensional (3D) self-organizing tissues, known as organoids, are able to recapitulate aspects of tissue architecture accurately but often suffer from heterogeneity and variability. MPS provide means to guide self-organization and control architecture using different technological approaches, like physical confinement or compartmentalization.

The vasculature and the intestine are essentially cylindrical tubes with diverging diameters (*Table 1*). To date, no single VoC has been designed that covers the entire range of true vessel diameters and most GoCs are at microscale and dimensions are not scaled accurately to the human intestine. VoC solutions for large structures like arteries and veins, that have both endothelial cells and smooth muscle cells, have been the main examples of OoCs converging with tissue engineering where pre-seeded 3D tissues, microfabrication and microfluidics are combined. For example, a new bio-compatible ink composed of alginate, gelatin methacrylate (GelMA), sodium alginate (SA) and glycidyl-methacrylate silk (SilkMA) was used to print tunable hollow microfibers, which could be attached to a microfluidic platform, providing a physiological, biocompatible microenvironment for cell adhesion and proliferation with dimensions comparable to *in vivo* (*Table 1*)<sup>17</sup>. VoCs with small diameters are either single tubular channel approaches, typically modeling vessels of 100-500  $\mu\text{m}$  diameter, while self-assembled vascular networks in hydrogels result in vessels with diameters ranging from 10 to 500  $\mu\text{m}$ <sup>10,14,15,110</sup>. However, these techniques either lack flexibility or diameters cannot be controlled. Laser photoablation has recently circumvented some of these issues. This technique allows high-precision patterning of lumenized structures in hydrogels using focused pulsed lasers<sup>13,39</sup>. This same technique is also suitable for GoC systems, generating perfusable tubular structures with 150  $\mu\text{m}$  diameter containing crypt- and villus-like architecture in a hydrogel<sup>24</sup>. Even though the tube dimensions differ from the human intestine, the method shows promise for emulating intestinal architecture in a controlled manner. Moreover, in most cases it is not the intention to have models the exact size of the human intestine. For scaled *in vitro* model systems, more relevant dimensions are the diameter-to-length ratio of the intestinal tube and diameter-to-height or diameter-to-depth ratio of the villus and crypt respectively, of which the latter is comparable to the human small intestine in the earlier example.

The heart consists of multiple open chambers with specific geometries that are essential for building up the internal pressure necessary to pump blood through the body. Most HoCs do not model the entire geometry of the heart or its individual chambers but rather generate functional cardiac muscle tissues. Some HoCs have modelled the entire architecture or individual chambers either at a macro-scale or by scaling down to microtissue level. Steps towards macro-scale heart chamber geometries have been made by creating ellipsoidal nanofibrous scaffolds, compatible with microfluidic systems and exogenous pressure application, seeded with ventricular human induced pluripotent stem cell (hiPSC)-

derived cardiomyocytes<sup>32</sup>. Ultimately, the chamber geometry and volume is an important determinant of the forces generated on- and by the cardiomyocytes in these engineered chambers. A micro-scale multi-chamber microfluidic device has been developed with integrated sensors capable of measuring the pressure within the chambers. This pressure was induced by pneumatic membranes creating fluid flow in a closed loop covered with HUVECs, with four solenoid valves ensuring unidirectional flow through the four chambers<sup>111</sup>.

For the brain, the most distinctive architectural feature is its spatial organization into different regions and the specific cellular layering within these regions. BoCs have been developed that mimic connections between- and within different mature brain regions by linking compartmentalized co-cultures containing different region-specific neuronal cell types (*Table 1*)<sup>33,35</sup>. On the other hand, mimicking the six neuronal layers of the cortex within these brain regions requires self-organization, which suffers from inherent variability, or compartmentalization of different cell types. This was achieved in a BoCs model using a PDMS stencil that created separate microchambers for seeding different neuronal cell types<sup>34</sup>. Although this BoC model does not completely mimic cortex development *in vivo*, the layered cellular architecture of the cortex can be recreated. In the future, combining these approaches for brain region specification and cellular layering could pave the way in recreating a full (micro)cortex.

These MPS examples describe the technical approaches being used to mimic physiological architecture. Importantly, as discussed for GoC, scaled-down versions of MPS are often practical in use but despite their size, can still be as biologically relevant. More extensive discussion of scaling in MPS technology is provided in the “Conclusion and Outlook” section.

### Fluid flow

Organs in the human body depend on fluid flow to receive nutrients and immune protection and dispose of waste products. Different types of fluid flow can be distinguished: luminal fluid flow, discussed below, and interstitial flow, discussed in *SI Note 5*.

Luminal fluid flow exerts mechanical forces on cells in the tubular wall and is proportional to the local fluid flow rate, local lumen geometry and the viscosity of the fluid. The resulting wall shear stress (WSS) is sensed by the cells and transduced into biological responses such as altered permeability and cellular remodeling. In the vasculature, large internal pressures in combination with wall elasticity result in circumferential strain as an additional force on these cells. Several microfluidic solutions allow establishment of physiologically relevant fluid flow in OoC devices. The highest flow rates in the body are in the arteries. This can best be replicated using peristaltic piezoelectric pumps as they can produce pulsatile flow with high flow rates because of their inherent high frequency output. This was demonstrated experimentally using a piezoelectric braille-pin system to actuate a peristaltic pump that induced high flow rates (30 mm/s) corresponding to up to 1.2 Pa of WSS on endothelial cell cultures<sup>48</sup>. As seen *in vivo*, endothelial cells align and elongate

with increasing flow rates. Pneumatic systems are also used because of their high force output which supports tunable high flow rates. It was shown for example that in hiPSC-derived endothelial cells, arteriovenous specification, quantified by arterial and venous marker expression, could be controlled in a microfluidic set-up with six parallel cell culture chambers with shear stresses of up to 1.5 Pa<sup>49</sup>. Arteriole-like flow profiles and flow rates can be achieved in various microfluidic systems, as long as they have pulsatile flow options. For example, a microfluidic heart-like valve was developed using a pressure system that could reproduce pulsatile flow accurately<sup>50</sup>. While this approach is promising, 0.42 Pa was the maximum achievable WSS, lower than that *in vivo*. Capillaries and venules both require low flow rates with laminar profiles inside a channel just a few microns in diameter. These requirements can be fulfilled in multiple ways. Hydrostatic pressure is one that is easy to use where low flow rates can be approximated by addition of different volumes of media in the microfluidic reservoirs of a device<sup>14</sup>. One disadvantage of this approach is the varying flow rate, and thus WSS, over time. For modeling veins, pressure-driven pumps are preferred since they reproduce a steady non-pulsatile pattern with high flow rate. This was exemplified in a study of the alignment of human umbilical vein endothelial cells (HUVECs) upon recirculation flow at shear stresses up to 1 Pa<sup>51</sup>. Pressure-driven pumps are also commonly used to model the luminal fluid flow in GoCs. One of the first GoCs, developed by the Wyss Institute, used this technique to expose the cells to a physiologically relevant WSS ranging from 0.6 to 6 mPa depending on fluid flow rate<sup>19</sup>. Of note, to simplify the design, most VoC and GoCs model the organ as a straight cylindrical or rectangular microchannel, thereby neglecting the irregular turns that can profoundly impact flow profiles in reality<sup>112</sup>. Recent work accounted for this in a GoC model that integrated a non-linear asymmetric flow profile allowing more precise representation of *in vivo* intestinal flow (*Table 1*)<sup>20</sup>.

Importantly, even though various technologies now support integration of physiologically relevant flow profiles in *in vitro* models, it is essential to verify the biological relevance of the resultant forces for the resident cells. Reporting WSS, instead of absolute fluid flow rate, provides a single measure that can be used to compare OoCs with human physiology since it takes into account channel geometry, fluid properties and flow parameters. Accurately modeling circumferential strain remains technically difficult, however, recent advances such as the use of a template-based tubular VoC coupled to a syringe pump, allowed mimicking of physiological values (*Table 1*)<sup>54</sup>. Future modelling of circumferential strain could be further improved by using new piezoelectric materials (see ‘Technical advances’ section).

### **Structural deformation**

Many organs contain muscle cells that structurally deform the tissue. MPS exploit several principles to induce these types of structural deformation and strain on cells. Several GoC systems include vacuum chambers flanking the microchannels that cause rhythmic

membrane deformation through cyclic suction to mimic peristalsis. This approach can generate physiologically relevant deformation ranging from 0-30% at 0.15 Hz frequency<sup>19</sup>. One recent GoC system displayed a non-linear bent channel, in which the flanking vacuum chambers induce multiaxial cellular deformation, rather than the biaxial deformation of linear microchannels. This better reflects complex human intestinal movement at both macroscopic- and microscopic (villus motility) levels (*Table 1*)<sup>20</sup>. Whereas muscle cells are absent in these GoC models the device design replaces muscle cell function. For MPS of the heart the design is used to stimulate and optionally control the contraction of (cardiac) muscle cells in the system. In this way, the design allows modelling of specific states of heart (or intestinal) contraction, such as afterload, a period of systolic contraction when cells are exposed to increased strain to pump against arterial pressure, or cyclic stretch. Cantilever-based Engineered Heart Tissues (EHTs) mimic afterload by organizing the cardiac tissues around pillars or micropoles on a flexible membrane to pneumatically increase the strain<sup>113</sup>. Alternatively, EHTs can contain small magnets controlled by a piezoelectric stage to modify afterload dynamically *in vitro*<sup>62</sup>. Further work implementing precise control of actuation and stimulation in MPS is ongoing using piezoelectric materials and ionic polymer-metal composites (see 'Technical advances' section).

### Tissue elasticity

Tissue elasticity influences many cellular responses and is often altered during disease as a result of fibrosis. Most cell types react to changes in mechanical properties of ECM by converting mechanical cues into biological responses. Changes in ECM elasticity can convert differentiation in endothelial cells to pathological angiogenesis<sup>64</sup>, cardiomyocyte maturation to heart failure<sup>114</sup>, intestinal stem cell expansion to cancer progression<sup>65</sup> and alter neuronal differentiation, wiring and plasticity<sup>70</sup>.

Tissue elasticity, described by the elastic modulus (E in Pascal) varies per organ in the human body from less than 1 kPa for some soft tissues like the brain and over 10 kPa for muscle tissues<sup>70</sup>. Conventional *in vitro* experiments are often carried out on glass or plastic which is too stiff (in the GPa range). Commonly used alternatives are very soft natural hydrogels such as collagen, fibrin or Matrigel (<1 kPa)<sup>115,116</sup>. Many MPS devices are composed of stiff materials, such as PDMS (0.8-4 MPa)<sup>117</sup>, coated with a thin layer of ECM. Since this does not accurately reflect soft tissue elasticity *in vivo*, natural hydrogels have been used to generate softer scaffolds within these systems. One GoC model used laser ablation to create a microchannel in polymerized hydrogel containing neutralized collagen and Matrigel, resulting in an elastic modulus of 0.75 kPa<sup>24</sup>. This approach led to successful generation of a perfusable microchannel containing villus-crypt architecture. Another way to model soft tissues is to use decellularized human tissue-derived ECM, as shown for a microfluidic BoC system. This provided not only physiologically relevant elasticity but also the wide range of biologically relevant components within the ECM. The model

showed improved cortical layering and electrophysiological function of hiPSC-derived brain organoids<sup>69</sup>. The obvious drawback of this method is the need for human tissue for ECM-derivation, although potential was shown for porcine-derived ECM. Most other tissues, including certain parts of the intestine, have tissue elasticities greater than 1 kPa and thus require modified- or alternative hydrogels. Moreover, as these natural hydrogels are too soft to generate standing structures, stiffer materials are necessary for some applications. One approach is to cross-link natural hydrogels, exemplified by a non-perfused scaffold-guided intestinal tissue model that used chemically cross-linked collagen to increase the hydrogel elasticity to 9.46 kPa<sup>66</sup>. This allowed molding of the hydrogel (via a PDMS stamp) into standing micropillars and microwells that mimicked the architecture of the human small intestine. Alternatively, tunable synthetic hydrogels can be used. These have been shown to be able to mimic the stiffened substrate of the heart during fetal (1 kPa), normal (13 kPa), and diseased (90 kPa) states in 2D<sup>67</sup> and for modeling angiogenic sprouting with physiologically relevant elasticity (1-6 kPa) in 3D (*Table 1*)<sup>63</sup>.

As shown in the examples above, using the right elasticity for MPS remains a balance between ease-of-use and biological compatibility. Future approaches could resolve these issues: for example, new materials, like soft thermoplastic elastomers and chemically enhanced versions of PDMS, are being developed that allow tuning of the elasticity in 3D-cultures and can be used in standard fabrication methods, such as injection molding, hot embossing, 3D printing or micromachining (*Table 1*)<sup>118-120</sup>. In addition, 'smart materials' could be used to quantitatively manage the mechanical properties more accurately, for example based on response to pH variation, ion concentration, temperature, electric field<sup>121,122</sup>.

### **Oxygen concentration**

The vasculature, intestine and heart have unique oxygen profiles that display steep gradients from one region to the other. Most MPS devices are made of gas-permeable polymers such as PDMS and cultured in standard cell culture incubators with supraphysiological oxygen conditions (21% O<sub>2</sub>). Several MPS approaches are available that mimic the *in vivo* oxygen concentration more closely. The most straightforward is placing the PDMS device in an anaerobic incubator. For example, a BoC/VoC-device that models the blood-brain-barrier (BBB) has shown that development under hypoxic conditions (5% O<sub>2</sub>) improved the formation of this barrier, resulting in higher impedance between microfluidic chambers and selective shuttling of drugs and antibodies<sup>8</sup>. Similarly, HoC devices, containing human 3D-cardiac tissues, were placed in environmental chambers with varying oxygen concentrations (1%, 5% and 21%)<sup>75</sup> to study hypoxia, which is crucial in myocardial infarction and to mimic the fibrosis that follows heart damage. While no differences in viability were seen across the different levels of oxygen, the myofibroblast marker,  $\alpha$ -smooth muscle actin, was upregulated and contractile function was impaired. Actively perfusing a system in an oxygen controlled environment can create aerobic and anaerobic compartments within the same device. This

is well-suited for a PDMS-based GoC device placed in an anaerobic chamber, perfused with deoxygenated medium in the top channel and oxygenated medium in the bottom<sup>73</sup>. This created an oxygen gradient that ensured survival of both the anaerobic micro-organisms in the top channel and the human epithelial cell layer growing on the membrane separating the top and bottom channel. Integrated sensors allowed real-time measurement of oxygen tension. Physiologically relevant oxygen concentrations were thus reached (below 0.3% in the epithelial channel; ~10% in the endothelial channel), which supported maintenance of complex human microbial cultures for five days. The same system can be used to create oxygen gradients along the length of the luminal chip channel. A more subtle solution for creating physiologically relevant oxygen concentrations in MPS was shown in a VoC where temporal and spatial regulation of oxygen distribution was achieved in a hydrogel culture chamber by using an oxygen scavenger in the adjacent microfluidic channels<sup>74</sup>. This resulted in controlled and easily adjustable oxygen concentrations within the physiological range of 1-5% and allowed the study of angiogenic bias to hypoxic environments (*Table 1*). In the future, a new generation of polymers for device fabrication with lower permeability to oxygen hold great potential for MPS devices to approximate physiologically relevant oxygen concentrations without using an anaerobic chamber or oxygen scavengers (see 'Technical advances').

## Emergent features

This section describes physiological features that develop as a consequence of device design, microenvironment and functional cell type, and can be measured as a system read-out. We focus on how these features have been modeled and measured quantitatively in MPS of the vasculature, intestine, heart and brain and emphasize considerations that should be taken into account in comparing *in vitro* with *in vivo* measurements. The quantified emergent features that are specific to a single organ are described in the *SI Note 6* and include cellular contraction for the heart, microbiome diversity, mucus layer thickness and digestion and absorption for the intestine and neuron-specific morphological features that support electrical signaling for the brain.

## Cell type diversity

Proper organ function relies on the presence of diverse, often organ-specific, cell types. Most MPS studies only quantify cell-type ratios as input into the system; however, the seeding composition does not necessarily reflect the cell-type diversity at the time that functional read-outs are made, since this will be influenced by the system microenvironment and whether the cells proliferate differentially. Quantification of cell type diversity at the time of read-out is essential for comparing different *in vitro* systems and investigating *in vivo* relevance.

Most MPS studies quantify different cell types by immunofluorescent staining,

which provides insight into both cell type diversity and localization but is limited to established markers and is difficult to quantify. Single-cell RNA sequencing (scRNAseq) is an emerging technique able to quantify cell type diversity in an unbiased manner. A recent GoC study used scRNAseq to provide an unbiased quantification of the intestinal epithelial cell type diversity<sup>24</sup> (Table 1). As an example, but also an exception, we have included this analysis based on intestinal epithelial cells from mice, as it shows the potential of scRNAseq in this context and the identification of rare cell types. However, it would be interesting to use the same technique to quantify intestinal epithelial subtypes of human origin in a GoC system and compare to human *in vivo* data. Aside from brain organoid scRNA studies, there is also a BoC scRNAseq dataset from brain region-specific neurons; however this focussed only on early stage progenitors and neurons and was far from recapitulating the full range of cells found in the adult brain<sup>36</sup>. Although scRNAseq has already been used to investigate cell type diversity of the adult vascular tree and heart *in vivo* (Table 1), it has not yet been used to assess this diversity in MPS. Current VoC systems remain unable to model the full complexity of the vascular tree and have therefore not yet been investigated for heterogeneity in much detail. Most HoC approaches use a combination of cardiomyocytes and fibroblasts, in a typical 4:1 ratio. In addition, certain devices have been fabricated to facilitate specific cellular niches such as a bilayer membrane microfluidic chip which allowed initial separation and transmigration of endothelial cells to the cardiac compartment<sup>123</sup>. However, for both types of HoC devices, cell heterogeneity and comparison to *in vivo* has not yet been assessed.

### **Cell type localization and interaction**

Tissue functionality not only depends on cell type diversity but also on the location of cells within a tissue and their interaction with each other. Spatial organization and co-localization of different cell types can provide insight into tissue-specific micro-environments and intercellular communication. These features have been quantified in different MPS using immunofluorescent staining and microscopy.

A study using a non-perfused scaffold-guided intestinal tissue model described an elegant manner to quantify the spatial organization of intestinal epithelial subtypes along the crypt-villus axis<sup>87</sup>. It was possible to control the distribution of different intestinal epithelial subtypes by creating growth factor gradients. Immunostaining that distinguished 'proliferative' and 'differentiated' epithelial populations was used to quantify their abundance and location along the crypt-villus length. A similar approach was used to characterize the developing human intestine *in vivo*<sup>88</sup>. This approach can be used in GoC models independent of whether tissue is scaffold-guided or self-organized and it allows almost direct comparison with the human intestine *in vivo* (Table 1). In a similar way, the spatial organization of neurons was modelled in a BoC system. The system incorporated microfluidics to mimic the growth factor-gradient along the rostral-caudal axis of the neural tube *in vivo*<sup>36</sup>. This allowed

microfluidic-controlled stem cell differentiation and regionalization, resulting in spatially organized neuronal subpopulations, much like those seen during human brain development

Besides using fluorescent read-outs to quantify cell localization, fluorescence also allows co-localization of different cell types to be studied, indicating possible cell-cell interaction. This method was used in a self-assembling VoC/BoC system of the BBB to quantify coverage of the endothelial abluminal side by both pericytes and astrocytes using maximum projection images of confocal z-stacks<sup>84</sup>. Similarly, the formation of synaptic connections in neuronal cells has been quantified in a BoC with two lateral chambers connected by a central channel through an array of microgrooves. This allows controlled quantification of dopaminergic synapses in the central channel by fluorescent labelling of pre- and post-synaptic markers<sup>90</sup>. However, this quantification was done on a z-projection of a 3D chip culture area; it is therefore challenging to directly compare with numbers in the human cortex which were quantified as the number of synapses per volume (*Table 1*). The potential for a more functional way of quantifying cell-cell interaction in neuronal synapses was exemplified in a BoC system that applied high-temporal resolution electroanalysis of neurotransmitter homeostasis *in vitro*<sup>92</sup>. The dynamics of dopamine uptake and release were quantified by continuous monitoring in human neuroblastoma cells using electrochemical sensing in a microfluidic device. Using this approach, it was possible to monitor kinetics on a 1-minute timescale *in vitro*, as an indirect measure of synaptic responses that occur in much shorter timeframes (~250 msec) (*Table 1*)<sup>94</sup>. A future improvement in quantification of cellular interactions and organization is spatial transcriptomics, which provides an unbiased quantification of cell type diversity and localization in both MPS and primary tissue<sup>124,125</sup>, or microwave technology for analysis in real-time which may provide even more precision (see 'Technical advances' section). Besides quantification of cell co-localization in MPS, functional read-outs are necessary to confirm actual cell-cell interactions within a model system, as exemplified for synaptic interactions in BoCs.

### Inflammatory response

All organs contain immune cells that surveil the tissue and determine when tolerance or an immune response should occur. An inflammatory response can be elicited to protect the body from harmful pathogens through a complex cascade of cellular interactions. This cascade involves the recruitment of circulatory- or tissue-resident immune cells into the affected tissue and is mediated by the secretion of cytokines as means of intercellular communication. Quantification of the number of transmigrated or infiltrated immune cells (discussed in *SI Note 6*) and cytokine secretion are thus clinically relevant proxies for the inflammatory and disease state<sup>126</sup>.

Cytokine secretion can be quantified in serum or blood samples, in principle enabling direct comparison of *in vivo* with *in vitro* concentrations within the vascular system. One VoC system which used this quantitative approach showed physiological

levels of interleukin (IL)-6 (*Table 1*)<sup>127</sup>. However, as cytokine production is local and context-dependent, systemic measurements in body fluids might not reflect concentrations *in vitro* and should be viewed rather as useful indicators. In order to compare cytokine secretion in MPS with different dimensions, normalization to cell number and media volume is required. An alternative is normalization to endothelial cell area, as was done in a template-based tubular system of the BBB<sup>95</sup>. Sampling internal fluids of different organs, such as the intestine, brain and heart, is often not possible, making direct *in vivo* to *in vitro* comparison challenging. One way to address this is to study relative changes in cytokine levels upon exposure to reference compounds (e.g. drugs) that have been studied extensively *in vivo*. This approach was shown to be effective in a GoC model containing two hydrogel-separated perfusable microchannels, one of which was seeded with primary intestinal epithelial cells. Cytokines were measured in the supernatant after stimulation with lipopolysaccharide (LPS) and interferon gamma (IFN- $\gamma$ ) to mimic inflammatory bowel disease (IBD)<sup>22</sup>. TPCA-1, a known anti-inflammatory compound *in vivo*, was shown to reduce this proinflammatory cytokine production of intestinal epithelial cells in a dose-dependent manner. This was more pronounced for basolateral production than apical, underlining the location-specific cytokine fluctuations and the relevance of having access to both sides of polarized cell layers in MPS. Cytokine secretion has also been measured in a 3D multi-cellular BoC-device to study neuroinflammatory responses<sup>97</sup>. The model consisted of hiPSC-derived neurons and astrocytes, grown together with primary human microglia. The activation of microglia was confirmed by the presence of pro-inflammatory cytokines in the culture medium. This model would be valuable to study relative changes induced by drugs or other reference compounds, as done for GoCs.

Since the inflammatory response is a feature that is often used in clinical diagnosis, the comparison of MPS and human observations is valuable for disease modelling and drug discovery. As shown here for selected examples, data from MPS can increasingly be compared directly with clinical outcomes. However, attention is still required for the quantification methods, units and scaling of the model system. If direct comparison is not possible, analysis of relative changes induced by reference compounds that are well-established *in vivo* will be essential to benchmark MPS.

### **Barrier integrity**

The body has several organs that act as selective barriers to regulate transport of nutrients, while protecting tissues from toxins. In the vasculature and intestine, this selective barrier is formed by the combined effect of tight- and adherens junctions between endothelial and epithelial cells, respectively, and the basement membrane. The intestine, as one of the mucosal tissues in the body, has an additional layer of protection from the environment: a layer of mucus covering the epithelial luminal side (discussed in *SI Note 6*).

The integrity of the barrier, for both mucosal and non-mucosal barrier tissues, is

often quantified *in vitro* or *ex vivo* by one of two methods: transendothelial/transepithelial electrical resistance (TEER) or fluorescent tracer leakage. TEER is often used in MPS but may show inconsistency across- or within models. Considerations on quantifying barrier integrity using TEER in a reliable way are given in the 'Technical advances' section. Leakage assays are somewhat easier for use in MPS as compartmentalization and controlled cell area for diffusion allow good reproducibility and standardization. One of the most intensively investigated barriers using this technique is the highly selective and therapeutically important BBB. BBB models are usually based on a standard VoC system to which various types of brain cells are added, most commonly astrocytes, resulting in similar quantification methods for both. Absolute values of solute permeability *in vivo* have been mimicked with a range of VoC models<sup>128</sup>; however, some systems remain more suitable than others for direct *in vivo* comparison. It is important that designed features influencing permeability, such as vessel geometry and flow rate, are standardized. This favors rectangular and tubular microchannel VoCs over self-assembling vascular networks with higher diameter variability. For example, standard diameter microchannels under continuous unidirectional flow that were suitable for long-term assessment of endothelial cell permeability indicated 70 kDa permeability ( $4 \times 10^{-7}$  cm/s), which is similar to rat vessels *in vivo* (Table 1)<sup>7</sup>. Application of unidirectional flow still requires more complex microfluidic set-ups, generally limiting the throughput of permeability measurements. One solution, which has been used for both VoC and GoC systems, is based on microtiter format plates that incorporate bi-directional flow and allow real-time monitoring of fluorescent tracer leakage into a hydrogel lining the tissue channel<sup>9,21</sup>. Distinct fluorescent tracers can be used to quantify bi-directional permeability of a barrier, as they are transported through passive paracellular absorption in the influx direction and carrier-mediated transport in the efflux direction, as was shown for rhodamine 123 in a perfused GoC microchamber<sup>25,129</sup>.

Whilst fluorescent tracers are valuable in comparing permeability of different model systems and *ex vivo* data, for comparison with human tissues *in vivo* it is essential to have a set of reference compounds for which translocation properties in humans are known, such as food-derived components or drugs. This was exemplified in a GoC study which described apparent permeability values of two reference molecules, caffeine and atenolol, with well-known transmucosal permeability *in vivo*<sup>23</sup> (Table 1). This can be advanced by the integration of electrochemical sensors in devices allowing real-time measurement of a diverse range of compounds in OoC flow-through with high sensitivity, as detailed in the 'Technical advances' section'.

### Electrical signaling

Multiple tissues in the human body use electrical signals to propagate functional information from cell to cell. In the brain, electrical signals orchestrate neuronal communication, while in the heart they are key for muscle contraction. These electrical signals are the result of highly

temporally regulated flow of ions across the plasma membrane of individual cells. While this basic mechanism is conserved, the architecture and function of the different organs has evolved such that these cells have very distinguishable features; this is discussed specifically for the brain in *SI Note 6*.

The specific morphology of electrically active cells results in efficient conduction of membrane currents. The conduction velocity of these currents within tissues depends on cell geometry and spatial patterning of the gap junctions which connect neighbouring cells<sup>130</sup>. Since PDMS is transparent, voltage-sensitive dyes can be used to measure conduction velocity in 3D tissues. One study using a pillar-based EHT model found that the conduction velocity in human embryonic stem cell derived-cardiomyocytes was comparable to that of healthy human heart (*Table 1*)<sup>104</sup>. Other electrophysiological parameters, such as resting membrane potential, action potential and excitation threshold are dependent on the abundance and localization of ion channels in the cardiomyocyte- and neuronal membranes<sup>131,132</sup>. Measuring these features *in vitro* involves impaling single cells with a glass electrode in a method referred to as whole-cell patch-clamp<sup>133</sup>. Similar (external) techniques are being used to assess the electrical activity of cells in MPS. For example, using 3D-cardiac tissue with standing pillars, impaled electrodes showed the resting membrane potential was slightly lower than physiological but the action potential amplitude was about  $97 \pm 2$  mV, close to that in mature cardiomyocytes<sup>103</sup> (*Table 1*). Sharp electrode measurements showed that hiPSC-derived cardiomyocytes from dissociated cardiac bio-wire models had similar resting membrane potentials ( $-97$  mV) to adult human cardiomyocytes. Nevertheless, these types of measurement remain low throughput and technically challenging while it would be beneficial to integrate electrical readout in the devices for continuous readout. One alternative with greater ease-of-use and continuous electrophysiological measurements are multielectrode arrays (MEAs). In MPS of the heart, MEAs have been integrated in flexible and patterned PDMS membranes allowing measurement of electrical activity in aligned myocardium to which mechanical strain can be applied to the monolayer simultaneously<sup>134</sup>. For MPS of the brain, 3D high-density MEAs have been developed to measure the dynamics in 3D brain organoids at cellular resolution<sup>135</sup>. Measurement of brain organoids on MEAs revealed complex oscillatory waves that mimic activity in preterm neonates<sup>38</sup>. Highly synchronous events were detected at 0.2 Hz burst frequency and 3 Hz local field potential, much like those *in vivo* (*Table 1*). New developments include MEAs made of flexible, optically transparent electrodes poly(3,4-ethylenedioxythiophene) polystyrene sulfonate (PEDOT:PSS)-based polymeric electrodes, which allow simultaneous imaging of cells and measurement of electrical field potential<sup>136</sup>, and the integration of flexible 3D electrodes into MEA platforms for spatial mapping across 3D tissue volumes<sup>137</sup>. Alternatives to these traditional electrophysiological measurements are high-frequency imaging using voltage- and calcium-sensitive dyes or genetically-encoded voltage- (GEVI) and calcium (GECI) indicators. These permit continuous monitoring of electrical activity in cell cultures, while

avoiding terminal endpoint measurements<sup>138</sup>.

### Renewal

Turnover and cell renewal rates vary greatly per organ. The intestine has one of the highest turnover rates and cells are replaced continuously, whilst the heart and brain have very little regenerative capacity<sup>139</sup>. The vasculature also has a relatively slow and location-dependent turnover rate but retains the capacity for wound healing and the formation of new blood vessels from existing ones (angiogenesis) after, for example, damage.

Intestinal epithelial cells undergo directional migration from the crypt to the villus tip to sustain the high turnover rate. This process has been studied in perfused tubular scaffold-based GoCs using 5-ethynyl-2'-deoxyuridine (EdU) pulse-chase to monitor cell division over time<sup>24</sup>. Four days after the EdU pulse, all labelled cells had been shed into the luminal space and none remained in the epithelial layer, marking full-turnover, in line with the turnover rate of the human intestine. Of note, the distance cells travel from the crypt to the villus tip in GoCs is often not representative of the distance travelled in the human intestine. Therefore, an alternative approach would be to quantify the migration speed of the epithelial cells. This was measured using the same EdU pulse-chase method to be 40  $\mu\text{m}/\text{day}$  in a non-perfused scaffold-guided intestinal tissue model<sup>66</sup>, which falls within the range measured in neonatal rat small intestine but is lower than values in mice (*Table 1*). A reference value for the human intestine has not been reported to our knowledge. Via similar immunostaining techniques, the migration of endothelial cells during angiogenesis was studied in VoC models. Since angiogenesis is often disease- or development-related, extrapolating *in vivo* values to benchmark *in vitro* assays is challenging. VoC models however do provide opportunities to study which parameters might influence the process. One such model consists of multiple parallel microfluidic channels which can be filled with either hydrogel or culture medium to investigate how mechanical cues, like interstitial flow modulated by hydrostatic pressure differences over the channels, affect angiogenesis (*Table 1*)<sup>106</sup>. Immunofluorescent imaging was used to quantify sprout number, length and nuclear translocation within the sprouts at different timepoints. Another study quantified sprout formation kinetics using fluorescently tagged vascular and lymphatic endothelial cells in two parallel microchannels to investigate vascular and lymph angiogenesis in the same hydrogel<sup>140</sup>. Quantitative comparison of angiogenesis in these VoC systems would benefit from consistent reporting of angiogenesis in  $\mu\text{m}/\text{hour}$ .

### Technical advances to improve quantification of physiological features in microphysiological systems

As evident from the previous sections, quantitative control of physiological features is still limited in MPS. This is in part due to lack of awareness on how important it is to report quantitative data and refer them to *in vivo* physiology. In addition, however, many quantitative

culture parameters are impossible to engineer or measure in the current generation of MPS. In the following section, we describe upcoming technologies which could improve or enable quantification in one or multiple organ model systems.

### **Designed features**

Technical advances in device design could lead to better approximation of the tissue environment or architecture to that *in vivo* or improve quantitative control of physiological features (Figure 6).

### **Materials**

MPS materials can profoundly impact the control of features as they dictate biocompatibility, stiffness, optical transparency, gas permeability, absorption of small molecules, manufacturability and reliability of the devices. PDMS is the most common elastomer used to manufacture MPS; however, despite many advantages, PDMS shows hydrophobic recovery<sup>141</sup>, high and non-specific absorption of small hydrophobic molecules<sup>142</sup>, and high gas permeability<sup>143,144</sup>, which challenges the control of some physiological features. For instance, maintaining hypoxia or an oxygen gradient in VoCs and GoCs requires tight regulation of oxygen concentration. In addition, PDMS may interfere with establishing growth factor gradients or measuring secreted molecules (e.g. neurotransmitters, cytokines, metabolized drugs). Alternatives to pristine PDMS include PDMS-based elastomers with tailored long-lasting bulk<sup>145</sup> and surface<sup>146,147</sup> hydrophilicity, thermoplastic elastomers (sTPE) and off-stoichiometric thiol-ene (OSTE) polymers. sTPEs are biocompatible, optically transparent, and amenable to high throughput fabrication (e.g. by injection moulding) since they combine the properties of thermoplastics and elastomers<sup>148</sup>. Importantly, sTPEs show lower small-molecule absorption<sup>149</sup> and oxygen permeability than PDMS (2-50 Barrer versus 500 Barrer)<sup>150</sup>. OSTE polymers are also optically-transparent elastomers featuring lower small-molecule absorption and more stable surface modification capabilities than PDMS, and a wide range of stoichiometry-dependent stiffness<sup>119</sup>. The lower oxygen permeability of both materials enables better modeling of hypoxic conditions in vessels and intestine without needing anaerobic incubators.

### **Actuation and stimulation**

Stimulation and actuation in MPS are important to mimic the dynamic microenvironment in some organs. Examples of actuation are mimicking the peristaltic movement in the intestine, recreating circumferential strain in the vasculature, or modeling of the strain seen in the beating heart.

Piezoelectric materials can be used for actuation of tissues within MPS. Unlike piezoresistive materials commonly used for strain sensing<sup>151,152</sup>, piezoelectric materials can transduce electrical signals to mechanical movement and reciprocally sense mechanical

motion to convert it to an electrical signal. They can thus be used as both micro-actuators and sensors in MPS. Piezoelectric cantilevers have been used to electrically induce mechanical bending; additionally, when hiPSC-derived cardiomyocytes were cultured directly on the cantilevers, their contraction dynamics and alterations upon drug exposure could be sensed by the cantilevers<sup>153</sup>. To a lesser extent, certain types of electro-active polymers also show reciprocal transduction between mechanical and electrical signals. Ionic polymer-metal composites (IPMCs) represent one such type of polymers, which in turn offer higher biocompatibility and softness than typical piezoelectric materials<sup>154</sup>. Additionally, IPMCs benefit from hydration with solutions containing ions, such as phosphate-buffered saline (PBS) and cell culture media, making them well-suited for use in long-term cell culture experiments. Besides their biocompatibility and low driving voltage, several examples illustrated the potential of IPMCs in modeling artificial muscles<sup>169</sup>, in the form of mechanical stimulation of tissues<sup>155</sup>, and enabling active microfluidic components such as micropumps<sup>156,157</sup>. Piezoelectric materials and IPMCs could conceivably be tailored to envelop tubular structures and thus induce mechanical motion: they could be integrated to generate physiologically relevant circumferential strain values in a vessel model and peristaltic movement in an intestine model, without needing external pressure sources and vacuum chambers. Although, at present, these materials exert less force than pneumatic alternatives, they hold great potential to simplify the geometry and fabrication of MPS by enabling electrically-activated movements in specified locations of the device (e.g. membranes, pillars).

One alternative for stimulation, optogenetics, requires genetic engineering of cells but can actuate muscle contraction very accurately. Local optogenetic stimulation of engineered light-sensitive tissues *in vitro* is enabled by the optical transparency of MPS, as demonstrated in a 3D model of 'Amyotrophic Lateral Sclerosis-on-Chip' where light was used to activate muscle contraction<sup>158</sup>.

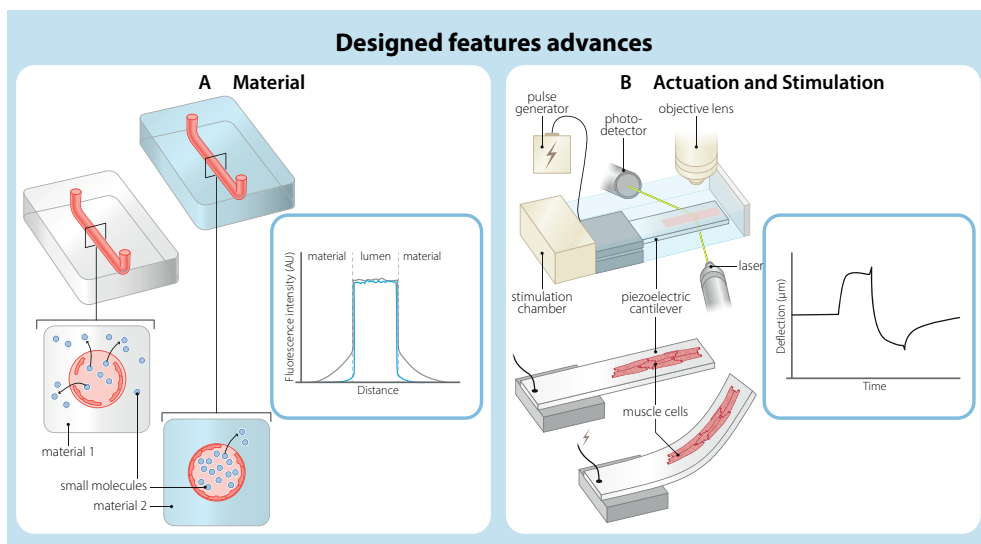


**Figure 6: Technical advances that improve the quantification of designed and emergent physiological features in microphysiological systems.**

Technical advances in materials and actuation or stimulation methods can improve the approximation of *in vivo* observations and quantitative control of designed features. A) Materials. Several features of structural materials can be tailored for MPS use. In particular, small molecule absorption by common elastomers such as PDMS can be overcome by using alternative polymers, as well as by implementing alternative elastomer formulations or targeted surface functionalizations, which enhance long-term hydrophilicity and may additionally favor cell adhesion. B) Actuation and stimulation. Local stimulation of tissues can be provided by means of mechanical structures made of electrically-responsive materials, such as piezoelectric materials and electro-active polymers. As an example, patterned piezoelectric cantilevers can bend upon electric input to provide controlled stretching to thin muscular films or cardiac tissues. Displacement of the cantilever can be tracked by optical means and correlated to induced tissue deformation. The inverse piezoelectric effect could in turn be exploited to detect inherent tissue motion. A) Based on REF.<sup>119,149</sup> B) Based on REF.<sup>153</sup>

## Emergent features

There are multiple technical advances that could improve quantification or real-time monitoring of physiological features in MPS. They can be subdivided into electrical, electrochemical, optical and microwave sensing (Figure 7). As discussed previously, most current and commonly used MPS lack embedded sensing modalities, thereby limiting the number of physiological features that can be quantified. The techniques discussed here can be integrated into MPS as sensors, which enables higher sensitivity and reliability due to reduced distance between biological cue and sensor (*in situ* sensing), and provides real-time data that can yield direct feedback in an ongoing experiment. It should be noted that in most cases the sensing structures integrated into the MPS need to be coupled to external input and/or readout units, which may limit the portability of the MPS itself and the use of the MPS in conditioned environments, such as cell culture incubators. Design of external units

which are portable or compact enough to be combined with- and ultimately embedded in the MPS should be encouraged. The standardized interfacing of open platforms can provide improvements to this end, as described in *SI Note 7*.

Electrical, electrochemical, optical and microwave sensing options enable the quantification of similar physiological features with different techniques. As the integration of these sensing modalities within MPS is still in development and will be further optimized, it is still too early to quantitatively compare and establish which technique is best suited for the measurement of which feature. In the future, quantification of features using different available sensing options will provide insight in this respect.

### Electrical Sensing

One of the most widely used electrical sensing systems is TEER, commonly employed in systems modeling barrier tissues, such as VoCs, GoCs and Skin-on-Chips for quantitative barrier integrity assessment, as described earlier. TEER is usually based on applying voltage at DC or at a single and low frequency (e.g. 12.5 Hz or 75 Hz in common commercially available tools). By contrast, impedance spectroscopy (IS) uses voltage frequency sweeps to additionally quantify capacitive contributions to impedance in combination with equivalent electric circuit analysis<sup>159</sup>. IS can be useful to quantify TEER and other features, such as villus-like fold formation in GoCs<sup>160</sup> and development of epidermal multilayer structure in Skin-on-Chip<sup>161</sup>. While straightforward for quantification, barrier integrity measurements are prone to inconsistency and are difficult to standardize, making comparisons difficult. Specifically, non-uniform current density over the area of cell coverage, monitoring the whole cell layer rather than around the electrodes only, differences in temperature, system-to-system differences and measurement repeatability, and long-term electrode saturation remain challenges. One solution is to use correction factors for some of these parameters<sup>162,163</sup>. Importantly, sensitivity field calculations can help optimize electrode geometry and configuration to focus the measurement on the desired device volume<sup>164</sup>. Higher sensitivity can be obtained by specifically placing and multiplexing electrodes either on the side of the device culture area<sup>165</sup> or on membranes<sup>166</sup>.

IS can be extended in a single MPS device by combination with additional multi-electrode arrays<sup>167</sup> and with sensors monitoring e.g. pH, oxygen content or specific biomarkers. The additional sensors may also be based on electric impedance measurement, as achieved through the functionalization of the electrode surface with selective chemistry<sup>168</sup>. IS can be further improved and adapted for 3D tissues and cell constructs by integrating electrodes within confining 3D geometries (e.g. microfluidic traps<sup>169</sup>, pendant drops<sup>170</sup>) and in combination with 3D scaffolds<sup>171</sup>. Whereas most common scaffolds, made from gels or hydrogels, are electrically passive, use of electroactive polymeric scaffolds for IS with promising outcomes has also been reported. For instance, hollow tubular PEDOT:PSS structures can be used to grow intestinal epithelial cells for 26 days. The electrical properties

of the PEDOT:PSS scaffold promote better coupling of cells to electrode, and the position of the electrodes allows them to have dual sensing modalities: electrode-mode and transistor-mode. This allows monitoring of cell substrate coverage and sensing constriction in tubular structures, as in vascular reactivity<sup>172</sup>.

### **Electrochemical sensing**

Electrochemical sensors convert the effect of electrochemical interactions between analytes and electrodes into electrical signals. The surface of sensing electrodes can be functionalized by biomarkers tailored for selectivity and sensitivity<sup>173</sup>. Integrated within MPS, miniature affinity-based electrochemical sensors can be used for continuous monitoring of (secreted) biomarkers, providing real-time read-outs of biological responses and thus opportunities to correct and control fluctuations within an experiment<sup>174</sup>. Multiplexing of read-outs from multiple selective sensors or sensor electrodes can additionally enable high-throughput sensing of several biochemical markers<sup>168</sup>. This makes electrochemical sensors powerful alternatives to standard enzyme-linked immunosorbent assay (ELISA) protein measurements in culture medium and enables the quantification of multiple physiological features in OoC flow-through in real-time, such as secreted cytokines, (drug) metabolites and transport of compounds over a cell layer<sup>175</sup>. Recently, functionalized electrochemical sensors were integrated into a multi-OoC platform (liver-heart) to measure three different biomarkers (albumin, GST- $\alpha$  and CK-MB). The reported detection limit of albumin (0.1 ng/mL) showed superior range and sensitivity<sup>176,177</sup> compared to clinical tests on blood and urine in which the normal range is between 0.034-0.054 g/mL. This demonstrates that this type of readout is particularly suitable for quantitative comparison of different biomarkers and small analytes in MPS with clinical measurements of the same compounds in urine and blood.

The functionality of electrochemical sensors depends on the spatial distribution and position of electrodes within the MPS. The use of miniaturized electrochemical sensors that inherently amplify electric signals, represented by a class of field-effect transistors (FETs), allows integration of many sensors, increasing the spatial resolution of detection of analytes throughout the system<sup>178</sup>.

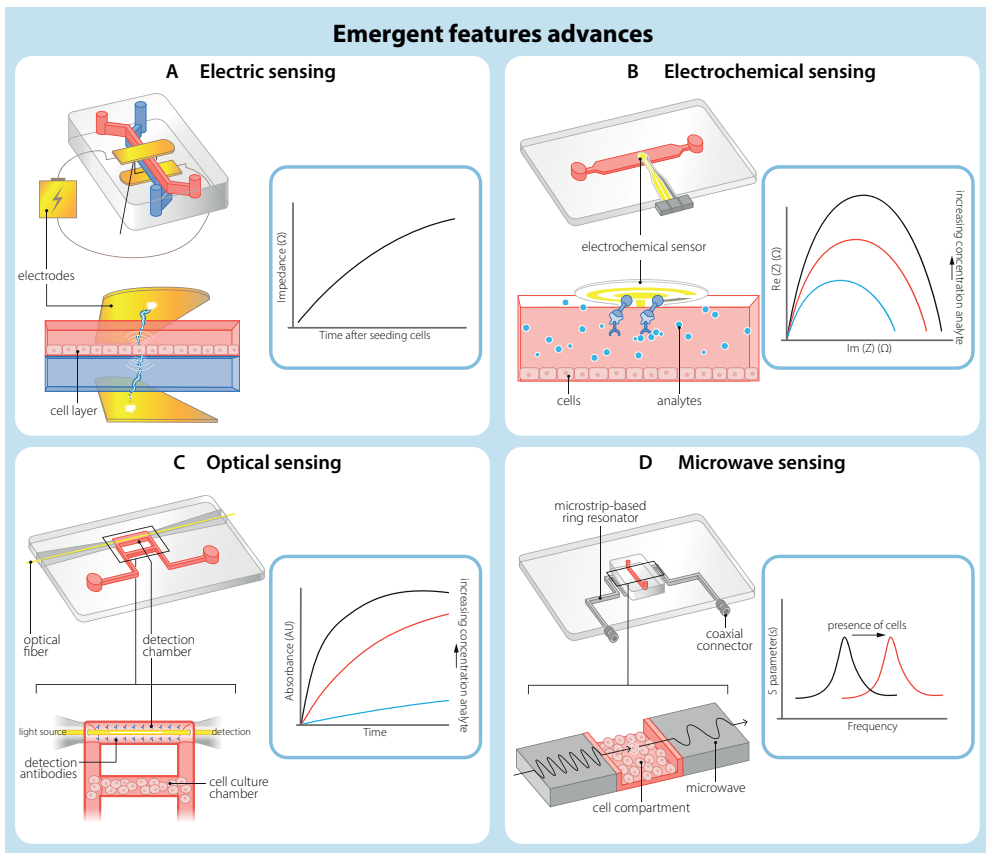


**Figure 7: Technical advances that improve the quantification of emergent physiological features in microphysiological systems.**

Technical advances in electrical sensing, electrochemical sensing, optical sensing and microwave sensing can yield advanced read-out systems that enable or improve quantification of emergent features. Most of these sensing solutions are based on electrodes and thin film technology originally developed for microelectronics, thus inheriting much available expertise and advantages in miniaturization, integrability and scalability. A) Electric sensing. Electric parameters of tissues, such as their resistance and capacitance (i.e. electric impedance), can be monitored continuously and correlated with their functionality (e.g. tightness of a tissue barrier, tissue composition). Measurements of trans-epithelial or -endothelial resistance and more generally impedance spectroscopy can be conducted by flanking tissues with pairs of electrodes and subjecting the tissues to electric fields of a range of frequencies. B) Electrochemical sensing. In electrochemical sensing, both amperometric and voltametric, surface chemical reactions can be exploited to trigger an electric output correlated to changes in the local microenvironment, as caused by e.g. tissue metabolism, medium composition. Selective surface functionalization of electrodes enables a high degree of selectivity and multiplexing. C) Optical sensing. Besides enabling optical inspection by microscopy, lightwaves are convenient sensing beacons, since parameters of lightwaves such as frequency, amplitude and their interference can be extremely sensitive to changes in the optical path, such as medium density and transparency. This makes integrating optical waveguiding structures such as optical fibers appealing for MPS applications. D) Microwave sensing. Microwaves occupy a specific portion of the electromagnetic spectrum, and can be injected and confined within microengineered structures, such as ring oscillators based on microstrip lines.

*They are thereby useful as sensitive detectors of local changes in permittivity induced by e.g. cells or medium composition. A) Based on REF.<sup>160</sup> B) Based on REF.<sup>179</sup> C) Based on REF.<sup>176</sup> D) Based on REF.<sup>180</sup>*

## **Optical Sensing**

Optical sensors commonly detect changes in optical or geometrical properties (e.g. color, luminescence, absorption, scattering, refractive index, size and shape depending on geometric boundaries) of media and of their local environment by measuring changes in the properties of optical waves (amplitude, wavelength, phase) used as probes. In MPS, the changes can be caused by a variety of factors, such as tissue metabolism and dynamics, and media composition including analytes of interest and optical reporters<sup>181</sup>.

Optical sensors can monitor small biological cues such as cytokines, providing opportunities to standardize MPS platforms. In one example, microfluidics was integrated with an optical fiber-based sensing unit measuring optical absorbance to quantify IL-2 secreted by lymphocytes. This photonic Lab-on-Chip (Ph-LoC) provides an alternative to an ELISA. IL-2 concentrations ranging from 50 to 1000 pg/mL could be measured in just 30 minutes. The range and application of this Ph-LoC depends on antibody availability but is already suitable for monitoring of most common cytokines<sup>179</sup>. It is also possible to multiplex this platform and simultaneously quantify different cytokines using an array of silicon photonic micro ring resonators. The shifts in resonance wavelength upon binding of the target molecule to the ring surface distinguishes the different cytokines, without needing specific labeling and enabling continuous measurements, opposite to currently used techniques<sup>182</sup>.

Quantification of many physiological features in MPS, such as the tissue architecture, cell morphology, mucus layer thickness, cell surface area and fluid flow rate, often relies on imaging technologies able to penetrate tissues and substrate materials while maintaining good resolution. Optical coherence tomography (OCT) provides an imaging method that allows real-time 3D imaging of (relatively large) structures in MPS without using immunostaining or fluorescent reporter lines<sup>183</sup>. The technique is based on measuring the interference between a reference light beam and backscattered light to reconstruct the profile of the sample under consideration; the imaging depth can reach to more than 1 mm<sup>184</sup>; however resolution is somewhat lower than conventional microscopy (~6 μm versus < 1 μm, respectively)<sup>185</sup>. This imaging technique enables in particular continuous monitoring and quantification of 3D (luminal) structures in MPS and was used to study sprouting angiogenesis in a VoC model and engineered microvessels in a MPS of the outer blood-retinal barrier<sup>185,186</sup>.

## **Microwave Sensing**

Similar to electric impedance and optical sensing, electromagnetic waves in the microwave range (~1-40 GHz) can be used for contactless sensing as well. In this case, the sensing

principle is based on measuring how the electromagnetic waves interact with and penetrate into materials. Penetration depends on frequency and the electrical characteristics of the material, mainly the permittivity. Electromagnetic waves at microwave frequencies can penetrate the cell, while leaving it intact<sup>187</sup>, and reveal information about the intracellular composition<sup>188</sup>. This biosensing alternative allows label-free, non-intrusive, real-time discrimination, localization and counting of cells<sup>189</sup>, and can specifically be useful to quantify cell type ratios at any given time in MPS.

A microwave sensor based on impedance spectroscopy was proposed which could determine cell diversity at the single-cell level, demonstrating label-free cell identification at microwave frequencies<sup>187</sup>. A real-time and flow-through sensor was developed within an integrated multi-mode microwave resonator which was able to distinguish two different cancer cell lines, HeLa and MDA-MB-157, in mixed populations<sup>190</sup>. In the future, integration of real-time microwave sensors could improve quantification of different cell types within a culture platform and reveal spatial information of individual cells within a 3D tissue. This real-time information on the numbers and ratios of different cell types in MPS will facilitate standardized quantification of other physiological features that depend on normalization to the number of a specific cell type.

Additionally, microwave supporting structures such as resonators and microstrip lines can be embedded into microfluidic systems as part of highly sensitive sensors for flow rates and fluid composition with an electric readout. Split ring microwave resonators coupled to an interferometric system were used for high-sensitivity measurement of glucose concentration in a microfluidic setup<sup>191</sup>. A fluid flow sensor embedded in a microfluidic device exploited the flow rate-dependent deformation of a thin circular membrane integrated within a planar microwave ring resonator, and the subsequent alteration of the effective permittivity of the surrounding medium, to measure flow rates in the range of 0.5 to 300  $\mu\text{L}/\text{min}$  with a resolution of 1  $\mu\text{L}/\text{min}$ <sup>192</sup>. These and similar systems are supported by accurate analytical and numerical models to predict and quantify sensor performance, and by electronic readout systems which could be integrated into compact electric layers (e.g. printed circuit boards) connected to the sensing structures.

## Conclusion and Outlook

MPS are clearly poised to contribute to biomedical research, but in order to take the technology to the next level and realize end-user and regulatory acceptance, it is essential to understand their predictive value. With the growing number of users in this relatively new field, it is widely accepted that consensus on qualification and standardization methods for MPS technology is urgent to realize their full potential. Quantification of physiological features in design and read-outs of MPS leads the way towards establishing accurate comparisons between different *in vitro* models and *in vivo* (human) physiology, contributing to development of measurable standards to qualify MPS as fit-for-purpose in application.

The comprehensive overview of quantified physiological features of healthy organ function in MPS, as provided in this review, serves as a resource for the development of these measurable standards and can be used as basis for the quantification of disease phenotypes and drug efficacy and toxicity, which are defined by deviations in the same physiological features. These type of quantifications will be key to uncover the predictive value of MPS and accelerate the implementation of MPS in the drug development pipeline.

MPS are specifically suitable for providing quantitative approximations of diverse physiological features as they allow versatile designs and integration of sensors and read-out methods. Categorizing the desired quantifiable physiological features in designed (directly translatable in device design or input) and emergent features (emerging cellular function) will facilitate quantification in MPS, as both types of features require different strategies. For quantifying designed features, it is essential to consider the relevant technology or material needed to incorporate a specific feature in MPS design in the desired range. Quantification of emergent features requires incorporation of the relevant sensing and read-out system to accurately monitor cellular responses using standardized methods and units. To further steer the exact value of an emergent feature, which might be required to qualify the system fit-for-purpose, the designed features that influence the emergent feature need to be determined and adapted. The examples and considerations highlighted in this review will allow users to select the relevant design options and sensing technologies to optimize quantification of the designed and emergent features of interest. These examples demonstrate that current work already allows direct comparison of data from MPS with *in vivo* measures, however, they also reveal room for improvement. Current limitations in quantitative comparisons of physiological features in MPS with *in vivo* observations include differences in scale, methods of quantification, resolution and duration.

While MPS generally try to mimic *in vivo* tissue architecture, their main goal is to recapitulate one or multiple functional features of an organ, depending on the research question of interest. As such, they do not necessarily have to recapitulate the exact dimensions of the human body. When functional features are investigated which are influenced by the dimensions of the tissue, scaling and normalization becomes a necessity. To compare *in vitro* MPS with *in vivo* measurements, it is essential to correct for differences in surface-to-volume and cell-to-volume ratios<sup>193</sup>. In some cases, it might be sufficient simply to normalize to liquid volume, number of cells and dimensions (e.g. when converting absolute fluid flow rate to WSS); however, for more complex features and systems there will be new opportunities to integrate *in silico* modeling to address this issue, as done previously for a multi-organ platform<sup>194</sup>.

When the quantification method of a specific physiological feature differs between systems, it becomes more difficult to compare data accurately. Specifically, for emergent features that describe complex cellular functions, many different quantification methods and units are used. More clarity is needed on how data is measured and reported in clinical

settings and whether it is feasible to replicate this in model systems. For certain features, this is more straightforward e.g. measurement of secreted products in circulation and flow through, than for others e.g. barrier integrity measurement. For physiological features that are not amenable to such a direct translation of measurement method, the field should reach consensus on how to quantify and report the data in a standardized way. This review has outlined a basis for the standardization of quantification methods and data reporting for some important physiological features.

Some of these features are location- and time-dependent and can be quantified in high resolution in MPS but not *in vivo* (e.g. cytokine secretion). For these features it is currently difficult to have a direct comparison between MPS and *in vivo* data. One solution is focusing on the relative changes in cellular function induced by clinically tested reference compounds. These will be valuable benchmark measures for drug development and useful for the uptake of MPS technology by regulatory authorities and pharmaceutical companies. In the future, coupling multi organ-chips might allow modelling of local and systemic responses.

MPS are designed at present to mimic and monitor aspects of tissue (patho) physiology over relatively short periods of days or weeks. Drug responses and clearance by tissues in the MPS are likewise acute, but chronic effects of drugs for example cannot be monitored since long-term culture of cells in the devices has only been realised in a limited number of cases. Achieving this will require at a minimum next-generation devices, materials, pumps and sensors as well as culture media that are better mimics of body fluids. It may then be possible to couple multiple MPS devices in series or parallel to mimic organ and tissue interactions in the human body as never before.

Finally, the next level of MPS will require greater precision in exactly what is being captured by sophisticated sensors and systems: are the responses typical of fetal, adult or even aged tissue and organs? Are pathological responses correctable by therapeutic approaches, and is the timing of such interventions relevant when compared to the actual progression of disease? If we are to develop MPS models that address such questions, this will critically depend on the quantitative approach outlined in the review. The concept of quantitatively measuring designed and emergent physiological features represents an important first step towards creating a database that is publicly-available and will facilitate the benchmarking of a diverse range of MPS to other MPS and to (human) *in vivo* data. One approach would be to create an open access MPS “atlas” much like the Human Cell Atlas. The adapted mission statement could be similar: to create comprehensive references of all human MPS as a basis for both understanding human health and diagnosing, monitoring, and treating disease. Such an atlas could contain the available quantifications of designed and emergent physiological features of a wide range of MPS and, besides functioning as reference dataset, provide insight into which designed features are important to implement in an MPS to steer an emergent feature of interest.

In conclusion, all considerations described are of importance to achieve proper quantification, standardization and extrapolation of *in vitro* to *in vivo* data improvements. Notably, with the many technical options available to design MPS and integrate sensors and read-outs, it becomes increasingly important to report the rationale of certain design choices and how they relate to the physiology that is recapitulated. In addition, by reporting the quantitative output of MPS in a comparable and translatable way, transparency is created in the potency of these models to accurately predict and replicate specific physiological processes. More emphasis and discussion on the quantification of physiological features in MPS, as opposed to qualitative implementation, will be essential to define measurable standards for model qualification and standardization in a time of rapidly increasing numbers of MPS designs and users.

### **Acknowledgements**

This work was supported by the Netherlands Organ-on-Chip Initiative, an NWO Gravitation project (024.003.001) funded by the Ministry of Education, Culture, and Science of the government of The Netherlands. We thank A. van den Berg, H. Clevers, P.M. Sarro, M.D. Ferrari, C. Wijmenga, S.A. Kushner, A.M.J.M. van den Maagdenberg and J. Gribnau for their leadership in the Netherlands Organ-on-Chip Initiative, constructive discussions and creating the collaborative environment on which this review was based. We thank Manon Zuurmond for her work as graphical designer on the figures. Some components of the figures were created using Biorender.com.

## References

1. Ingber, D. E. Human organs-on-chips for disease modelling, drug development and personalized medicine. *Nat. Rev. Genet.* (2022) doi:10.1038/s41576-022-00466-9.
2. Vunjak-Novakovic, G., Ronaldson-Bouchard, K. & Radisic, M. Organs-on-a-chip models for biological research. *Cell* **184**, 4597–4611 (2021).
3. Mastrangeli, M., Millet, S. & van den Eijnden-Van Raaij, J. Organ-on-chip in development: Towards a roadmap for organs-on-chip. *ALTEX* **36**, 650–668 (2019).
4. Ingber, D. E. Reverse Engineering Human Pathophysiology with Organs-on-Chips. *Cell* **164**, 1105–1109 (2016).
5. Low, L. A., Mummery, C. L., Berridge, B. R., Austin, C. P. & Tagle, D. A. Organs-on-chips: into the next decade. *Nat. Rev. Drug Discov.* (2020) doi:10.1038/s41573-020-0079-3.
6. Mastrangeli, M. *et al.* Building blocks for a European organ-on-chip roadmap. *ALTEX* **36**, 481–492 (2019).
7. Qiu, Y. *et al.* Microvasculature-on-a-chip for the long-term study of endothelial barrier dysfunction and microvascular obstruction in disease. *Nat Biomed Eng* **2**, 453–463 (2018).
8. Park, T.-E. *et al.* Hypoxia-enhanced Blood-Brain Barrier Chip recapitulates human barrier function, drug penetration, and antibody shuttling properties. *Nat. Commun.* 482463 (2019) doi:10.1101/482463.
9. Van Duinen, V. *et al.* 96 Perfusable Blood Vessels To Study Vascular Permeability in Vitro. *Sci. Rep.* **7**, 1–11 (2017).
10. de Graaf, M. N. S. *et al.* Scalable microphysiological system to model three-dimensional blood vessels. *APL Bioeng.* **3**, 026105 (2019).
11. Linville, R. M. *et al.* Human iPSC-derived blood-brain barrier microvessels: validation of barrier function and endothelial cell behavior. *Biomaterials* **190–191**, 24–37 (2019).
12. Brandenburg, N. & Lutolf, M. P. In Situ Patterning of Microfluidic Networks in 3D Cell-Laden Hydrogels. *Adv. Mater.* **28**, 7450–7456 (2016).
13. Enrico, A. *et al.* Three Dimensional Microvascularized Tissue Models by Laser-Based Cavitation Molding of Collagen. *Adv. Mater.* **34**, (2022).
14. Kim, S., Lee, H., Chung, M. & Jeon, N. L. Engineering of functional, perfusable 3D microvascular networks on a chip. *Lab Chip* **13**, 1489–1500 (2013).
15. Campisi, M. *et al.* 3D self-organized microvascular model of the human blood-brain barrier with endothelial cells, pericytes and astrocytes. *Biomaterials* **180**, 117–129 (2018).
16. Vila Cuenca, M. *et al.* Engineered 3D vessel-on-chip using hiPSC-derived endothelial- and vascular smooth muscle cells. *Stem Cell Reports* **16**, (2021).
17. Wu, Z. *et al.* Microfluidic Printing of Tunable Hollow Microfibers for Vascular Tissue Engineering. *Adv. Mater. Technol.* **6**, (2021).
18. Gao, W. *et al.* One-Step Formation of Protein-Based Tubular Structures for Functional Devices and Tissues. *Adv. Healthc. Mater.* **10**, (2021).
19. Kim, H., Huh, D., Hamilton, G. & Ingber, D. Human gut-on-a-chip inhabited by microbial flora that experiences intestinal peristalsis-like motions and flow. *Lab Chip* **12**, 2165–2174 (2012).
20. Shin, Y. C. *et al.* Three-dimensional regeneration of patient-derived intestinal organoid epithelium in a physiodynamic mucosal interface-on-a-chip. *Micromachines* **11**, 663 (2020).
21. Naumovska, E. *et al.* Direct on-chip differentiation of intestinal tubules from induced pluripotent stem cells. *Int. J. Mol. Sci.* **21**, (2020).
22. Beaurivage, C. *et al.* Development of a human primary gut-on-a-chip to model inflammatory processes. *Sci. Rep.* **10**, (2020).
23. Pocock, K. *et al.* Intestine-on-A-Chip Microfluidic Model for Efficient in Vitro Screening of Oral Chemotherapeutic Uptake. *ACS Biomater. Sci. Eng.* **3**, 951–959 (2017).
24. Nikolaev, M. *et al.* Homeostatic mini-intestines through scaffold-guided organoid morphogenesis. *Nature* **585**, 574–578 (2020).
25. Shim, K. Y. *et al.* Microfluidic gut-on-a-chip with three-dimensional villi structure. *Biomed. Microdevices* **19**, (2017).
26. Mills, R. J. *et al.* Functional screening in human cardiac organoids reveals a metabolic mechanism for cardiomyocyte cell cycle arrest. *Proc. Natl. Acad. Sci.* **114**, E8372–E8381 (2017).
27. Dostanić, M. *et al.* A Miniaturized EHT Platform for Accurate Measurements of Tissue Contractile

- Properties. *J. Microelectromechanical Syst.* **29**, 881–887 (2020).
28. Mannhardt, I. *et al.* Comparison of 10 Control hPSC Lines for Drug Screening in an Engineered Heart Tissue Format. *Stem Cell Reports* **15**, 983–998 (2020).
  29. Zhao, Y. *et al.* A Platform for Generation of Chamber-Specific Cardiac Tissues and Disease Modeling. *Cell* **176**, 913–927 (2019).
  30. Vivas, A. *et al.* Generation and Culture of Cardiac Microtissues in a Microfluidic Chip with a Reversible Open Top Enables Electrical Pacing, Dynamic Drug Dosing and Endothelial Cell Co-Culture. *Adv. Mater. Technol.* **7**, (2022).
  31. Mathur, A. *et al.* Human iPSC-based cardiac microphysiological system for drug screening applications. *Sci. Rep.* **5**, 8883 (2015).
  32. MacQueen, L. A. *et al.* A tissue-engineered scale model of the heart ventricle. *Nat. Biomed. Eng.* **2**, 930–941 (2018).
  33. Sarkar, A. *et al.* Efficient Generation of CA3 Neurons from Human Pluripotent Stem Cells Enables Modeling of Hippocampal Connectivity In Vitro. *Cell Stem Cell* **22**, 684–697 (2018).
  34. Odawara, A., Gotoh, M. & Suzuki, I. A three-dimensional neuronal culture technique that controls the direction of neurite elongation and the position of soma to mimic the layered structure of the brain. *RSC Adv.* **3**, 23620–23630 (2013).
  35. Dauth, S. *et al.* Neurons derived from different brain regions are inherently different in vitro: A novel multiregional brain-on-a-chip. *J. Neurophysiol.* **117**, 1320–1341 (2017).
  36. Rifés, P. *et al.* Modeling neural tube development by differentiation of human embryonic stem cells in a microfluidic WNT gradient. *Nat. Biotechnol.* **38**, 1265–1273 (2020).
  37. Nordström, U., Jessell, T. M. & Edlund, T. Progressive induction of caudal neural character by graded Wnt signaling. *Nat. Neurosci.* **5**, 525–532 (2002).
  38. Trujillo, C. A. *et al.* Complex Oscillatory Waves Emerging from Cortical Organoids Model Early Human Brain Network Development. *Cell Stem Cell* **25**, 558–569 (2019).
  39. Brandenburg, N. & Lutolf, M. P. In Situ Patterning of Microfluidic Networks in 3D Cell-Laden Hydrogels. *Adv. Mater.* **28**, 7450–7456 (2016).
  40. Pollet, A. M. A. O. & den Toonder, J. M. J. Recapitulating the vasculature using Organ-on-Chip technology. *Bioengineering* **7**, 1–18 (2020).
  41. Helander, H. F. & Fändriks, L. Surface area of the digestive tract-revisited. *Scand. J. Gastroenterol.* **49**, 681–689 (2014).
  42. Hasan, M. & Ferguson, A. Measurements of intestinal villi in non-specific and ulcer-associated duodenitis - correlation between area of microdissected villus and villus epithelial cell count. *J. Clin. Pathol.* **34**, 1181–1186 (1981).
  43. Marsh, M. N. & Swift, J. A. A study of the small intestinal mucosa using the scanning electron microscope. *Gut* **10**, 940–949 (1969).
  44. Trbojević-Stanković, J. B. *et al.* Morphometric study of healthy jejunal and ileal mucosa in adult and aged subjects. *Histol Histopathol* **25**, 153–158 (2010).
  45. Lin, F. Y. *et al.* Cardiac Chamber Volumes, Function, and Mass as Determined by 64-Multidetector Row Computed Tomography. *JACC Cardiovasc. Imaging* **1**, 782–786 (2008).
  46. Adler, D. H. *et al.* Characterizing the human hippocampus in aging and Alzheimer’s disease using a computational atlas derived from ex vivo MRI and histology. *Proc. Natl. Acad. Sci. U. S. A.* **115**, 4252–4257 (2018).
  47. Nowakowski, T. J., Pollen, A. A., Sandoval-Espinosa, C. & Kriegstein, A. R. Transformation of the Radial Glia Scaffold Demarcates Two Stages of Human Cerebral Cortex Development. *Neuron* **91**, 1219–1227 (2016).
  48. Song, J. W. *et al.* Computer-controlled microcirculatory support system for endothelial cell culture and shearing. *Anal. Chem.* **77**, 3993–3999 (2005).
  49. Arora, S., Lam, A. J. Y., Cheung, C., Yim, E. K. F. & Toh, Y. C. Determination of critical shear stress for maturation of human pluripotent stem cell-derived endothelial cells towards an arterial subtype. *Biotechnol. Bioeng.* **116**, 1164–1175 (2019).
  50. Chen, H. *et al.* Cardiac-like flow generator for long-term imaging of endothelial cell responses to circulatory pulsatile flow at microscale. *Lab Chip* **13**, 2999–3007 (2013).
  51. Satoh, T. *et al.* A pneumatic pressure-driven multi-throughput microfluidic circulation culture system. *Lab Chip* **16**, 2339–2348 (2016).

52. Popel, A. S. & Johnson, P. C. Microcirculation and hemorrheology. *Annual Review of Fluid Mechanics* vol. 37 43–69 (2005).
53. Callaghan, F. M. & Grieve, S. M. Normal patterns of thoracic aortic wall shear stress measured using four-dimensional flow MRI in a large population. *Am. J. Physiol. - Hear. Circ. Physiol.* **315**, H1174–H1181 (2018).
54. Dessalles, C. A., Ramón-Lozano, C., Babataheri, A. & Barakat, A. I. Luminal flow actuation generates coupled shear and strain in a microvessel-on-chip. *Biofabrication* **14**, (2021).
55. Dobrin, P. B. Mechanical properties of arteries. *Physiol. Rev.* **58**, (1978).
56. Morrison, T. M., Choi, G., Zarins, C. K. & Taylor, C. A. Circumferential and longitudinal cyclic strain of the human thoracic aorta: Age-related changes. *J. Vasc. Surg.* **49**, 1029–1036 (2009).
57. Wasson, E. M., Dubbin, K. & Moya, M. L. Go with the flow: modeling unique biological flows in engineered in vitro platforms. *Lab Chip* **21**, 2095–2120 (2021).
58. Dutton, J. S., Hinman, S. S., Kim, R., Wang, Y. & Allbritton, N. L. Primary Cell-Derived Intestinal Models: Recapitulating Physiology. *Trends Biotechnol.* **37**, 744–760 (2019).
59. Park, J. *et al.* Three-dimensional brain-on-a-chip with an interstitial level of flow and its application as an in vitro model of Alzheimer’s disease. *Lab Chip* **15**, 141–150 (2015).
60. Lindstrøm, E. K., Ringstad, G., Mardal, K. A. & Eide, P. K. Cerebrospinal fluid volumetric net flow rate and direction in idiopathic normal pressure hydrocephalus. *NeuroImage Clin.* **20**, 731–741 (2018).
61. Basson, M. D. Paradigms for Mechanical Signal Transduction in the Intestinal Epithelium. *Digestion* **68**, 217–225 (2003).
62. Rodriguez, M. L., Werner, T. R., Becker, B., Eschenhagen, T. & Hirt, M. N. Magnetics-Based Approach for Fine-Tuning Afterload in Engineered Heart Tissues. *ACS Biomater. Sci. Eng.* **5**, 3663–3675 (2019).
63. Trappmann, B. *et al.* Matrix degradability controls multicellularity of 3D cell migration. *Nat. Commun.* **8**, (2017).
64. Gordon, E., Schimmel, L. & Frye, M. The Importance of Mechanical Forces for in vitro Endothelial Cell Biology. *Front. Physiol.* **11**, (2020).
65. Onfroy-Roy, L., Hamel, D., Foncy, J., Malaquin, L. & Ferrand, A. Extracellular Matrix Mechanical Properties and Regulation of the Intestinal Stem Cells: When Mechanics Control Fate. *Cells* **9**, 1–23 (2020).
66. Wang, Y. *et al.* A microengineered collagen scaffold for generating a polarized crypt-villus architecture of human small intestinal epithelium. *Biomaterials* **128**, 44–55 (2017).
67. Pasqualini, F. S. *et al.* Traction force microscopy of engineered cardiac tissues. *PLoS One* **13**, 1–14 (2018).
68. McCain, M. L., Yuan, H., Pasqualini, F. S., Campbell, P. H. & Parker, K. K. Matrix elasticity regulates the optimal cardiac myocyte shape for contractility. *Am. J. Physiol. - Hear. Circ. Physiol.* **306**, 1525–1539 (2014).
69. Cho, A. N. *et al.* Microfluidic device with brain extracellular matrix promotes structural and functional maturation of human brain organoids. *Nat. Commun.* **12**, (2021).
70. Barnes, J. M., Przybyla, L. & Weaver, V. M. Tissue mechanics regulate brain development, homeostasis and disease. *J. Cell Sci.* **130**, 71–82 (2017).
71. Lam, S. F., Shirure, V. S., Chu, Y. E., Soetikno, A. G. & George, S. C. Microfluidic device to attain high spatial and temporal control of oxygen. *PLoS One* **13**, 1–16 (2018).
72. Carreau, A., Hafny-Rahbi, B. El, Matejuk, A., Grillon, C. & Kieda, C. Why is the partial oxygen pressure of human tissues a crucial parameter? Small molecules and hypoxia. *J. Cell. Mol. Med.* **15**, 1239–1253 (2011).
73. Jalili-firoozinezhad, S. *et al.* A complex human gut microbiome cultured in an anaerobic intestine-on-a-chip. *Nat. Biomed. Eng.* **3**, 520–531 (2019).
74. Ast, T. & Mootha, V. K. Oxygen and mammalian cell culture: are we repeating the experiment of Dr. Ox? *Nat. Metab.* **1**, 858–860 (2019).
75. Veldhuizen, J. *et al.* Cardiac ischemia on-a-chip to investigate cellular and molecular response of myocardial tissue under hypoxia. *Biomaterials* **281**, (2022).
76. Winegrad, S., Henrion, D., Rappaport, L. & Samuel, J. L. Self-protection by cardiac myocytes against hypoxia and hyperoxia. *Circ. Res.* **85**, 690–698 (1999).
77. Erecińska, M. & Silver, I. A. Tissue oxygen tension and brain sensitivity to hypoxia. *Respir. Physiol.* **128**, 263–276 (2001).
78. Winkler, E. A. *et al.* A single-cell atlas of the normal and malformed human brain vasculature. *Science*

- (80- ). **7377**, 1–23 (2022).
79. Wang, Y. *et al.* Single-cell transcriptome analysis reveals differential nutrient absorption functions in human intestine. *J. Exp. Med.* **217**, (2019).
  80. Tucker, N. R. *et al.* Transcriptional and Cellular Diversity of the Human Heart. *Circulation* **142**, 466–482 (2020).
  81. Litviňuková, M. *et al.* Cells of the adult human heart. *Nature* **588**, 466–472 (2020).
  82. Miterko, L. N., Lackey, E. P., Heck, D. H. & Sillitoe, R. V. Shaping Diversity Into the Brain's Form and Function. *Frontiers in Neural Circuits* vol. 12 83 (2018).
  83. Bhaduri, A. *et al.* An atlas of cortical arealization identifies dynamic molecular signatures. *Nature* **598**, 200–204 (2021).
  84. Winkelman, M. A. *et al.* Interstitial flow enhances the formation, connectivity, and function of 3D brain microvascular networks generated within a microfluidic device. *Lab Chip* **22**, 170–192 (2022).
  85. Mathiesen, T. M., Lehre, K. P., Danbolt, N. C. & Ottersen, O. P. The perivascular astroglial sheath provides a complete covering of the brain microvessels: An electron microscopic 3D reconstruction. *Glia* **58**, 1094–1103 (2010).
  86. Armulik, A., Genové, G. & Betsholtz, C. Pericytes: Developmental, Physiological, and Pathological Perspectives, Problems, and Promises. *Dev. Cell* **21**, 193–215 (2011).
  87. Hinman, S. S., Wang, Y. & Allbritton, N. L. Photopatterned Membranes and Chemical Gradients Enable Scalable Phenotypic Organization of Primary Human Colon Epithelial Models. *Anal. Chem.* **91**, 15240–15247 (2019).
  88. Elmentaite, R. *et al.* Single-Cell Sequencing of Developing Human Gut Reveals Transcriptional Links to Childhood Crohn's Disease. *Dev. Cell* **55**, 771–783 (2020).
  89. Wang, Y. F., Liu, C. & Xu, P. F. Deciphering and reconstitution of positional information in the human brain development. *Cell Regen.* **10**, 1–13 (2021).
  90. Iannielli, A. *et al.* Reconstitution of the Human Nigro-striatal Pathway on-a-Chip Reveals OPA1-Dependent Mitochondrial Defects and Loss of Dopaminergic Synapses. *Cell Rep.* **29**, 4646–4656 (2019).
  91. Alonso-Nanclares, L., Gonzalez-Soriano, J., Rodriguez, J. R. & DeFelipe, J. Gender differences in human cortical synaptic density. *Proc. Natl. Acad. Sci. U. S. A.* **105**, 14615–14619 (2008).
  92. Yu, Y. *et al.* A microfluidic platform for continuous monitoring of dopamine homeostasis in dopaminergic cells. *Microsystems Nanoeng.* **5**, (2019).
  93. Gonon, F. Prolonged and extrasynaptic excitatory action of dopamine mediated by D1 receptors in the rat striatum in vivo. *J. Neurosci.* **17**, 5972–5978 (1997).
  94. Ford, C. P., Phillips, P. E. M. & Williams, J. T. The time course of dopamine transmission in the ventral tegmental area. *J. Neurosci.* **29**, 13344–13352 (2009).
  95. Herland, A. *et al.* Distinct contributions of astrocytes and pericytes to neuroinflammation identified in a 3D human blood-brain barrier on a chip. *PLoS One* **11**, (2016).
  96. Calandra, T., Gerain, J., Heumann, D., Baumgartner, J. D. & Glauser, M. P. High circulating levels of interleukin-6 in patients with septic shock: Evolution during sepsis, prognostic value, and interplay with other cytokines. *Am. J. Med.* **91**, 23–29 (1991).
  97. Park, J. *et al.* A 3D human triculture system modeling neurodegeneration and neuroinflammation in Alzheimer's disease. *Nat. Neurosci.* **21**, 941–951 (2018).
  98. Leng, F. & Edison, P. Neuroinflammation and microglial activation in Alzheimer disease: where do we go from here? *Nat. Rev. Neurol.* **17**, 157–172 (2021).
  99. Yuan, W., Lv, Y., Zeng, M. & Fu, B. M. Non-invasive measurement of solute permeability in cerebral microvessels of the rat. *Microvasc. Res.* **77**, 166–173 (2009).
  100. Nejdofors, P., Ekelund, M., Jeppsson, B. & Weström, B. R. Mucosal in vitro permeability in the intestinal tract of the pig, the rat, and man: Species- and region-related differences. *Scand. J. Gastroenterol.* **35**, 501–507 (2000).
  101. Nunes, S. S. *et al.* Biowire: A platform for maturation of human pluripotent stem cell-derived cardiomyocytes. *Nat. Methods* **10**, 781–787 (2013).
  102. Zhao, Y. *et al.* Towards chamber specific heart-on-a-chip for drug testing applications. *Adv. Drug Deliv. Rev.* **165–166**, 60–76 (2020).
  103. Tiburcy, M. *et al.* Defined engineered human myocardium with advanced maturation for applications in heart failure modeling and repair. *Circulation* **135**, 1832–1847 (2017).
  104. Thavandiran, N. *et al.* Design and formulation of functional pluripotent stem cell-derived cardiac

- microtissues. *Proc. Natl. Acad. Sci.* **110**, E4698–E4707 (2013).
105. Gyorgy, B. & Andreas, D. Neuronal Oscillations in Cortical Networks. *Science (80-. )*. **304**, 1926–1929 (2004).
  106. Kim, S., Chung, M. & Jeon, N. L. Three-dimensional biomimetic model to reconstitute sprouting lymphangiogenesis in vitro. *Biomaterials* **78**, 115–128 (2016).
  107. Darwich, A. S., Aslam, U., Ashcroft, D. M. & Rostami-Hodjegan, A. Meta-analysis of the turnover of intestinal epithelia in preclinical animal species and humans. *Drug Metab. Dispos.* **42**, 2016–2022 (2014).
  108. Moutairou, K. *et al.* Epithelial cell migration on small intestinal villi in the neonatal rat. Comparison between [3H] thymidine and cytoplasmic labelling after Pu-citrate ingestion. *Biol. Cell* **65**, 265–269 (1989).
  109. Parker, A. *et al.* Cell proliferation within small intestinal crypts is the principal driving force for cell migration on villi. *FASEB J.* **31**, 636–649 (2017).
  110. Linville, R. M. *et al.* Human iPSC-derived blood-brain barrier microvessels: validation of barrier function and endothelial cell behavior. *Biomaterials* **190–191**, 24–37 (2019).
  111. Chen, Y. *et al.* A microfluidic circulatory system integrated with capillary-assisted pressure sensors. *Lab Chip* **17**, 653–662 (2017).
  112. Wasson, E. M., Dubbin, K. & Moya, M. L. Go with the flow: modeling unique biological flows in engineered in vitro platforms. *Lab Chip* **21**, 2095–2120 (2021).
  113. Parsa, H., Wang, B. Z. & Vunjak-Novakovic, G. A microfluidic platform for the high-throughput study of pathological cardiac hypertrophy. *Lab Chip* **17**, 3264–3271 (2017).
  114. Schroer, A., Pardon, G., Castillo, E., Blair, C. & Pruitt, B. Engineering hiPSC cardiomyocyte in vitro model systems for functional and structural assessment. *Prog. Biophys. Mol. Biol.* **144**, 3–15 (2019).
  115. Mason, B. N., Starchenko, A., Williams, R. M., Bonassar, L. J. & Reinhart-King, C. A. Tuning three-dimensional collagen matrix stiffness independently of collagen concentration modulates endothelial cell behavior. *Acta Biomater.* **9**, 4635–4644 (2013).
  116. Soofi, S. S., Last, J. A., Lliensiek, S. J., Nealey, P. F. & Murphy, C. J. Elastic modulus of Matrigel as determined by AFM. *J. Struct. Biol.* **167**, 216–219 (2009).
  117. Fuard, D., Tzvetkova-Chevolleau, T., Decossas, S., Tracqui, P. & Schiavone, P. Optimization of poly-dimethyl-siloxane (PDMS) substrates for studying cellular adhesion and motility. *Microelectron. Eng.* **85**, 1289–1293 (2008).
  118. Roy, E., Galas, J.-C. & Veres, T. Thermoplastic elastomers for microfluidics: Towards a high-throughput fabrication method of multilayered microfluidic devices. *Lab Chip* **11**, 3193 (2011).
  119. Carlborg, C. F., Haraldsson, T., Öberg, K., Malkoch, M. & van der Wijngaart, W. Beyond PDMS: off-stoichiometry thiol-ene (OSTE) based soft lithography for rapid prototyping of microfluidic devices. *Lab Chip* **11**, 3136 (2011).
  120. Radisic, M. & Loskill, P. Beyond PDMS and Membranes: New Materials for Organ-on-a-Chip Devices. *ACS Biomater. Sci. Eng.* **7**, 2861–2863 (2021).
  121. Buguin, A., Li, M. H., Silberzan, P., Ladoux, B. & Keller, P. Micro-actuators: When artificial muscles made of nematic liquid crystal elastomers meet soft lithography. *J. Am. Chem. Soc.* **128**, 1088–1089 (2006).
  122. Guin, T. *et al.* Layered liquid crystal elastomer actuators. *Nat. Commun.* **9**, 2531 (2018).
  123. Chen, M. B., Srigunapalan, S., Wheeler, A. R. & Simmons, C. A. A 3D microfluidic platform incorporating methacrylated gelatin hydrogels to study physiological cardiovascular cell-cell interactions. *Lab Chip* **13**, 2591–2598 (2013).
  124. Vickovic, S. *et al.* High-definition spatial transcriptomics for in situ tissue profiling. *Nat. Methods* **16**, 987–990 (2019).
  125. Srivatsan, S. R. *et al.* Embryo-scale, single-cell spatial transcriptomics. *Science (80-. )*. **373**, 111–117 (2021).
  126. Fajgenbaum, D. C. & June, C. H. Cytokine Storm. *N. Engl. J. Med.* **383**, 2255–2273 (2020).
  127. Hajal, C. *et al.* Engineered human blood–brain barrier microfluidic model for vascular permeability analyses. *Nat. Protoc.* **17**, 95–128 (2022).
  128. Hajal, C., Roi, B. Le, Kamam, R. D. & Maoz, B. M. Biology and Models of the Blood-Brain barrier. *Annu Rev Biomed Eng* (2021).
  129. Tan, H. Y. *et al.* A multi-chamber microfluidic intestinal barrier model using Caco-2 cells for drug transport studies. *PLoS One* **13**, (2018).

130. Yang, X., Pabon, L. & Murry, C. E. Engineering adolescence: Maturation of human pluripotent stem cell-derived cardiomyocytes. *Circ. Res.* **114**, 511–523 (2014).
131. Zwi, L. *et al.* Cardiomyocyte differentiation of human induced pluripotent stem cells. *Circulation* **120**, 1513–1523 (2009).
132. van Meer, B. J., Tertoolen, L. G. J. & Mummery, C. L. Measuring Physiological Responses of Human Pluripotent Stem Cell Derived Cardiomyocytes to Drugs and Disease. *Stem Cells* **34**, 2008–2015 (2016).
133. Brandao, K. O., Tabel, V. A., Atsma, D. E., Mummery, C. L. & Davis, R. P. Human pluripotent stem cell models of cardiac disease: From mechanisms to therapies. *Dis. Model. Mech.* **10**, 1039–1059 (2017).
134. Gaio, N. *et al.* Cytostretch, an Organ-on-Chip platform. *Micromachines* **7**, (2016).
135. Shin, H. *et al.* 3D high-density microelectrode array with optical stimulation and drug delivery for investigating neural circuit dynamics. *Nat. Commun.* **12**, (2021).
136. Blau, A. *et al.* Flexible, all-polymer microelectrode arrays for the capture of cardiac and neuronal signals. *Biomaterials* **32**, 1778–1786 (2011).
137. Soscia, D. A. *et al.* A flexible 3-dimensional microelectrode array for in vitro brain models. *Lab Chip* **20**, 901–911 (2020).
138. van Meer, B. J., Tertoolen, L. G. J. & Mummery, C. L. Measuring physiological responses of human pluripotent stem cell derived cardiomyocytes to drugs and disease. *Stem Cells* **34**, 2008–2015 (2016).
139. Sender, R. & Milo, R. The distribution of cellular turnover in the human body. *Nat. Med.* **27**, 45–48 (2021).
140. Tatsuya Osaki, Serrano, J. C. & Kamm, R. D. Cooperative Effects of Vascular Angiogenesis and Lymphangiogenesis. *Regen Eng Transl Med* **4**, 120–132 (2018).
141. Eddington, D. T., Puccinelli, J. P. & Beebe, D. J. Thermal aging and reduced hydrophobic recovery of polydimethylsiloxane. *Sensors Actuators, B Chem.* **114**, 170–172 (2006).
142. van Meer, B. J. *et al.* Small molecule absorption by PDMS in the context of drug response bioassays. *Biochem. Biophys. Res. Commun.* **482**, 323–328 (2017).
143. Lambert, A., Marasso, S. L. & Cocuzza, M. PDMS membranes with tunable gas permeability for microfluidic applications. *RSC Adv.* **4**, 61415–61419 (2014).
144. Firpo, G., Angeli, E., Repetto, L. & Valbusa, U. Permeability thickness dependence of polydimethylsiloxane (PDMS) membranes. *J. Memb. Sci.* **481**, 1–8 (2015).
145. O'Brien, D. J. *et al.* Systematic Characterization of Hydrophilized Polydimethylsiloxane. *J. Microelectromechanical Syst.* **29**, 1216–1224 (2020).
146. Nakano, H., Kakinoki, S. & Iwasaki, Y. Long-lasting hydrophilic surface generated on poly(dimethyl siloxane) with photoreactive zwitterionic polymers. *Colloids Surfaces B Biointerfaces* **205**, (2021).
147. Holczer, E. & Fürjes, P. Effects of embedded surfactants on the surface properties of PDMS; applicability for autonomous microfluidic systems. *Microfluid. Nanofluidics* **21**, (2017).
148. McMillan, A. H. *et al.* Rapid fabrication of membrane-integrated thermoplastic elastomer microfluidic devices. *Micromachines* **11**, (2020).
149. Lachaux, J. *et al.* Thermoplastic elastomer with advanced hydrophilization and bonding performances for rapid (30 s) and easy molding of microfluidic devices. *Lab Chip* **17**, 2581–2594 (2017).
150. Busek, M. *et al.* Thermoplastic elastomer (TPE)–poly(methyl methacrylate) (PMMA) hybrid devices for active pumping PDMS-free organ-on-a-chip systems. *Biosensors* **11**, (2021).
151. Kim, D. S., Jeong, Y. J., Lee, B. K., Shanmugasundaram, A. & Lee, D. W. Piezoresistive sensor-integrated PDMS cantilever: A new class of device for measuring the drug-induced changes in the mechanical activity of cardiomyocytes. *Sensors Actuators, B Chem.* **240**, 566–572 (2017).
152. Lind, J. U. *et al.* Instrumented cardiac microphysiological devices via multimaterial three-dimensional printing. *Nat. Mater.* **16**, 303–308 (2017).
153. Coln, E. A. *et al.* Piezoelectric bioMEMS cantilever for measurement of muscle contraction and for actuation of mechanosensitive cells. *MRS Commun.* **9**, 1186–1192 (2019).
154. Wang, Y. & Sugino, T. *Ionic Polymer Actuators: Principle, Fabrication and Applications*. *Actuators* (2018). doi:10.5772/intechopen.75085.
155. Mastrangeli, M. *et al.* Microelectromechanical Organs-on-Chip. *21st Int. Conf. Solid-State Sensors, Actuators Microsystems, TRANSDUCERS 2021* 102–107 (2021) doi:10.1109/Transducers50396.2021.9495646.
156. Mirfakhrai, T., Madden, J. D. W. & Baughman, R. H. Polymer artificial muscles. *Mater. Today* **10**, 30–38 (2007).

157. Annabestani, M. & Fardmanesh, M. Ionic Electro active Polymer-Based Soft Actuators and Their Applications in Microfluidic Micropumps, Microvalves, and Micromixers: A Review. in *arXiv* (2019).
158. Osaki, T., Uzel, S. G. M. & Kamm, R. D. Microphysiological 3D model of amyotrophic lateral sclerosis (ALS) from human iPSC-derived muscle cells and optogenetic motor neurons. *Sci. Adv.* **4**, (2018).
159. Gerasimenko, T. *et al.* Impedance Spectroscopy as a Tool for Monitoring Performance in 3D Models of Epithelial Tissues. *Front. Bioeng. Biotechnol.* **7**, (2020).
160. van der Helm, M. W. *et al.* Non-invasive sensing of transepithelial barrier function and tissue differentiation in organs-on-chips using impedance spectroscopy. *Lab Chip* **19**, 452–463 (2019).
161. Groeber, F. *et al.* Impedance Spectroscopy for the Non-Destructive Evaluation of in Vitro Epidermal Models. *Pharm. Res.* **32**, 1845–1854 (2015).
162. Yeste, J. *et al.* Geometric correction factor for transepithelial electrical resistance measurements in transwell and microfluidic cell cultures. *J. Phys. D. Appl. Phys.* **49**, (2016).
163. Blume, L. F., Denker, M., Gieseler, F. & Kunze, T. Temperature corrected transepithelial electrical resistance (TEER) measurement to quantify rapid changes in paracellular permeability. *Pharmazie* **65**, 19–24 (2010).
164. Grimnes, S. & Martinsen, Ø. G. Sources of error in tetrapolar impedance measurements on biomaterials and other ionic conductors. *J. Phys. D. Appl. Phys.* **40**, (2007).
165. Bossink, E. G. B. M., Zakharova, M., De Bruijn, D. S., Odijk, M. & Segerink, L. I. Measuring barrier function in organ-on-chips with cleanroom-free integration of multiplexable electrodes. *Lab Chip* **21**, 2040–2049 (2021).
166. Matthiesen, I., Voulgaris, D., Nikolakopoulou, P., Winkler, T. E. & Herland, A. Continuous Monitoring Reveals Protective Effects of N-Acetylcysteine Amide on an Isogenic Microphysiological Model of the Neurovascular Unit. *Small* **17**, (2021).
167. Maoz, B. M. *et al.* Organs-on-Chips with combined multi-electrode array and transepithelial electrical resistance measurement capabilities. *Lab Chip* **17**, 2294–2302 (2017).
168. Liu, F., Ni, L. & Zhe, J. Lab-on-a-chip electrical multiplexing techniques for cellular and molecular biomarker detection. *Biomicrofluidics* **12**, (2018).
169. Curto, V. F., Ferro, M. P., Mariani, F., Scavetta, E. & Owens, R. M. A planar impedance sensor for 3D spheroids. *Lab Chip* **18**, 933–943 (2018).
170. Schmid, Y. R. F., Bürgel, S. C., Misun, P. M., Hierlemann, A. & Frey, O. Electrical Impedance Spectroscopy for Microtissue Spheroid Analysis in Hanging-Drop Networks. *ACS Sensors* **1**, 1028–1035 (2016).
171. Alexander, F., Eggert, S. & Price, D. Label-Free Monitoring of 3D Tissue Models via Electrical Impedance Spectroscopy. *Bioanal. Rev.* **2**, 111–134 (2019).
172. Moysidou, C. M. *et al.* 3D Bioelectronic Model of the Human Intestine. *Adv. Biol.* **5**, (2021).
173. Zhu, Y. *et al.* State of the art in integrated biosensors for organ-on-a-chip applications. *Curr. Opin. Biomed. Eng.* **19**, (2021).
174. Kieninger, J., Weltin, A., Flamm, H. & Urban, G. A. Microsensor systems for cell metabolism-from 2D culture to organ-on-chip. *Lab Chip* **18**, 1274–1291 (2018).
175. Oliveira, M., Conceição, P., Kant, K., Ainla, A. & Diéguez, L. Electrochemical sensing in 3d cell culture models: New tools for developing better cancer diagnostics and treatments. *Cancers (Basel)*. **13**, (2021).
176. Aleman, J., Kilic, T., Mille, L. S., Shin, S. R. & Zhang, Y. S. Microfluidic integration of regeneratable electrochemical affinity-based biosensors for continual monitoring of organ-on-a-chip devices. *Nat. Protoc.* **16**, 2564–2593 (2021).
177. Zhang, Y. S. *et al.* Multisensor-integrated organs-on-chips platform for automated and continual in situ monitoring of organoid behaviors. *Proc. Natl. Acad. Sci. U. S. A.* **114**, (2017).
178. Kaisti, M. Detection principles of biological and chemical FET sensors. *Biosens. Bioelectron.* **98**, 437–448 (2017).
179. Usuba, R. *et al.* Photonic Lab-on-a-Chip for Rapid Cytokine Detection. *ACS Sensors* **1**, 979–986 (2016).
180. Narang, R. *et al.* Sensitive, Real-time and Non-Intrusive Detection of Concentration and Growth of Pathogenic Bacteria using Microfluidic-Microwave Ring Resonator Biosensor. *Sci. Rep.* **8**, (2018).
181. Shaegh, S. A. M. *et al.* A microfluidic optical platform for real-time monitoring of pH and oxygen in microfluidic bioreactors and organ-on-chip devices. *Biomicrofluidics* **10**, (2016).
182. Luchansky, M. S. & Bailey, R. C. Rapid, multiparameter profiling of cellular secretion using silicon photonic microring resonator arrays. *J. Am. Chem. Soc.* **133**, 20500–20506 (2011).
183. Podoleanu, A. G. Optical coherence tomography. *J. Microsc.* **247**, 209–219 (2012).

184. Braaf, B. *et al.* *OCT-Based Velocimetry for Blood Flow Quantification. High Resolution Imaging in Microscopy and Ophthalmology* (2019). doi:10.1007/978-3-030-16638-0\_7.
185. Arik, Y. B. *et al.* Microfluidic organ-on-a-chip model of the outer blood-retinal barrier with clinically relevant read-outs for tissue permeability and vascular structure. *Lab Chip* **21**, 272–283 (2021).
186. Pauty, J. *et al.* A Vascular Endothelial Growth Factor-Dependent Sprouting Angiogenesis Assay Based on an In Vitro Human Blood Vessel Model for the Study of Anti-Angiogenic Drugs. *EBioMedicine* **27**, 225–236 (2018).
187. Dalmay, C. *et al.* Ultra sensitive biosensor based on impedance spectroscopy at microwave frequencies for cell scale analysis. *Sensors Actuators, A Phys.* **162**, 189–197 (2010).
188. Artis, F. *et al.* Microwaving biological cells: Intracellular analysis with microwave dielectric spectroscopy. *IEEE Microw. Mag.* **16**, 87–96 (2015).
189. Grenier, K. *et al.* Recent advances in microwave-based dielectric spectroscopy at the cellular level for cancer investigations. *IEEE Trans. Microw. Theory Tech.* **61**, 2023–2030 (2013).
190. Kelleci, M., Aydogmus, H., Aslanbas, L., Erbil, S. O. & Selim Hanay, M. Towards microwave imaging of cells. *Lab Chip* **18**, 463–472 (2018).
191. Jang, C., Park, J.-K., Lee, H.-J., Yun, G.-H. & Yook, J.-G. Sensitivity-Enhanced Fluidic Glucose Sensor Based on a Microwave Resonator Coupled With an Interferometric System for Noninvasive and Continuous Detection. *IEEE Trans Biomed Circuits Syst* **15**, 1017–1026 (2021).
192. Zarifi, M. H., Sadabadi, H., Hejazi, S. H., Daneshmand, M. & Sanati-Nezhad, A. Noncontact and Nonintrusive Microwave-Microfluidic Flow Sensor for Energy and Biomedical Engineering. *Sci. Rep.* **8**, (2018).
193. Wikswo, J. P. *et al.* Scaling and systems biology for integrating multiple organs-on-a-chip. *Lab Chip* **13**, 3496–3511 (2013).
194. Herland, A. *et al.* Quantitative prediction of human pharmacokinetic responses to drugs via fluidically coupled vascularized organ chips. *Nat. Biomed. Eng.* **4**, 421–436 (2020).

## Supplementary information

### Contents

- 1 **Methodology**
- 2 **Organ physiology and biological features of the human vasculature, intestine, heart and brain**  
Including Supplemental figure 1:  
Schematic overview of physiological features of four selected organs: human vasculature, intestine, heart and brain
- 3 **General designed features: Cell source and media**
- 4 **Supplemental table 1:**  
Quantification of designed and emergent physiological features in microphysiological systems and human in vivo
- 5 **Supplemental discussion designed feature**  
Fluid flow – Interstitial flow
- 6 **Supplemental discussion emergent features**  
  
Cell type diversity – Microbiome – bacterial diversity  
  
Inflammatory response – Patrolling monocyte speed and Immune cell infiltration  
  
Barrier integrity - Mucus layer thickness  
  
Electrical activity – Axon length, Myelin thickness, Myelin length, Axonal transport speed of mitochondria  
  
Cellular contraction – Contraction frequency, Contractile force, Force-frequency relationship, Cardiomyocyte alignment, Systolic ventricular pressure  
  
Digestion and absorption – Cell surface area, Microvilli density, Digestive enzyme activity, Drug metabolizing enzyme activity
- 7 **Standardization and open platforms**  
  
**Supplemental references**

# 1 Methodology

The current review is the outcome of the Netherlands Organ-on-Chip Initiative, a program with specific interest in developing advanced OoC systems for the vasculature, intestine, heart and brain. The decision to focus on the vasculature, intestine, heart and brain was developmentally driven: including derivatives of all three germ layers, an endodermal (intestine), ectodermal (brain) and mesodermal (heart) organ, with the vasculature as a link to all.

The review was based on the following stepwise approach:

1. Determine the specific physiological features of each organ of interest. Of note: for each selected organ, we discuss an extensive but not exhaustive list of physiological features that have been quantitatively modelled in MPS. In addition, for some features, the implications for a specific MPS can be extrapolated to other organs.
2. Identify literature describing MPS of each selected organ that meets the following criteria;
  - The model system falls within our MPS definition. A broad and inclusive definition of MPS was adopted, to capture all of those relevant for the four organs selected. Microdevices containing cells in 2D or 3D cultures that either replicate the mechanical microenvironment by integrating fluid flow or mechanical actuation, or that integrate sensing modalities. We included systems that employ direct cell culture inside microfluidic or actuating systems, as well as those that integrate pre-engineered 3D tissues in these systems. The majority of discussed systems are microfluidic systems, which we refer to as Organ-on-Chip (OoC). Exceptions to this definition are clearly indicated in the text with the reason of inclusion. We excluded organoid cultures, since their stochastic, self-organizing nature generally precludes controlled confinement, and systems that model organ-organ connections in light of our focus on organ-specific features.
  - Reports accurate quantification of one of the defined physiological features of an organ or tissue in a healthy state. We focused on quantification of a healthy organ or tissue as this provides a baseline for comparing aberrant organ functions in disease.
  - Human cells were used in the system (primary, immortalized or iPSC-derived). Exceptions in which uses animal cells in a MPS are clearly indicated in the text.
3. Extract quantitative MPS values from the papers

4. Determine the best example to highlight. Selection was based on the most accurate quantification method, comparability with *in vivo* observations, the most suitable MPS type or an example which highlights an important consideration regarding quantification of that specific physiological feature.
5. Search for and extract, whenever possible, *in vivo* quantification of the specific physiological feature in human tissue. If human observations *in vivo* were not available, we sometimes included animal data. The result of these steps can be seen in *Table 1* and Supplemental table 1.
6. Identify technical advances which could overcome limitations in the current quantification methods of each physiological feature. Applicable technologies for MPS were considered which could improve quantification by either increasing the accuracy of measurement or improving the *in vivo* comparability. The proposed advances were grouped into several overarching technological areas to enable a more general overview on MPS technology and its areas of potential improvement.

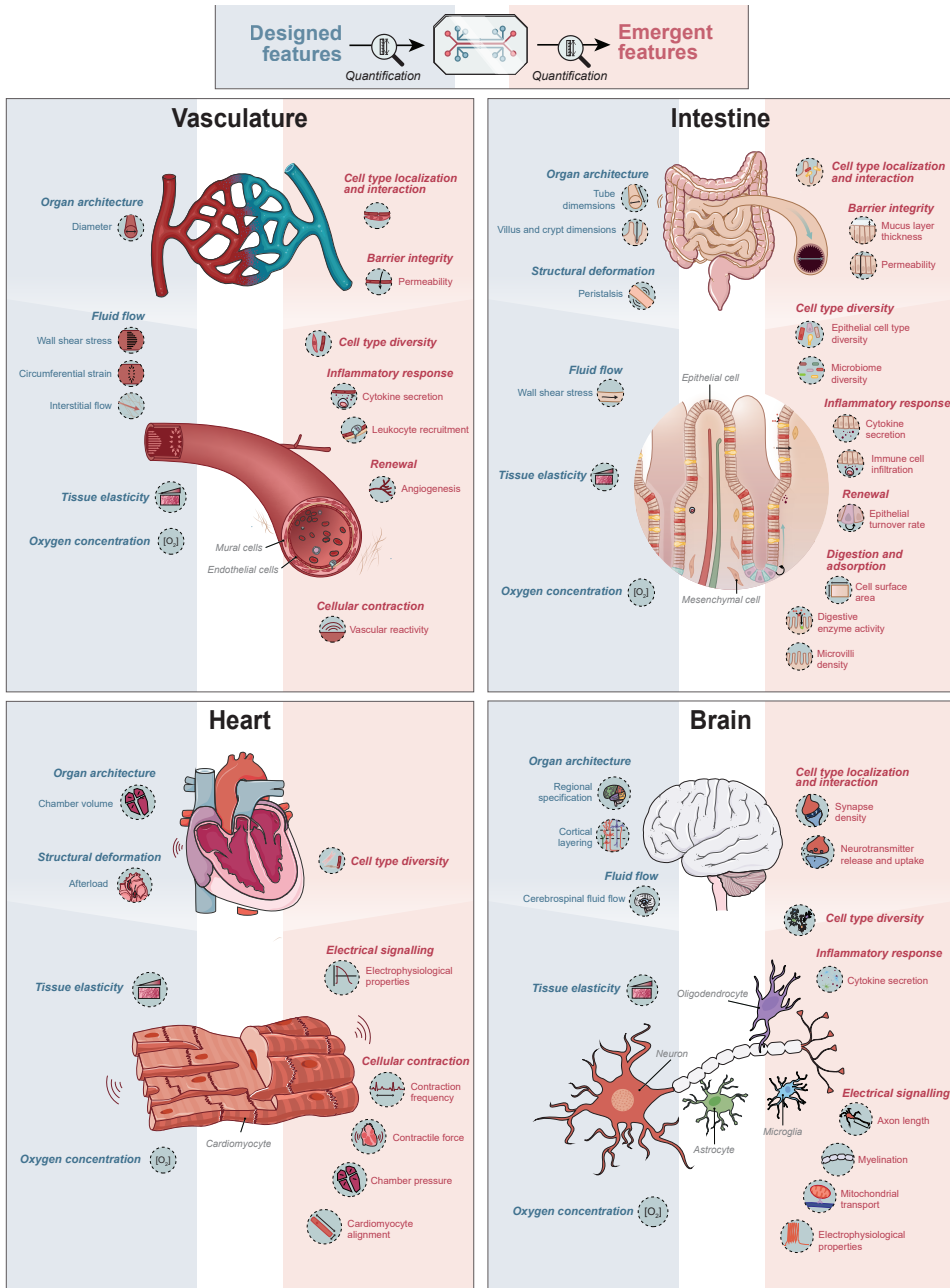
## **2 Organ physiology and biological features of the human vasculature, intestine, heart and brain**

Physiological features can be divided into 'designed' (blue) and 'emergent' (red) (*Supplemental figure 1*). Features may belong to either or both groups depending on the specific model and functional read-out required. In this review, they are divided for simplicity into one of the categories depending on the context discussed in this review. Microphysiological systems (MPS) can quantitatively control and monitor physiological features. Accurate quantification of these features is essential for system-to-system comparisons and understanding *in vivo* relevance which will facilitate development of measurable standards to designate a system as 'fit for purpose'. Here, we describe the basic organ physiology and biological features for the human vasculature, intestine, heart and brain (*Supplemental figure 1*).

**Vasculature.** Blood vessels are cylindrical tubes with diverging diameters which transport oxygen and nutrients through the body and remove waste products. The vessel wall consists of a single layer of endothelial cells surrounded by either smooth muscle cells or pericytes, depending on tissue location. There is also broad molecular heterogeneity within the vascular bed depending on the position in the vascular tree and the microenvironment of the surrounding tissue. Vascular cells sense and respond to many biomechanical and biochemical cues. Hemodynamic forces such as wall shear stress and circumferential strain or exerted by interstitial flow, tissue elasticity and the local oxygen concentration are examples of such cues. Blood vessels can actively respond to these signals by contracting or dilating (vascular reactivity), forming new blood vessels from those pre-existing (angiogenesis), or adjusting barrier integrity between the blood and the surrounding tissue to transport cytokines, hormones and other plasma constituents. Among the most important functions of blood vessels is responding to inflammatory stimuli by secreting cytokines and enabling immune cell transmigration.

**Intestine.** The intestine digests and selectively transports nutrients from its lumen to the bloodstream (small intestine) and absorbs remaining water and salts (large intestine). The enormous absorption capacity is related to the specific organization of the epithelial lining into finger-like structures (villi) and crypts, which increase the effective surface area. Epithelial cells start as stem cells in the crypts, migrate along the villus while maturing into functional cells and reach the tip of the villus after 3-4 days, which marks the end of their life cycle. They are organized along the villi according to their function (e.g. production of digestive enzymes, hormones and mucus along the villus length; epithelial regeneration and production of anti-microbial peptides in the crypt). The uptake of nutrients and transport of waste is facilitated by the mechanical microenvironment: peristaltic motion caused by a layer of longitudinal and circular (smooth) muscle cells resulting in continuous flow of luminal content. The intestine is also an important barrier that actively controls the transport of luminal content to the circulatory system. The mucus layer forms the first mechanical barrier, followed by the tight epithelial layer that maintains barrier integrity

and intestinal homeostasis. Immune cell surveillance of the epithelial barrier determines whether tolerance is maintained or inflammation elicited in response to digested and transported macromolecules. Oxygen gradients from the small- to the large intestine and from the lumen to the *lamina propria* allows survival of specific commensal microorganisms in each region without compromising the survival of adjacent intestinal epithelial cells. The commensal microorganisms that thrive in the anaerobic environment of the intestine are essential for both digestion and regulation of the intestinal immune response.



**Supplemental figure 1: Schematic overview of physiological features of four selected organs: human vasculature, intestine, heart and brain. Features may belong to either or both groups depending on the specific model and functional read-out required.**

Heart. The heart pumps blood through the vasculature to distribute oxygen and nutrients and remove carbon dioxide and metabolic waste. It consists of four chambers (two upper atrial chambers and two lower ventricular chambers), which synchronously pump blood to either the lungs or rest of the body using valves to prevent blood backflow. It is made up of the contractile cardiomyocytes and multiple non-cardiomyocyte cell types such as fibroblasts, endothelial-, endocardial-, epicardial-, neuronal and immune cells. The sinoatrial node, which acts as the pacemaker, works in combination with the atrioventricular node and the Purkinje fibers to propagate electrical signals throughout the myocardial wall regulating cardiomyocyte contraction. The resulting contractile frequency and force are highly dependent on the cellular organization (e.g. coupling, alignment) of the cardiomyocytes and other cell types. Resident fibroblasts ensure the extracellular matrix (ECM) is well-maintained via protein turnover, thus controlling heart tissue elasticity. In the heart, varying (or reduced) oxygen concentrations are key in the onset or development of cardiac disease, as in myocardial infarction.

Brain. The human brain is organized in distinct functional and structural domains: the cerebrum, cerebellum and brainstem. Different brain regions, such as the hippocampus, cerebellum and the prefrontal cortex, have distinct topographical structures. Higher cognitive functioning is thought to arise from the prefrontal cortex, a layered sheet of neural tissue with topographic separation into functional domains. Each brain region and neural cell type are distinct in their function and interaction, ensuring proper brain function. Besides blood flow, the brain is perfused by cerebrospinal fluid. This fluid is continuously produced by the choroid plexus and is involved in the distribution of nutrients and clearance of waste products. The brain is a highly active organ, so adequate oxygen levels are essential for maintaining proper brain function. At a cellular level, diverse neuronal subtypes and glial cells, such as astrocytes, microglia and oligodendrocytes, form neural networks that produce the brain output. Neurons communicate via these neural networks between- and within brain regions by propagating electrical signals (action potentials) along their axons, ultimately transmitting these through synapses using various neurotransmitters. This energy-consuming process requires mitochondrial anterograde transport along the axons for molecules and ions to reach the axon terminal, whereas retrograde transport is important for removing damaged organelles and debris. Astrocytes promote neuronal maturation and synapse development, maintain the blood-brain-barrier, provide neurons with metabolites and govern network activity. Oligodendrocytes produce an insulating layer, myelin, around the axons of neurons, ensuring efficient propagation of action potentials. The brain is a soft organ, more than 20% of this organ is made up of ECM, providing a scaffold for neural cells to migrate and make connections to other brain regions. Upon injury, microglia and astrocytes release and respond to inflammatory cytokines, creating scar tissue and removing debris from the extracellular space.

### **3 General designed features: Cell source and media**

Two designed features relevant for any *in vitro* model are the cell source and cell culture medium used. These features largely influence the emergent features.

#### **Cell source**

The most commonly used cell sources are primary human cells (either commercially available or patient-derived) or immortal(ized) or cancer cell lines since they are generally easy-to-use. All three are inexpensive and can show features of their tissue or organ source<sup>1</sup>. More recently, advances in stem cell biology enabled increasing application of either adult human stem cells (most easily derived from endodermal organs) or human induced pluripotent stem cells (hiPSCs) which are derived by reprogramming somatic cells to a state from which they can form derivatives of all organs<sup>2</sup>. hiPSC lines can be generated from healthy individuals or patients with genetic disorders and can be genetically engineered to introduce- or remove disease-specific mutations or variants for disease modelling<sup>1</sup>. They can also be genetically modified to incorporate cell type-specific (fluorescent) reporter constructs or phenotypic sensors. Drawbacks include cost, operator skill and an often immature phenotype although the latter can for some cells be obviated by inclusion in the MPS.

#### **Media composition**

MPS provide complex culture systems often with the inclusion of multiple tissue cell types from any of the sources above. Maintaining tissue-specific cell types requires the correct combination of nutrients, metabolites and growth factors. Blood vessels would normally be exposed to blood; cells in organs are generally either exposed to interstitial fluid or components of blood that have passed through the blood vessel wall. However, most current MPS have limited compatibility with physiological perfusates, such as whole blood, and there is to date no universal medium that can serve as a 'blood mimetic'<sup>3</sup>. Current MPS usually address this by either mixing media with different compositions that support the individual cell types in the system and examining the outcome empirically, or by compartmentalizing the device to 'feed' different cell types independently.

4. Supplemental Table 1   Quantification of designed and emergent physiological features in microphysiological systems and human in vivo						
Category	Organ	Feature	MPS		Ref In Vivo	
			Method	Quantification	In vivo (human)	Quantification
<b>Fluid flow</b>	Vessel	Interstitial flow	Pressure pump	1.3 $\mu\text{m/s}$	0.1-2 $\mu\text{m/s}$ (rabbit)	4 5
<b>Cell type diversity</b>	Intestine	Microbiome – bacterial diversity	CFU count; 16S rRNA sequencing	118-135 OTUs (primary cells, ileum) and 200 OTUs (Caco-2)	280 OTUs	6 7
<b>Inflammatory response</b>	Vessel	Patrolling monocyte speed	Real-time fluorescent imaging	3-12 $\mu\text{m/min}$	9-36 $\mu\text{m/min}$ (mouse)	8 9
	Intestine	Immune cell infiltration	IF	22-25 CD103+ cells / $\mu\text{m}^2$ in epithelial layer upon LPS stimulation	$\leq 25$ IELs / 100 epithelial cells (Duodenum, healthy)	10 11
<b>Barrier integrity</b>	Intestine	Mucus layer thickness	Dark field microscopy and beads	Outer layer: 370 $\mu\text{m}$ , inner layer: 200 $\mu\text{m}$	SI: 50-450 $\mu\text{m}$ ; LI: outer layer 300-700 $\mu\text{m}$ , inner layer 100-400 $\mu\text{m}$	12 13
<b>Electrical signaling</b>	Brain	Axon length	Compartmentalized system	9 - 12 cm	> 1 meter	14 15
		Myelin thickness	Electron microscopy on compartmentalized system	Average G-ratio of 0.57 $\pm 0.16$	G-ratio of 0.68-0.8	16 17
		Myelin length	IF and artificial 'axons'	10 - 120 $\mu\text{m}$	18.28-57.36 $\mu\text{m}$ (mouse)	18 19
		Axonal transport speed of mitochondria	Directed axonal growth in compartmentalized system	0.6 $\mu\text{m/s}$	0.22 $\mu\text{m/s}$ (mouse)	20 21

4. Supplemental Table 1 | continued

Category	Organ	Feature	MPS		Ref In Vivo	
			Method	Quantification		
Cellular contraction	Heart	Contraction frequency	Video tracking	55-80 BPM	22	23
			Video tracking	43-57 BPM	24	
			Pillar tracking	32 BPM	25	
		Contractile force	Pillar tracking	6.2 ± 0.8 mN/mm <sup>2</sup>	26	27
	Pillar tracking		~12.5 μN	28		
			Pillar tracking	~3 mN/mm <sup>2</sup>	29	
		Force Frequency Relationship	Video tracking	Positive	28	30
		Cardiomyocyte Alignment		88-96/12.5-13.5 μm (Aspect ratio: 7.6±0.4:1)	26	31
	Systolic ventricular pressure	Intraventricular pressure sensor	50 μmHg	32	33	
			141/19 μm (aspect ratio: 7.4:1)			
			120 mmHg			

4. Supplemental Table 1   continued				Ref In	
Category	Organ	Feature	MPS	MPS	
			Method	In vivo (human)	
			Quantification	Quantification	
Digestion and absorption	Intestine	Cell surface area	Imaging and computational 3D reconstructions	Enlargement factor (apical cell surface compared to monolayer): 1.7-fold (excluding microvilli)	Enlargement factor villi: 4.5-8.6 (SI). Enlargement factor microvilli: 9.2-15.7 (SI), 6.4-6.7 (LI)
		Microvilli density	SEM and ImageJ	7/ $\mu\text{m}^2$	Jejunum: 114/ $\mu\text{m}^2$ (Villus crest), 22/ $\mu\text{m}^2$ (Intervillus space), 15/ $\mu\text{m}^2$ (Crypt)
		Glucose uptake rate	Quantification of glucose in medium	$\sim 280 \text{ mmol L}^{-1} \text{ h}^{-1}$ , $\sim 0.3 \text{ nmol cell}^{-1} \text{ h}^{-1}$	Vmax= 83/25 mmol/h/15-cm segment and Km= 154/50 mmol/L (Jejunum/Ileum)
		Digestive enzyme activity	Amino peptidase activity assay, A4N	9, 12 fmol/min/cell (flow, flow and strain)	NA
				0.92 fmol/min/cell	
		Sucrase-isomaltase activity assay (30 mM sucrose to glucose)	15-40 U/g protein	Vmax=83/36 mmol/h/15-cm segment and Km=142/74 mmol/L (Jejunum/Ileum)	
		Drug metabolizing enzyme activity	LC-MS of metabolized drug in outflow (testosterone to 6 $\beta$ -OH-T)	0.36-2.46 nmol/min/mg protein (Jejunum)	

Data was included based on the criteria as stated in Supplement Methodology 1.2. Abbreviations: MPS=microphysiological system, NA=not available, SI=small intestine, LI=large intestine, IEL=intraepithelial lymphocyte, CFU=colony-forming unit, OTU=operational taxonomic unit, LC-MS=liquid chromatography-mass spectrometry, IF=immunofluorescence, LPS=lipopolysaccharide, 6 $\beta$ -OH-T=6 $\beta$ -hydroxytestosterone, m=meter, BPM=beats per minute, N=Newton, h=hour, min=minute, s=second, ref=reference.

## 5 Supplemental discussion designed feature

### Fluid flow – interstitial flow

Interstitial flow describes the movement of fluid through the ECM and its resident cells and is the type of flow present in almost all tissues and organs. The forces exerted on cells by interstitial flow are more challenging to measure or calculate *in vivo* and *in vitro* and are therefore expressed as fluid flow speed. In the vasculature, interstitial flow has been described in great detail and it has been associated with vasculogenesis, lymphogenesis and lymphatic drainage of blood plasma which has leaked from the micro-vasculature. A similar process takes place in the brain, where cerebral spinal fluid (CSF), produced by cells of the choroid plexus, flows via the four ventricles of the brain to subarachnoid spaces, clearing waste products, distributing trophic factors and maintaining brain pH balance in the process<sup>44</sup>. OoCs have been able to model interstitial flow using 3D hydrogel compartments with known biophysical parameters suitable for convection of fluid at controllable velocities. In one technologically-advanced approach, a hydrogel containing a self-assembled vascular network was pressurized using a pump to apply constant interstitial flow<sup>4</sup>. Both computational simulation of flow velocities and verification using fluorescence recovery after photobleaching (FRAP) showed that interstitial flow was in the physiological range (*SI Table 1*). Interestingly, the device design also allowed direct sampling of the interstitial fluid enabling investigation of therapeutic molecule distribution. This type of system is suitable for use on tissues embedded in a hydrogel; however, it cannot be applied to free floating tissues in culture. This is exemplified by a BoC system which uses rat cortical neurospheroids to study the effect of flow on waste clearance and neuronal maturation. Here, an osmotic micropump was used to apply a constant flow of 0.15  $\mu\text{l}/\text{min}$  over spheroids trapped in concave microwells at the bottom of the microfluidic channel<sup>45</sup>. Improved neuronal differentiation and synapse formation was observed within the neurospheroid, suggesting that a rudimentary model of CSF flow can already benefit neuronal maturation. As described, there are multiple technological solutions to create interstitial flow. Important for correct quantitative implementation of these forces is the correct verification within the system. Multiple methods can be used to do so, including computational simulation and FRAP as previously discussed for VoCs<sup>4</sup>.

## 6 Supplemental discussion designed feature

### Cell type diversity – microorganisms

Non-human cells, such as commensal microorganisms in the intestine, can be quantified using another type of analysis: 16S rRNA sequencing. This technique was used to quantify microbiome diversity in a GoC system<sup>6</sup> (SI Table 1). The healthy human microbiome is composed of ~200 species<sup>46</sup>. Modeling the microbiome *in vitro* thus requires a complex environment that supports many different species, with different needs in terms of oxygen concentration, nutrition and space. A GoC system containing over 200 unique operational taxonomic units (OTUs) from healthy human stool specimens was reportedly sustained for at least five days, comparing favorably with 280 OTUs in human intestinal aspirates<sup>6</sup>. Sequencing 16S rRNA is suitable to quantify microbial diversity in *in vitro* models, since the same methods can be used to characterize microbial diversity in intestinal brush border or stool samples. Alternatively, metagenomic sequencing provides insight in active microbial metabolic pathways and is applied to different areas of the human intestine to get insight into the contribution of location-specific microbiome niches.

### Immune cell migration speed

Quantification of the number of transmigrated or infiltrated immune cells are clinically relevant proxies for the inflammatory and disease state<sup>47</sup>. The quantification of transmigrated or infiltrated immune cells requires normalization to the total tissue area analyzed<sup>48,49</sup>. This principle has been applied in both VoC and GoC systems. One VoC model quantified transmigration of neutrophils on a template-based vessel containing several cylindrical ECM-filled stacks with known volume<sup>50</sup>. Accordingly, the number of transmigrated neutrophils per tissue volume could be derived in a similar way as in mice. Also self-assembled 3D vascular networks have proven useful for investigating the dynamics of monocyte transmigration in real-time<sup>51</sup>. However, both models lack continuous perfusion and cannot be used to quantify flow-related parameters such as monocyte patrolling speed. This still requires more classical *in vitro* approaches; for example an endothelial cell monolayer under physiologically-relevant shear flow was used to quantify monocyte migration speed (3-12  $\mu\text{m}/\text{min}$ ); this was shown to be close to that in mice (SI Table 1)<sup>8,9</sup>. To increase *in vivo* relevance further, future VoC models should include fluid flow and appropriate tissue elasticity. The importance of this was shown recently in work combining hydrostatic pressure driven flow over microfluidic channels in a collagen-based ECM<sup>52</sup>. The former VoC work can be extended by analysis of the migration of immune cells through an endothelial cell layer into a tissue, as was done in a GoC system. This multi-cell type systems contained a microchannel with an intestinal epithelial cell layer membrane-separated from a microchannel with an endothelial cell layer and monocyte-derived macrophages and dendritic cells. Using this system the number of dendritic cells invading the epithelial layer upon LPS stimulation was quantified to be ~22-25 CD103<sup>+</sup> cells/ $\mu\text{m}^2$  of the epithelial layer<sup>10</sup>. Essentially the same method is used to

study chronic inflammatory diseases. For example, to diagnose celiac disease, the number of invading inflammatory immune cells is measured in human intestinal biopsies. Of note, the units slightly differ making direct comparison difficult: for GoCs the number of immune cells/ $\mu\text{m}^2$  of epithelial cell layer was reported, whilst for intestinal biopsies they reported the number of intraepithelial lymphocytes per 100 epithelial cells which circumvents the need to determine surface area (*SI Table 1*). A similar unit can be used to express invading immune cells in GoCs. To date, the number of HoC models that incorporate components of the immune system are limited and robust quantifications on inflammatory response are lacking.

### **Barrier integrity – Mucus layer**

Several GoC studies have quantified mucus production, either as dissociated mucin proteins in flow-through fluid<sup>6,42</sup> or as mucus layer thickness after fixation<sup>34</sup>, which alters mucus layer structure. Dark-field microscopy is a non-invasive alternative allows study of the mucus layer in live cultures over time<sup>12</sup>. The outer and inner mucus layers can be distinguished based on pore size using fluorescently-labelled beads. Their thickness was estimated as 370  $\mu\text{m}$  and 200  $\mu\text{m}$ , respectively after 14 days in a GoC containing primary colon tissue. The chip design used required the removal of thin layers of PDMS parallel to the channels and subsequent analysis of the chips on a glass slide. Altering device design or advanced imaging methods might overcome this limitation (see ‘Technical advances’ for advanced imaging).

### **Electrical activity – brain**

Neurons in the brain show great diversity in axon length, extending away from the cell body, to establish connectivity within the brain and relay signals to the remainder of the body using motor neurons<sup>15</sup>. Modelling the extension of these long axons has been done using a compartmentalized microfluidic devices<sup>14</sup>. In these BoC devices, hiPSC-derived motor neurons grew as bundles of axon up to 9-12 cm in length. Whilst remarkably long, the neurons were nevertheless approximately 100-fold shorter than *in vivo* equivalents. To relay signals throughout these elongated cells effectively, action potential conduction velocity needs to be ensured. For this, neurons require both myelination of their axons and active transport of mitochondria along these axons. Robust modelling and quantification of myelination and the build-up of small lipid-rich insulators, has only been described in a few MPS platforms. Among these is a nerve-on-chip device which described myelination of peripheral motor-neuron axons by Schwann cells, during guided outgrowth of axons from 3D spheroids<sup>16</sup>. Importantly, the model could be directly compared with *in vivo* measurements by using the same method and unit (*SI Table 1*). Electron microscopy was used to quantify the G-ratio i.e. the ratio between the inner and the outer diameter of the myelin sheath as a measure of myelin thickness. The BoC value was slightly lower than the G-ratio described for the human central nervous system (*SI Table 1*). This fits the notion that G-ratios in the peripheral

nervous system are generally lower; however, these values have not been quantified *in vivo* to our knowledge. Another MPS of the brain was used to quantify myelin length in rat oligodendrocytes using immunofluorescent microscopy (*SI Table 1*)<sup>18</sup>. Values were similar to the myelin length in mouse brain<sup>19</sup>. Active transport of mitochondria was measured in BoCs with microtunnel-separated culture compartments for the neuronal *soma* and thus forcing directed axonal outgrowth through the microtunnels and enabling live tracking of the mitochondria. This set-up allowed anterograde and retrograde transport of mitochondria to be distinguished with rates around 0.6  $\mu\text{m/s}$ , the same order of magnitude as *in vivo*<sup>20</sup> (*SI Table 1*).

### Cellular contraction

Contraction is the functional output of muscle tissues. The heart relies on the synchronized and timely contraction of muscle cells to pump blood through the body. Alignment of contractile myocytes is essential in efficient unidirectional muscle contraction, therefore, it also serves as one output of *in vitro* maturity and increased physiological mimicry.

Alignment of muscle cells can be quantified using their aspect (length to width) ratio in the direction of contraction<sup>53</sup>. Aspect ratios can increase in response to the cardiomyocyte environment and mechanical or chemical signals<sup>54–56</sup>. For instance, in EHTs made in an oval cell culture chamber with standing pillars, cardiomyocyte alignment is induced by the chamber shape and subsequently by unidirectional load from the pillars. Aspect ratios of  $7.6 \pm 0.4$  have been reported in EHTs which resembles that of healthy human adult myocardium<sup>26</sup> (*SI Table 1*).

The overall output of the contraction of the cells can be described by its frequency, force and the force-frequency relationship (FFR). Cardiac muscle contraction frequency or rate is measured in beats per minute (BPM). This is easily quantified in MPS of the heart, for example by video tracking, but varies based on mechanical environment, cell-source and medium composition. Nevertheless, identifying factors affecting beat rate can provide insight into human physiology and facilitate drug discovery. For instance, beta-adrenergic signaling affects beating frequency<sup>57</sup>: in a cantilever-based cardiac model, seeded with hiPSC-derived cardiomyocytes in a constrained gel, baseline beat-rates were close to those in human heart and increased by  $\pm 60\%$  upon beta-adrenergic stimulation (*SI Table 1*). Importantly, many cardiac diseases or drug side effects manifest as arrhythmias which can be detected by irregular beating.

Quantification of force is in most MPS of the heart only possible indirectly, optical displacement of cells being taken as a measure of contraction<sup>58</sup>. Other studies optically track anchoring points with known stiffness to calculate the force of contraction needed for their displacement. Pillars, wires, force-transducers or 2D-tissue strips are all used<sup>29,59,60</sup>. Recently, MPS of the heart that simultaneously measure contractile force and extracellular field potential have been described. Cardiomyocytes were cultured on a flexible electronic

parylene-SR film with integrated gold-electrodes; contraction deflected the thin, flexible film and this generated compressive strain which was transmitted to allow direct, real-time monitoring of the excitation-contraction coupling<sup>61</sup>. The maximum force measured *in vivo* and *in vitro* depends on the tissue cross-section. Tissue force is thus best normalized to cross-sectional area, in principle enabling *in vitro* and *in vivo* comparisons. Nonetheless, measuring force as a function of the displacement of anchoring points as in EHTs is still prone to variability caused by differences in height of the tissue suspension points, insufficient information on the mechanical properties of anchoring points and differences in cross-sectional areas. Therefore, anchoring the tissue to a calibrated force-transducer still gives the best comparison with adult myocardium. The highest force values reported to date for MPS of the heart containing hiPSC-derived cardiomyocytes is  $6.2 \pm 0.8$  mN/mm<sup>2</sup>, achieved using standing pillars with serum-free medium<sup>26</sup>. This is similar to human infant myocardial force but still lower than adult heart *in vivo* (SI Table 1). In addition to the maximum contraction force, dynamics in the contraction transient (e.g. contraction time, relaxation time) provide insight into the drug mechanism of action and report expected effect *in vivo*. For example, the myosin activator omecamtiv mecarbil has been shown to increase both force of contraction and contraction time in hiPSC-derived cardiomyocyte EHTs<sup>62</sup>, predicting the positive inotropic response in patients. A large study across multiple platforms showed that hiPSC-derived cardiomyocytes cultured in 2D and 3D are high predictive when based on output parameters such as time to peak, relaxation- and contraction time<sup>57</sup>.

Adult human myocardial muscle strips show increased force at higher beating frequencies i.e. a positive FFR. This is not the case in mouse, failing or fetal hearts<sup>30</sup>. EHTs show positive FFR values after metabolic or electrical conditioning<sup>26,28</sup>. Relatively high baseline frequencies of spontaneously beating EHTs can mask the FFR. For this reason, ivabradine, a ‘funny current’ inhibitor, has been used to reduce the spontaneous beat-rate of EHTs to reveal a positive FFR, which could increase to about 200% of the baseline force. Ultimately, force is needed *in vivo* to generate enough pressure to circulate the blood through the body which is a highly relevant clinical read-out. Several different HoC systems have been designed to generate such pressure by engineering chambers and measured this pressure to assess the physiological relevance of their system. A HoC modelling ventricular chambers was used to perform pressure-volume loop measurements in a bioreactor and determined a maximum pressure of 50  $\mu$ mHg<sup>32</sup>, still far from the 120 mmHg *in vivo*<sup>33</sup>. While measuring output pressure is easier to compare with clinical values than force of contraction, the models require more complex engineering and typically higher cell numbers.

### **Digestion and absorption**

The main function of the small intestine is to digest and absorb nutrients as source of energy for the body. The architecture of the epithelial barrier of the small intestine sustains this function through villi and microvilli, which greatly increase the surface area for nutrient

breakdown and absorption into the bloodstream. The enterocytes, which form the main cell type of the small intestinal epithelial barrier, produce digestive- and drug metabolizing enzymes to enhance the bioavailability of food and drugs after oral intake.

In GoC devices, the epithelial cells can self-organize into 3D villus-like folds when exposed to continuous flow in the top and bottom channel. Computational 3D surface reconstruction based on microscopic Z-stack images showed a 2-fold increase in epithelial surface area within two days of seeding Caco-2 cells in the upper microchannel of a GoC system<sup>34</sup>. Increasing the microchannel height above 150  $\mu\text{m}$  might have allowed the villi to grow closer to the  $\sim 700 \mu\text{m}$  described for human intestine and achieve the same 4.5-8.6 surface area enlargement (*SI Table 1*). The surface area is further enlarged by the presence of microvilli on the surface of enterocytes, quantified to range from  $\sim 15/\mu\text{m}^2$  in the crypts to  $\sim 200/\mu\text{m}^2$  on the villus tips in human intestinal biopsies. Microvilli are often shown on enterocytes in GoCs but are rarely quantified. Exceptionally, one GoC study did quantify the microvilli density on the apical surface of primary duodenal tissue using electron microscopy and found upon dynamic force  $\sim 7$  microvilli per  $\mu\text{m}^2$ <sup>37</sup>. This finding underlines the importance of quantification to further improve GoC systems and increase their physiological relevance.

Nutrient absorption by intestinal epithelial cells can be relatively easily measured in GoC systems. A GoC investigated glucose uptake rates by the intestinal epithelial barrier by perfusing glucose-containing medium through the apical channel and glucose-free medium through the basal channel, then quantifying the glucose concentrations at the channel outlets and the total number of epithelial cells in the system<sup>34</sup> (*SI Table 1*). Multiple GoC studies have measured the activity of digestive enzymes such as sucrase-isomaltase<sup>42</sup> and aminopeptidase<sup>40,41</sup>. Both aminopeptidase studies confirmed increased enzyme activity upon fluid flow, however the kinetics are difficult to correlate with *in vivo* measurements of enzyme activity, as these mainly quantify substrates or metabolites in the systemic bloodstream after processing by multiple organs. In contrast, *in vitro* studies usually investigate the conversion rate of a substrate into a metabolite in a specific tissue or step of metabolism. The same issue arises when quantifying drug metabolizing enzyme activity. In very few cases, *in vivo* enzyme kinetics are described for a tissue specifically and can be compared directly to *in vitro* values. In a GoC system containing primary duodenal tissue for example, CYP3A4 enzymes transformed testosterone to  $6\beta$ -hydroxytestosterone ( $6\beta$ -OH-T) with a metabolic rate of 0.056 nmol/min/mg protein which is lower than *in vivo* testosterone hydroxylation levels in human jejunum<sup>37,43</sup> (*SI Table 1*). In contrast, other GoC studies used non-physiological substrates that are metabolized to fluorescent derivatives, which are not comparable with *in vivo* measurements. This illustrates the need for sets of validated reference compounds, for which the effects in the human body are well described. More complex GoC systems, linked to other organs, and *in silico* modeling may address this in the future and eventually allow relevant quantification of a more complete digestion and drug metabolism process.

## 7 Standardization and open platforms

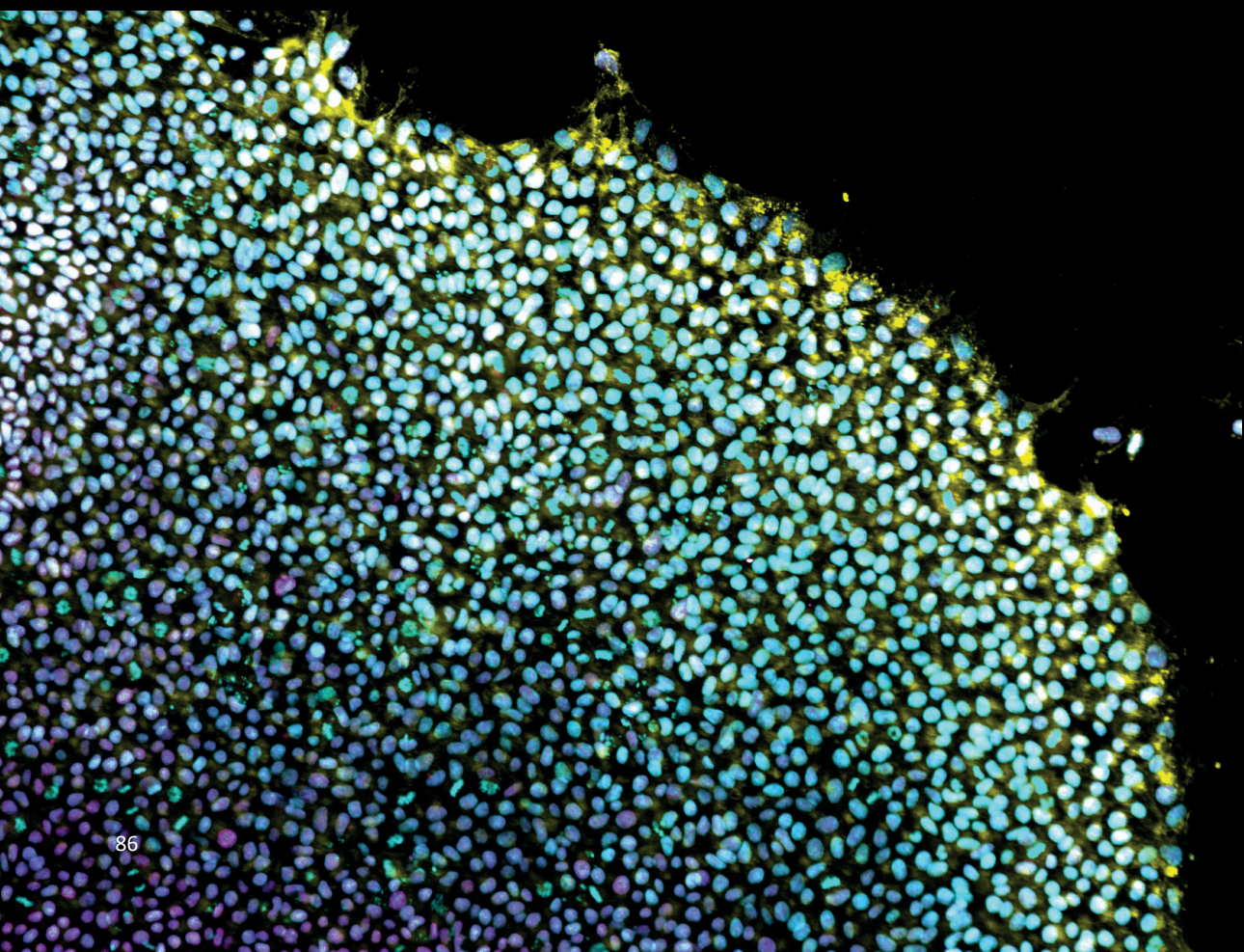
Accurate comparisons of different MPS have become increasingly challenging as MPS use has grown and customized MPS designs have emerged. To achieve system-to-system and lab-to-lab comparability, standardization is required at multiple levels. Among these, agreement on methods for quantification of designed and emergent features in MPS is crucial to develop measurable standards applicable to (customized or commercial) MPS designs and platforms. This includes standardization of sensitivity and accuracy of the methods, reporting of data, and the use of reference compounds or methods that have been well-established *in vivo*. Developing MPS that can achieve measurable standards might require additional consensus on the materials and cells used, interfacing with existing lab infrastructure and various MPS, and operating strategies<sup>63</sup>. One approach that facilitates standardization is using MPS platforms with standardized interface that can accommodate and interconnect different types of MPS<sup>64</sup>. MPS platforms could incorporate the multiplicity of existing MPS within the uniformity of a familiar and standardized interface. Commercial platforms already partly offer this type of standardization. Other initiatives, such as the Translational Organ-on-Chip Platform (TOP)<sup>65</sup> and the Moore4Medical's Smart Multi-Well Plate<sup>66</sup>, implement standardized constraints for chip geometry and interfaces<sup>67</sup>, and may provide more generally applicable open technology platforms in which new MPS designs can be implemented interchangeably in 'plug-and-play' formats. These open technology platforms will enable the modular integration of sensors or use of existing laboratory equipment to generate quantitative read-outs of emergent features in MPS without having to develop tailored solutions for individual MPS platforms. It has been argued that, by embedding a variety of MPS with a uniform and standardized interface, MPS platforms could contribute to establishing more reproducible and lab-independent MPS practice, amenable to wider adoption by end users and regulatory acceptance. To facilitate this, MPS developers should inform the design of their devices with the standards for geometry and interfaces adopted in the MPS platforms, in a process that gradually converges towards eliciting a set of shared templates for MPS design. In this way, these platforms will aid in standardizing the design and operation of MPS and pave the way to multi-organ systems.

## Supplementary references

1. Van Den Berg, A., Mummery, C. L., Passier, R. & Van der Meer, A. D. Personalised organs-on-chips: functional testing for precision medicine. *Lab Chip* **19**, 198–205 (2019).
2. Sharma, A., Sances, S., Workman, M. J. & Svendsen, C. N. Multi-lineage Human iPSC-Derived Platforms for Disease Modeling and Drug Discovery. *Cell Stem Cell* **26**, 309–329 (2020).
3. Low, L. A., Mummery, C. L., Berridge, B. R., Austin, C. P. & Tagle, D. A. Organs-on-chips: into the next decade. *Nat. Rev. Drug Discov.* (2020) doi:10.1038/s41573-020-0079-3.
4. Offeddu, G. S. *et al.* Application of Transmural Flow Across In Vitro Microvasculature Enables Direct Sampling of Interstitial Therapeutic Molecule Distribution. *Microcirculation-on-Chip* **1902393**, (2019).
5. Swartz, M. A. & Fleury, M. E. Interstitial flow and its effects in soft tissues. *Annu. Rev. Biomed. Eng.* **9**, 229–256 (2007).
6. Jalili-firoozinezhad, S. *et al.* A complex human gut microbiome cultured in an anaerobic intestine-on-a-chip. *Nat. Biomed. Eng.* **3**, 520–531 (2019).
7. Villmones, H. C. *et al.* Species Level Description of the Human Ileal Bacterial Microbiota. *Sci. Rep.* **8**, (2018).
8. Collison, J. L., Carlin, L. M., Eichmann, M., Geissmann, F. & Peakman, M. Heterogeneity in the Locomotory Behavior of Human Monocyte Subsets over Human Vascular Endothelium In Vitro. *J. Immunol.* **195**, 1162–1170 (2015).
9. Buscher, K., Marcovecchio, P., Hedrick, C. C. & Ley, K. Patrolling Mechanics of Non-Classical Monocytes in Vascular Inflammation. *Front. Cardiovasc. Med.* **4**, (2017).
10. Maurer, M. *et al.* A three-dimensional immunocompetent intestine-on-chip model as in vitro platform for functional and microbial interaction studies. *Biomaterials* **220**, (2019).
11. Hayat, M., Cairns, A., Dixon, M. F. & O'Mahony, S. Quantitation of intraepithelial lymphocytes in human duodenum: what is normal? *J. Clin. Pathol.* **55**, 393–395 (2002).
12. Sontheimer-Phelps, A. *et al.* Human Colon-on-a-Chip Enables Continuous In Vitro Analysis of Colon Mucus Layer Accumulation and Physiology. *Cell Mol Gastroenterol Hepatol.* **9**, 507–526 (2020).
13. Dutton, J. S., Hinman, S. S., Kim, R., Wang, Y. & Allbritton, N. L. Primary Cell-Derived Intestinal Models: Recapitulating Physiology. *Trends Biotechnol.* **37**, 744–760 (2019).
14. Spijkers, X. M. *et al.* A directional 3D neurite outgrowth model for studying motor axon biology and disease. *Sci. Rep.* **11**, 2080 (2021).
15. Stifani, N. Motor neurons and the generation of spinal motor neuron diversity. *Front. Cell. Neurosci.* **8**, (2014).
16. Sharma, A. D. *et al.* Engineering a 3D functional human peripheral nerve in vitro using the Nerve-on-a-Chip platform. *Sci. Rep.* **9**, (2019).
17. Cercignani, M. *et al.* Characterizing axonal myelination within the healthy population: a tract-by-tract mapping of effects of age and gender on the fiber g-ratio. *Neurobiol. Aging* **49**, 109–118 (2017).
18. Espinosa-Hoyos, D. *et al.* Engineered 3D-printed artificial axons. *Sci. Rep.* **8**, (2018).
19. Tomassy, G. S. *et al.* Distinct Profiles of Myelin Distribution Along Single Axons of Pyramidal Neurons in the Neocortex. *Science (80-. )*. **344**, 319–324 (2014).
20. Lu, X., Kim-Han, J. S., O'Malley, K. L. & Sakiyama-Elbert, S. E. A microdevice platform for visualizing mitochondrial transport in aligned dopaminergic axons. *J. Neurosci. Methods* **209**, 35–39 (2012).
21. Takihara, Y. *et al.* In vivo imaging of axonal transport of mitochondria in the diseased and aged mammalian CNS. *Proc. Natl. Acad. Sci. U. S. A.* **112**, 10515–10520 (2015).
22. Mathur, A. *et al.* Human iPSC-based cardiac microphysiological system for drug screening applications. *Sci. Rep.* **5**, 8883 (2015).
23. Drouin, E., Charpentier, F., Gauthier, C., Laurent, K. & Le Marec, H. Electrophysiologic characteristics of cells spanning the left ventricular wall of human heart: Evidence for presence of M cells. *J. Am. Coll. Cardiol.* **26**, 185–192 (1995).
24. Tulloch, N. L. *et al.* Growth of engineered human myocardium with mechanical loading and vascular coculture. *Circ. Res.* **109**, 47–59 (2011).
25. Mills, R. J. *et al.* Functional screening in human cardiac organoids reveals a metabolic mechanism for cardiomyocyte cell cycle arrest. *Proc. Natl. Acad. Sci.* **114**, E8372–E8381 (2017).
26. Tiburcy, M. *et al.* Defined engineered human myocardium with advanced maturation for applications in heart failure modeling and repair. *Circulation* **135**, 1832–1847 (2017).

27. Hasenfuss, G. *et al.* Energetics of isometric force development in control and volume-overload human myocardium. Comparison with animal species. *Circ. Res.* **68**, 836–846 (1991).
28. Zhao, Y. *et al.* Towards chamber specific heart-on-a-chip for drug testing applications. *Adv. Drug Deliv. Rev.* **165–166**, 60–76 (2020).
29. Ronaldson-Bouchard, K. *et al.* Advanced maturation of human cardiac tissue grown from pluripotent stem cells. *Nature* **556**, 239–243 (2018).
30. Wiegerinck, R. F. *et al.* Force frequency relationship of the human ventricle increases during early postnatal development. *Pediatr. Res.* **65**, 414–419 (2009).
31. Gerdes, A. M. *et al.* Structural remodeling of cardiac myocytes in patients with ischemic cardiomyopathy. *Circulation* **86**, 426–430 (1992).
32. MacQueen, L. A. *et al.* A tissue-engineered scale model of the heart ventricle. *Nat. Biomed. Eng.* **2**, 930–941 (2018).
33. Timmis, A. *et al.* European society of cardiology: Cardiovascular disease statistics 2019. *Eur. Heart J.* **41**, 12–85 (2020).
34. Kim, H. & Ingber, D. Gut-on-a-Chip microenvironment induces human intestinal cells to undergo villus differentiation. *Integr. Biol.* **5**, 1130–1140 (2013).
35. Helander, K. G., Åhren, C., Philipson, B. M., Samuelsson, B. M. & Ójerskog, B. Structure of mucosa in continent ileal reservoirs 15 to 19 years after construction. *Hum. Pathol.* **21**, 1235–1238 (1990).
36. Helander, H. F. & Fändriks, L. Surface area of the digestive tract-revisited. *Scand. J. Gastroenterol.* **49**, 681–689 (2014).
37. Kasendra, M. *et al.* Duodenum intestine-chip for preclinical drug assessment in a human relevant model. *Elife* **9**, (2020).
38. Brown, A. L. Microvilli of the human jejunal epithelial cell. *J Cell Biol.* **12**, 623–627 (1962).
39. Gray, G. M. & Ingelfinger, F. J. Intestinal absorption of sucrose in man: interrelation of hydrolysis and monosaccharide product absorption. *J. Clin. Invest.* **45**, 388–398 (1966).
40. Kim, H., Huh, D., Hamilton, G. & Ingber, D. Human gut-on-a-chip inhabited by microbial flora that experiences intestinal peristalsis-like motions and flow. *Lab Chip* **12**, 2165–2174 (2012).
41. Shim, K. Y. *et al.* Microfluidic gut-on-a-chip with three-dimensional villi structure. *Biomed. Microdevices* **19**, (2017).
42. Kasendra, M. *et al.* Development of a primary human Small Intestine-on-a-Chip using biopsy-derived organoids. *Sci. Rep.* **8**, (2018).
43. Obach, R. S., Zhang, Q. Y., Dunbar, D. & Kaminsky, L. S. Metabolic characterization of the major human small intestinal cytochrome P450s. *Drug Metab. Dispos.* **29**, 347–352 (2001).
44. Lun, M. P., Monuki, E. S. & Lehtinen, M. K. Development and functions of the choroid plexus-cerebrospinal fluid system. *Nat. Rev. Neurosci.* **16**, 445–457 (2015).
45. Park, J. *et al.* Three-dimensional brain-on-a-chip with an interstitial level of flow and its application as an in vitro model of Alzheimer’s disease. *Lab Chip* **15**, 141–150 (2015).
46. Scepanovic, P. *et al.* A comprehensive assessment of demographic, environmental, and host genetic associations with gut microbiome diversity in healthy individuals. *Microbiome* **7**, 130 (2019).
47. Fajgenbaum, D. C. & June, C. H. Cytokine Storm. *N. Engl. J. Med.* **383**, 2255–2273 (2020).
48. Woodfin, A. *et al.* The junctional adhesion molecule JAM-C regulates polarized transendothelial migration of neutrophils in vivo. *Nat. Immunol.* **12**, 761–769 (2011).
49. Proebstl, D. *et al.* Pericytes support neutrophil subendothelial cell crawling and breaching of venular walls in vivo. *J. Exp. Med.* **209**, 1219–1234 (2012).
50. McMinn, P. H., Hind, L. E., Huttenlocher, A. & Beebe, D. J. Neutrophil trafficking on-a-chip: an in vitro, organotypic model for investigating neutrophil priming, extravasation, and migration with spatiotemporal control. *Lab Chip* **19**, 3697–3705 (2019).
51. Boussommier-Calleja, A. *et al.* The effects of monocytes on tumor cell extravasation in a 3D vascularized microfluidic model. *Biomaterials* **198**, 180–193 (2019).
52. Pérez-Rodríguez, S., Huang, S. A., Borau, C., García-Aznar, J. M. & Polacheck, W. J. Microfluidic model of monocyte extravasation reveals the role of hemodynamics and subendothelial matrix mechanics in regulating endothelial integrity. *Biomicrofluidics* **15**, (2021).
53. Bray, M. A., Sheehy, S. P. & Parker, K. K. Sarcomere alignment is regulated by myocyte shape. *Cell Motil. Cytoskeleton* **65**, 641–651 (2008).
54. Ribeiro, M. C. *et al.* Functional maturation of human pluripotent stem cell derived cardiomyocytes

- invitro - Correlation between contraction force and electrophysiology. *Biomaterials* **51**, 138–150 (2015).
55. Ariyasinghe, N. R., Lyra-Leite, D. M. & McCain, M. L. Engineering cardiac microphysiological systems to model pathological extracellular matrix remodeling. *Am. J. Physiol. Circ. Physiol.* **315**, H771–H789 (2018).
  56. Salick, M. R. *et al.* Micropattern width dependent sarcomere development in human ESC-derived cardiomyocytes. *Biomaterials* **35**, 4454–4464 (2014).
  57. Saleem, U. *et al.* Blinded, Multicenter Evaluation of Drug-induced Changes in Contractility Using Human-induced Pluripotent Stem Cell-derived Cardiomyocytes. *Toxicol. Sci.* **176**, 103–123 (2020).
  58. Marsano, A. *et al.* Beating heart on a chip: a novel microfluidic platform to generate functional 3D cardiac microtissues. *Lab Chip* **16**, 599–610 (2016).
  59. Wijnker, P. J. M. *et al.* Comparison of the effects of a truncating and a missense MYBPC3 mutation on contractile parameters of engineered heart tissue. *J. Mol. Cell. Cardiol.* **97**, 82–92 (2016).
  60. Grosberg, A., Alford, P. W., McCain, M. L. & Parker, K. K. Ensembles of engineered cardiac tissues for physiological and pharmacological study: Heart on a chip. *Lab Chip* **11**, 4165–4173 (2011).
  61. Ohya, T. *et al.* Simultaneous measurement of contractile force and field potential of dynamically beating human iPSC cell-derived cardiac cell sheet-tissue with flexible electronics. *Lab Chip* **21**, 3899–3909 (2021).
  62. Saleem, U. *et al.* Force and Calcium Transients Analysis in Human Engineered Heart Tissues Reveals Positive Force-Frequency Relation at Physiological Frequency. *Stem Cell Reports* **14**, 312–324 (2020).
  63. Piergiovanni, M., Leite, S. B., Corvi, R. & Whelan, M. Standardisation needs for organ on chip devices. *Lab Chip* **21**, 2857–2868 (2021).
  64. Mastrangeli, M. *et al.* Building blocks for a European organ-on-chip roadmap. *ALTEX* **36**, 481–492 (2019).
  65. Vollertsen, A. R. *et al.* Facilitating implementation of organs-on-chips by open platform technology. *Biomicrofluidics* **15**, (2021).
  66. Mastrangeli, M. *et al.* Microelectromechanical Organs-on-Chip. *21st Int. Conf. Solid-State Sensors, Actuators Microsystems, TRANSDUCERS 2021* 102–107 (2021) doi:10.1109/Transducers50396.2021.9495646.
  67. ISO 22916: 2022. Microfluidic devices — Interoperability requirements for dimensions, connections and initial device classification. <https://www.iso.org/standard/74157.html>.



# Chapter 3

## Genetic repair of a human induced pluripotent cell line from patient with Dutch-type cerebral amyloid angiopathy

### Abstract

Dutch-type cerebral amyloid angiopathy (D-CAA), also known as hereditary cerebral haemorrhage with amyloidosis-Dutch type (HCHWA-D), is an autosomal dominant disorder caused by a G to C transversion in codon 693 of the amyloid precursor protein (APP) that results in a Gln-to-Glu amino acid substitution. CRISPR-Cas9 editing was used for genetic correction of the mutation in a human induced pluripotent stem cell (hiPSC-) line established previously. The isogenic hiPSCs generated showed typical pluripotent stem cell morphology, expressed all markers of undifferentiated state, displayed a normal karyotype and had the capacity to differentiate into the three germ layers.

*This chapter is adapted from:  
Stem Cell Research. Sep;71 (2023)*

*Dennis M. Nahon, Sravya Ganesh, Francijna E. van den Hil, Christian Freund,  
Christine L. Mummery, and Valeria V. Orlova*

## Resource Table

Unique stem cell lines identifier	LUMCi005-A-3 ( <a href="https://hpscereg.eu/cell-line/LUMCi005-A-3">https://hpscereg.eu/cell-line/LUMCi005-A-3</a> ) LUMCi005-A-4 ( <a href="https://hpscereg.eu/cell-line/LUMCi005-A-4">https://hpscereg.eu/cell-line/LUMCi005-A-4</a> )
Alternative names of stem cell lines	Iso1LUMC0074iHCHWAD01 Iso3LUMC0074iHCHWAD01
Institution	Leiden University Medical Center, LUMC
Contact information of distributor	Valeria V. Orlova ( <a href="mailto:v.orlova@lumc.nl">v.orlova@lumc.nl</a> ) Dennis M. Nahon ( <a href="mailto:d.nahon@lumc.nl">d.nahon@lumc.nl</a> ) Christian Freund ( <a href="mailto:c.m.a.h.freund@lumc.nl">c.m.a.h.freund@lumc.nl</a> )
Type of cell lines	hiPSCs
Origin	Human
Additional origin info	Age: 56 Sex: Female Ethnicity: Caucasian
Cell Source	Fibroblasts
Method of reprogramming	Sendai virus, OCT3/4, SOX2, KLF4 and MYC
Clonality	Clonal
Evidence of the reprogramming transgene loss (including genomic copy if applicable)	qRT-PCR
Cell culture system used	hiPSCs cultured on Vitronectin in mTeSR plus
Type of Genetic Modification	Genetic correction of heterozygous point mutation in the APP gene
Associated disease	Dutch-type cerebral amyloid angiopathy (D-CAA), also known as hereditary cerebral haemorrhage with amyloidosis-Dutch type (HCHWA-D).
Gene/locus	APP 21q21.3 Corrected Heterozygous APP c.2077 C >G; c.2082 T >C; c.2085 G >C
Method of Modification	CRISPR/Cas9
User-customisable nuclease (UCN) delivery method	Electroporation

All double-stranded DNA genetic material molecules introduced into the cells	N/A
Analysis of the nuclease-targeted allele status	Sequencing of the targeted allele
Method of the off-target nuclease activity prediction and surveillance	Targeted PCR/sequencing
Descriptive name of the transgene	N/A
Eukaryotic selective agent resistance cassettes (including inducible, gene/cell type-specific)	N/A
Inducible/constitutive expression system details	N/A
Date archived/stock date	27/02/2020
Cell line repository/bank	<a href="https://hpscereg.eu/cell-line/LUMCi005-A-3">https://hpscereg.eu/cell-line/LUMCi005-A-3</a> <a href="https://hpscereg.eu/cell-line/LUMCi005-A-4">https://hpscereg.eu/cell-line/LUMCi005-A-4</a>
Ethical approval	NL45478.058.13/P13.080, Medical Ethical Committee(MEC), Leiden University Medical Center (LUMC).
Addgene/public access repository recombinant DNA sources' disclaimers (if applicable)	N/A

**Table 1: Characterization and validation**

Classification	Test	Result	Data
Morphology	Brightfield microscopy	Normal morphology	Fig. 1 panel A
Phenotype	Qualitative analysis of IF staining	Positive immunostaining markers of undifferentiated state: SSEA4, OCT3/4 & NANOG	Fig. 1 panel D
	Quantitative analysis by FACS	Increased fluorescent signal over negative control of markers of undifferentiated state: SSEA4, OCT3/4 & NANOG	Fig. 1 panel B

Karyotype	G-band Karyotyping 5-10Mb	Normal karyotype: 46, XX for both lines	Fig. 1 panel E
Genotyping for the desired genomic alteration/allelic status of the gene of interest	PCR across the edited site and sequencing	PCR + Sanger sequencing confirmed presence edited allele (APP c.2077 C >G; c.2082 T >C; c.2085 G >C)	Fig. 1 panel C
	Evaluation of the homozygous status of introduced genomic alteration(s)	PCR + Sanger sequencing confirmed presence of edited allele (APP c.2077 C >G; c.2082 T >C; c.2085 G >C)	Fig. 1 panel C
	Transgene-specific PCR	N/A	N/A
Verification of the absence of random plasmid integration events	PCR/Southern	N/A	N/A
Parental and modified cell line genetic identity evidence	Microsatellite PCR (mPCR) OR	Not performed	N/A
	STR analysis	24 sites tested; all sites matched	Submitted in archive with journal
Off-target nuclease activity analysis	PCR across top 5 predicted top likely off-target sites	Demonstration of the lack mutations in predicted off-target sites	Supplementary Fig. S1
Specific pathogen-free status	Mycoplasma	RT-PCR analysis: Negative	Supplementary Table S1
Multilineage differentiation potential	Short-term differentiation in vitro by IF analysis	Positive immunostaining of the three germ layer markers: ectodermal (NES, PAX6), endodermal (FOXA2, GATA4), mesodermal (T, VIM)	Fig. 1F
Donor screening (OPTIONAL)	N/A	N/A	N/A

Genotype additional info (OPTIONAL)	Blood group genotyping	N/A	N/A
	HLA tissue typing	N/A	N/A

### Resource utility

D-CAA is a neurodegenerative disorder, caused by a heterozygous mutation in exon 17 of the APP gene on chromosome 21 (E22Q; c.2077 G > C)<sup>1</sup>. The mutation results in accumulation of amyloid beta (A $\beta$ ) inside the cerebral vascular wall. D-CAA patient hiPSC lines and CRISPR-Cas9 corrected isogenically paired hiPSC-lines are a valuable tool for studying the underlying disease mechanisms.

### Resource Details

D-CAA is caused by a point mutation in the APP gene resulting in severe amyloid deposition in the cerebral vascular wall, vascular dementia and recurrent hemorrhagic strokes from the fifth decade of life onwards, significantly reducing life expectancy<sup>2</sup>. The heterozygous mutation in the APP gene, results in a Gln-to-Glu amino acid substitution leading to charge alterations in the A $\beta$  protein<sup>3</sup>. The altered A $\beta$  is less efficiently degraded and cleared over the blood-brain barrier and induces death of cerebrovascular smooth muscle cells, reducing the stability of the vascular wall. Previously generated D-CAA patient hiPSC-lines<sup>4</sup> have been useful for modeling certain aspects of the disease<sup>5</sup>. In the current study, isogenic lines were created to further this research by correcting the mutation in the hiPSC-line generated previously using a Cas9-ribonucleoprotein (RNP) complex, with a mutation-specific single guide RNA (sgRNA) and a single-stranded oligodeoxynucleotide (ssODN) donor template containing the wildtype sequence with two additional silent mutations, one to introduce a AatII restriction site and the other to disrupt the protospacer adjacent motif (PAM) site (Table 2). Two different guide RNAs (gRNAs) were used in separate targeting experiments of the same line, which resulted in an isogenically corrected line with two clones generated using the first sgRNA and the two other clones generated using the other sgRNA. Single-cell derived colonies were screened for repair using the AatII restriction of PCR amplified APP exon 17 region. One clone per sgRNA, hereafter named LUMCi005-A-3 (gRNA1), LUMCi005-A-4 (gRNA2), was selected and characterized (Table 1). Correction of the mutation (c.2077 C > G) and incorporation of silent mutations was confirmed by Sanger sequencing (Fig 1C). The isogenic clones displayed typical stem cell morphology with high nucleus to cytoplasm ratio (Fig. 1A) and a normal karyotype was confirmed by G-banding (Fig. 1E). The pluripotency status was confirmed by expression and localization of markers of the undifferentiated state: SSEA4, NANOG and OCT3/4, using flow-cytometry (Fig 1B) and Immunofluorescence staining (Fig 1D). The differentiation potential of the lines was confirmed by short-term differentiation assay *in vitro*, with subsequent immunofluorescence staining for markers of the three germ layers; NESTIN and PAX6 (ectoderm), FOXA2 and GATA4 (endoderm), Brachyury (T), CDX2 and Vimentin (mesoderm) (Fig 1F). Clones were tested negative for

mycoplasma (Supplemental Table 1). Finally, the absence of off-target mutations was confirmed by Sanger sequencing of the five most likely off-target sites within coding regions as predicted by CRISPOR (crispor.tefor.net; Fig S1)<sup>6</sup>.

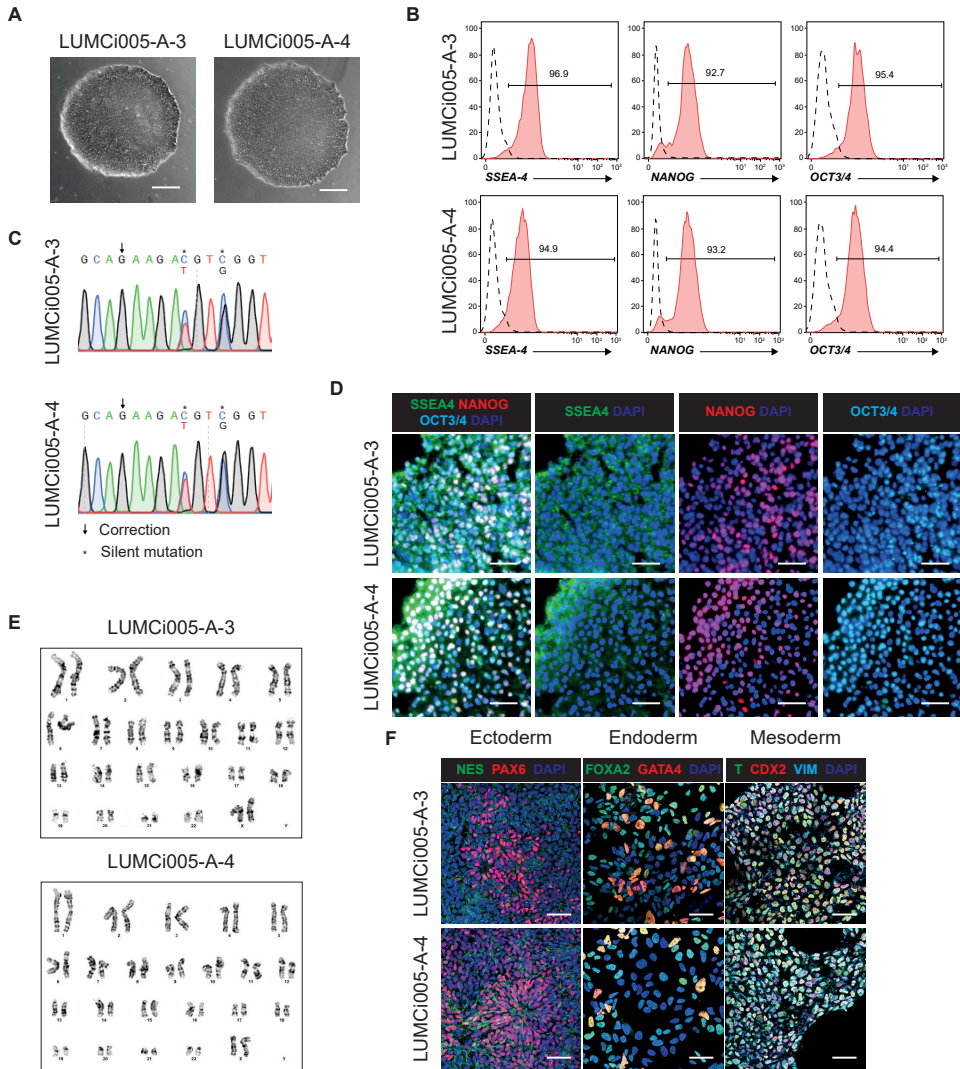


**Figure 1: Generation and characterization of hiPSC lines LUMCi005-A-3, LUMCi005-A-4.** Lines are CRISPR-Cas9 edited to correct an autosomal mutation in the amyloid precursor protein (APP) in a Dutch-type cerebral amyloid angiopathy (D-CAA) patient line. Scale bar in A: 100  $\mu$ m, scale bars in D and F: 50  $\mu$ m.

**Table 2: Reagents details**

Antibodies used for immunocytochemistry/flow-cytometry			
	Antibody	Dilution	Company Cat # and RRID
Markers of the undifferentiated state (FACS)	BV421 Mouse Anti-OCT3/4	1:25 (100k cells in 80 ul)	BD Biosciences Cat# 565644, RRID:AB_2739320
Markers of the undifferentiated state (FACS)	Mouse Anti-Human NANOG Monoclonal Antibody, PE Conjugated	1:5 (100k cells in 80 ul)	BD Biosciences Cat# 560483, RRID:AB_1645522
Markers of the undifferentiated state (FACS)	Anti-SSEA-4-FITC antibody	1:25 (100k cells in 80 ul)	Miltenyi Biotec Cat# 130-098-371, RRID:AB_2653517
Markers of the undifferentiated state (Immunocytochemistry)	Mouse IgG2b anti-OCT3/4	1:100	Santa Cruz Biotechnology Cat# sc-5279 RRID: AB_628051
Markers of the undifferentiated state (Immunocytochemistry)	Mouse IgG1 anti-NANOG	1:150	Santa Cruz Biotechnology Cat# sc-293121 RRID: AB_2665475
Markers of the undifferentiated state (Immunocytochemistry)	Mouse IgG3 anti-SSEA4	1:30	BioLegend Cat# 330402, RRID:AB_1089208
Differentiation markers (Immunocytochemistry)	Nestin-Alexa488	1:200	Technology Cat#33475. RRID:AB_2799037
Differentiation markers (Immunocytochemistry)	PAX6-Alexa647	1:200	Cell Signaling Technology Cat#60433. RRID:AB_2797599
Differentiation markers (Immunocytochemistry)	FOXA2-Alexa555	1:500	Cell Signaling Technology Cat#8186. RRID:AB_10891055
Differentiation markers (Immunocytochemistry)	GATA4-Alexa647	1:200	Cell Signaling Technology Cat#36966. RRID:AB_2799108Cell Signaling
Differentiation markers (Immunocytochemistry)	Brachyury-Alexa488	1:200	Cell signalling Technology Cat#81694. RRID:AB_2799983
Differentiation markers (Immunocytochemistry)	Vimentin-Alexa647	1:200	Cell signalling Technology Cat#5741. RRID:AB_10695459

Secondary antibodies (Immunocytochemistry)	Donkey anti-Mouse IgG (H+L) Highly cross-adsorbed Secondary, Alexa Fluor 488	1:500	Molecular Probes Cat# A-21206, RRID:AB_2535792
Secondary antibodies (Immunocytochemistry)	Donkey anti-Goat Mouse IgG (H+L) Highly cross-adsorbed Secondary, Alexa Fluor 647	1:500	Thermo Fisher Scientific Cat# A-11031, RRID:AB_144696
Secondary antibodies (Immunocytochemistry)	Goat anti-Mouse IgG3 Cross-adsorbed Secondary Antibody, Alexa Fluor 488	1:250	Thermo Fisher Scientific Cat# A-21151, RRID:AB_2535784
Secondary antibodies (Immunocytochemistry)	Goat anti-Mouse IgG1 Cross-adsorbed Secondary Antibody, Alexa Fluor 568	1:500	Thermo Fisher Scientific Cat# A-21124, RRID:AB_2535766
Secondary antibodies (Immunocytochemistry)	Goat anti-Mouse IgG2b Cross-adsorbed Secondary Antibody, Alexa Fluor 647	1:250	Thermo Fisher Scientific Cat# A-21242, RRID:AB_2535811

---

#### Site-specific nuclease

---

Nuclease information	Nuclease type/ version	Alt-R Cas9-RNP
Delivery method	Electroporation	Neon Transfection System (program 6)
Selection strategy	Single cell cloning + restriction site analysis	

---

#### Primers and Oligonucleotides used in this study

---

	Target	Forward/Reverse primer (5'-3')
Correction confirmation (PCR/ sequencing)	APP exon 17	GCCCACCACTAATAACCATTG/ TTCAGGATCCCACATCAGAG
gRNA1 off-target site 1	WNT9B	AATTGGTGGGGATGGAGGTT/ TTCCAAAGTCCTGTTAGTGCCT
gRNA1 off-target site 2	ATG16L2	CGCCTTCCTCTTCGGTTTG/ TGTATTGCCCTGGAGTAAGCC
gRNA1 off-target site 3	PTPRJ	ACGAGCCAGGCTATTTTTGGA/ GCATCGAGACAGCACCGATA
gRNA1 off-target site 4	XKR6	AGCTTTCTTTCCAGTCGCTGT/ CCGAATTATTGCGGTGGCTT

gRNA1 off-target site 5	RP11-659P15.1	AATTTTGGGAGCCAGGGAGTTT/ CTGTCCAGTGATGTGGAGGAAG
gRNA2 off-target site 1	GPR158	CACTGTAGTCACCATCCTCAGAC/ GGATAGAACAGTCACAGACAGAG
gRNA2 off-target site 2	RP11-246A10.1	TTGGGTGTGAGATACACTGCTA/ GTGTAGTTGGCCCTTACCC
gRNA2 off-target site 3	AMFR	CACGTCGTGGGGTAACATCTG/ TGGATTCTCCAAAAGGACTACC
gRNA2 off-target site 4	KIAA1598	ATTTGTGTGACTTATTGTCTGGG/ TATGTCGTCTGCAAGGTCCC
gRNA2 off-target site 5	HEATR5A	ACCACAGCTGGCAAGAGATT/ TCAGTGCTGCTGTGGTATGT
gRNA1		GGTGTCTTTGCaAAGATG
gRNA2		GTGTTCTTTGCaAAGATG
ssODN		AATTGTAAATTATATTGCATTTAGAAATTA AAATTCTTTTCTTAATTTGTTTTCAAGGT GTTCTTTGCaAAGACGTCGGTTCAAACA AAGGTGCAATCATTGGACTCATGGTGGGC GGTGTTCATAGCGACAGTGA

## Materials and Methods

### Ethical statement

This study was approved by the LUMC Medical Ethical Committee (MEC) and informed consent was obtained from the HCHWA-D patient (NL45478.058.13/P13.080).

### Cell culture and mutation correction

For generation of the parental hiPSC line LUMCi005-A, see previous publication<sup>4</sup>. Cells maintained at at 37°C and 5% CO<sub>2</sub> and were passaged weekly by dissociating using Gentle Cell Dissociation Reagent (Stem Cell Technologies). For genetic repair 1\*10<sup>5</sup> LUMCi005-A cells were electroporated at passage 20 with the Alt-R Cas9-RNP complex and the ssODN (both IDT) using program 6 of the Neon Transfection System (Invitrogen) and subsequently cultured in 2 Synthemax II-SC (Corning)-coated wells of a 12-well plate in TESR-plus with CloneR2 (Stem Cell Technologies). For single cell cloning, 1000 cells were plated onto a Synthemax II-SC-coated 10 cm dish in TESR-plus with CloneR2. After 8-12 days hiPSC colonies were split into VN-coated 2x wells of a 96-well plate in TESR-plus. The region of interest was amplified by PCR using the Terra PCR Direct Polymerase Mix (TaKaRa) from DNA isolated from one well (QuickExtract solution, Lucigen). Successfully edited clones were identified by AatII enzyme (New England Biolabs) activity and confirmed by Sanger sequencing performed by the Leiden Genome Technology Centre (LGTC). Off-target analysis was performed by PCR amplification and Sanger sequencing of the five most likely off-target

sites within coding regions as predicted by CRISPOR (crispor.tefor.net; Fig S1)<sup>6</sup>.

### **Immunofluorescence staining**

hiPSCs at passage 10 were fixed in 2% PFA for 30 min, permeabilized with 0.1% Triton X-100, and blocked with 4% normal swine serum (NSS, DAKO) at room temperature (RT) for 1 h. Primary antibodies were added and incubated overnight at 4°C. After washing, secondary antibodies were added for 1 h at RT (Table 2). Nuclei were stained with DAPI, and coverslips were mounted using Mowiol (Merck Millipore). Images were acquired on a Leica TCS SP8 microscope or the EVOS M7000.

### **FACS staining**

hiPSCs were dissociated at passage 15 with TrypLE for 5 min at 37°C. Samples were fixed for 15 min in 200 µl of Reagent A of the fix & perm kit (Thermo Fisher Scientific). The cells were washed once in FACS buffer (PBS without Ca<sup>2+</sup> and Mg<sup>2+</sup> with 0.5% BSA and 2 mM EDTA), resuspended in 80 µl of Reagent B with the conjugated antibodies (Table 2) and incubated in the dark for 60 min at RT. Subsequently, the samples were washed once and resuspended in FACS buffer before being measured on the MACSQuant VYB flow cytometer (Miltenyi Biotec). Analysis was performed using the FlowJo<sup>tm</sup> v.10.6.1.

### **In vitro trilineage differentiation**

The ability of hiPSCs to differentiate into the three germ layers (ectoderm, mesoderm, and endoderm) was assessed using differentiation with the Trilineage differentiation kit (Stem Cell Technologies). The differentiation was done according to the manufacturer's instructions on hESC-qualified Matrigel (Corning) coverslips. After 5 or 7 days of culture cells were fixed using 2%PFA.

### **Karyotype analysis**

hiPSCs at passage 9 were karyotyped by Cell Guidance systems (UK) and a total of 20 metaphases were counted.

### **Sequencing**

Genomic DNA was isolated from hiPSCs using Quick Extract (Lucigen) according to the manufacturer's instructions. The genes of interest were amplified using Platinum<sup>TM</sup> Taq DNA Polymerase High Fidelity (Invitrogen) for mutation and off-target analysis using the primers listed in Table 2.

### **Mycoplasma test**

All lines were tested for the absence of mycoplasma and other human pathogens at passage 9 using the IDEXX BioAnalytics PCR analysis. (Supplementary Material 1).

## **Acknowledgements**

This work was supported by The Netherlands Organ-on-Chip Initiative, an NWO Gravitation project funded by the Ministry of Education, Culture and Science of the government of the Netherlands (024.003.001) and the Novo Nordisk Foundation Center for Stem Cell Medicine supported by Novo Nordisk Foundation grants (NNF21CC0073729).

## **Competing interests**

Christine L. Mummery is co-founder of Pluriomics bv (now Ncardia bv).

## References

1. Levy, E., Carman, M.D., Fernandez-Madrid, I.J., Power, M.D., Lieberburg, Ivan., van Duinen, S.G., Bots, G.Th.A.M., Luyendijk, W., and Frangione, Blas. (1990). Mutation of the Alzheimer's Disease Amyloid Gene in Hereditary Cerebral Hemorrhage, Dutch Type. *Science* (1979) 248, 1124–1126.
2. Kamp, J.A., Moursel, L.G., Haan, J., Terwindt, G.M., Lesnik Oberstein, S.A.M.J., Van Duinen, S.G., and Van Roon-Mom, W.M.C. (2014). Amyloid  $\beta$  in hereditary cerebral hemorrhage with amyloidosis-Dutch type. *Rev Neurosci* 25, 641–651. <https://doi.org/10.1515/revneuro-2014-0008>.
3. Herzig, M.C., Winkler, D.T., Burgermeister, P., Pfeifer, M., Kohler, E., Schmidt, S.D., Danner, S., Abramowski, D., Stürchler-pierrat, C., Bürki, K., et al. (2004). A $\beta$  is targeted to the vasculature in a mouse model of hereditary cerebral hemorrhage with amyloidosis. *Nat Neurosci* 7, 954–960. <https://doi.org/10.1038/nn1302>.
4. Daoutsali, E., Buijsen, R.A.M., van de Pas, S., Jong, A. t., Mikkers, H., Brands, T., Eussen, B., de Klein, A., van der Graaf, L.M., Pepers, B.A., et al. (2019). Generation of 3 human induced pluripotent stem cell lines LUMCi005-A, B and C from a Hereditary Cerebral Hemorrhage with Amyloidosis-Dutch type patient. *Stem Cell Res* 34, 101359. <https://doi.org/10.1016/j.scr.2018.101359>.
5. Daoutsali, E., Pepers, B.A., Stamatakis, S., van der Graaf, L.M., Terwindt, G.M., Parfitt, D.A., Buijsen, R.A.M., and van Roon-Mom, W.M.C. (2023). Amyloid beta accumulations and enhanced neuronal differentiation in cerebral organoids of Dutch-type cerebral amyloid angiopathy patients. *Front Aging Neurosci* 14. <https://doi.org/10.3389/fnagi.2022.1048584>.
6. Haeussler, M., Schönig, K., Eckert, H., Eschstruth, A., Mianné, J., Renaud, J.B., Schneider-Maunoury, S., Shkumatava, A., Teboul, L., Kent, J., et al. (2016). Evaluation of off-target and on-target scoring algorithms and integration into the guide RNA selection tool CRISPOR. *Genome Biol* 17. <https://doi.org/10.1186/s13059-016-1012-2>.

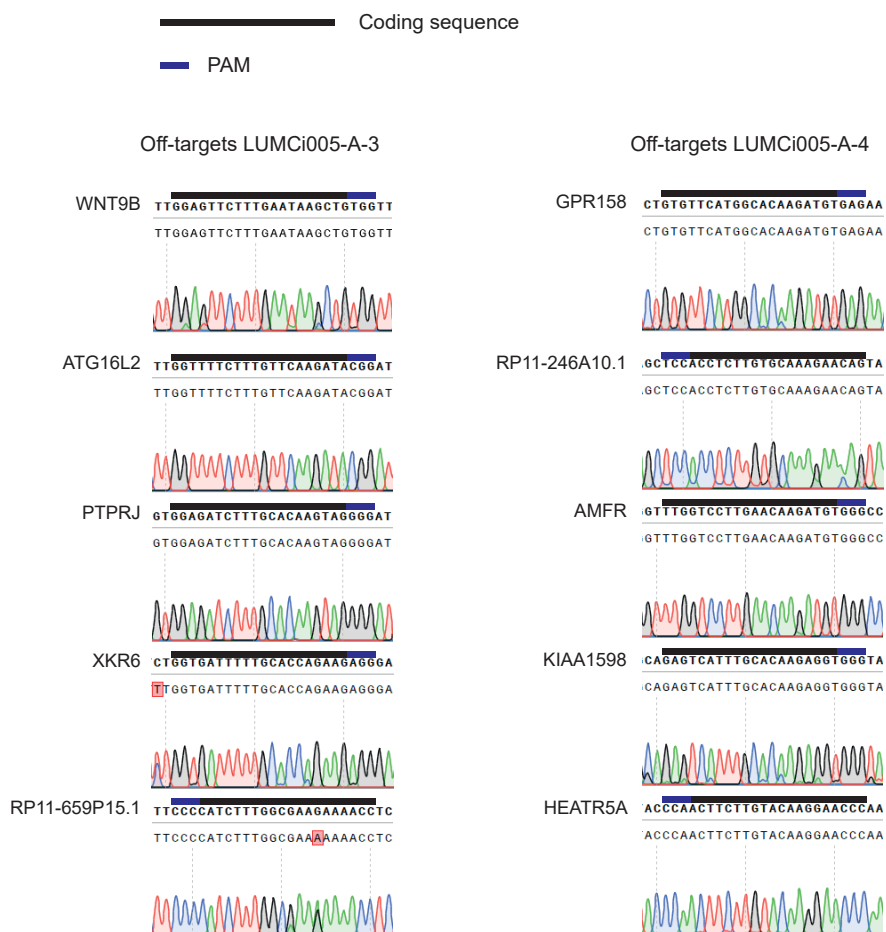
## Supplementary Material

### Contents

**Figure S1:** Sanger sequencing of potential off-targets

**Table S1:** Mycoplasma test

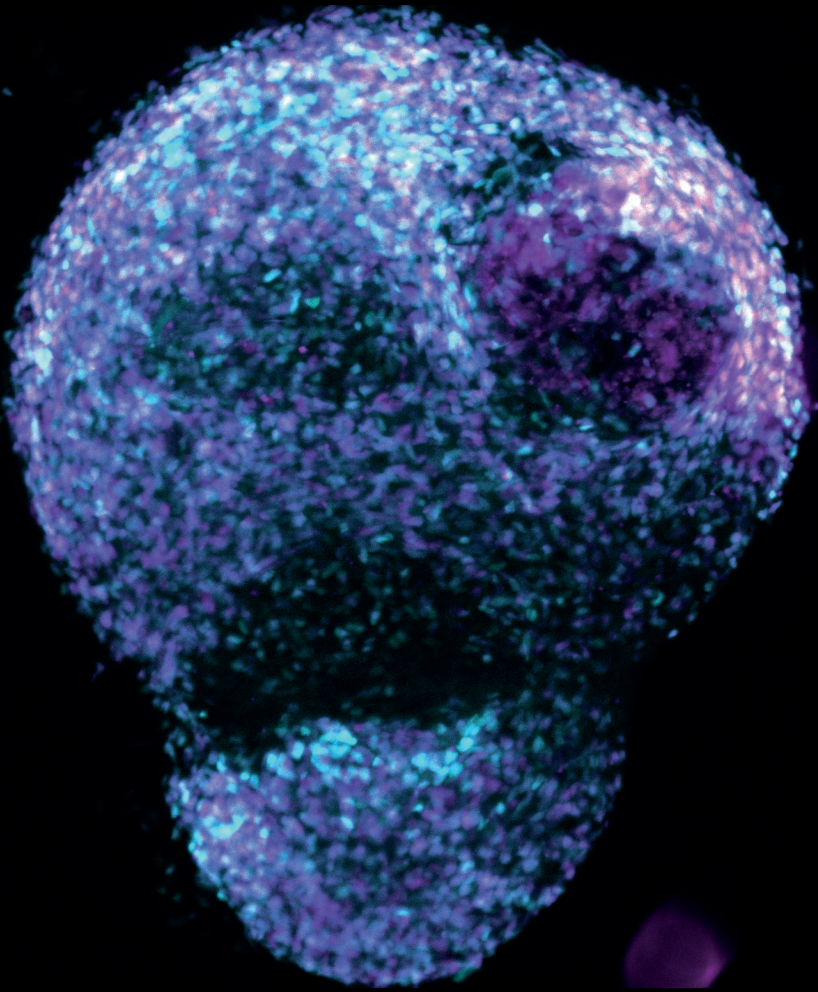
## Supplementary Figure 1



Supplementary Figure 1: Sanger sequencing of potential off-targets

### Supplementary Table 1: Mycoplasma test

	Measurement 1	Measurement 2	Ratio2/1	Mycoplasma
Positive control	70	2596	37.09	Positive
Negative control	138	32	0.231	Negative
LUMCi005-A-3	51	43	0.843	Negative
LUMCi005-A-4	51	33	0.647	Negative



# Chapter 4

## Characterization of endothelial cell functionality in RVCL-S using patient-derived hiPSCs

### Abstract

Retinal vasculopathy with cerebral leukoencephalopathy and systemic manifestations (RVCL-S) is a rare autosomal dominant small vessel disorder caused by C-terminus truncating mutations in TREX1, a DNA-specific exonuclease. RVCL-S can serve as a genetic model for small vessel diseases and vascular dementia. It is characterized by vasculopathies in highly vascularized organs including the retina, liver, kidney and brain. Although the exact underlying mechanism causing these pathologies remains to be elucidated; endothelial cell (EC) dysfunction and inflammation appear to contribute to the disease pathology. Despite the development of transgenic RVCL-S mouse models, because of likely discrepancies between human and mouse manifestations, there is a need to develop in vitro human models of the disease. Human induced pluripotent stem cells (hiPSC) represent an opportunity to explore these differences in vitro human models. Here, we generated hiPSCs from RVCL-S patients (RVCL-S-hiPSCs) and their isogenic, genetically-corrected counterparts to investigate function in RVCL-S-hiPSC-derived ECs (hiPSC-ECs). Genotype, genomic stability, expression of pluripotency markers and spontaneous three germ-lineage differentiation were confirmed in mutant and genetically-corrected RVCL-S hiPSC lines. EC morphology, marker expression, proliferation and barrier function were however, similar in diseased and corrected hiPSC-ECs. These results suggest that uncovering EC defects observed in RVCL-S patients in hiPSC-ECs might require more complex models that also include immune cells or stimulatory cytokines.

*This chapter is adapted from a manuscript in preparation.*

*Dennis M. Nahon\*, Dhanesh G. Kasi\*, Francijna E. van den Hil, Marga J. Bouma, Albert Blanch-Asensio, Ruben W.J. van Helden, Richard P. Davis, Michel D. Ferrari, Gisela M. Terwindt, Christian Freund, Christine L. Mummery, Arn M.J.M. van den Maagdenberg, Valeria V. Orlova.*

## Introduction

Retinal vasculopathy with cerebral leukoencephalopathy and systemic manifestations (RVCL-S) is a rare, autosomal dominant small vessel disease caused by truncating mutations in the C-terminus of abundantly expressed 3'-5' DNA exonuclease; TREX1<sup>1</sup>. Patients with this mutation most commonly start developing symptoms related to vasculopathies from 30-50 years of age in multiple, highly vascularized organs such as the retina, brain, liver and kidney. The symptoms are diverse and may include progressive visual impairment, stroke, migraine, cognitive decline, apathy, and pneumonia which often leads to premature death<sup>2,3</sup>. Current treatment options are very limited and focus on alleviating symptoms.

The dysfunctional TREX1 protein in RVCL-S retains its exonuclease function, but truncation of its endoplasmic reticulum (ER)-localization domain results in a disruption of both the ER interaction and localization<sup>1,4,5</sup>. How this change in subcellular localization results in the disease phenotype remains to be elucidated; however, previous work indicated a role of both the endothelium and an auto-inflammation response. Disease hypotheses were strengthened by the discovery of TREX1 expression in microglia in the brain<sup>6</sup> and in ECs of the vasculature<sup>7</sup>. In addition, recent studies seem to have demonstrated that the TREX1 C-terminus is a critical regulator of oligosaccharyltransferase (OST) activity, an enzyme that facilitates N-glycosylation of polypeptides<sup>5</sup>. So in addition to a loss of localization, a truncated TREX1 protein seems to lead to dysregulated OST activity, ultimately generating immunogenic free glycans. The glycans are known to induce expression of pro-inflammatory genes known as IFN-stimulated genes (ISGs)<sup>5</sup>. Regardless of the published findings, OST involvement has to be confirmed by other studies. Another disease hypothesis is built around observed alterations in patient vessels that manifest both structurally as thickening of the vessel wall e.g. multi-laminated basement membranes<sup>8</sup>, and functionally, as reduced flow-mediated dilatation responses<sup>9</sup>. Vascular involvement was further confirmed by a study demonstrating elevated levels of the endothelial damage-related markers von Willebrand factor (vWF) and angiotensin-2 in RVCL-S patients<sup>10</sup>.

Notably, the findings were partially supported by genetic RVCL-S mouse models. A mouse model with a knock-in of the human *TREX1* gene carrying the most common V235fs RVCL-S mutation demonstrated increased auto-inflammation by showing a distinct auto-antibody profile<sup>11</sup>. An independent mouse model with a specific knock-in of the same truncation mutation resulted in increased mortality and reduced blood flow and vascular function<sup>12</sup>. Even though homozygous mice were investigated- whereas patients are heterozygous - both mouse model were unable to reproduce the histological abnormalities in various organs or structural abnormalities in the vasculature seen in human patients. Admittedly though, no in-depth characterization was performed that would reveal the abnormalities seen in the patients. A logical complication of recapitulating all pathology seen in humans is the shorter lifespan of the mice given the late onset in patients (mice live 2 years and the disease is evident in humans at middle age), it would remain beneficial for

human *in vitro* models to be developed to recapitulate aspects of the human pathology.

Human induced pluripotent stem cells (hiPSCs) have demonstrated utility in human disease modeling since they often capture the disease phenotypes and are amenable to reproducible and large-scale production should that be required for drug screening. In addition, the ability to derive organ-specific cells while retaining the patient's genetic background and the possibility of generating isogenic controls could allow personalized medicine research and effective drug development<sup>13</sup>. The current study aims to investigate whether in a simple model of vasculature *in vitro*, intrinsic EC defects are evident in patient-derived RVCL-S-hiPSC-ECs using isogenic hiPSCs as a control.

## Results and discussion

### Generation and CRISPR/Cas9 correction of the hiPSC line from an RVCL-S patient

Skin fibroblasts were obtained from a 52-year-old female RVCL-S patient carrying the most common Val235fs RVCL-S mutation as a result of a single nucleotide insertion (c.703dupG) in the *TREX1* gene (Fig 1A). Fibroblasts were reprogrammed using the Sendai virus to generate the RVCL-S<sup>c.703dupG</sup> hiPSC line, and three independent clones were characterized. An isogenic hiPSC line was generated by correcting the mutation in the patient hiPSC line using a Cas9-ribonucleoprotein (RNP) complex with a mutation-specific single-guide RNA (sgRNA) and a single-stranded oligodeoxynucleotide (ssODN) donor template. The ssODN donor template contained the wildtype sequence with one additional silent mutation to introduce a novel BsaHI restriction site and disrupt the protospacer adjacent motif (PAM) site (See Table 1 for gRNA and ssODN details). Single cell-derived colonies were screened for repair using the BsaHI restriction enzyme of the amplified RVCL-S exon. This resulted in the generation of three independent clones of isogenic genetically-corrected hiPSC; RVCL-S<sup>corr</sup>. Genomic integrity of the RVCL-S<sup>corr</sup> clones was confirmed by assessing the copy number of the 24 most commonly altered loci in hiPSCs (Fig S1A). The RVCL-S causing mutation in the parental RVCL-S<sup>c.703dupG</sup> hiPSC line and the incorporation of the silent mutation was confirmed by Sanger sequencing (Fig 1B). Additional confirmation was done by performing digital droplet PCR (ddPCR) on genomic DNA isolated from a healthy wildtype hiPSC line (LUMC0054iCTRL02), the parental RVCL-S<sup>c.703dupG</sup> hiPSC line and the three independent clones from the RVCL-S<sup>corr</sup> hiPSC line using probes that specifically distinguish the wildtype (WT), mutant (MUT) or corrected (Corr) alleles (Fig S1B and C). DdPCR using both the WT and Corr probes showed two separate populations of the WT probe amplitude caused by suboptimal binding to the mutant allele in the RVCL-S<sup>c.703dupG</sup> hiPSC line with the expected ratio of Corr probe / WT probe for the RVCL-S<sup>corr</sup> hiPSC clones. A second ddPCR using the WT and Mut probe demonstrated the presence of the Mut allele only in the RVCL-S<sup>c.703dupG</sup> hiPSC line. In addition, two populations for the WT probe amplitude indicated suboptimal binding of the WT probe also on the corrected allele in the RVCL-S<sup>corr</sup> hiPSC clones, again confirming proper genetic targeting. The hiPSCs displayed typical stem cell morphology with high nucleus-

to-cytoplasm ratio (Fig 1C); normal karyotype was confirmed by G-banding (Fig 1D). The pluripotent status was confirmed by expression and localization of proteins associated with the undifferentiated state: SSEA4, NANOG and OCT3/4 using immunofluorescence staining (Fig 1F). The differentiation potential of the lines was confirmed in a short-term *in vitro* differentiation assay and subsequent immunofluorescence staining for markers associated with the three germ layers: NESTIN and PAX6 (ectoderm), FOXA2 and GATA4 (endoderm), Brachyury (T), CDX2 and Vimentin (mesoderm) (Fig 1E).

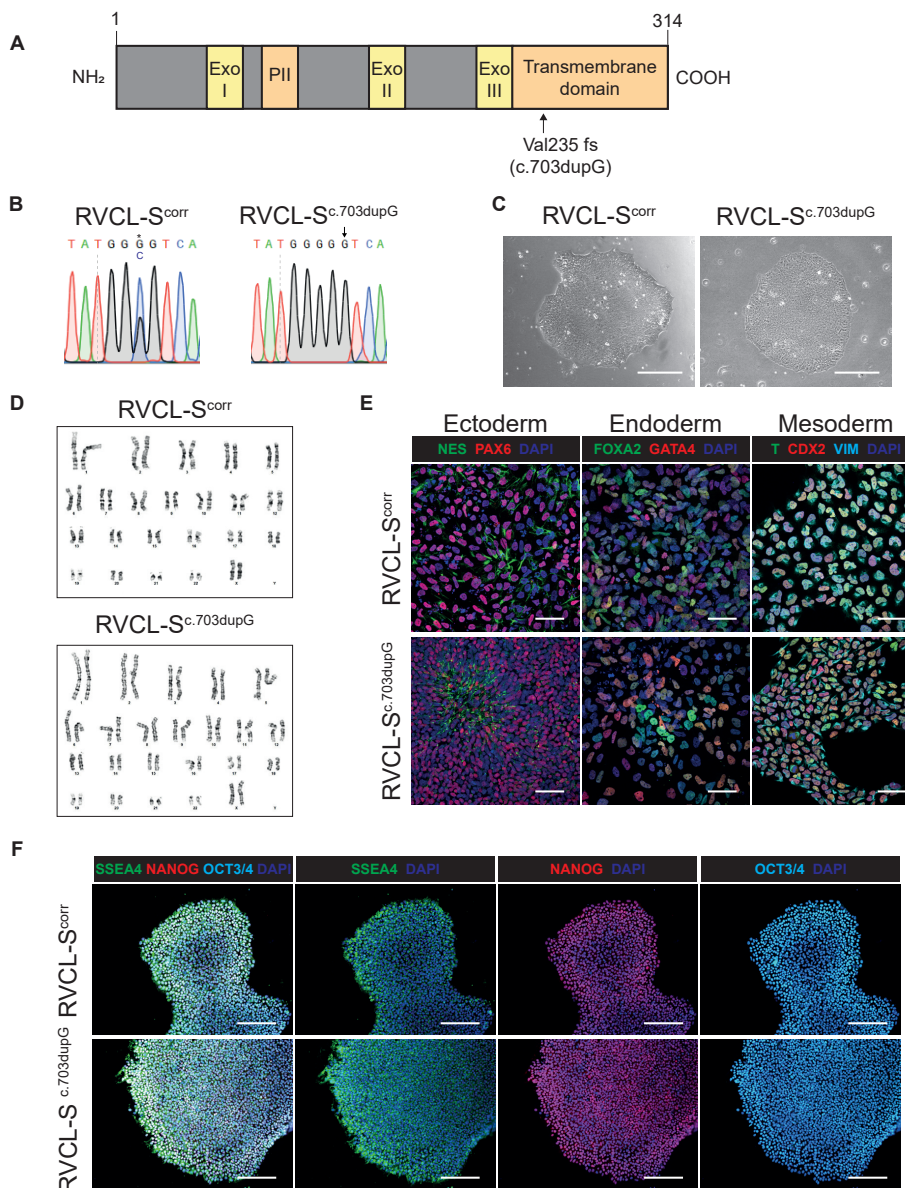


**Figure 1. Generation and characterization of RVCL-S patient hiPSC line and CRISPR/Cas9 corrected isogenic control**

A) Schematic overview of the TREX1 protein with its exonuclease domains (Exo), proline II motif (PII) and transmembrane domain with the most common Val235fs RVCL-S causing mutation shown. B) Sanger sequencing of genomic DNA isolated from corrected and mutant hiPSC clones confirming repair of the TREX1 mutation (arrow) and the introduction of a silent mutation (c.701G>C) (asterisk) that creates a new restriction site for BsaHI. C) Representative brightfield images showing hiPSC colony morphology. Scale bars: 250  $\mu\text{m}$ . D) Representative karyograms (G-banding) of corrected and mutant hiPSC clones. E) Immunofluorescent images of the short term differentiation demonstrating derivatives of the three germ layers: NES and PAX6 (ectoderm), FOXA2 and GATA4 (endoderm), Brachyury (T), CDX2 and Vimentin (VIM) (mesoderm). Scale bars: 50  $\mu\text{m}$ . F) Immunofluorescent images of expression of markers of the undifferentiated state: SSEA4 (green), NANOG (red) and OCT3/4 (cyan). Nuclei stained with DAPI (blue). Scale bars: 200  $\mu\text{m}$ .

Over the last several years it has been noted that female hiPSC lines may have differences in X-chromosome inactivation (XCI) status. XCI is a dosage compensation mechanism enabling similar expression of X-linked genes in XY males and XX females<sup>14</sup>. Aberrant XCI states, as defined by the change from an inactivated X-chromosome to an eroded X-chromosome, could potentially shift hiPSCs to a more malignant phenotype with upregulation of oncogenes and decreased differentiation potential *in vivo*<sup>15,16</sup>. In addition, it has been shown that erosion of human XCI in *in vitro* cultures could result in major changes in dosage compensation leading to alterations in the total protein content in hiPSCs<sup>17</sup>. To ensure that results in hiPSC-derivatives are comparable, we assessed the XCI status of RVCL-S hiPSC clones. We included three previously characterized lines<sup>18</sup> as controls: an eroded female line (hESC line H9 purchased from the WiCell institute), a male line (LUMC0072iCTRL01) and a female line with normal XCI status (LUMC0099iCTRL04). Expression of the main initiator of X-chromosome inactivation, long non-coding RNA *XIST*, showed differences in expression between clones (Fig S2A). RVCL-S<sup>corr</sup> Clone 1 and RVCL-S<sup>c.703dupG</sup> Clone 2 had the highest expression, similar to the control hiPSC line with the normal XCI status. In addition, we analyzed the presence of ‘repressive’ mark H3K27me3<sup>19</sup> on the X-chromosome by immunofluorescence staining (Fig S2B and C). This confirmed the variability between XCI status of lines and clones. Because of the discrepancy between the clones, we decided to continue with one clone for both RVCL-S-lines to ensure comparable dosage compensation between the lines, and thus potentially, a more comparable differentiation potential. Therefore, all remaining experiments were performed with three independent differentiations from RVCL-S<sup>corr</sup> Clone 1 and RVCL-S<sup>c.703dupG</sup> Clone 2 that was used as a parental clone for CRISPR/Cas9 correction.

### Generation of RVCL-S-hiPSC-ECs

Since RVCL-S pathologies have been linked to EC dysfunction<sup>2,9</sup>, we differentiated hiPSCs into ECs using a previously described protocol<sup>20,21</sup>. CD31<sup>+</sup> hiPSC-ECs were isolated at day 10 of differentiation, expanded for one passage and finally cryopreserved until use. RVCL-S<sup>corr</sup> and RVCL-S<sup>c.703dupG</sup> hiPSC-ECs showed typical EC morphology (Fig 2A). Fluorescence-activated

cell sorting (FACS) analysis demonstrated a similar percentage of CD31, vascular endothelial cadherin (VEC) double-positive cells, indicating comparable differentiation efficiency (Fig 2B and C). In addition, these CD31 VEC double-positive hiPSC-ECs showed no differences in expression of EC-specific surface markers, such as vascular endothelial growth factor receptor (VEGFR2/KDR), VEGFR3 (/FLT4), Endoglin (ENG or CD105) and C-X-C chemokine receptor type 4 (CXCR4/CD184) (Fig 2B and C). Additionally, immunofluorescence staining confirmed the presence and proper localization of EC-associated markers VEC, CD31 and vWF (Fig 2D). Notably, immunofluorescence staining for the same markers in hiPSC-ECs from all RVCL-*S<sup>corr</sup>* and RVCL-*S<sup>c.703dupG</sup>* clones demonstrated a reduced expression in clones 2 and 3 of RVCL-*S<sup>corr</sup>* (Fig S3A). This was confirmed by expression at the RNA level using RNA sequencing (Fig S3B). This might relate to the reduced XCI observed in these clones, something which was also confirmed at the RNA level in hiPSC-ECs (Fig S3E), similar to the previous observation in the undifferentiated hiPSC. This hypothesis is, however, not fully supported by the high expression of EC-markers by RVCL-*S<sup>c.703dupG</sup>* Clone 3, which also showed a lower expression of XIST and an lower percentage of H3K27me3 staining. Hence a more in-depth analysis is needed to further elucidate differences between the generated clones.

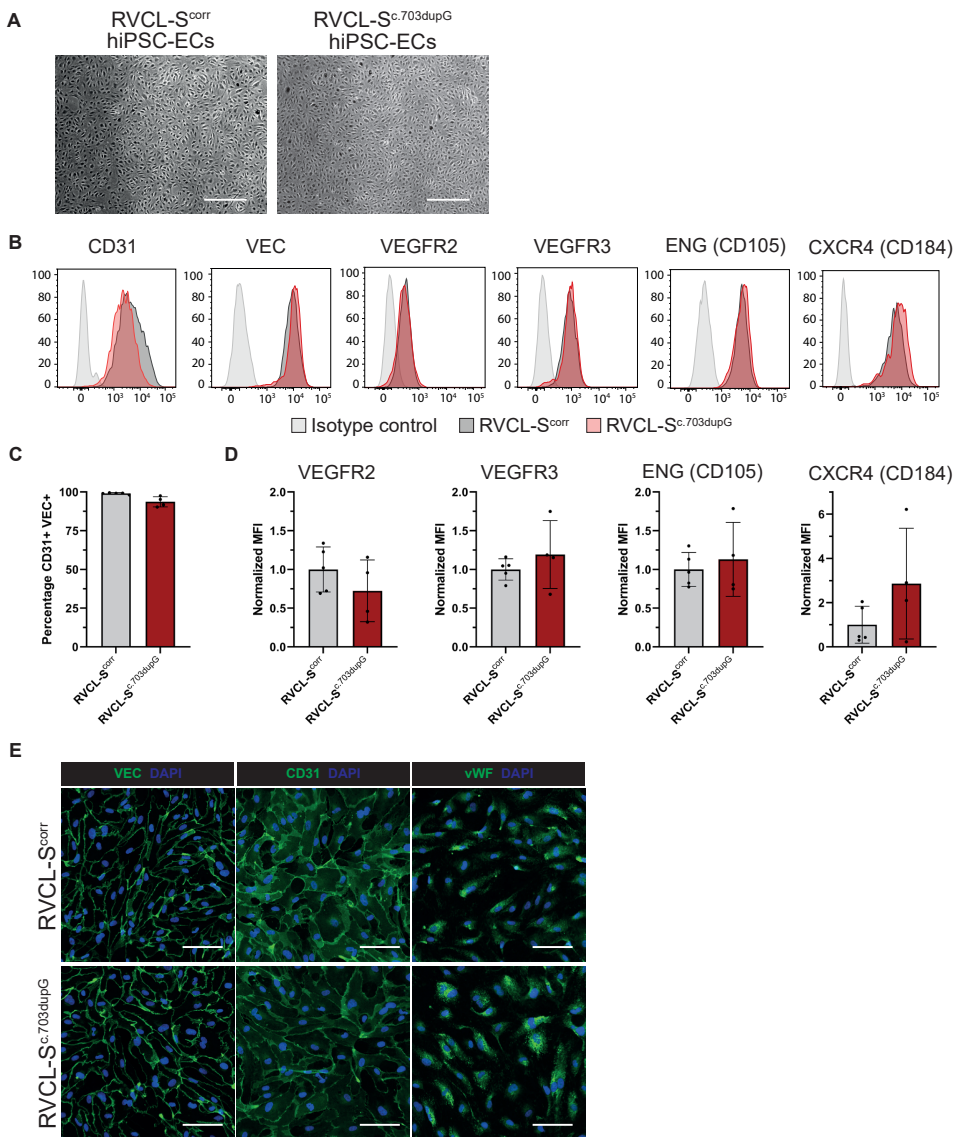


**Figure 2. Characterization of RVCL-S-hiPSC-ECs**

A) Representative brightfield images showing typical EC morphology of hiPSC-ECs. Scale bars: 500  $\mu$ m. B) Representative histograms of fluorescence-activated cell sorting (FACS) analysis of EC surface marker expression on isolated RVCL-S<sup>corr</sup> and RVCL-S<sup>c.703dupG</sup> hiPSC-ECs, and corresponding isotype controls. C) Quantification of percentage of CD31+VEG+ hiPSC-ECs (P2) differentiated from RVCL-S<sup>corr</sup> and RVCL-S<sup>c.703dupG</sup> hiPSCs. N=4 from three independent differentiations. D) Quantification of relative surface expression of EC markers VEG, CD31, KDR, VEGFR3, CD105 and CXCR4 on hiPSC-ECs (P2) differentiated from RVCL-S<sup>corr</sup> and RVCL-S<sup>c.703dupG</sup> hiPSCs. Data are shown as median fluorescent intensity values  $\pm$  SD and are normalized to RVCL-S<sup>corr</sup>. N=4 from three independent differentiations. E) Immunofluorescent images of EC markers VEG, CD31 and vWF on hiPSC-ECs (P2) differentiated from RVCL-S<sup>corr</sup> and RVCL-S<sup>c.703dupG</sup> hiPSCs. Scale bars: 100  $\mu$ m.

### Functional characterization of RVCL-S-hiPSC-ECs shows no apparent differences

To test the functionality of the RVCL-S<sup>corr</sup> and RVCL-S<sup>c.703dupG</sup> hiPSC-ECs, we assessed proliferation and barrier function. Proliferation was investigated by live-cell imaging and quantification by staining of hiPSC-ECs using a nuclear dye and imaging every three hours using an IncuCyte® S3 Live-Cell Analysis System (Fig 3A). Nuclei counts were normalized to a specific time-point per experiment to remove differences in cell seeding density. Low variability in proliferation was observed between differentiation batches within RVCL-S<sup>corr</sup> (Fig 3B) and RVCL-S<sup>c.703dupG</sup> (Fig 3C) hiPSC-ECs. Notably, only linear growth was observed, instead of exponential growth. This could be potentially caused by contact inhibition or limited nutrient availability. Follow-up experiments using additional control lines and primary ECs, sensitive to either of these mechanisms should be performed to explain the cause for the difference in proliferation profile for the RVCL-S<sup>corr</sup> and RVCL-S<sup>c.703dupG</sup> hiPSC-ECs. Regardless, no differences were observed in proliferation (Fig 3D), quantified as doubling time (Fig 3D and E) between the disease and corrected hiPSC-ECs. Observed doubling times were slightly higher than those observed for primary ECs *in vitro* (12 – 48 hours), and these differences correlated with the lack of exponential growth phase.

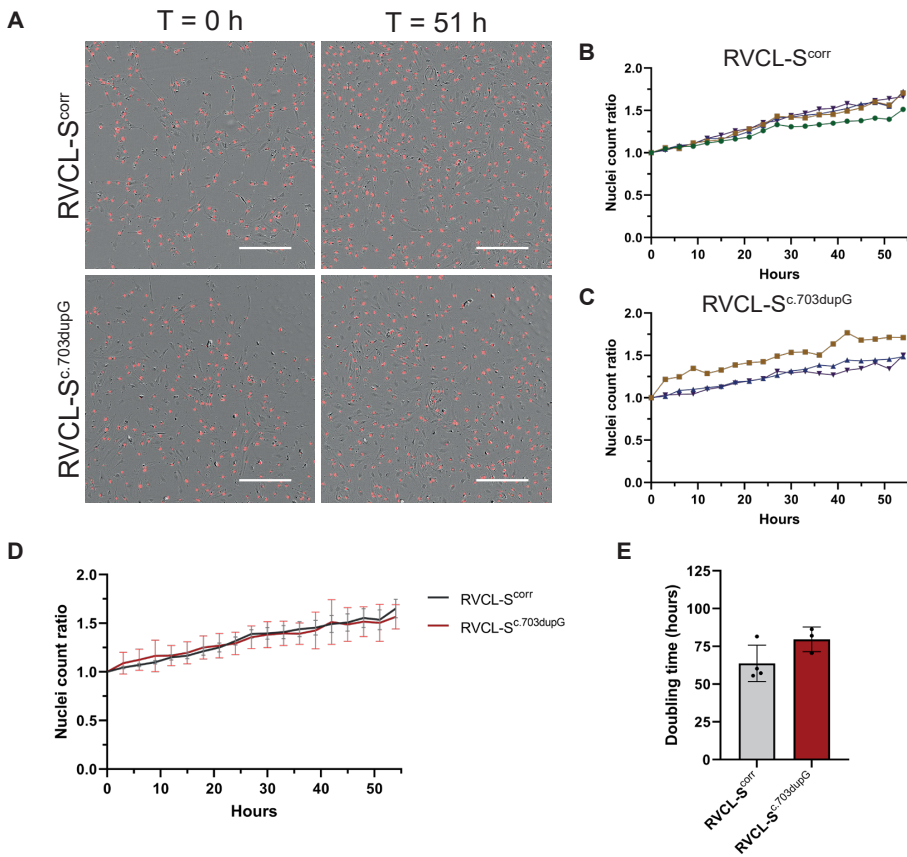


**Figure 3. Assessment of proliferation of RVCL-S-hiPSC-ECs**

A) Representative overlay image of brightfield and incucyte nuclear identification in proliferation assay at  $t = 0$  h and  $t = 51$  h of RVCL-S<sup>corr</sup> and RVCL-S<sup>c.703dupG</sup> hiPSC-ECs. Scale bars: 400  $\mu$ m. B) Normalized nuclear count ratio for proliferation assay with RVCL-S<sup>corr</sup> hiPSC-ECs. N=3 from three independent differentiations. C) Normalized nuclear count ratio for proliferation assay with RVCL-S<sup>c.703dupG</sup> hiPSC-ECs. N=3 from two independent differentiations. D) Mean normalized nuclear count ratio for proliferation assay with RVCL-S<sup>corr</sup> hiPSC-ECs and RVCL-S<sup>c.703dupG</sup> hiPSC-ECs. Data are shown as mean values  $\pm$  SD of N=4 from three independent differentiations for RVCL-S<sup>corr</sup> and N=3 from 2 independent differentiations for RVCL-S<sup>c.703dupG</sup> hiPSC-ECs. E) Quantification of doubling time for RVCL-S<sup>corr</sup> hiPSC-ECs and RVCL-S<sup>c.703dupG</sup> hiPSC-ECs. Data are shown as mean values  $\pm$  SD of N=4 from three independent differentiations for RVCL-S<sup>corr</sup>, and N=3 from two independent differentiations for RVCL-S<sup>c.703dupG</sup> hiPSC-ECs.

Barrier function and EC migration were assessed by real-time impedance spectroscopy using an integrated assay of electrical wound healing as previously described<sup>20</sup>. Both the absolute resistance and migration rates of the RVCL-S<sup>corr</sup> hiPSC-EC monolayers had low variability between independent differentiation batches (Fig 4A and E). Higher variability was observed for the same parameters for RVCL-S<sup>c.703dupG</sup> hiPSC-EC monolayers (Fig 4B and F). This was in contrast to previous data which indicated low batch-to-batch variability of CD31<sup>+</sup> hiPSC-ECs from two independent lines<sup>20</sup>. Overall, no significant differences were observed in barrier function and EC migration between the RVCL-S<sup>corr</sup> and RVCL-S<sup>c.703dupG</sup> hiPSC-ECs (Fig 4C, D, G and H).

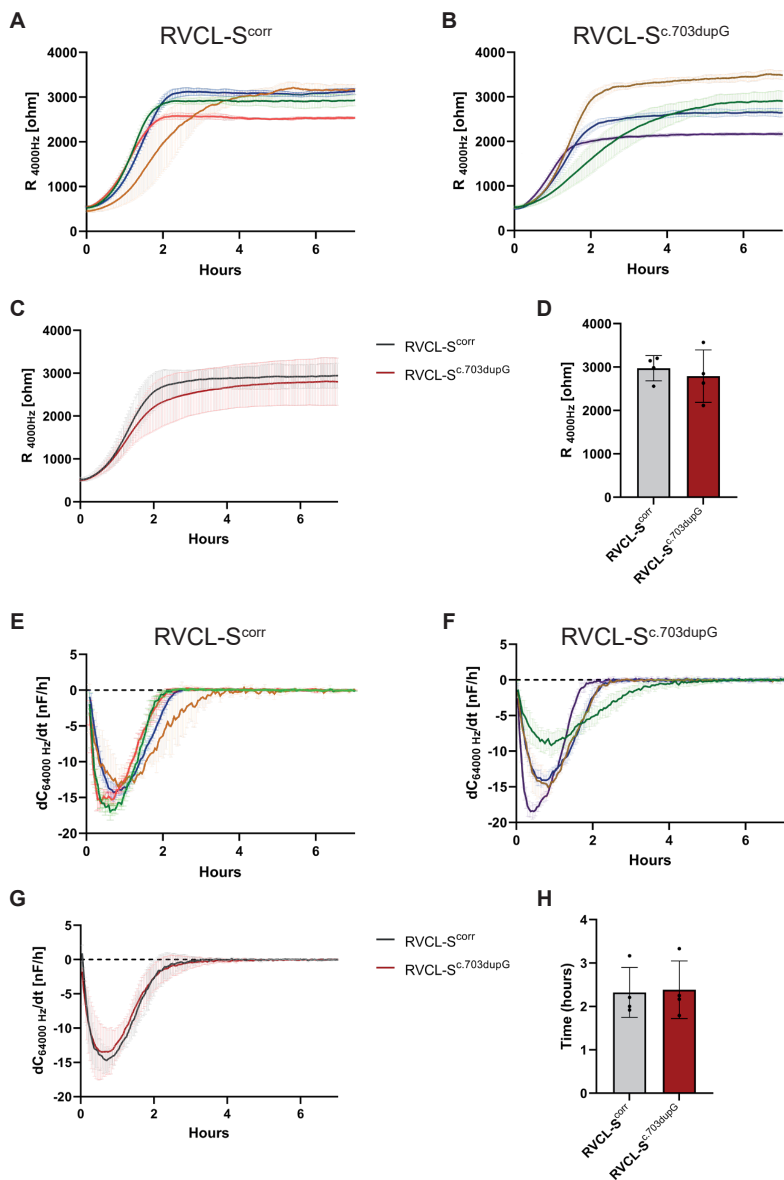


**Figure 4. Assessment of barrier function and real-time migration of RVCL-S-hiPSC-ECs**

A) Absolute resistance values at 4000 Hz of RVCL-S<sup>corr</sup> hiPSC-EC monolayers. Data are shown as mean values  $\pm$  SD of N=4, each indicated with a different color, from three independent differentiations. B) Absolute resistance values at 4.000 Hz of RVCL-S<sup>c.703dupG</sup> hiPSC-EC monolayers. Data are shown as mean values  $\pm$  SD of N=4, each indicated with a different color, from three independent differentiations. C) Mean absolute resistance values at 4000 Hz of RVCL-S<sup>corr</sup> and RVCL-S<sup>c.703dupG</sup> hiPSC-EC monolayers. Data are shown as combined mean values  $\pm$  SD of N=4 from three independent differentiations. D) Quantification of absolute resistance values at 4000 Hz of RVCL-S<sup>corr</sup> and RVCL-S<sup>c.703dupG</sup> hiPSC-EC monolayers. Data shown as mean values  $\pm$  SD of N=4 from three independent differentiations. E) Speed of migration ( $dC/dt$ ) determined as a change in capacitance at 64000 Hz over time after

electrical wound healing for RVCL-S<sup>corr</sup> hiPSC-ECs. Data are shown as mean values  $\pm$  SD of N=4, each indicated with a different color, from three independent differentiations. F) Speed of migration (dC/dt) determined as a change in capacitance at 64000 Hz over time after electrical wound healing for RVCL-S<sup>c.703dupG</sup> hiPSC-ECs. Data are shown as mean values  $\pm$  SD of N=4, each indicated with a different color, from three independent differentiations. G) Mean speed of migration (dC/dt) determined as a change in capacitance at 64000 Hz over time after electrical wound healing for RVCL-S<sup>corr</sup> and RVCL-S<sup>c.703dupG</sup> hiPSC-ECs. Data are shown as combined mean values  $\pm$  SD of N=4 from three independent differentiations. H) Quantification of migration rates determined as time upon wound closure DC/dt > (-0.1 nF/h). Data are shown as mean values  $\pm$  SD of N=4 from three independent differentiations.

## Conclusion and future perspective

We generated hiPSC lines from one RVCL-S patient and corrected the mutation using CRISPR/Cas9 to create isogenic genetically-corrected control hiPSC line. We did not examine whether the TREX1 protein expression and localization in these clones had been altered by the disease as in patients due to lack of appropriate antibodies targeting the unaltered N-terminus of the TREX1 protein<sup>1,5</sup>. The lines all differentiated to hiPSC-ECs using our standard protocol. We confirmed the expected genotypes but in a series of simple assays (migration, EC barrier function) we did not find any differences between the diseased and corrected hiPSC-ECs. There may be several reasons for this: (i) the identity of the ECs derived using our protocol did not correspond to those in the tissues manifesting the disease in patients (eye, brain, liver, kidney); (ii) any EC defects only manifest in a more complex model systems; that was previously the case in our study on hereditary hemorrhagic telangiectasia (HHT) where a disease phenotype was only apparent when hiPSC-ECs were included a 3D vessel-on-chip system<sup>22</sup>. An inflammatory component might be required in the model system to induce the phenotype; this could be either stimulating the hiPSC-ECs with pro-inflammatory cytokines or co-culturing them with inflammatory cells.

In summary, we have created isogenic pairs of diseased and control RVCL-S-hiPSC-ECs but found no differences between them in basic EC assays *in vitro*. However, these lines can form a basis for future investigation into the mechanisms underlying RVCL-S pathology but then in more complex models with additional disease-promoting microenvironments.

## Material and Methods

### HiPSC lines and maintenance

Skin biopsies were taken from a female RVCL-S patient (with informed consent approved by Leiden University Medical Center ethics committee under the P13.080 "Parapluprotocol: hiPSC.") for the generation of the RVCL-S hiPSC line (LUMC0210iTREX). Fibroblasts were isolated from the skin biopsies and cultured in fibroblast medium (FM) composed of DMEM/F12 Glutamax supplemented with 10% Fetal Bovine Serum (FBS), 1% Non-Essential Amino Acids, 0.18%  $\beta$ -mercaptoethanol, 1% penicillin/streptomycin (all from ThermoFisher Scientific: #31331; #10270; #11140 #31350; #15070) and 10  $\mu$ g/mL Ascorbic acid (Sigma-Aldrich, #A5960). At passage 3, 10<sup>5</sup> cells were transduced with Sendai virus (SeVdp

(KOSM302L), MOI 7.5). 16 h after transduction, cells were plated at the density of  $10^3$  cells/cm<sup>2</sup> on Matrigel coated plates (Corning, #354277) in FM. The next day, cells were refreshed and subsequently maintained with ReproTeSR™ (Stemcell Technologies, #05921, #05922, #05923). At day 18, culture was shifted to TeSRTM E8™ medium (Stemcell Technologies, #05990). After mechanical picking, hiPSCs were maintained in TeSRTM-E8™ on vitronectin-coated plates (Stemcell Technologies, #07180) at 37 °C, 5% CO<sub>2</sub> and 20% O<sub>2</sub>. HiPSCs were passaged once a week as small aggregates using Gentle Cell Dissociation Reagent (Stemcell Technologies, #07174) with a splitting ratio of 1:25. The following hiPSC lines were used: LUMC0210iTREX (female, reprogrammed from skin fibroblasts using Sendai virus, mutation Val235fs), IsoLUMC0210iTREX02 (CRISPR-Cas9 edited to remove the Val235fs mutation) and LUMC0054iCTRL02 (<https://hpscereg.eu/cell-line/LUMCi001-A>).

### CRISPR-Cas9 mutation correction

For genetic repair,  $1 \times 10^5$  LUMC0210iTREX02 cells were electroporated at passage 15 with the Alt-R Cas9-RNP complex and the ssODN (both IDT) using a factory-defined program (program 6) of the Neon Transfection System (Invitrogen). Subsequently, cells were cultured in two Synthemax II-SC (Corning)-coated wells of a 12-well plate in TESR-plus with Cloner2 (Stem Cell Technologies). For single-cell cloning, 1000 cells were plated onto a Synthemax II-SC-coated 10 cm dish in TESR-plus with Cloner2. After 8-12 days, hiPSC colonies were split into two VN-coated wells of a 96-well plate in TESR-plus. The gene region of interest was amplified by PCR using the Terra PCR Direct Polymerase Mix (TaKaRa) from DNA isolated from one well (QuickExtract solution, Lucigen). Successfully edited clones were identified by AatII enzyme (New England Biolabs) activity and confirmed by Sanger sequencing performed by the Leiden Genome Technology Centre (LGTC).

**Table 1. Primers, gRNA and ssODN used in this study**

	Target	Forward/Reverse primer (5'-3')
Correction confirmation (PCR/sequencing)	RVCL-S exon 1	CACACAATGGTGACCGCTACG/ TGACCATCCTGCTAGGGAAAGTG
gRNA		ACCATCAGGCCCATGTATGG
ssODN		ACCACAGGCCCTGCTGCGGTGGGTGGATGCTCACGC CAGGCCTTTCGGCACCATCAGGCCCATGTATGGcGTC ACAGCCTCTGCTAGGACCAAGCCAAGACCATCTGCT GTCACAACCACTGCACACCTGGCCACAACCA
qPCR primer	hARP	CACCATTGAAATCCTGAGTGATGT/ TGACCAGCCCAAAGGAGAAG
qPCR primer	XIST	CAGCATGGTTGGTGACACCTAAG/ TGGAATGAGCAGTGTGCGAT

### Immunofluorescence staining

HiPSCs at passage 17 for LUMC0210iTREX01, LUMC0210iTREX02 and LUMC0210iTREX03 or passage 24 for Iso1LUMC0210iTREX02, Iso2LUMC0210iTREX02, Iso3LUMC0210iTREX02 were fixed in 2% PFA for 30 min, permeabilized with 0.1% Triton X-100, and blocked with 4% normal swine serum (NSS, DAKO) at room temperature (RT) for 1 h. Primary antibodies were added and incubated overnight at 4°C (See Table 2 for antibodies used). After washing, secondary antibodies were added for 1 h at RT. Nuclei were stained with DAPI, and coverslips were mounted using Mowiol (Merck Millipore). Images were acquired on a Leica TCS SP8 microscope or an EVOS M7000 microscope (ThermoFisher Scientific). For quantification of H3K27me3, cells (n>1000 cells per cell line) were imaged by generating a maximum intensity projection (MIP) from a z-stack using an EVOS M7000 microscope. Subsequently, the MIP was used to manually count cells positive for the H3K27me3 marker.

**Table 2. List of antibodies used**

Antibody	Species	Use	Source	Dilution	Catalog #
OCT3/4-BV421	Mouse	FACS	BD Biosciences	1:25	565644
NANOG-PE	Mouse	FACS	BD Biosciences	1:5	560483
SSEA4-FITC	Mouse	FACS	Miltenyi Biotec	1:25	130-098-371
OCT3/4	Mouse	IF	Santa Cruz	1:100	sc-5279
NANOG	Mouse	IF	Santa Cruz	1:150	sc-293121
SSEA4	Mouse	IF	BioLegend	1:30	330402
Nestin-Alexa488	Mouse	IF	Cell Signaling Technology	1:200	60433
PAX6-Alexa647	Rabbit	IF	Cell Signaling Technology	1:200	60433
FOXA2-Alexa555	Rabbit	IF	Cell Signaling Technology	1:500	8186
GATA4-Alexa647	Rabbit	IF	Cell Signaling Technology	1:200	36966
Brachyury-Alexa488	Rabbit	IF	Cell Signaling Technology	1:200	81694
Vimentin-Alexa647	Rabbit	IF	Cell Signaling Technology	1:300	5741
VEC	Rabbit	IF	Cell Signaling Technology	1:300	2158
CD31	Mouse	IF	DAKO	1:300	M0823
vWF	Rabbit	IF	A0082	1:200	A0082

### FACS staining

HiPSCs were dissociated at passage 15 with TrypLE for 5 min at 37°C. Samples were fixed for 15 min in 200 µL of Reagent A of the fix & perm kit (ThermoFisher Scientific). Cells were

washed once in FACS buffer (PBS without  $\text{Ca}^{2+}$  and  $\text{Mg}^{2+}$  with 0.5% BSA and 2 mM EDTA), resuspended in 80  $\mu\text{L}$  of Reagent B with conjugated antibodies (Table 2) and incubated in the dark for 60 min at RT. Subsequently, samples were washed once and resuspended in FACS buffer before being measured on the MACSQuant VYB flow cytometer (Miltenyi Biotec). Analysis was performed using FlowJo v.10.6.1 software.

### **In vitro trilineage differentiation**

The ability of hiPSCs to differentiate into the three germ layers (ectoderm, mesoderm, and endoderm) was assessed using differentiation with a Trilineage differentiation kit (Stem Cell Technologies). Differentiation was done according to the manufacturer's instructions on hESC-qualified Matrigel (Corning) coated coverslips. After 5 to 7 days of culture cells were fixed using 2% PFA.

### **Karyotype analysis**

HiPSCs at passage 9 were karyotyped by Cell Guidance systems (UK) and a total of 20 metaphases were counted.

### **RNA isolation and quantitative RT-PCR**

RNA was extracted from hiPSC-ECs monolayers using the NucleoSpin RNA XS kit (Macherey-Nagel) and cDNA was synthesized using an iScript-cDNA Synthesis kit (Bio-Rad). ITaq Universal SYBR Green Supermixes (Bio-Rad) and Bio-Rad CFX384 real-time system were used for the PCR reaction and detection. CDNA from three lines was added as controls, namely eroded female (hESC line H9 purchased from the WiCell institute), male (LUMC0072iCTRL01), and female with normal XCI status (LUMC0099iCTRL04)<sup>18</sup>. Primers used can be found in Table 1. Relative gene expression was calculated using the  $\Delta\text{Ct}$  method and normalized to housekeeping gene hARP.

### **RNA Sequencing**

RNA was isolated and purified using the NucleoSpin RNA-kit (Macherey-Nagel). RNA-sequencing and whole-genome transcriptome data were generated by Novogene (UK) on the Illumina NovaSeq6000 platform, paired-end sequencing and read length of 150bp with a sequencing depth of 20M raw reads per sample.

Raw RNA-seq reads were processed using the open-source BOWDL RNAseq pipeline v5.0.0 developed at the LUMC. The pipeline performs FASTQ preprocessing (including quality control, quality trimming, and adapter clipping), RNA-Seq alignment, read quantification, and optionally transcript assembly. FastQC was used for checking raw read QC. Adapter clipping was performed using Cutadapt (v2.4) with default settings. RNA-Seq reads' alignment was performed using STAR (v2.7.5a) on GRCh38 human reference genome. Gene read quantification was performed using featureCounts (v2.0.1) with the setting “-M

-O --fraction". Gene annotation used for quantification was Ensembl version 105. Count tables were normalized using EdgeR<sup>23</sup>, and genes were filtered based on their expression across all the samples according to previous publication<sup>23</sup>.

### **Proliferation Assay**

HiPSC-ECs were seeded on bovine fibronectin (Sigma, F1141, 20 µg/mL) coated 96 well plates (Greiner, 655160) at a density of 9.375 K/cm<sup>2</sup> (= 3K/well) in EGM-2 culture medium (PromoCell) supplemented with 1:2000 IncuCyte NucLight Rapid Red Reagent (Sartorius, Cat# 4717). Plates were left undisturbed at RT for 1 h to allow cell attachment before placing them in the IncuCyte<sup>®</sup> S3 Live-Cell Analysis System. Wells were imaged every 3 h with a 4X objective in the red channel (excitation 567-607 nm, emission 622-704 nm) with an acquisition time of 500 ms. Images were analyzed using the built-in Incucyte analysis software to extract cell count per well over time. Data was extracted and plotted using GraphPad Prism 9 software. Doubling time was calculated by first fitting a linear regression curve on the data and extracting the slope using Graphpad Prism 9 software. To determine the doubling time from this linear part of the curve, the following formula was used: doubling time =  $\ln(2) / (\text{growth rate})$ , in which the growth rate is the slope of the fitted linear regression.

### **Endothelial barrier function analysis**

Endothelial barrier function and real-time migration analysis was performed using electric cell-substrate impedance sensing (ECIS Z $\theta$ , Applied Biophysics) as described previously<sup>20</sup>. In brief, CD31+ hiPSC-ECs were seeded on fibronectin-coated (50 µg/mL) ECIS arrays (8W10E PET, Applied Biophysics) at a density of ~50,000 cells/cm<sup>2</sup> and left undisturbed at RT for 2h to allow cell attachment. For barrier function and migration studies, cells were left for at least 6h to establish a confluent monolayer before refreshing half of the medium with fresh EGM-2. One hour after medium change, the electric wound (10 sec pulse of 5000 µA at 60 kHz) was applied. Recovery of the barrier was monitored over the next 12h. Multiple frequency/time (MFT) mode was used for real-time assessment of the barrier and monolayer confluence. The absolute resistance values at 4000 Hz were quantified by taking the mean of 6h of stable absolute resistance after wound closure. Quantification of migration rates was determined as a time upon closing the wound  $DC/dt > (-0.1 \text{ nF/h})$ .

### **Droplet digital PCR (ddPCR)**

DdPCR experiments were performed and analyzed using a Q200 AutoDG thermocycler (Bio-Rad), a QX200 Droplet Digital PCR System (Bio-Rad) and QuantaSoft software (Bio-Rad). DdPCR assays comprised premixtures of a primer pair (18 µM each) and a FAM- or HEX-conjugated hydrolysis probe (5 µM). Details regarding the assays are listed in Table 3. Reactions (22 µL) were prepared using 2X ddPCR Supermix for Probes (no dUTP, Bio-

Rad), 900 nM of each primer, 250 nM of the probe, 30 ng of gDNA and 2-5 U of HindIII (NEB). Automated droplet generation, PCR amplification procedure and analysis were all performed following the manufacturer's instructions.

#### *WT/Cor and WT/Mut assays*

Probes were designed to specifically distinguish the WT allele (HEX-conjugated) over the Corrected and Mutant alleles (FAM-conjugated). Locked nucleic acids were used to reduce the length of the probes, thereby increasing their specificity (See Table 3).

#### *iCS-digital™ PSC 24-probes assay*

The genome integrity was assessed using the iCS-digital™ PSC 24-probes kit (Stemgenomics) following the manufacturer's instructions.

**Table 3. Primer-Probe sets used for ddPCR assays.**

Name	Sequence (5'-3')	Fluorophore-Quencher
TREX1_Primer_Fwd	TCAGCATCTGTCAGTGGAGA	-
TREX1_Primer_Rev	GTGACAGCAGATGGTCTTG	-
TREX1_Probe_Cor	ATG G+C+G +TC+A C+AG C	FAM-ZEN-IBFQ
TREX1_Probe_Mut	ATG GG+G +G+T+C ACA G	FAM-ZEN-IBFQ
TREX1_Probe_WT	ATG GG+G +T+C+A CAG C	HEX-ZEN-IBFQ

*+ symbol indicates the following nucleotide is a locked nucleic acid*

## Acknowledgements

We thank N. Nakanishi (National Institute of Advanced Industrial Science and Technology, Japan) for providing SeV and the Laboratorium voor Diagnostische Genoom Analyse (LGDA, LUMC) for karyotype analysis. We thank Yolanda Chang and Susana M. Chuva de Sousa Lopes for discussion on XCI, trial of the XIST antibody and providing cDNA for the XIST RT-PCR controls. This work was supported by The Netherlands Organ-on-Chip Initiative, an NWO Gravitation project funded by the Ministry of Education, Culture and Science of the government of the Netherlands (024.003.001) and the Novo Nordisk Foundation Center for Stem Cell Medicine, supported by Novo Nordisk Foundation grants (NNF21CC0073729).

## Author Contributions

Conceptualization, G.M.T. and V.V.O.; methodology, D.M.N., D.G.K. and V.V.O.; investigation, D.M.N., D.G.K., F.E.v.d.H., M.J.B., A.B. and R.W.J.v.H.; visualization, D.M.N.; resources, C.L.M., A.M.J.M.v.d.M and V.V.O.; writing – original draft, D.M.N., D.G.K., A.M.J.M.v.d.M and V.V.O.; writing – review & editing, D.M.N., D.G.K., C.L.M. and V.V.O.; supervision, C.F., C.L.M. and V.V.O.; project administration, V.V.O.; funding acquisition, C.L.M. and V.V.O.

## Conflict of interest

The authors declare no competing interests.

## References

1. Richards, A. *et al.* C-terminal truncations in human 3'-5' DNA exonuclease TREX1 cause autosomal dominant retinal vasculopathy with cerebral leukodystrophy. *Nat Genet* 39, 1068–1070 (2007).
2. Stam, A. H. *et al.* Retinal vasculopathy with cerebral leukoencephalopathy and systemic manifestations. *Brain* 139, 2909–2922 (2016).
3. Wilms, A. E., de Boer, I. & Terwindt, G. M. Retinal Vasculopathy with Cerebral Leukoencephalopathy and Systemic manifestations (RVCL-S): An update on basic science and clinical perspectives. *Cereb Circ Cogn Behav* 3, 100046 (2022).
4. DiFrancesco, J. C. *et al.* TREX1 C-terminal frameshift mutations in the systemic variant of retinal vasculopathy with cerebral leukodystrophy. *Neurological Sciences* 36, 323–330 (2015).
5. Hasan, M. *et al.* Cytosolic Nuclease TREX1 Regulates Oligosaccharyltransferase Activity Independent of Nuclease Activity to Suppress Immune Activation. *Immunity* 43, 463–474 (2015).
6. Kothari, P. H. *et al.* TREX1 is expressed by microglia in normal human brain and increases in regions affected by ischemia. *Brain Pathology* 1–16 (2018) doi:10.1111/bpa.12626.
7. Saito, R. *et al.* Retinal vasculopathy with cerebral leukodystrophy: Clinicopathologic features of an autopsied patient with a heterozygous TREX 1 mutation. *J Neuropathol Exp Neurol* 78, 181–186 (2019).
8. Kolar, G. R. *et al.* Neuropathology and genetics of cerebretinal vasculopathies. *Brain Pathol* 24, 510–518 (2014).
9. de Boer, I. *et al.* RVCL-S and CADASIL display distinct impaired vascular function. *Neurology* 91, e956–e963 (2018).
10. Pelzer, N. *et al.* Circulating Endothelial Markers in Retinal Vasculopathy With Cerebral Leukoencephalopathy and Systemic Manifestations. *Stroke* (2017) doi:10.1161/STROKEAHA.117.018556.
11. Sakai, T. *et al.* DNase-active TREX1 frame-shift mutants induce serologic autoimmunity in mice. *J Autoimmun.* 31, 872–881 (2017).
12. Mulder, I. A. *et al.* Increased Mortality and Vascular Phenotype in a Knock- In Mouse Model of Retinal Vasculopathy With Cerebral Leukoencephalopathy and Systemic Manifestations. *Stroke* 1–8 (2020) doi:10.1161/STROKEAHA.119.025176.
13. Passier, R., Orlova, V. V. & Mummery, C. L. Complex Tissue and Disease Modeling using hiPSCs. *Cell Stem Cell* 18, 309–321 (2016).
14. Loda, A., Collombet, S. & Heard, E. Gene regulation in time and space during X-chromosome inactivation. *Nat Rev Mol Cell Biol* 23, 231–249 (2022).
15. Anguera, M. C. *et al.* Molecular signatures of human induced pluripotent stem cells highlight sex differences and cancer genes. *Cell Stem Cell* 11, 75–90 (2012).
16. Geens, M. & Chuva De Sousa Lopes, S. M. X chromosome inactivation in human pluripotent stem cells as a model for human development: back to the drawing board? *Hum Reprod Update* 23, 520–532 (2017).
17. Brenes, A. J. *et al.* Erosion of human X chromosome inactivation causes major remodeling of the iPSC proteome. *Cell Rep* 35, (2021).
18. Chang, Y. W. *et al.* Tissue of origin, but not XCI state, influences germ cell differentiation from human pluripotent stem cells. *Cells* 10, (2021).
19. Patrat, C., Ouimette, J. F. & Rougeulle, C. X chromosome inactivation in human development. *Development (Cambridge)* vol. 147 Preprint at <https://doi.org/10.1242/dev.183095> (2020).
20. Halaidych, O. V. *et al.* Inflammatory Responses and Barrier Function of Endothelial Cells Derived from Human Induced Pluripotent Stem Cells. *Stem Cell Reports* 10, 1642–1656 (2018).
21. Orlova, V. V. *et al.* Generation, expansion and functional analysis of endothelial cells and pericytes derived from human pluripotent stem cells. *Nat Protoc* 9, 1514–1531 (2014).
22. Orlova, V. V. *et al.* Vascular defects associated with hereditary hemorrhagic telangiectasia revealed in patient-derived isogenic iPSCs in 3D vessels on chip. *Stem Cell Reports* 17, 1536–1545 (2022).
23. Chen, Y., Lun, A. T. L. & Smyth, G. K. From reads to genes to pathways: differential expression analysis of RNA-Seq experiments using Rsubread and the edgeR quasi-likelihood pipeline. *F1000Res* 5, 1438 (2016).

## Supplementary Material

### Contents

#### Supplemental Figures:

**Figure S1. Related to Figure 1.** Assessment of genomic stability and correct CRISPR-Cas9 editing in RVCL-S hiPSCs.

**Figure S2. Related to Figure 1.** Assessment of X-chromosome inactivation status in RVCL-S hiPSCs.

**Figure S3. Related to Figure 2.** Immunofluorescence staining and RNA expression of EC markers in RVCL-S hiPSC-ECs.

## Supplementary Figure 1

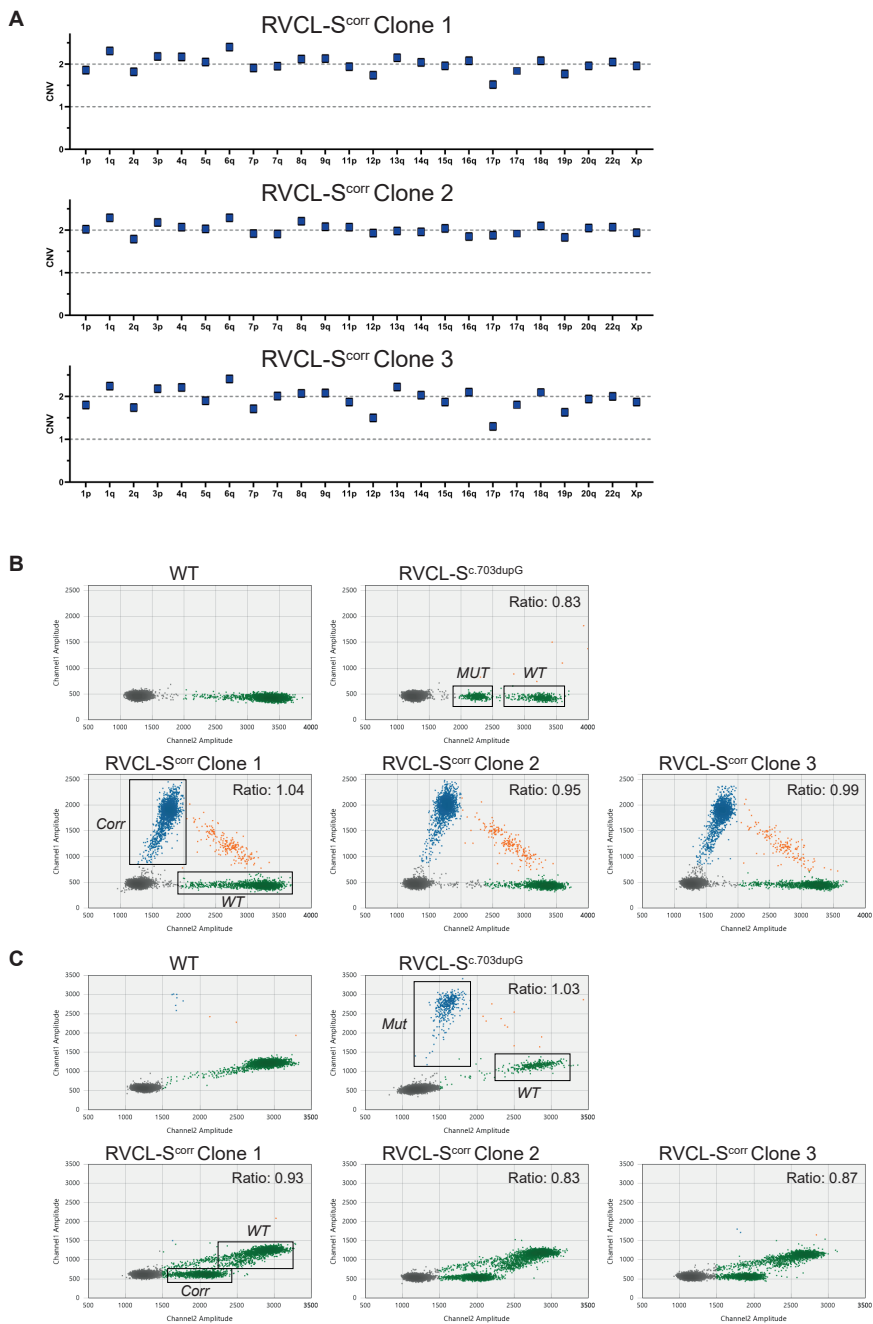
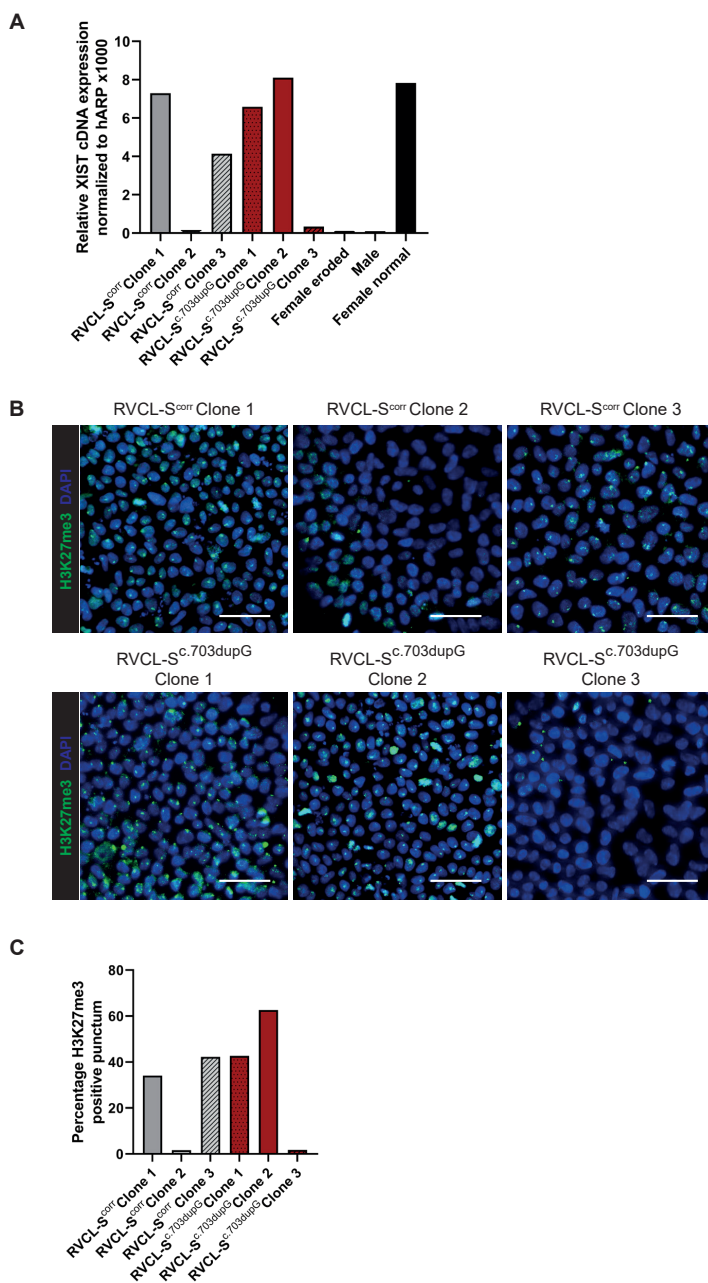


Figure S1: Assessment of genomic stability and correct CRISPR-Cas9 editing in RVCL-S

### hiPSCs.

A) DdPCR examining genomic integrity of the RVCL-S<sup>corr</sup> hiPSC clones by determining the copy number variation (CNV) of the 24 genomic locations that consist of 92% of the most recurrent genomic abnormalities in hPSCs. B) DdPCR dot plots demonstrating the presence of the wildtype (WT), Mutant (MUT) or Corrected (Corr) allele. Genomic DNA of the WT hiPSC line, the parental RVCL-S<sup>c.703dupG</sup> hiPSC line and the three clones of the RVCL-S<sup>corr</sup> hiPSC line were investigated. Dots represent droplets containing the Corr sequence on channel 1 and the WT sequence on channel 2. Suboptimal binding of the WT probe on the MUT allele results in a separate population in the RVCL-S<sup>c.703dupG</sup> plot. In the RVCL-S<sup>c.703dupG</sup> plot, the ratio between the MUT population and WT population is displayed. In the RVCL-S<sup>corr</sup> clones plots, the ratio between the Corr population and WT population is displayed. C) DdPCR dot plots demonstrating the presence of the wildtype (WT), Mutant (MUT) or Corrected (Corr) allele. Genomic DNA of the WT hiPSC line, the parental RVCL-S<sup>c.703dupG</sup> hiPSC line and the three clones of the RVCL-S<sup>corr</sup> hiPSC line were investigated. Dots represent droplets containing the Mut sequence on channel 1 and the WT sequence on channel 2. Suboptimal binding of the WT probe on the Corr allele results in a separate population in the RVCL-S<sup>corr</sup> clones plots. In the RVCL-S<sup>corr</sup> clones plots, the ratio between the Corr population and WT population is shown.

## Supplementary Figure 2



**Figure S2. Assessment of X-chromosome inactivation status in RVCL-S hiPSCs.**

A) Gene expression, as assessed by RT-qPCR, of XIST for the three clones of both RVCL-S<sup>corr</sup>

and RVCL-S<sup>c.703dupG</sup> hiPSCs. B) Representative immunofluorescence staining for H3K27me3 for the three clones of both RVCL-S<sup>corr</sup> and RVCL-S<sup>c.703dupG</sup> hiPSCs. C) Quantification of H3K27me3 positive cells (percentage). N> 1000 cells per clone quantified.

## Supplementary Figure 3

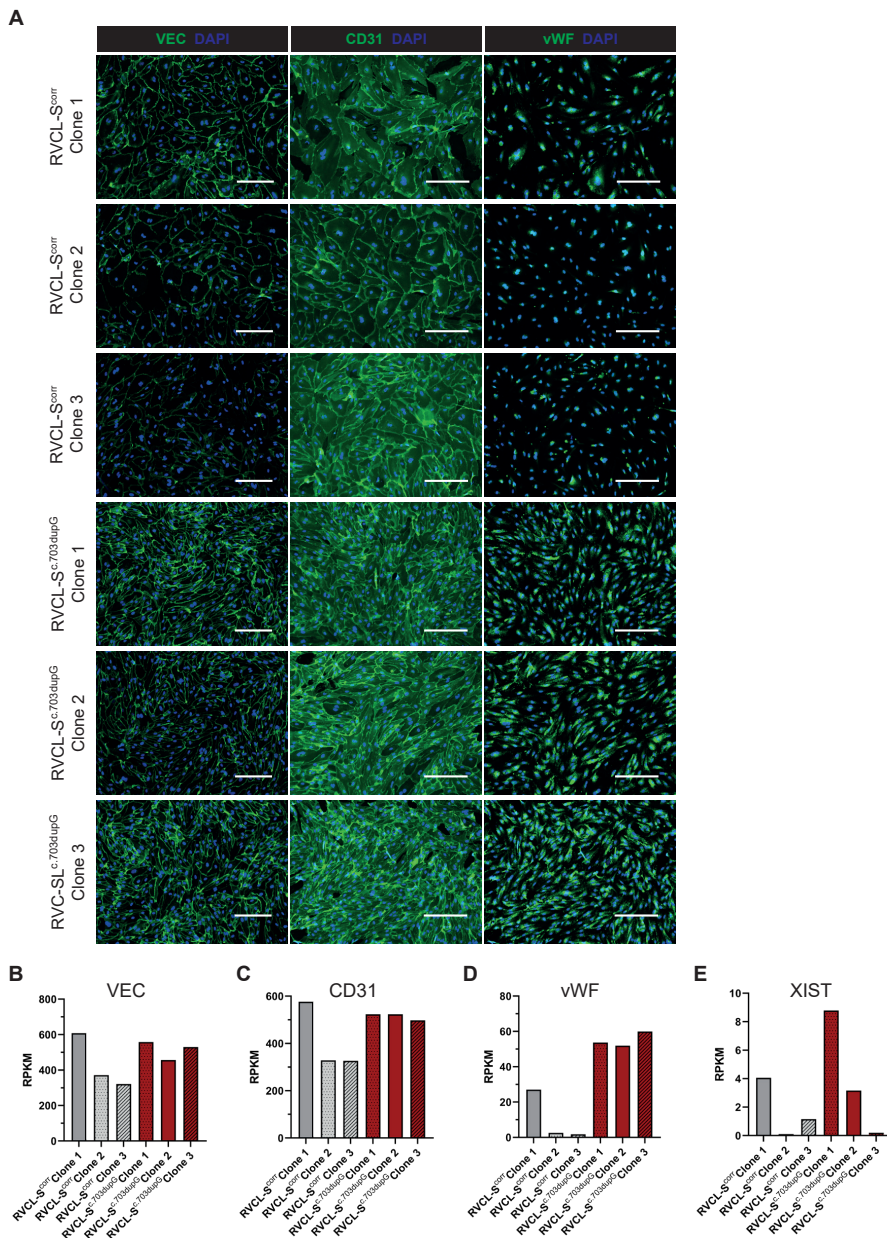
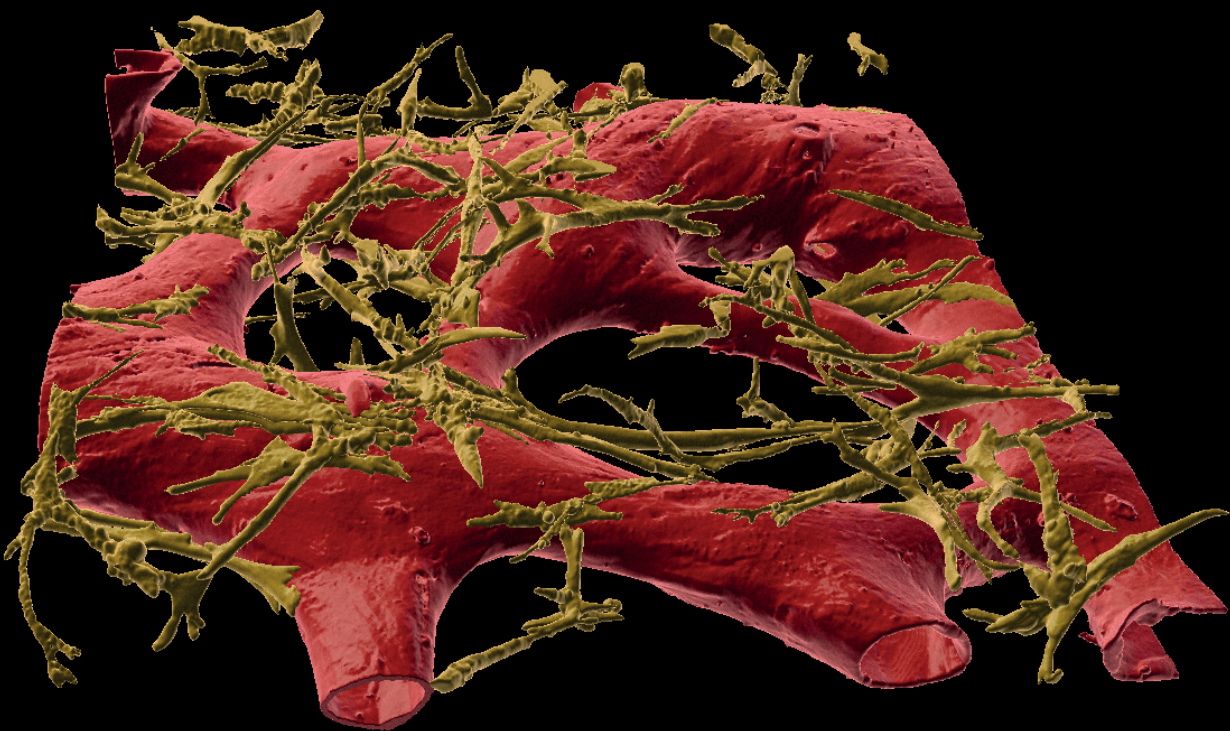


**Figure S3. Immunofluorescence staining and RNA expression of EC markers in RVCL-S hiPSC-ECs.**

A) Immunofluorescence staining of EC markers VEC, CD31 and vWF of RVCL-S<sup>corr</sup> and RVCL-S<sup>c.703dupG</sup> hiPSC-ECs. Scale bars: 100  $\mu$ m. (B-D) Gene expression, as assessed by RNA

sequencing, for EC-markers VEC (B), CD31 (C), vWF (D) and XIST (E).



# Chapter 5

## Vascular defects associated with Hereditary Haemorrhagic Telangiectasia revealed in patient-derived isogenic iPSCs in 3D vessels-on-chip

### Abstract

Hereditary Haemorrhagic Telangiectasia (HHT) is a genetic disease characterized by weak blood vessels. HHT1 is caused by mutations in the ENDOGLIN (ENG) gene. Here, we generated induced pluripotent stem cells (hiPSC) from a rare mosaic HHT1 patient with tissues containing both mutant (ENGc.1678C>T) and normal cells, enabling derivation of isogenic diseased and healthy hiPSCs respectively. We showed reduced ENG expression in HHT1-endothelial cells (HHT1-hiPSC-ECs), reflecting haploinsufficiency. HHT1c.1678C>T-hiPSC-ECs and the healthy isogenic control behaved similarly in 2D culture, forming functionally indistinguishable vascular networks. However, when grown in 3D organ-on-chip devices under microfluidic flow, lumenized vessels formed in which defective vascular organisation was evident: interaction between inner endothelial cells (ECs) and surrounding pericytes was decreased and there was evidence for vascular leakage. Organs-on-Chip thus revealed features of HHT in hiPSC-derived blood vessels that were not evident in conventional 2D assays.

*This chapter is adapted from Stem Cell Reports. 12;17 (2022)*

*Valeria V. Orlova, Dennis M. Nahon, Amy Cochrane, Xu Cao, Christian Freund, Francijna van den Hil, Cornelius J.J. Westermann, Repke J. Snijder, Johannes Kristian Ploos van Amstel, Peter ten Dijke, Franck Lebrin, Hans-Jurgen Mager, Christine L. Mummery*

## Introduction

Hereditary haemorrhagic telangiectasia (HHT) is an inherited genetic disorder caused by autosomal dominant mutations in Endoglin (*ENG*, HHT1), Activin receptor like kinase-1 (*ACVRL1*, HHT2) or *SMAD4* (HHT3), genes that mediate signalling by transforming growth factor  $\beta$  (TGF $\beta$ ) and bone morphogenetic protein (BMP) in vascular endothelial cells (ECs)<sup>1</sup>. Phenotypically, HHT causes tortuous defects in blood vessels, particularly evident in the skin and mucous membranes, that are prone to haemorrhage (Govani and Shovlin, 2009). These abnormalities, called telangiectases, consist of enlarged and dilated capillaries that lack the pericyte/smooth muscle cell coverage of normal vessels. Studies in mice indicated that *ENG* deficiency can lead to abnormal endothelial-pericyte cell interactions caused by defective paracrine signaling by ECs lacking *ENG*<sup>2,3</sup>. More severe abnormalities, evident as arteriovenous malformations (AVMs) in the brain, lung, liver and gastrointestinal tract, can be fatal if haemorrhage occurs<sup>4</sup>. To date there are no therapies that prevent the formation of these abnormalities in HHT patients or reverse them once they have occurred. At most, current therapies, such as surgical intervention or cauterization of vessels to divert blood flow, ameliorate symptoms of the disease but are not cures<sup>5</sup>. Medical treatments under investigation include anti-angiogenic, anti-inflammatory and anti-fungal drugs such as humanized anti-vascular endothelial cells growth factor (VEGF) antibody (bevacizumab)<sup>6</sup>, thalidomide<sup>2</sup>, itraconazole<sup>7</sup> and other drugs (reviewed in<sup>8</sup>). Genetic models of HHT in mice, in which the genes responsible for the disease in humans are deleted, show clear vascular defects but they have not shed much light on the specific genotype/phenotype relationships in HHT patients<sup>9</sup>. Attempts to model HHT using primary umbilical vein endothelial cells (HUVECs) isolated from newborn HHT patients failed to recapitulate the phenotype<sup>10</sup>. Blood outgrowth endothelial cells (BOECs) or peripheral blood monocytes (PBMCs) from HHT patients could be alternative sources of cells to model HHT<sup>11-13</sup> but their poor proliferation *in vitro* makes them unsuitable as a renewable source of ECs for reproducibly modeling the disease in humans and for drug discovery.

In the present study we aimed to establish an efficient and scalable system that would recapitulate the formation of defective blood vessels in HHT patients, based on patient-derived induced pluripotent stem cells (HHT1-hiPSCs). We hypothesized that HHT1-hiPSCs might be useful for (i) identifying mechanisms underlying disease predisposition and modeling clinical features of HHT1 *in vitro*, and (ii) investigating defective endothelial-pericyte interactions.

## Results

### **HHT1-hiPSC-ECs reflect *ENG* haploinsufficiency with no apparent differences in functionality**

hiPSC lines were generated from somatic tissue from an HHT1 patient with a heterozygous

nonsense mutation in *ENG* (NM\_001114753.2 (*ENG*):c.1678C>T; p.(Gln560\*)), which causes *ENG* haploinsufficiency<sup>14</sup>. The patient was identified as being a genetic mosaic allowing generation of isogenic pairs of hiPSC lines, with and without the mutation (HHT1<sup>c.1678C>T</sup> and HHT1<sup>WT</sup>) (Figure S1A-C and unpublished). HHT1-hiPSC clones had normal karyotypes and were verified as pluripotent using standard methods (PluriTest, expression of pluripotency markers and spontaneous differentiation towards three germ cell lineages) (Figure S1D-G). HHT1-hiPSCs were then induced to differentiate to ECs<sup>15,16</sup>. Surface *ENG* (CD105) was significantly downregulated in HHT1<sup>c.1678C>T</sup>-hiPSC-ECs compared to HHT1<sup>WT</sup>-hiPSC-ECs (Figure 1A,B). By contrast, surface expression of other major EC markers such as vascular endothelial cadherin (VEC), platelet and endothelial adhesion molecule (CD31/PECAM1) and kinase insert domain receptor (KDR), also known as vascular endothelial growth factor receptor 2 (VEGFR2) was similar among lines (Figure 1B). *ENG* haploinsufficiency had no apparent effect on the proliferation of HHT1-hiPSC-ECs (Figure S2A). HHT1-hiPSC-ECs showed similar responses upon short-term stimulation with bone morphogenetic protein 9 (BMP9) and transforming growth factor- $\beta$  (TGF $\beta$ ), except that *ID1* expression was significantly upregulated in HHT1<sup>c.1678C>T</sup>-hiPSC-ECs after 2 hours of TGF $\beta$  treatment (Figure S2B).

Immunostaining showed comparable expression and localization of VEC, CD31 and intracellular von Willebrand Factor (vWF) (Figure 1C). Barrier function was assessed by real-time impedance spectroscopy (ECIS) in an integrated assay of electric wound healing for migration, as previously described<sup>17</sup>. Barrier function in 2D was similar in healthy and HHT1-hiPSC-ECs in “complete” EC growth medium (CGM) (Figure 1D,E) and migration rates identical (data not shown). Barrier function was increased in growth factor-free medium (1% platelet-poor plasma serum, PPS) (Figure S2C,D), in line with our previous findings (Halaidych et al., 2018). BMP9 addition reduced barrier function equally in healthy and HHT1<sup>c.1678C>T</sup>-hiPSC-ECs (Figure S2C,D). TGF $\beta$  addition significantly reduced barrier function in HHT1<sup>c.1678C>T</sup>-hiPSC-ECs but had no significant effect in HHT1<sup>WT</sup>-hiPSC-ECs (Figure S2C,D), which is also in line with the differences in responses in HHT1-hiPSC-ECs upon TGF $\beta$  treatment. Migration rates were similar in all conditions examined (Figure S2E).

Finally, the ability to form 2D vascular networks *in vitro* was examined, as described previously<sup>15-17</sup>. HHT1-hiPSC-ECs formed well-organized vascular networks when cultured with stromal cells and these were indistinguishable from healthy controls. Furthermore, stromal cells adjacent to ECs upregulated expression of the contractile smooth muscle cell marker SM22 (Figure 1F). Quantification of vascular networks formed by HHT1<sup>c.1678C>T</sup>-hiPSC-ECs and HHT1<sup>WT</sup>-hiPSC-ECs showed similar total vessel length and number of branches (Figure 1G), and well as total number of SOX17<sup>+</sup> ECs and number of adjacent SM22<sup>+</sup> cells (data not shown).

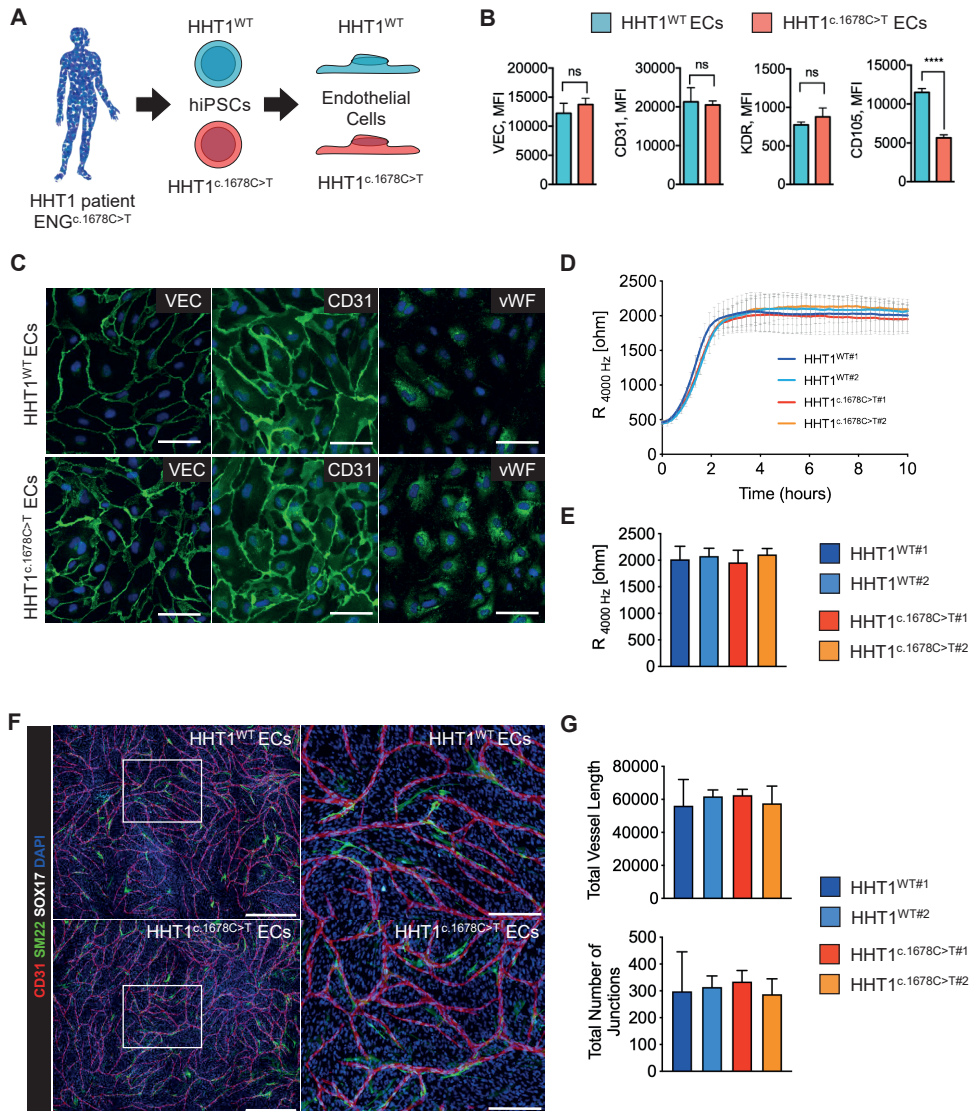


**Figure 1. Characterization of HHT1-hiPSC-ECs.**

A) Schematic overview of ECs differentiated from HHT1 patient-derived isogenic hiPSCs. B) FACS analysis of surface VEC, CD31, KDR and ENG (CD105) expression on isolated ECs (P2) from HHT1<sup>WT</sup> and HHT1<sup>c.1678C>T</sup> hiPSC lines. ECs differentiated from three independent hiPSC clones were analysed. Median fluorescent intensity values are shown. Error bars are  $\pm$ SD. Unpaired t-test. \*\*\*\*  $p < 0.001$ . C) Immunofluorescent analysis of EC markers VEC, CD31 and vWF on isolated ECs from HHT1 patient-derived isogenic hiPSCs (P2). Scale bar 75 $\mu$ m. D) Absolute resistance of the EC monolayer at 4000 Hz in complete EC growth medium (CGM). ECs differentiated from two independent hiPSC clones were analysed. Error bars are  $\pm$ SD of three to five independent biological experiments per clone. E) Quantification of absolute resistance values at 4000 Hz from D. Error bars are shown as  $\pm$ SD of five independent biological experiments. F) Representative immunofluorescent images of an *in vitro*

*vasculogenesis sprouting assay at day 10 of the co-culture of ECs differentiated from two independent clones of HHT1 patient-derived isogenic hiPSCs and CD31- cells differentiated from an independent control hiPSC line. ECs are stained with anti-CD31 (red) and anti-SOX17 (grey), contractile CD31- cells with anti-SM22 (green) and nuclei stained with DAPI (blue). Left panels: automatically stitched images (10x objective, 4 x 4 focus planes) are shown; scale bar represents 750 mm. Right panels: magnification of the framed area in the left panel, scale bar represents 250 mm. G) Quantification of EC sprouting network at day 10 of the co-culture. The total vessel length and total number of junctions are shown. Data are shown as  $\pm$ SD of three independent biological experiments.*

### **HHT1-hiPSC-ECs show defective vascular organization in 3D microfluidic chips**

The ability of HHT1-hiPSC-ECs to form microvascular networks in a 3D vessel-on-chip model (VoC) was then examined (Figure 2A). Primary human brain vascular pericytes (HBVPs) were used to support microvascular network formation, as described previously<sup>36</sup>. Vascular networks developed around day 2-3 of culture; lumenized microvessels were observed around day 5 (Figure S3A). Microfluidic chips were immunostained with antibodies against CD31/PECAM1 and an EC-specific transcription factor SOX17. The ability to form microvascular networks in microfluidic chips was compromised in HHT1<sup>c.1678C>T</sup>-hiPSC-ECs compared to HHT1<sup>WT</sup>-hiPSC-ECs (Figure 2B,C), despite similar initial seeding densities (Figure S3A). Quantification of microvascular networks showed reduced vascular density, the diameter of the vessels and number of ECs (SOX17+ nuclei), and an increase of the total length of the vessels of the networks formed by HHT1<sup>c.1678C>T</sup>-hiPSC-ECs (Figure 2C and S3C,D). HHT1<sup>WT</sup>-hiPSC-ECs from two independent hiPSC clones behaved similarly (Figure S3B). Furthermore, proliferation of HHT1<sup>c.1678C>T</sup>-hiPSC-ECs was lower than HHT1<sup>WT</sup>-hiPSC-ECs, as evidenced by fewer EdU positive nuclei (Figure S3E,F). To demonstrate that the microvascular networks formed by HHT1-hiPSC-ECs were hollow, fluorescent beads were perfused through the vessels (Supplementary video 1). Notably, the beads moved at a considerably lower rate in the microvascular networks formed by HHT1<sup>c.1678C>T</sup>-hiPSC-ECs compared to HHT1<sup>WT</sup>-hiPSC-ECs, indicating reduced flow through 3D vessels formed by HHT1<sup>c.1678C>T</sup>-hiPSC-ECs.

Junctional integrity was examined by immunostaining of the microvascular networks with VEC and ZO1 (Figure 2D,E). The results showed that although VEC junctional distribution was comparable, junctional distribution of ZO1 was reduced in the microvascular networks formed by HHT1<sup>c.1678C>T</sup>-hiPSC-ECs compared to HHT1<sup>WT</sup>-hiPSC-ECs.

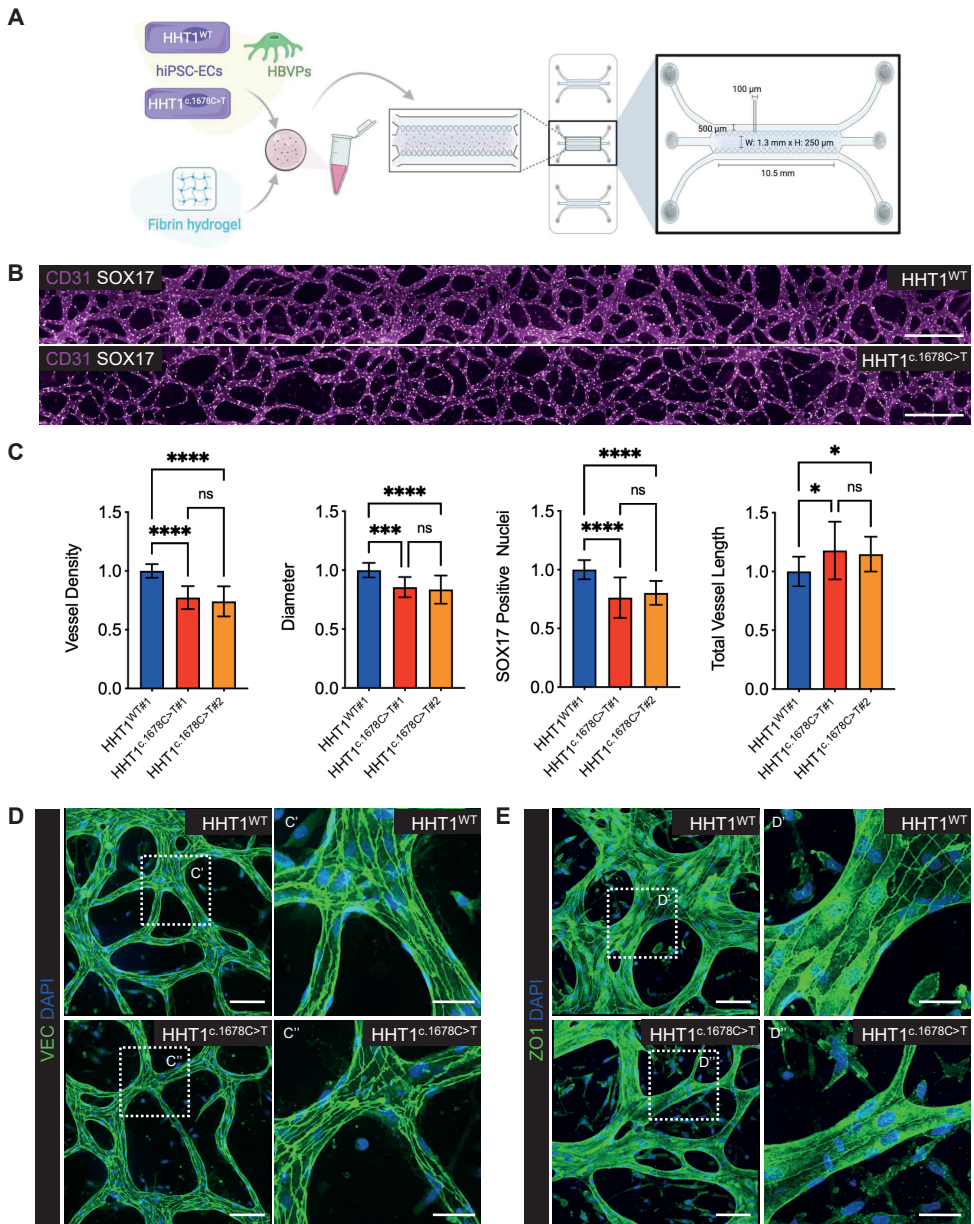


**Figure 2. HHT1-hiPSC-ECs show defective vascular organization in 3D microfluidic chips.**

A) Schematic showing generation of 3D vascular networks in microfluidic chips using hiPSC-ECs and HBVPs. B) Representative images of vascular networks formed by HHT1-hiPSC-ECs differentiated from HHT1<sup>WT</sup> and HHT1<sup>c.1678C>T</sup> hiPSC lines in microfluidic chips. ECs are stained with anti-CD31 (magenta) and anti-SOX17 (yellow). Scale bar represents 500  $\mu$ m. C) Quantification of HHT1-hiPSC-EC vascular network showing vessel density, diameter, number of HHT1-hiPSC-ECs (SOX17+ nuclei) and total vessel length. Data are shown as  $\pm$ SD, Unpaired t-test. \*\*\*\*  $p < 0.0001$ , \*\*\*  $p < 0.0005$ , \*  $p < 0.05$ , ns = not significant. Normalized values from independent experiments are shown. From  $N=3, n=9$ ; three independent experiments with three microfluidic channels per experiment (HHT1<sup>WT</sup>#1, HHT1<sup>c.1678C>T</sup>#1). From  $N=5, n=15$ ;

five independent experiments with three microfluidic channels per experiment (HHT<sup>WT#1</sup>, HHT<sup>c.1678C>T#2</sup>). (D-E) Representative confocal images showing VEC (D) and ZO1 (E). Nuclei are stained with DAPI (blue). Inserts are magnifications of framed areas to show VEC and ZO1 localization. Scale bar represents 100  $\mu\text{m}$  (left panels) and 40  $\mu\text{m}$  (right panels).

### **HHT1-hiPSC-ECs show defective EC-pericyte interaction**

We next analyzed the interaction between HHT1-hiPSC-ECs and HBVPs in the VoC model. Microfluidic chips were immunostained with antibodies against CD31/PECAM1 and the contractile smooth muscle cell marker SM22 (Figure 3A). Quantification of microvascular networks formed by HHT1<sup>c.1678C>T</sup>-hiPSC-ECs showed reduced pericyte coverage compared to HHT1<sup>WT</sup>-hiPSC-ECs (Figure 3B and S4A,B). HHT1<sup>c.1678C>T</sup>-hiPSC-ECs also showed increased pericyte distance from ECs when compared to HHT1<sup>WT</sup>-hiPSC-ECs (Figure 3C,D). Surface rendering of confocal images revealed that pericytes in vascular segments formed by HHT1<sup>c.1678C>T</sup>-hiPSC-ECs were positioned more distally from ECs compared to vascular segments formed by HHT1<sup>WT</sup>-hiPSC-ECs (Figure 3E,F). No significant differences were found in extracellular matrix (ECM) organization in microvascular networks formed by HHT1<sup>WT</sup>-hiPSC-ECs and HHT1<sup>c.1678C>T</sup>-hiPSC-ECs, as demonstrated by counterstaining with VEC and Collagen IV (COLIV) (Figure S4C,D,E).

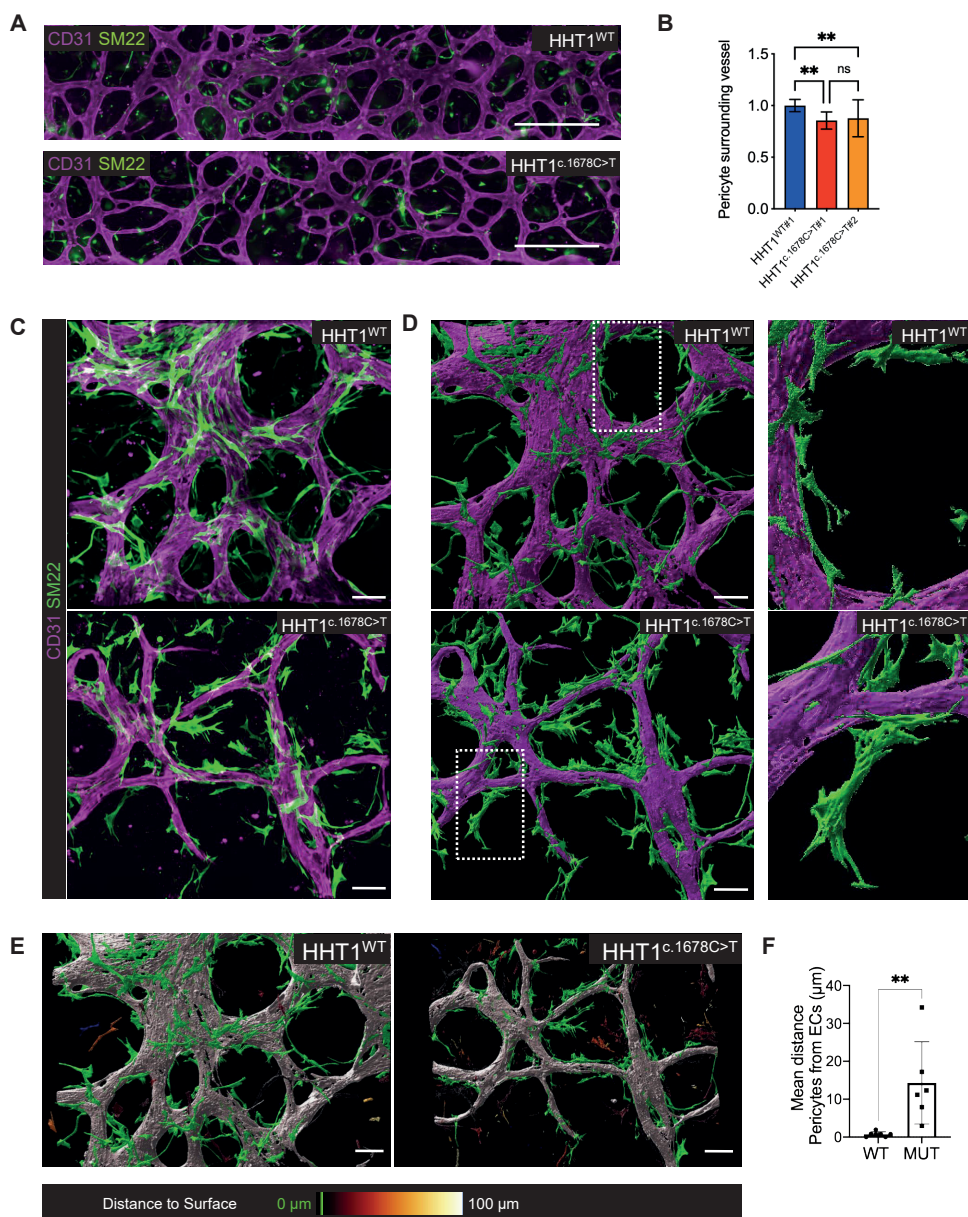


### Figure 3. HHT1-hiPSC-ECs show defective EC-pericyte cell interaction

A) Representative images of vascular networks formed by HHT1-hiPSC-ECs differentiated from HHT1<sup>WT</sup> and HHT1<sup>c.1678C>T</sup> hiPSC lines in microfluidic chips. ECs are stained with anti-CD31 (magenta) and anti-SM22 (green). Scale bar represents 500  $\mu$ m. B) Quantification of % pericytes surrounding vessel and average length of pericytes using CellProfiler. Normalized values from independent experiments are shown. From N=3, n=9; three independent experiments with three microfluidic channels per experiment (HHT1<sup>WT#1</sup>, HHT1<sup>c.1678C>T#1</sup>). From N=5, n=15; five independent experiments with three microfluidic channels per experiment (HHT1<sup>WT#1</sup>, HHT1<sup>c.1678C>T#2</sup>). Error bars are  $\pm$ SD, Unpaired t-test. \*\*

$p < 0.005$ . C) Representative spinning disk confocal images of vascular networks of HHT1-hiPSC-ECs differentiated from HHT1<sup>WT</sup> and HHT1<sup>c.1678C>T</sup> hiPSC lines and HBVPs in 3D microfluidic chips with hiPSC-EC (magenta; CD31) and HBVPs (green; SM22). Scale bar represents 100  $\mu\text{m}$ . D) Left panels: Surface rendering of images in B processed using IMARIS 9.5 software (Bitplane, Oxford Instruments). Scale bar represents 100  $\mu\text{m}$ . Right panels: magnification of the framed area in the left panel. E) Surface rendering images processed using Imaris 9.5 software (Bitplane, Oxford Instruments) from spinning disk confocal images showing vascular networks formed by HHT1-hiPSC-ECs (grey; CD31) differentiated from HHT1<sup>WT</sup> and HHT1<sup>c.1678C>T</sup> hiPSC lines in microfluidic chips. Color code for HBVPs showing green for objects touching the vessel and color scale representing distance from the vessel. Scale bar 30  $\mu\text{m}$ . F) Quantification of average distance of surface rendered SM22 cells to CD31 surface rendered objects using IMARIS 9.5 software (Bitplane, Oxford Instruments). From N=5, n=7 (WT) and n=6 (MUT); five independent experiments with one to three areas of each channel quantified. Error bars are  $\pm\text{SD}$ , Unpaired t-test. \*\*  $p < 0.01$ .

We next performed a fluorescent dextran leakage assay to test whether reduced EC-pericyte interaction cause the 3D vessels to be more fragile and prone to leak. Fluorescently labelled dextran (FITC-Dextran, 40 kDa) was added into the medium channel of the Organ-on-Chip device and real-time videos of vascular segments pre-stained using fluorescent agglutinin were made (Figure 4A and supplementary video 2). Quantification of permeability coefficient showed increased leakage of 3D vascular segments formed from HHT1<sup>c.1678C>T</sup>-hiPSC-ECs compared to HHT1<sup>WT</sup>-hiPSC-ECs (Figure 4B,C).

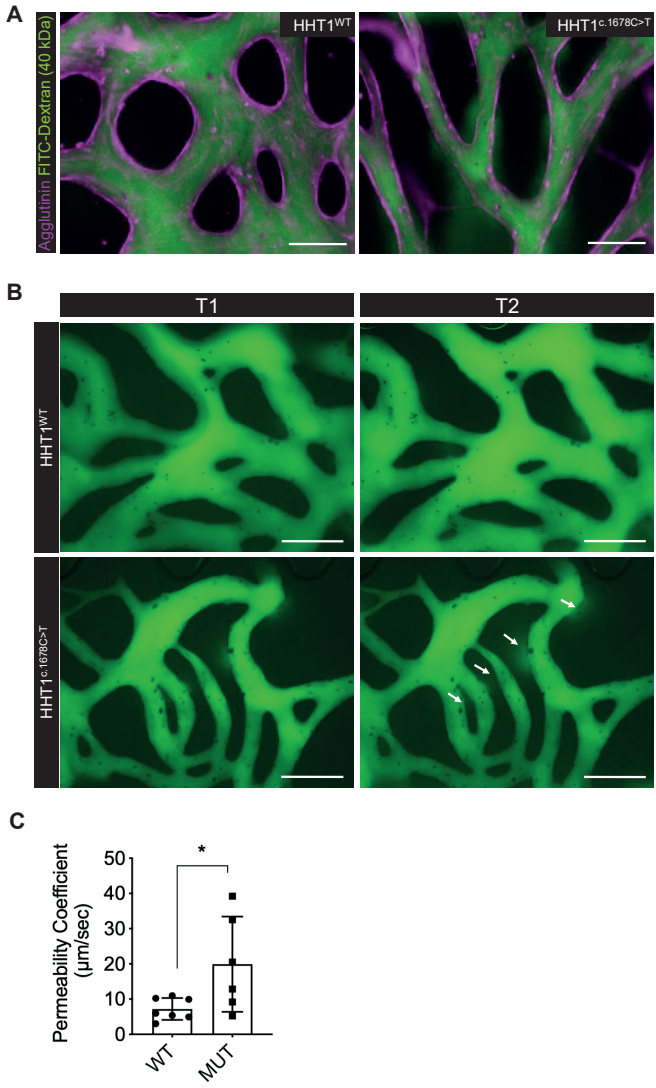


**Figure 4. HHT1-hiPSC-ECs form leaky vessels.**

A) Representative immunofluorescent images of vascular network formed by HHT1-hiPSC-ECs differentiated from HHT1<sup>WT</sup> and HHT1<sup>c.1678C>T</sup> hiPSC lines and HBVPs in 3D microfluidic chips with hiPSC-EC (magenta; Agglutinin) and Dextran (40 kDa, green). 10x (EVOS) scale bar 200 μm. B) Representative immunofluorescent images of vascular networks perfused with Dextran (40 kDa, green) at two different timepoints (T1=0 sec and T2=30 sec). White arrows show Dextran leakage in vascular network formed by HHT1<sup>c.1678C>T</sup> hiPSC-ECs. C) Quantification of permeability coefficient from N=3, n=7; three independent biological replicates with duplicate or triplicate microfluidic channels per experiment. Data are shown as ±SD, Unpaired t-test. \* p<0.05.

**Discussion**

In this study we developed a human *in vitro* model for the genetic vascular disorder HHT

using hiPSCs derived from patients with mutations in the *ENG* gene (HHT1). The results showed that we likely capture the direct effects of reduced ENG protein on the EC surface without compensation or adaptation mechanisms that normally occur *in vivo*, notably in mutant mice<sup>18</sup>. Thus, even though differences in vessels were observed, aspects of the HHT phenotype were masked although the poor EC-pericyte interaction was similar to that reported previously in *Eng*<sup>+/-</sup> mutant mice<sup>19</sup> would contribute to vessel instability and could cause the leaky 3D vascular network formed by HHT1<sup>c.1678C>T</sup>-hiPSC-ECs, in line with observations in patients.

The results in the HHT1-hiPSC-EC 2D model differ from earlier studies in which siRNA was used to knockdown *Eng* transiently in mouse embryonic ECs<sup>20</sup>. Complete *Eng* knockdown in mouse embryonic ECs resulted in reduced EC proliferation and TGFβ signalling in 2D assays. On the other hand, *ENG* haploinsufficiency had no effect on EC function in 2D, with proliferation, barrier function and sprouting angiogenesis in ECs derived from HHT1<sup>c.1678C>T</sup>-hiPSC clones indistinguishable from isogenic controls.

To establish HHT1-hiPSC-ECs VoC model, we used a commercially available microfluidic chip that supports formation of an interconnected microvascular network<sup>21-23</sup>. The model allows simultaneous analysis of both the early steps of the 3D vascular network formation, such as EC cell proliferation, migration, lumen formation, remodeling and pruning (regression), and end point analysis. This includes high-resolution microscopy for EC-pericyte interaction, perfusion studies and vascular leakage assays. Gravity-driven flow in these chips is sufficient for the maintenance of the vascular segments that are perfused with non-perfused vascular segments regressing overtime, similarly as observed *in vivo*<sup>24,25</sup>.

Overall, we found that HHT1<sup>c.1678C>T</sup>-hiPSC-ECs showed multiple similarities to *Eng*<sup>+/-</sup> mutant mice<sup>2,3,26</sup> although there were some differences. These included the formation of narrower vessels with fewer ECs by HHT1<sup>c.1678C>T</sup>-hiPSC-ECs than healthy controls. Furthermore, HHT1<sup>c.1678C>T</sup>-hiPSC-ECs showed reduced junctional localization of ZO1, although localization of VEC was comparable. This could be a result of reduced EC-matrix adhesion, which in turn could affect cell-cell junctions<sup>37</sup> and reduced perfusion and increased regression of vascular networks as described previously in *eng* mutant zebrafish<sup>38</sup>, resulting in reduced EC-pericyte interaction. However, the role of ENG in regulation of cell-to-cell and cell-to-matrix adhesion is beyond the scope of the present study. Thus, despite some shortcomings of the vessel-on-chip model in capturing the complete HHT patient phenotype, we believe the model is a valuable tool to investigate underlying causes of poor EC-pericyte interaction and identify drugs to reverse it and mediate vascular normalization.

Additional triggers of AVM formation include somatic mutations that reduce ENG function, local loss of ENG protein caused by inflammation and pro-angiogenic triggers<sup>9,27</sup>. Loss of ENG function in mutant mice was shown to induce defective migration against blood flow and EC enlargement which caused vessels to dilate<sup>28</sup>. This in turn results in higher hemodynamic forces and peripheral hypoxia that support the enlargement of AVMs<sup>29</sup>.

Our current model mainly addressed *ENG* haploinsufficiency due to *ENG* gene defects and lacked the additional triggers that cause *ENG* loss of function, such as exposure to pro-angiogenic stimuli and hemodynamic force. The particular advantage of using HHT patient-derived hiPSC lines is that they can be engineered to allow inducible *ENG* knockdown or degron-based *ENG* deletion. We expect that this, in combination with incorporation of pro-inflammatory triggers, such as pro-inflammatory macrophages, into the model will allow complete recapitulation of the phenotype in the future, such that these next generation models can be implemented in screening for new therapeutic interventions and drug discovery using mechanism-based approaches with opportunities for validation using ECs from patient-derived hiPSCs.

## Material and Methods

### HHT1 patient-derived hiPSC lines

Biopsies were taken with an informed consent at the St. Antonius Hospital, Nieuwegein, The Netherlands. The generation of the lines was approved by the Leiden University ethics committee under the P13.080 “Parapluprotocol: hiPSC. Patient samples, fibroblast from skin biopsy and erythroblast isolated from peripheral blood were used for reprogramming. Reprogramming with episomal vectors was done as described, except that a newer generation of vectors without *TP53* shRNA were used<sup>30</sup>. hiPSCs were routinely cultured on Matrigel (BD) in mTeSR1 and/or on Vitronectin XF in TeSR-E8 (all from Stem Cell Technologies) according to the manufacturer’s protocol. Standard characterization of hiPSCs was performed as described previously<sup>31–34</sup>. Karyotype analysis of undifferentiated cells was performed using combined binary ratio labelling-fluorescence in situ hybridization (COBRA-FISH)<sup>35</sup>, and pluripotency of the hiPSC clones was confirmed by PluriTest, immunofluorescent staining for OCT3/4, SSEA-4, NANOG and TRA-1-81 and spontaneous differentiation towards three germ lineages. Sample identity has been confirmed by analysis with the DNA analysis software GeneMarker V2.6.0 (SoftGenetics, State College, PA, USA) of fragments generated by the AmpFISTR® Profiler Plus PCR Amplification Kit (Applied Biosystems, Foster City, CA, USA) that have been run on a 3730 DNA Analyzer (Applied Biosystems). All tests were performed according to the instructions of the manufacturers.

### Statistics

One-way ANOVA, non-parametric Student’s t-test for unpaired measurements were applied as appropriate to test for differences in means between the groups. Detailed statistics are indicated in each figure legend. Data are expressed and plotted as the Mean ± SD. Statistical significance was indicated in each figure legend. Statistical analysis was performed with GraphPad Prism 9.0.2.

## Acknowledgements

The LUMC human iPSC Hotel generated and carried out initial characterization of hiPSC lines. The LUMC confocal imaging facility (Lennard Voortman, Annelies Boonzaier - van der Laan) are thanked for help with imaging; Karoly Szuhai and Danielle de Jong for help with COBRA-FISH; HHT patients for their contribution to research; Lucas Hawikels and Gonzalo Sánchez-Duffhues for discussion and Douwe Atsma for collecting patient samples. Illustrations created using Biorender.com.

This work was supported by the Netherlands Organization for Health Research and Development (ZonMw): PTO 446002501 in collaboration with CVON-PHAEDRA Impact; The Netherlands Organ-on-Chip Initiative is an NWO Gravitation project (024.003.001) funded by the Ministry of Education, culture and Science of the government of the Netherlands; European Research Council (ERCAdG 323182 STEMCARDIOVASC); the Association Maladie de Rendu-Osler (AMRO) and the Kees Westermann Fund; the European Union's Horizon 2020 research and innovation programme under the Marie Skłodowska Curie grant agreement No 707404.

### **Author contributions**

VVO: designed the research, established functional assays, performed experiments and wrote the manuscript; DMN, AC: performed experiments in 3D vascular chips, imaging and performed quantification; XC: performed EC differentiation; C.F.: performed reprogramming experiments; FEvdH: conducted EC differentiation and isolation, FACS; FL: assisted with quantification of microfluidic experiments; C.JJ.W., R.J.S., H.J.M. provided HHT patient samples; J.K. PvA: conducted genetic analysis; P.t.D. and F.L. helped analyse the data. CLM: designed the research and wrote the manuscript.

### **Declaration of Interests**

The authors declare no competing interests.

## References

1. Goumans, M.-J., Liu, Z. & Dijke, P. ten. TGF- $\beta$  signaling in vascular biology and dysfunction. *Cell Res* 19, 116–127 (2009).
2. Lebrin, F. *et al.* Thalidomide stimulates vessel maturation and reduces epistaxis in individuals with hereditary hemorrhagic telangiectasia. *Nature Medicine* 16, 420–428 (2010).
3. Carvalho, R. L. C. *et al.* Defective paracrine signalling by TGF $\beta$  in yolk sac vasculature of endoglin mutant mice: a paradigm for hereditary haemorrhagic telangiectasia. *Development* 131, 6237–6247 (2004).
4. Govani, F. S. & Shovlin, C. L. Hereditary haemorrhagic telangiectasia: a clinical and scientific review. *European Journal of Human Genetics* 17, 860–871 (2009).
5. Shovlin, C. L. Hereditary haemorrhagic telangiectasia: pathophysiology, diagnosis and treatment. *Blood reviews* 24, 203–219 (2010).
6. Dupuis-Girod, S. *et al.* Bevacizumab in Patients With Hereditary Hemorrhagic Telangiectasia and Severe Hepatic Vascular Malformations and High Cardiac Output. *Jama* 307, 948–955 (2012).
7. Kroon, S. *et al.* Oral itraconazole for epistaxis in hereditary hemorrhagic telangiectasia: a proof of concept study. *Angiogenesis* 1–8 (2020) doi:10.1007/s10456-020-09758-2.
8. Snodgrass, R. O., Chico, T. J. A. & Arthur, H. M. Hereditary Haemorrhagic Telangiectasia, an Inherited Vascular Disorder in Need of Improved Evidence-Based Pharmaceutical Interventions. *Genes-basel* 12, 174 (2021).
9. Tual-Chalot, S., Oh, S. P. & Arthur, H. M. Mouse models of hereditary hemorrhagic telangiectasia: recent advances and future challenges. *Frontiers in Genetics* 6, 25 (2015).
10. Chan, N. L. M. *et al.* Umbilical Vein and Placental Vessels from Newborns with Hereditary Haemorrhagic Telangiectasia Type 1 Genotype are Normal despite Reduced Expression of Endoglin. *Placenta* 25, 208–217 (2004).
11. Begbie, M. E., Wallace, G. M. F. & Shovlin, C. L. Hereditary haemorrhagic telangiectasia (Osler-Weber-Rendu syndrome): a view from the 21st century. *Postgraduate Medical Journal* 79, 18–24 (2003).
12. Fernandez-L, A. *et al.* Blood outgrowth endothelial cells from Hereditary Haemorrhagic Telangiectasia patients reveal abnormalities compatible with vascular lesions. *Cardiovascular Research* 68, 235–248 (2005).
13. Laake, L. W. van *et al.* Endoglin Has a Crucial Role in Blood Cell-Mediated Vascular Repair. *Circulation* 114, 2288–2297 (2006).
14. Letteboer, T. G. W. *et al.* Hereditary hemorrhagic telangiectasia: ENG and ALK-1 mutations in Dutch patients. *Human genetics* 116, 8–16 (2005).
15. Orlova, V. V. *et al.* Functionality of endothelial cells and pericytes from human pluripotent stem cells demonstrated in cultured vascular plexus and zebrafish xenografts. *Arteriosclerosis Thrombosis Vasc Biology* 34, 177–86 (2014).
16. Orlova, V. V. *et al.* Generation, expansion and functional analysis of endothelial cells and pericytes derived from human pluripotent stem cells. *Nat Protoc* 9, 1514–1531 (2014).
17. Halaidych, O. V. *et al.* Inflammatory Responses and Barrier Function of Endothelial Cells Derived from Human Induced Pluripotent Stem Cells. *Stem Cell Rep* 10, 1642–1656 (2018).
18. El-Brolosy, M. A. & Stainier, D. Y. R. Genetic compensation: A phenomenon in search of mechanisms. *PLOS Genetics* 13, e1006780-17 (2017).
19. Galaris, G., Thalgott, J. H. & Lebrin, F. P. G. Pericyte Biology in Disease. *Adv Exp Med Biol* 1147, 215–246 (2019).
20. Lebrin, F. *et al.* Endoglin promotes endothelial cell proliferation and TGF- $\beta$ /ALK1 signal transduction. *The EMBO Journal* 23, 4018–4028 (2004).
21. Shin, Y. *et al.* Microfluidic assay for simultaneous culture of multiple cell types on surfaces or within hydrogels. *Nature Protocols* 7, 1247–1259 (2012).
22. Campisi, M. *et al.* 3D self-organized microvascular model of the human blood-brain barrier with endothelial cells, pericytes and astrocytes. *Biomaterials* 180, 117–129 (2018).
23. Chen, M. B. *et al.* On-chip human microvasculature assay for visualization and quantification of tumor cell extravasation dynamics. *Nature Protocols* 12, 865–880 (2017).
24. Franco, C. A. *et al.* Dynamic Endothelial Cell Rearrangements Drive Developmental Vessel Regression. *Plos Biol* 13, e1002125 (2015).

25. Kochhan, E. *et al.* Blood Flow Changes Coincide with Cellular Rearrangements during Blood Vessel Pruning in Zebrafish Embryos. *Plos One* 8, e75060 (2013).
26. Arthur, H. M. *et al.* Endoglin, an Ancillary TGF $\beta$  Receptor, Is Required for Extraembryonic Angiogenesis and Plays a Key Role in Heart Development. *Developmental Biology* 217, 42–53 (2000).
27. Mahmoud, M. *et al.* Pathogenesis of arteriovenous malformations in the absence of endoglin. *Circulation Research* 106, 1425–1433 (2010).
28. Sugden, W. W. *et al.* Endoglin controls blood vessel diameter through endothelial cell shape changes in response to haemodynamic cues. *Nature Cell Biology* 19, 653–665 (2017).
29. Sugden, W. W. & Siekmann, A. F. Endothelial cell biology of Endoglin in hereditary hemorrhagic telangiectasia. *Current Opinion in Hematology* 25, 1–8 (2018).
30. Okita, K. *et al.* A more efficient method to generate integration-free human iPSCs. *Nature Methods* 8, 409–412 (2011).
31. Dambrot, C. *et al.* Polycistronic lentivirus induced pluripotent stem cells from skin biopsies after long term storage, blood outgrowth endothelial cells and cells from milk teeth. *Differentiation; research in biological diversity* 85, 101–109 (2013).
32. Bouma, M. J. *et al.* Differentiation-Defective Human Induced Pluripotent Stem Cells Reveal Strengths and Limitations of the Teratoma Assay and In Vitro Pluripotency Assays. *STEMCR* 8, 1340–1353 (2017).
33. Freund, C., Davis, R. P., Gkatzis, K., Oostwaard, D. W. & Mummery, C. L. The first reported generation of human induced pluripotent stem cells (iPS cells) and iPS cell-derived cardiomyocytes in the Netherlands. *Netherlands heart journal : monthly journal of the Netherlands Society of Cardiology and the Netherlands Heart Foundation* 18, 51–54 (2010).
34. Bouma, M. J. *et al.* Generation and genetic repair of 2 iPSC clones from a patient bearing a heterozygous c.1120del18 mutation in the ACVRL1 gene leading to Hereditary Hemorrhagic Telangiectasia (HHT) type 2. *Stem Cell Res* 46, 101786 (2020).
35. Szuhai, K. & Tanke, H. J. COBRA: combined binary ratio labeling of nucleic-acid probes for multi-color fluorescence in situ hybridization karyotyping. *Nature Protocols* 1, 264–275 (2006).
36. Vila Cuenca, M., Cochrane, A., Hil, F.E. van den, Vries, A.A.F. de, Oberstein, S.A.J.L., Mummery, C.L., and Orlova, V.V. (2021). Engineered 3D vessel-on-chip using hiPSC-derived endothelial- and vascular smooth muscle cells. *Stem Cell Rep.* 16, 2159–2168.
37. Yamamoto, H., Ehling, M., Kato, K., Kanai, K., Lessen, M. van, Frye, M., Zeuschner, D., Nakayama, M., Vestweber, D., and Adams, R.H. (2015). Integrin b1 controls VE-cadherin localization and blood vessel stability. *Nat. Commun.* 6, 6429
38. Sugden, W.W., Meissner, R., Aegerter-Wilmsen, T., Tsaryk, R., Leonard, E.V., Busmann, J., Hamm, M.J., Herzog, W., Jin, Y., Jakobsson, L., *et al.* (2017). Endoglin controls blood vessel diameter through endothelial cell shape changes in response to haemodynamic cues. *Nat. Cell Biol.* 19, 653–665.

## Supplementary Material

### Contents

#### Supplemental Figures and Legends:

**Figure S1. Related to Figure 1.** Characterization of HHT1 patient-derived hiPSCs.

**Figure S2. Related to Figure 1.** Characterization of HHT1-hiPSC-ECs.

**Figure S3. Related to Figure 2.** HHT1-hiPSC-ECs show defective vascular organization in VoC.

**Figure S4. Related to Figure 3.** HHT1-hiPSC-ECs show defective EC-pericyte cell interaction in VoC.

#### Supplemental Tables:

**Supplemental Table 1.** List of FACS antibodies.

**Supplemental Table 2.** List of antibodies for IF.

#### Supplemental Videos:

**Supplemental Video 1.** Perfusion of fluorescent beads in 3D vessels formed by HHT1<sup>WT</sup>-hiPSC-ECs and HHT1<sup>c.1678C>T</sup>-hiPSC-ECs. Related to Figure 2.

**Supplemental Video 2.** Perfusion of FITC-Dextran (40 kDa) in 3D vessels formed by HHT1<sup>WT</sup>-hiPSC-ECs and HHT1<sup>c.1678C>T</sup>-hiPSC-ECs. Related to Figure 4.

#### Supplemental Experimental Procedures

#### Supplemental References

## Supplementary Figure 1

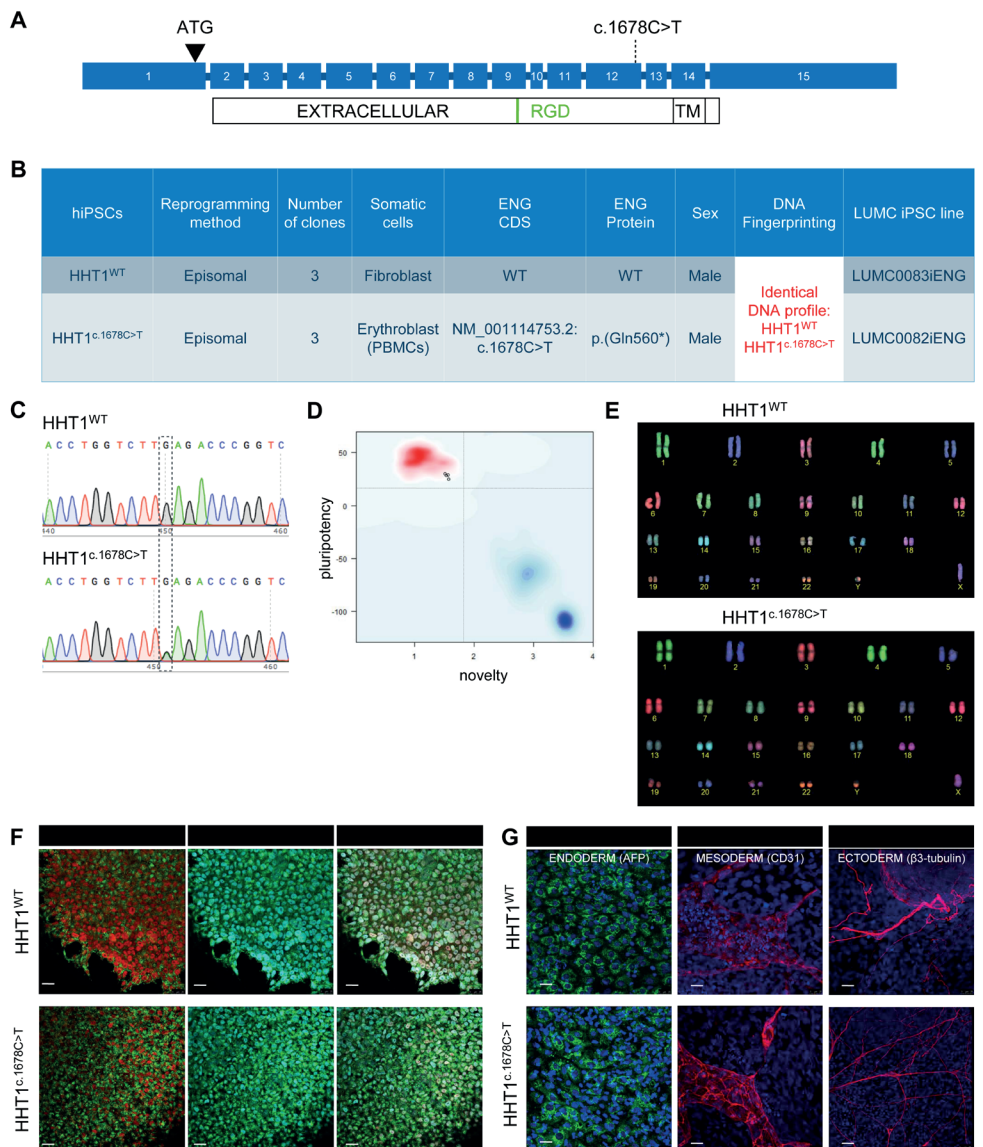


**Figure S1. Related to Figure 1. Characterization of HHT1 patient-derived hiPSCs.**

A) Schematic overview of *ENG* genomic map, protein map and location of the mutation. B) Overview of HHT-hiPSC lines. C) Sanger sequencing of the genomic DNA from HHT1 patient-derived hiPSC lines to confirm the mutation. D) Bioinformatic assessment of pluripotency of HHT1 patient-derived hiPSCs (PluriTest): two clones per hiPSC line (HHT1<sup>WT</sup> and HHT1<sup>c.1678C>T</sup>

hiPSCs) were analyzed. E) COBRA-FISH analysis of karyotype of HHT1 patient-derived hiPSCs. F) Immunofluorescent images of expression of pluripotency markers: OCT3/4, SSEA4 and Nanog. Scale bar 25  $\mu\text{m}$ . G) Immunofluorescent images of the spontaneous differentiation demonstrating derivatives of all three germ layers:  $\beta$ III-tubulin for neuroectoderm, CD31 for mesoderm, AFP for endoderm. Scale bar 25 $\mu\text{m}$ .

## Supplementary Figure 2

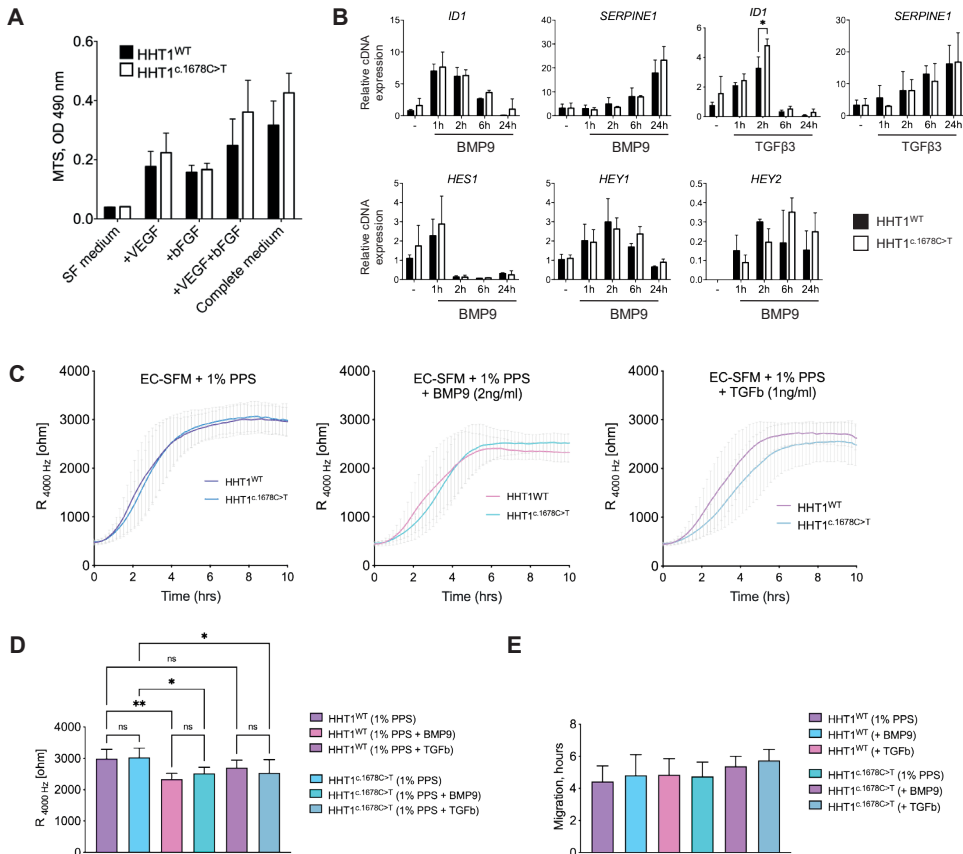


**Figure S2. Related to Figure 1. Characterization of HHT1-hiPSC-ECs.**

A) Assessment of EC proliferation in serum-free medium (SF medium), SF medium + VEGF (+VEGF), SF medium + bFGF (+bFGF), SF medium VEGF + bFGF (+VEGF+bFGF) or complete EC growth medium (Complete medium) at 72h after medium change. The analysis was performed on ECs differentiated from three independent clones of HHT1 patient-derived isogenic hiPSCs. Error bars are  $\pm$ SD. B) Gene expression analysis of expression of *ID1*, *SERPINE1*, *HES1*, *HEY1* and *HEY2* (upon BMP9 1ng/ml stimulation) and *ID1*, *SERPINE1* (upon TGF $\beta$  1ng/ml stimulation). ECs differentiated from two independent hiPSC clones were analyzed. Data are shown  $\pm$ SD from three independent experiments. One-way ANOVA. \* $p < 0.05$  C) Absolute resistance of the EC monolayer at 4000 Hz in growth factor-free medium supplemented with 1% PPS (1% PPS), or 1% PPS supplemented with BMP9 (2 ng/ml)(+ BMP9) or 1% PPS supplemented with TGF $\beta$  (1 ng/ml)(+ TGF $\beta$ ) is shown. ECs differentiated from two independent hiPSC clones were analysed. Error bars are  $\pm$ SD of six independent biological experiments. D) Quantification of absolute resistance values at 4000 Hz from C.

Error bars are shown as  $\pm$ SD of five independent biological experiments. E) Quantification of migration rates. Error bars are shown as  $\pm$ SD of six independent biological experiments. One-way ANOVA. \*\* $p < 0.01$ , \* $p < 0.05$ .

### Supplementary Figure 3

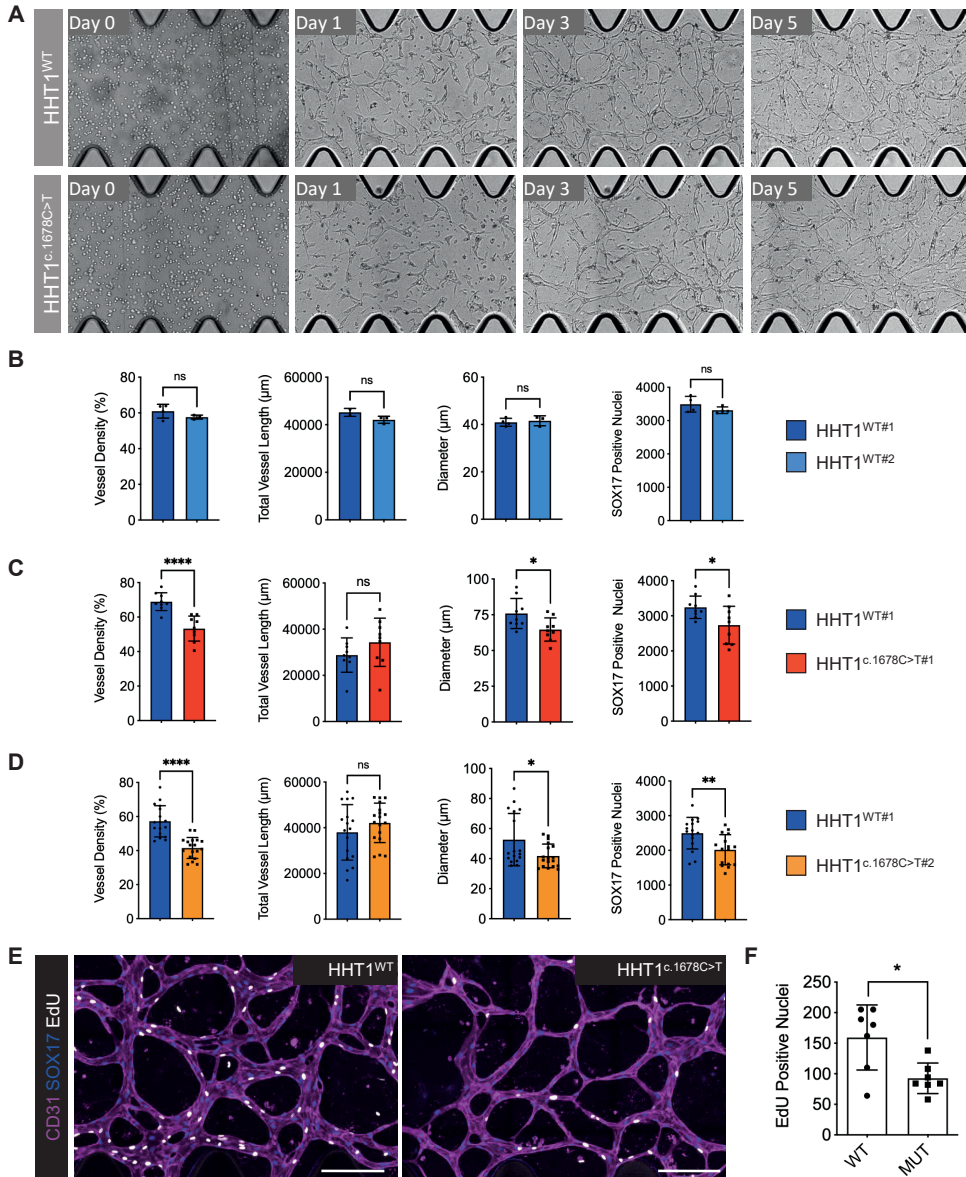


**Figure S3. Related to Figure 2. HHT1-hiPSC-ECs show defective vascular organization in VoC.**

A) Representative images of microfluidic chips seeded with ECs from HHT1 patient-derived isogenic hiPSCs. Images were taken every 24h from day 0 (after seeding) till day 5. B) Quantification of HHT1-hiPSC-EC vascular network showing vessel density (%), total vessel length (μm), diameter (μm) and number of HHT1-hiPSC-ECs (SOX17+ nuclei). Data

are shown as  $\pm$ SD, Unpaired t-test. ns = not significant. From N=1, n=3; one independent biological experiment with three microfluidic channels. (C,D) Quantification of HHT1-hiPSC-EC vascular network showing vessel density (%), total vessel length ( $\mu$ m), diameter ( $\mu$ m) and number of HHT1-hiPSC-ECs (SOX17+ nuclei). Data are shown as  $\pm$ SD, Unpaired t-test. \*\*\*\*  $p < 0.001$ , \* $p < 0.05$ , ns = not significant. From N=3, n=9; three independent biological experiments with three microfluidic channels per experiment (C). From N=5, n=15; five independent biological experiments (with three microfluidic channels per experiment (D). E) Representative images showing proliferative (EdU positive) (white) HHT1-hiPSC-ECs differentiated from HHT1<sup>WT</sup> and HHT1<sup>c.1678C>T</sup> hiPSC lines and HBVPs in 3D microfluidic chips. Scale bar represents 200  $\mu$ m. F) Quantification of proliferative (EdU positive) HHT1-hiPSC-ECs in 3D vascular network in the microfluidic chip. Error bars are  $\pm$ SD of four microfluidic cultures (one independent biological experiment). Unpaired t-test. \*  $p < 0.05$ .

## Supplementary Figure 4

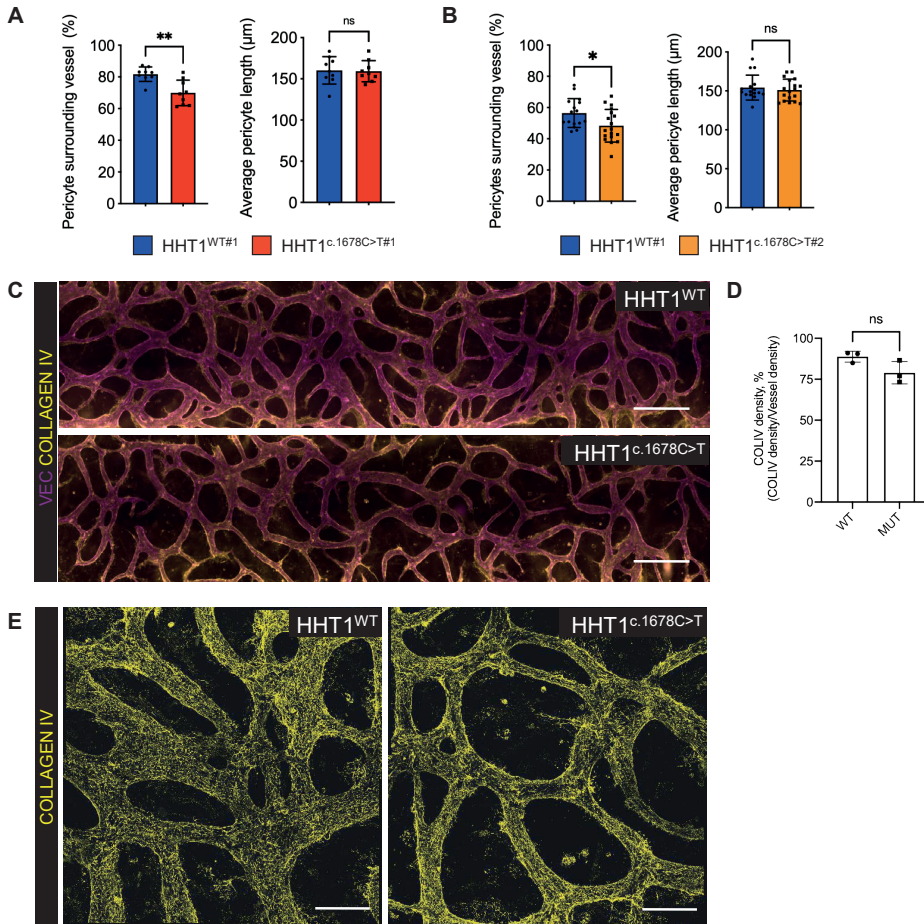


**Figure S4. Related to Figure 3. HHT1-hiPSC-ECs show defective EC-pericyte cell interaction in VoC.**

(A, B) Quantification of % pericytes surrounding vessel and average length of pericytes using CellProfiler. From N=3, n=9; three independent biological experiments with mean from triplicate microfluidic channels per experiment (A). From N=5, n=15; five independent biological experiments with mean from triplicate microfluidic channels per experiment (B). Error bars are  $\pm$ SD, Unpaired t-test. \*  $p < 0.05$ . C) Representative images of vascular networks formed by HHT1-hiPSC-ECs differentiated from HHT1<sup>WT</sup> and HHT1<sup>c.1678C>T</sup> hiPSC lines in microfluidic chips. ECs are stained with anti-VEC (magenta) and anti-COLIV (yellow). Scale bar represents 500  $\mu$ m. D) Quantification of collagen IV density (%). Data are shown as  $\pm$ SD from N=1, n = 3; one independent biological experiment, three microfluidic channels. Unpaired t-test. ns = not significant. E) Representative spinning disk confocal images showing HHT1-hiPSC-EC vascular network stained for ECM (yellow; COLLAGEN IV). Scale bar 30  $\mu$ m.

## Supplemental Tables

**Supplemental Table 1. List of FACS antibodies**

Antibody	Fluorochrome	Source	Dilution	Catalog #
VE-Cadherin	A488	eBiosciences	1:50	53-1449-42
CD31	APC	eBiosciences	1:100	17-0319-42
KDR	PE	R&D systems	1:20	FAB357P
ENG	VioBlue	Miltenyi Biotec	1:20	130-099-666
ENG	PE-Vio-770	Miltenyi Biotec	1:20	130-099-889

**Supplemental Table 2. List of antibodies for IF**

Antibody	Species	Source	Dilution	Catalog #
SSEA-4	Mouse	Biolegend	1:30	330402
Nanog	Mouse	Santa Cruz	1:150	sc-293121
OCT3/4	Mouse	Santa Cruz	1:100	sc-5279
AFP	Rabbit	Quartett	1:25	2011200530
CD31	Mouse	Dako	1:200	M0823
βIII-tubulin	Mouse	Covance	1:4000	MMS-435P
VEC	Rabbit	CellSignaling	1:200	2158S
vWF	Rabbit	Dako	1:200	A0082
SOX17	Goat	R&D systems	1:200	AF1924
SM22	Rabbit	Abcam	1:200	AB14106
Collagen IV	Goat	Sigma	1:200	AB769
Laminin	Rabbit	Merck	1:100	AB19012
Alexa Fluor 488	Mouse IgG	Invitrogen	1:500	A11001
Alexa Fluor 568	Mouse IgM	Invitrogen	1:200	A21043
Alexa Fluor 488	Mouse IgG3	Invitrogen	1:250	A21151
Alexa Fluor 568	Mouse IgG1	Invitrogen	1:250	A21124
Alexa Fluor 647	Mouse IgG2b	Invitrogen	1:250	A21242
Alexa Fluor 568	Mouse IgG	Invitrogen	1:500	A11031
Alexa Fluor 488	Rabbit IgG	Invitrogen	1:500	A21206

## Supplemental Experimental Procedures

### Sanger sequencing

*ENG* mutations were confirmed by Sanger sequencing. DNA was extracted using the Genra Puregene Cell Kit (QIAGEN) according to the manufacturer's protocol. PCR was performed to amplify *ENG* exon 12 (FW: CCAGAGTCAGGAGGGAGACA; RV: GCGTCCAGGATAGATTGCCT, Product size: 974 bp). The PCR products were purified using the QIAquick PCR Purification Kit and were send for Sanger sequencing (BaseClear).

### Differentiation of hiPSC-ECs

hiPSC differentiation towards endothelial cells and CD31 magnetic bead isolation were performed as described previously<sup>1-3</sup>. Briefly, hiPSCs were passaged in normal culture conditions one day before inducing differentiation. Mesoderm differentiation was induced by changing the media to B(P)EL with a high concentration CHIR99021 (8  $\mu$ M). At day 3, 6 and 9 of differentiation the cells were refreshed with B(P)EL with VEGF (50 ng/ml) and SB43152 (10  $\mu$ M, Tocris). ECs were purified with CD31 coupled magnetic beads at day 10 (Life Technologies) and the culture was further scaled up on 0,1% gelatin coated tissue culture flasks in human endothelial serum free media (EC-SFM)(Life Technologies) with additional VEGF (30 ng/ml), bFGF (20 ng/ml, R&D) and 1% platelet poor serum (PPS) (Hycultec). Functional assays were performed on cells between passages 2-3.

### FACS analysis of hiPSC-ECs

FACS analysis was performed as described previously<sup>1-3</sup>. Purified hiPSC-ECs were dissociated with TrypLE Select (Life Technologies). Combinations of the following antibodies were used in flow cytometry experiments (see supplemental table 1): VE-Cadherin-A488 (1:50, eBiosciences), CD31-APC (1:100, eBiosciences), KDR-PE (1:20, R&D Systems), *ENG*-VioBlue or PE-Vio-770 (1:20, Milteny Biotec). Samples were analysed either on LSRII (BD) with the following instrument setup: Blue/488 FITC, A488: 505LP-530/30, PerCP-Cy5.5: 630LP-670/14; Yellow/561 PE: 570LP-582/15, APC: 635LP-660/20; or on MACSQuant VYB (Miltenyi) with the following instrument setup: Blue/488 FITC, A488: 525/50; Yellow/561 PE: 586/15, APC: 661/20, APC-Cy7: 750LP.

### Immunofluorescent staining of hiPSC-ECs

Immunofluorescent staining was performed as described previously<sup>1-3</sup>. Briefly, ECs were seeded on FN-coated 96-well black imaging plates (Corning) at the seeding density  $\sim$ 10,000cells/well in complete EC growth culture medium (EC-SFM supplemented with VEGF 30 ng/ml, bFGF 20 ng/ml and 1% PPS). 48h post-seeding ECs were fixed with 4% paraformaldehyde (PFA, Sigma), permeabilized with the 0.1%TX-100 and stained with anti-CD31 (1:200, Dako) and anti-vWF (1:200, Dako) or VEC (CellSignaling)(supplemental table 2).

High magnification images were acquired with the WLL1 confocal microscope (Leica), using 40x DRY objective.

### **Endothelial cell proliferation (MTS assay)**

hiPSC-ECs were seeded into on FN-coated 96-well plates at the seeding density 2,000 cells/well in EC-SFM for 12 h and subsequently refreshed with EC-SFM containing various stimuli. After 4 days the MTS assay (CellTiter, Promega) was used to determine the relative number of ECs.

### **Assessment of hiPSC-ECs functionality in an in vitro vasculogenesis assay**

The co-culture experiments with hiPSC-ECs or primary ECs and stromal cells were performed as described previously<sup>1-3</sup>. The co-cultures were stopped at day 10 and post-fixed and stained with anti-CD31 (1:200, Dako) and anti-SOX17 (1:200, R&D), and anti-SM22 (1:200, Abcam) antibodies (supplemental table 2). The co-cultures were imaged with the EVOS FL AUTO2 Imaging system (ThermoFischer Scientific) with the 10X Objective for quantifications with autofocus on CD31, and auto stitching 4X4 focus planes or 20X Objective for CD31 and SOX17 images. The co-cultures were quantified using publicly available software AngioTool<sup>4</sup>.

### **Endothelial barrier function analysis**

Endothelial barrier function was measured using impedance-based cell monitoring with an electric cell-substrate impedance sensing system (ECIS Z $\theta$ , Applied Biophysics), as described previously<sup>1</sup>. hiPSC-ECs were seeded on FN-coated ECIS arrays each containing 8 wells with 10 gold electrodes per well (8W10E PET, Applied Biophysics). The cell seeding density was estimated  $\sim$ 50,000cells/cm<sup>2</sup>. For barrier function and migration studies the cells were seeded for at least 24h in complete EC growth medium followed by 6h serum starvation step in EC-SFM. For the assessment of cell migration after serum starvation, the medium was changed to complete EC growth medium or EC-SFM supplemented with 1% PPS, BMP9 (2ng/ml) and TGF $\beta$ 3 (1ng/ml), and electric wound (10 sec pulse of 5V at 60 kHz) was applied to the cells 1h after medium change. Recovery of the barrier was monitored in real time over 6-12h. Multiple frequency/time (MFT) mode was used for the real-time assessment of the barrier and monolayer confluence.

### **Generation of perfused vascular networks in microfluidic chips**

Vascular networks were generated as described previously<sup>5</sup> with some adjustments that were developed during optimization of the protocol with hiPSC-ECs and primary human brain vascular pericytes (HBVPs)(ScienceCell), and microfluidic chips with one gel channel and two media channels (AIM Biotech). Cells were resuspended in EGM-2 supplemented with thrombin (4 U/ml) at 10x10<sup>6</sup> cells/ml for hiPSC-ECs and 0.5x10<sup>6</sup> cells/ml for HBVPs or 2x10<sup>6</sup> cells/ml for HBVPs (note: higher HBVP numbers promote vessel formation, although

earlier experiments were conducted with a lower number of HBVPs with comparable results). The cell suspension was mixed with an equal volume of fibrinogen solution (10 mg/ml; final concentration 5 mg/ml) and injected into the gel channel of the microfluidic chip; this was left for 15 min at room temperature (RT) to allow fibrin gel to form. EGM-2 supplemented with VEGF (50 ng/ml) was added to each of the flanking media channels. Interstitial flow through the gel was achieved by adding a larger volume of medium to one of the media inlets, generating a pressure gradient. The microfluidic chips were refreshed every 24 hours with EGM-2 supplemented with VEGF (50 ng/ml) and  $\gamma$ -secretase inhibitor N-[N-(3,5-difluorophenacetyl)-l-alanyl]-s-phenylglycine-butyl ester (DAPT, 10  $\mu$ M) (DAPT supplementation was performed on day 1 for 24 hours). For immunofluorescent staining, 3D cultures were fixed with 4% paraformaldehyde (PFA; Sigma) for 20 min at RT, permeabilized with 0.5% TX-100 for 15 min at RT and blocked with 3% bovine serum albumin (BSA) in PBS for 3 hours at RT. Samples were stained by anti-CD31 (1:200, Dako), anti-SOX17 (1:200, R&D), and anti-SM22 (1:200, Abcam). Details of antibodies are given in supplemental table 2. Primary antibodies were prepared in 2% BSA and incubated overnight at 4°C and secondary antibodies were prepared in 2% BSA and incubated for 2 hours at RT. Fluorescence images for quantification were acquired using EVOS AUTO2 using 10x magnification objective and high magnification images were acquired with a DragonFly spinning disk (Andor) microscope using 40x magnification objective post-processing, performed and processed using Imaris 9.5 software (Bitplane, Oxford Instruments).

### **EdU assay for EC proliferation in 3D microfluidic chips**

Proliferation was measured using an EdU Click-iT kit Alexa-488 (ThermoFisher Scientific #C10337) according to manufacturer's protocol. Briefly, on day 6 of culture, microfluidic chips were refreshed with EGM-2 (VEGF 50 ng/ml and DAPT 10  $\mu$ M) additionally supplemented with EdU (1:1000) for 8 hours. Cells were fixed with 4% PFA for 30 minutes, permeabilized with 0.5% TX-100 for 15 minutes at RT. Freshly prepared Click-iT reaction cocktail was added for 30 minutes at RT. Microfluidic chips were washed twice with 3% BSA-PBS and blocked in 3% BSA-PBS for 1-2 hours at RT, followed by co-staining with primary and secondary antibodies.

### **Quantification of 3D vessels in microfluidic chips**

Microfluidic chips were imaged with the EVOS FL AUTO2 or M7000 Imaging system (ThermoFisher Scientific) using the 10X Objective with autofocus either on the cells in phase-contrast mode (for time series experiments) or on CD31 for fixed samples, and automatic image stitching to cover the entire gel channel for quantification of microvascular networks. Parameters were quantified using pipelines developed on the free open source CellProfiler software (<https://cellprofiler.org/>)<sup>6</sup>. Briefly, for EC nuclei number, pre-processing steps were used to enhance image features and filter non-specific object identification. A Gaussian

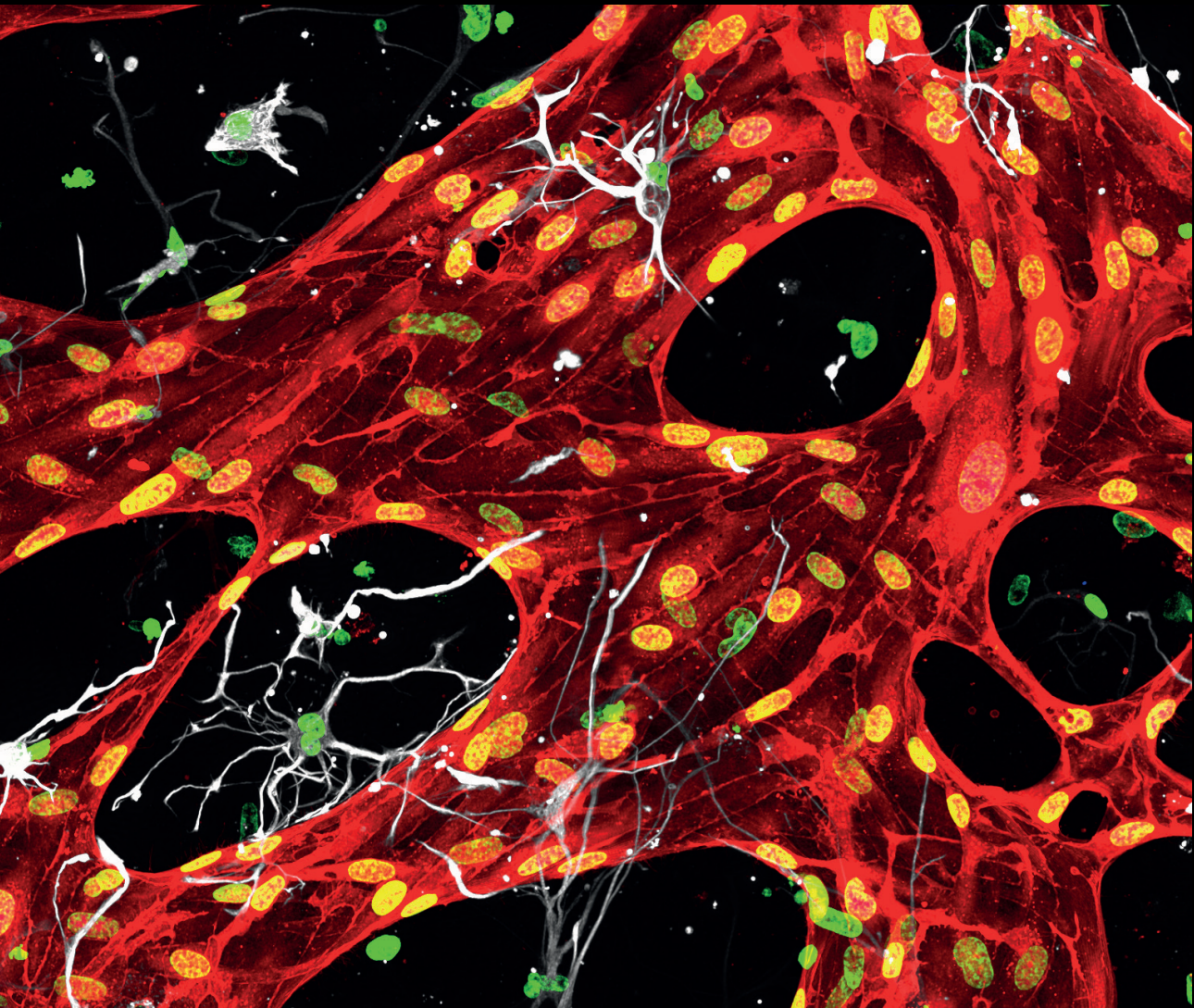
filter was applied to mural cell images before object identification was used to measure object morphology and interaction with hiPSC-EC network. Filter steps were applied to images of vascular network to reduce non-specific segmentation from cell junction staining and a minimum cross-entropy thresholding method was used to produce a binarized image. The binarized images from the CellProfiler output were then analysed using freely available ImageJ software with the plugin (<https://imagej.nih.gov/ij/>, <https://imagej.net/DiameterJ>)<sup>7</sup>. For ECM quantification, binarized vessel images were used as masks to ensure Collagen IV staining intensity was quantified only at the vessel regions excluding any background noise. The number of EdU and SOX17 positive nuclei were quantified with a custom-made pipeline in CellProfiler<sup>6</sup>. Additional quantification of the distance between SM22- and CD31 positive cells was obtained using Imaris 9.5 software (Bitplane, Oxford Instruments).

### **Perfusion assessment in vessels in microfluidic chips**

For perfusion assessment, the chip was placed on day 6 in the EVOS AUTO2 with on stage incubator for time-lapse image acquisition. First, basal fluorescence activity was captured before the addition of fluorescent tracers. Next, 70  $\mu$ l of 40KDa FITC-Dextran (1:1000, Sigma) or 405-beads (1:10, Fluoro-Max Dyed Blue Aqueous Fluorescent Particles, B0200, ThermoFisher Scientific) in EGM-2 was added to one medium port and 50  $\mu$ l of EGM-2 to all other media ports to induce interstitial gravity flow. Then, images were captured simultaneously at 20 fps using a 10x magnification objective for 30 seconds. For quantification of permeability coefficient, images acquired at T1 (time 0 seconds) and T2 (30 seconds of perfusion) were quantified using pipelines developed with CellProfiler<sup>6</sup>. Briefly, a mask for vessel area inside image acquired was created to ensure intensity was measured in area outside the vessel wall only. Calculation for permeability coefficient was based on the previously established method<sup>8</sup>.

## Supplemental References

1. Halaidych, O. V. *et al.* Inflammatory Responses and Barrier Function of Endothelial Cells Derived from Human Induced Pluripotent Stem Cells. *Stem Cell Rep* **10**, 1642–1656 (2018).
2. Orlova, V. V. *et al.* Functionality of endothelial cells and pericytes from human pluripotent stem cells demonstrated in cultured vascular plexus and zebrafish xenografts. *Arteriosclerosis Thrombosis Vasc Biology* **34**, 177–86 (2014).
3. Orlova, V. V. *et al.* Generation, expansion and functional analysis of endothelial cells and pericytes derived from human pluripotent stem cells. *Nat Protoc* **9**, 1514–1531 (2014).
4. Zudaire, E., Gambardella, L., Kurcz, C. & Vermeren, S. A Computational Tool for Quantitative Analysis of Vascular Networks. *PLoS ONE* **6**, e27385-12 (2011).
5. Chen, M. B. *et al.* On-chip human microvasculature assay for visualization and quantification of tumor cell extravasation dynamics. *Nature Protocols* **12**, 865–880 (2017).
6. Carpenter, A. E. *et al.* CellProfiler: image analysis software for identifying and quantifying cell phenotypes. *Genome Biology* **7**, R100 (2006).
7. Hotaling, N. A., Bharti, K., Kriel, H. & Simon, C. G. DiameterJ: A validated open source nanofiber diameter measurement tool. *Biomaterials* **61**, 327–338 (2015).
8. Campisi, M. *et al.* 3D self-organized microvascular model of the human blood-brain barrier with endothelial cells, pericytes and astrocytes. *Biomaterials* **180**, 117–129 (2018).



# Chapter 6

## Self-assembling 3D vessel-on-chip model with hiPSC-derived astrocytes

### Abstract

Precisely regulated crosstalk between endothelial cells (ECs), pericytes and astrocytes is essential to the development and stability of the blood-brain-barrier (BBB) so that it can regulate transport of molecules in- and out of the central nervous system. There are currently few experimental models mimicking these complex in vivo interactions, the most convincing based on freshly isolated primary brain cells. Here, we investigated whether human induced pluripotent stem cells (hiPSC) could be an alternative cell source for the astrocyte component. We developed a 3D vessel-on-chip (VoC) model which incorporates hiPSC-derived ECs (hiPSC-ECs), human brain vascular pericytes (HBVPs) and hiPSC-derived astrocytes (hiPSC-Astros). When the vascular cells and astrocytes were combined within a fibrin hydrogel, they self-organized into lumenized microvascular networks, with direct interaction between the cell-types included. hiPSC-Astros and human primary astrocytes (pAstro) behaved very similarly in VoC triple cultures with no apparent differences in the morphology or expression of contractile- and reactive markers in either HBVPs or astrocytes. Unexpectedly, microvascular network formation was reduced in the presence of astrocytes with apparent local disruptions in the EC layer. We then showed that continuous perfusion of the vasculature or activation of cAMP signaling rescued vascular organization and decreased vascular permeability in the 3D VoC-hiPSC-Astro model. However, inclusion of astrocyte had no effect on the expression adherens- and tight junction, transport and extracellular matrix proteins indicating that hiPSC-ECs still do not acquire BBB-like identity in the 3D VoC model with astrocytes.

*This chapter is adapted from:*

*Self-assembling 3D Vessel-on-Chip model with hiPSC-derived astrocytes. Stem Cell Reports. (2024) In press*

*Dennis M. Nahon, Marc Vila Cuenca, Francijna E. van den Hil, Michel Hu, Tessa de Korte, Jean-Philippe Frimat, Arn M.J.M. van den Maagdenberg, Christine L. Mummery and Valeria V. Orlova.*

## Introduction

The Blood-Brain-Barrier (BBB) is formed through direct interactions between endothelial cells (ECs), pericytes and astrocytes in the central nervous system. An intact BBB is essential in regulating transport of nutrients and preventing toxins from entering the brain<sup>1</sup>. BBB dysfunction is increasingly recognized as a contributor to multiple neurodegenerative diseases<sup>2</sup>. This has led to many attempts to develop human *in vitro* models that recapitulate complex interactions between astrocytes and the vasculature<sup>3</sup>. Some aspects of the BBB *in vitro*, such as high transendothelial electrical resistance (TEER) and low permeability to soluble tracers, has been achieved by co-culturing primary brain microvascular- or cord blood-derived ECs with brain pericytes and astrocytes on a porous membrane<sup>4,5</sup>. However, primary brain cells are difficult to obtain and even from commercial sources, show batch-to-batch variability. Here, we asked whether human induced pluripotent stem cells (hiPSC) might be an alternative source, since they can be derived easily from any individual and can capture genomes associate with degenerative brain diseases. Several studies have described hiPSC-derived brain microvascular endothelial cells (BMECs)<sup>6-8</sup>. Even though these have been widely used in engineering approaches for the BBB<sup>3</sup> it later turned out that these actually resembled epithelial cells rather than ECs<sup>9,10</sup>; this explained their abnormally high TEER values. More recently alternative protocols to differentiate brain-like microvascular ECs that more closely resemble true ECs based on the expression of EC-specific markers and responses to proinflammatory stimuli have been developed<sup>11,12</sup>. These were useful for studying intrinsic defects in hiPSC-ECs derived from multiple sclerosis (MS) patient<sup>13</sup>. However, the field could benefit from further advancing the models via inclusion of other cellular components, especially for diseases where several cell types are affected, as in cerebral amyloid angiopathy and other forms of vascular dementia for instance.

Vessel-on-chip (VoC) is one type of *in vitro* model that can mimic essential *in vivo* features of the 3D environment such as complex multi-cellular interactions and mechanical forces as a result of blood flow<sup>14</sup>. Several VoC models have been developed which combine the three most important cell types of the BBB: ECs, pericytes and astrocytes. However, whilst they have some value, some of these models lack the direct heterotypic cell-cell and cell-matrix interactions typically seen *in vivo*<sup>15,16 17,18</sup>. The models that do recapitulate these interactions using vasculogenesis or angiogenesis as starting points, usually incorporate primary cells, as mentioned earlier, specifically primary astrocytes<sup>19-21</sup>.

In this study, we aimed to develop an hiPSC-based 3D VoC model that integrates ECs from hiPSCs (hiPSC-ECs), human brain vascular pericytes (HBVPs) and hiPSC-derived astrocytes (hiPSC-Astros). We used our earlier protocol to differentiate ECs from hiPSCs<sup>22</sup> and showed that astrocytes derived from hiPSCs could be integrated into the VoC and behaved much like human primary astrocytes (pAstros). hiPSC-Astros incorporated into a VoC triple culture containing both hiPSC-ECs and HBVPs, self-assembled into microvascular networks in 3D with hiPSC-Astros and HBVPs assuming positions surrounding the vascular

wall in the microfluidic chip. Finally, we demonstrated two ways of improving microvascular network formation and organization in the VoC model including hiPSC-Astros: activating the cAMP pathway or introducing continuous microfluidic flow. However, despite improvements in incorporating relevant cell interaction and reproducibility, the model still falls short in reproducing a true BBB.

## Results

### 3D VoC integrating hiPSC-derived astrocytes

A 3D VoC model was established by combining hiPSC-ECs and HBVPs in a fibrin hydrogel and injecting the cell/gel mix into a commercially available AIM Biotech idenTx9 3D culture chip using a protocol described previously<sup>23</sup> (Figure 1A). Either hiPSC-Astros or pAstros were included in the VoC model to mimic BBB cell-cell interactions. First, hiPSC-derived neural progenitor cells (NPCs) were generated as previously described<sup>24</sup> (Figure S1A). hiPSC-derived neural organoids contained neural rosette-like structures (Figure S1B) and more of these organoids could be formed in the expansion phase (Figure S1C). Proper patterning and differentiation were confirmed by expression of the NPC markers SRY-Box Transcription Factor 2 (SOX2) and Paired Box 6 (PAX6) and the forebrain marker Forkhead Box G1 (FOXP1) (Figure S1D). We then derived hiPSC-Astros in two different ways: one already published<sup>24</sup> (iAstros), the other using a commercially available kit (iSCT Astros) (Figure S1A). iAstros and iSCT Astros showed comparable expression of key astrocyte markers, such as Glial Fibrillary Acidic Protein (GFAP), Fatty Acid Binding Protein 7 (FABP7), S100 Calcium Binding Protein B (S100B), Vimentin, Solute Carrier Family 1 Member 3 (SLC1A3/GLAST) (Figure S1E and S1F). In addition, iAstros showed increased intracellular  $Ca^{2+}$  release upon stimulation with adenosine triphosphate (ATP) (3  $\mu$ M and 300  $\mu$ M) (Figure S1G and S1H) and efficient uptake of the neurotransmitter glutamate (Figure S1F), confirming their functionality.

A triple culture of hiPSC-ECs derived from a control mCherry reporter hiPSC line, HBVPs and iAstros derived from a control hiPSC line with  $\alpha$ -tubulin-mEGFP reporter (AISC0012, TUBA)<sup>25</sup> was monitored from day 1 to day 6 (Figure 1B). hiPSC-ECs self-organized into interconnected microvascular networks within 2-3 days, with fully lumenized structures by day 7 (Figure 1B). In addition, iAstros localized in the extravascular space, interacting directly with the developing microvascular network (Figure 1B). The development of a robust VoC triple culture model was confirmed by similarly including iSCT Astros from two independent hiPSC lines (FLB or TUBA) (Figure S2). The remaining experiments were performed using iAstros, and not iSCT Astros, as these can be cryopreserved at the end-point of differentiation and used as an efficient cell source for 3D VoC triple culture setups. The vascular beds thus established and were compared between VoC double cultures (only containing hiPSC-ECs and HBVPs) and VoC triple cultures including either pAstros or iAstros from two independent hiPSC lines (FLB or TUBA). All cell combinations formed an interconnected microvascular network by day 7 in a highly reproducible manner across

independent experiments (Figure 1C-F). Quantification of vessel parameters showed that inclusion of any astrocyte source in our VoC model, reduced vascular density (% , Figure 1D) and average vessel diameter ( $\mu\text{m}$ , Figure 1E) and increased average vessel length ( $\mu\text{m}$ , Figure 1F) relative to the double cultures. Significant differences were observed in vessel parameters between pAstro and iAstro triple cultures depending on the hiPSC line used. This is in line with batch-to-batch variability of pAstros previously described<sup>26</sup>. Specifically, incorporating iAstros from either the FLB or TUBA hiPSC line into our VoC model resulted in a significant decrease in vascular density compared to pAstros (Figure 1D). However, only iAstros differentiated from the TUBA hiPSC line also resulted in a significant decrease in average vessel diameter and increase in average vessel length (Figure 1D-F).

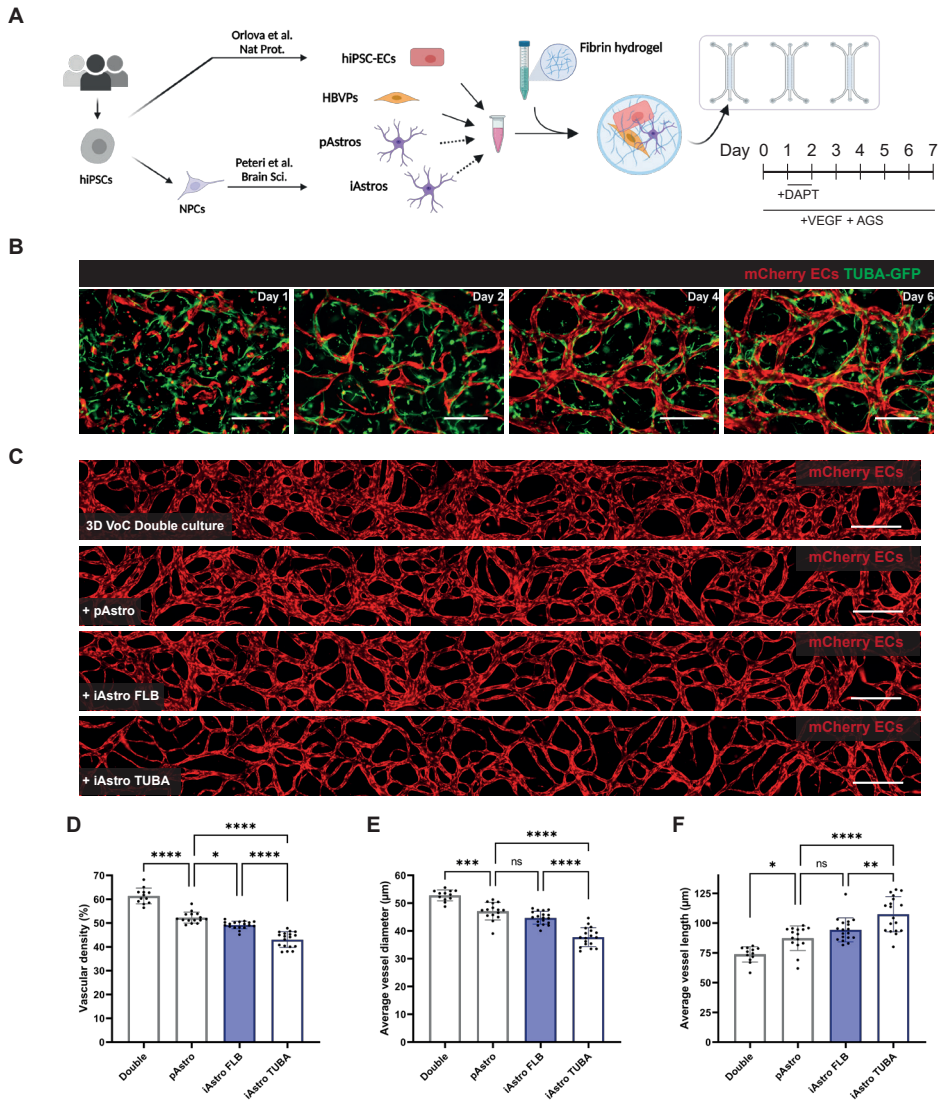


### Figure 1. iAstros incorporated into 3D VoC model

A) Schematic of VoC protocol using hiPSC-ECs with HBVP and pAstros or iAstros. Cells were mixed in a fibrin hydrogel and the cell/gel mix was injected in the microfluidic chip (AIM Biotech). Medium was refreshed daily with EGM-2 supplemented with 50 ng/mL VEGF and 1% AGS. On day 1, the medium was additionally supplemented with 10  $\mu$ M DAPT for 24 hours. B) Representative immunofluorescence images of a 3D VoC triple culture containing hiPSC-ECs, HBVPs and iAstros at day 1, 2, 4 and 6 showing hiPSC-mCherry ECs (red) and iAstros differentiated from the TUBA hiPSC line (green, TUBA-GFP). Scale bars: 250  $\mu$ m. C) Representative immunofluorescence images of microvascular networks in microfluidic chips on day 7 showing hiPSC-mCherry ECs (red). Images showing microvascular networks from a VoC double culture (hiPSC-ECs and HBVPs) or 3D VoC triple cultures including either pAstros or iAstros from two independent hiPSC lines (FLB or TUBA). Scale bars: 250  $\mu$ m. (D-F) Quantification of full channel images of microvascular networks showing vascular density at end-point day 7 showing (D), average vessel diameter (E) and average vessel length (F). Data are shown as mean  $\pm$  SD. All conditions are N =

3,  $n = 12-18$ ; three independent experiments with minimum of 3 microfluidic channels per experiment. One-way ANOVA with Sidaks multiple comparison test. \* $p < 0.05$ , \*\* $p < 0.01$ , \*\*\* $p < 0.001$ , \*\*\*\* $p < 0.0001$ ; ns, non-significant.

### **Characterization of astrocytes and HVBPs in the 3D VoC model**

We next analyzed the astrocyte morphology and interaction with hiPSC-EC in microvascular networks in the VoC model. Both pAstros and iAstros from either the FLB or TUBA hiPSC lines stained positively for GFAP and showed uniform distribution through the entire microfluidic channel with no significant differences in the total number of GFAP-positive cells (Figure 2A and 2B). Astrocytes in all conditions showed a distinct stellate morphology and were positioned closely to the abluminal side of the microvascular networks (Figure 2C, Video S1). No significant differences in the average astrocyte length ( $\mu\text{m}$ , Figure 2D) or the percentage of astrocytes associated with the microvascular network (% , Figure 2E) were observed between the different sources of astrocytes upon quantification of the confocal images. In addition, iAstros stained positively for the astrocyte-specific water channel AQP4 (Figure 2F), although the staining was distributed across the plasma membrane without polarized expression in the astrocyte endfoot.

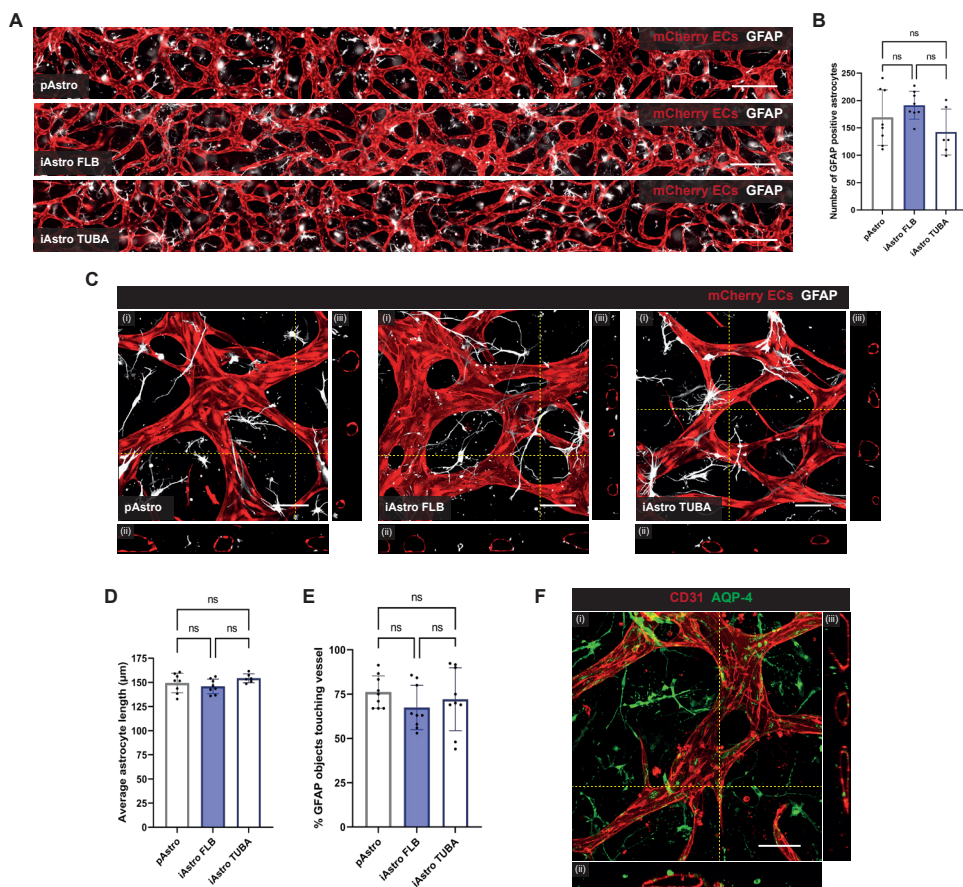


**Figure 2. Comparable structural properties of primary and hiPSC-Astros in a 3D VoC model**

A) Representative immunofluorescence images of microvascular networks in microfluidic chips on day 7 showing hiPSC-mCherry ECs (red) and astrocytes (silver; GFAP). Images showing VoC triple cultures of hiPSC-ECs with HBVPs and pAstros or iAstros from FLB or TUBA hiPSC line. Scale bars: 500 μm. B) Quantification of astrocytes in VoC triple cultures showing number of GFAP positive astrocytes in ±80% of full microfluidic channel. C) Representative immunofluorescence confocal images of microvascular networks in microfluidic chips showing hiPSC-mCherry ECs (red) and astrocytes (silver; GFAP). Images displaying xyz (i), xy (ii), and yz cross-sectional perspectives (iii). Images showing VoC triple cultures of hiPSC-ECs with HBVPs and pAstros or iAstros from the FLB or TUBA hiPSC lines. Scale bars: 100 μm. (D-E) Quantification of astrocytes in VoC model showing average astrocyte length (D) and % of GFAP objects touching the microvascular network (E). Data are shown as mean ± SD. For (B, D) N = 3, n = 6-8; three independent experiments with a minimum of two microfluidic channels per experiment. For (E) N = 3, n = 3; three independent experiments, one microfluidic channel per experiment with three ROIs per channel. One-way ANOVA with Tukey's multiple comparison. ns, non-significant. F) Representative immunofluorescence confocal image of microvascular network in microfluidic chips showing ECs (red; CD31) and astrocytes (green; Aqp4) in a VoC triple culture of hiPSC-ECs with HBVPs and iAstros from the FLB hiPSC line. Images displaying xyz (i), xy (ii), and yz cross-sectional perspectives (iii). Scale bar: 100 μm.

We confirmed the identity of the HBVPs in the 3D VoC culture by overlaying

immunostaining for the pericyte marker NG2 and contractile marker SM22 (Figure 3A). We previously demonstrated that SM22 is indicative of heterotypic cell-cell contact-induced HBVP cell maturation in VoC culture<sup>23</sup> and confirmed similar cell-cell interactions in our current VoC setup (Video S1). By using SM22, we therefore investigated whether HBVPs were affected by the addition of astrocytes. Staining of the VoC triple cultures showed SM22 in both HBVPs and astrocytes. To distinguish HBVPs from astrocytes, we used the fluorescently tagged TUBA-GFP iAstros and co-stained the VoC model including pAstros with the glial marker FABP7. Surface rendering of confocal images and identification of SM22+ HBVPs revealed similar numbers of HBVPs in the VoC double cultures and VoC triple cultures including pAstro or iAstros (Figure 3B and 3C). SM22+ HBVPs in the microvascular network had a reduced average volume and normalized average SM22 intensity in the VoC triple cultures with astrocytes ( $\mu\text{m}^3$ , Figure 3D and 3E). No significant differences were observed in the direct interaction of the HBVPs with the microvascular network between the different conditions (Figure 3B; %, 3F).

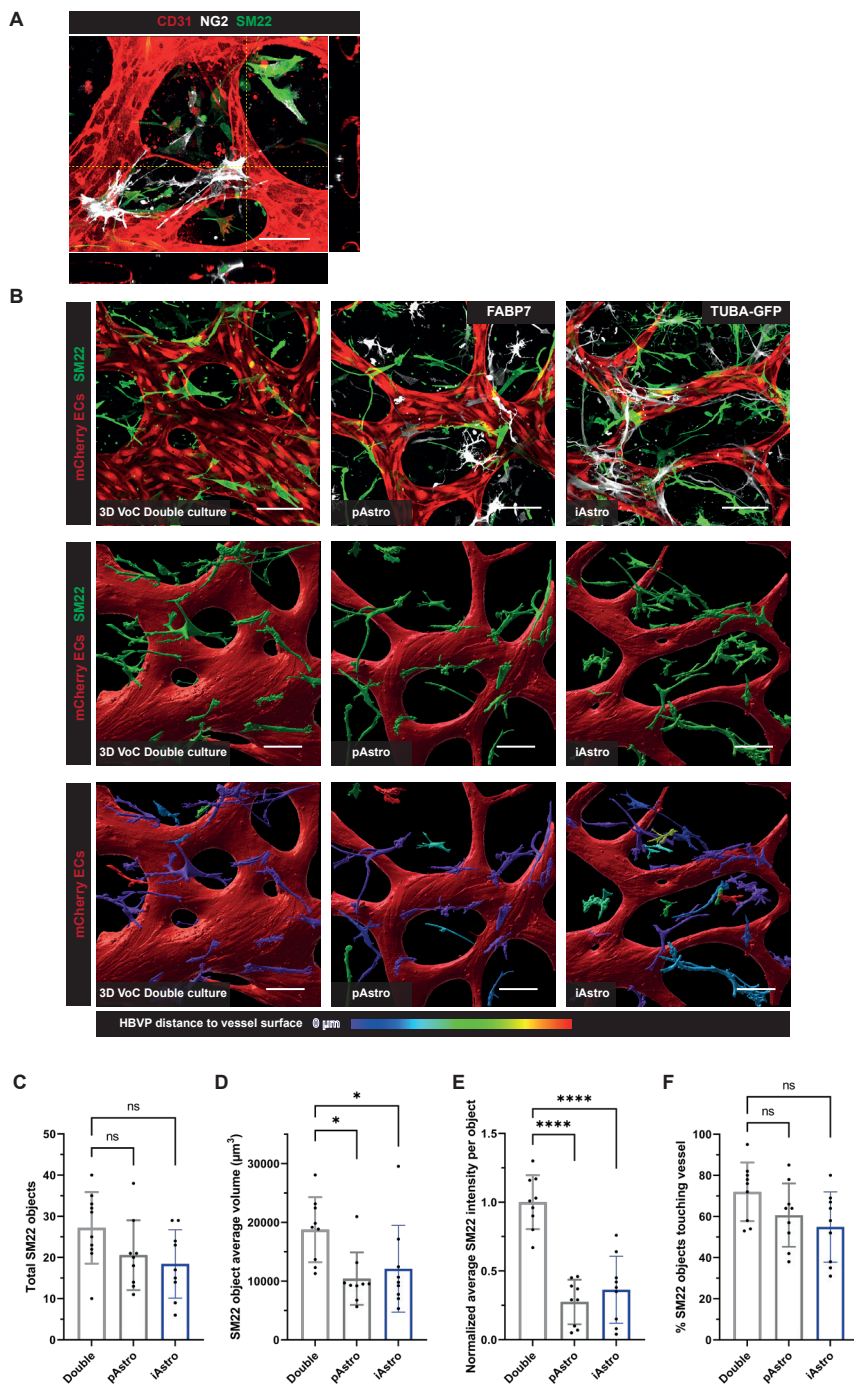


**Figure 3. Comparable structural properties of HBVPs in a 3D VoC model including astrocytes**  
 A) Representative immunofluorescence confocal image of microvascular network in microfluidic chips

showing ECs (red; CD31) and HBVPs (silver; NG2, green; SM22) in a VoC double culture of hiPSC-ECs with HBVPs. Images displaying xyz (i), xy (ii), and yz cross-sectional perspectives (iii). Scale bar: 100  $\mu$ m. B) Representative immunofluorescence confocal images of microvascular networks in microfluidic chips on day 7 showing hiPSC-mCherry ECs (red), HBVPs (green; SM22) and pAstros (silver, FABP7) or iAstros from the TUBA hiPSC line (silver, TUBA-GFP), surface-rendered images and color-coded images of HBVPs distance to the vessel surface. Images showing VoC double cultures (hiPSC-ECs with HBVPs) and VoC triple cultures including either pAstros or iAstros from the TUBA hiPSC line. (C-F) Quantification of HBVPs in VoC double and triple cultures containing iAstros from the TUBA hiPSC line showing number of SM22 positive objects (C), average SM22 object volume (D), normalized average SM22 intensity per object (E) and percentage of SM22 objects touching the microvascular network (F). Data are shown as mean  $\pm$  SD. For (C-F) N = 3, n = 9-10; three independent experiments, one microfluidic channel per experiment with three or four ROIs per channel. Scale bars: 100  $\mu$ m. One-way ANOVA with Sidaks multiple comparison test. \* $p < 0.05$ , \*\*\*\* $p < 0.0001$ ; ns, non-significant.

### **Continuous perfusion or activation of cAMP signaling improves vascular organization and reduces permeability in the 3D VoC model**

In addition to reduced microvascular network density and diameter and SM22 volume and intensity, more detailed examination showed local disruptions in the EC layer in both pAstro and iAstro triple culture conditions, although not in the double culture condition (Figure S3A). To further optimize the triple culture VoC model, we investigated whether culture conditions postulated to modulate maturation of astrocytes<sup>27,28</sup> and certain hiPSC derivatives<sup>29</sup> or microfluidic flow might improve organization of the microvascular networks (Figure 4A). Specifically, we investigated the effect of activation of the cAMP pathway since it has not only been reported to improve astrocyte maturity and immune response<sup>27,28</sup>, it is also protective for endothelial integrity and barrier function in the BBB<sup>30</sup>. The influence of continuous flow was studied since mechanical forces resulting from luminal flow through blood vessels are known to promote EC survival, migration and proliferation<sup>31</sup>. VoC triple cultures including iAstros were thus either supplemented daily with dbcAMP (250  $\mu$ M) or subjected to continuous flow from day 3 till day 7 (Figure 4A). Both dbcAMP addition and continuous flow in VoC triple cultures including iAstros increased vascular density over time (%; Figure 4B). This was most evident on day 7, where both the cAMP and continuous flow conditions significantly increased vascular density, average vessel diameter and decreased average vessel length in comparison to standard VoC triple cultures (Figure 4C; %, 4D;  $\mu$ m, 4E;  $\mu$ m, 4F).

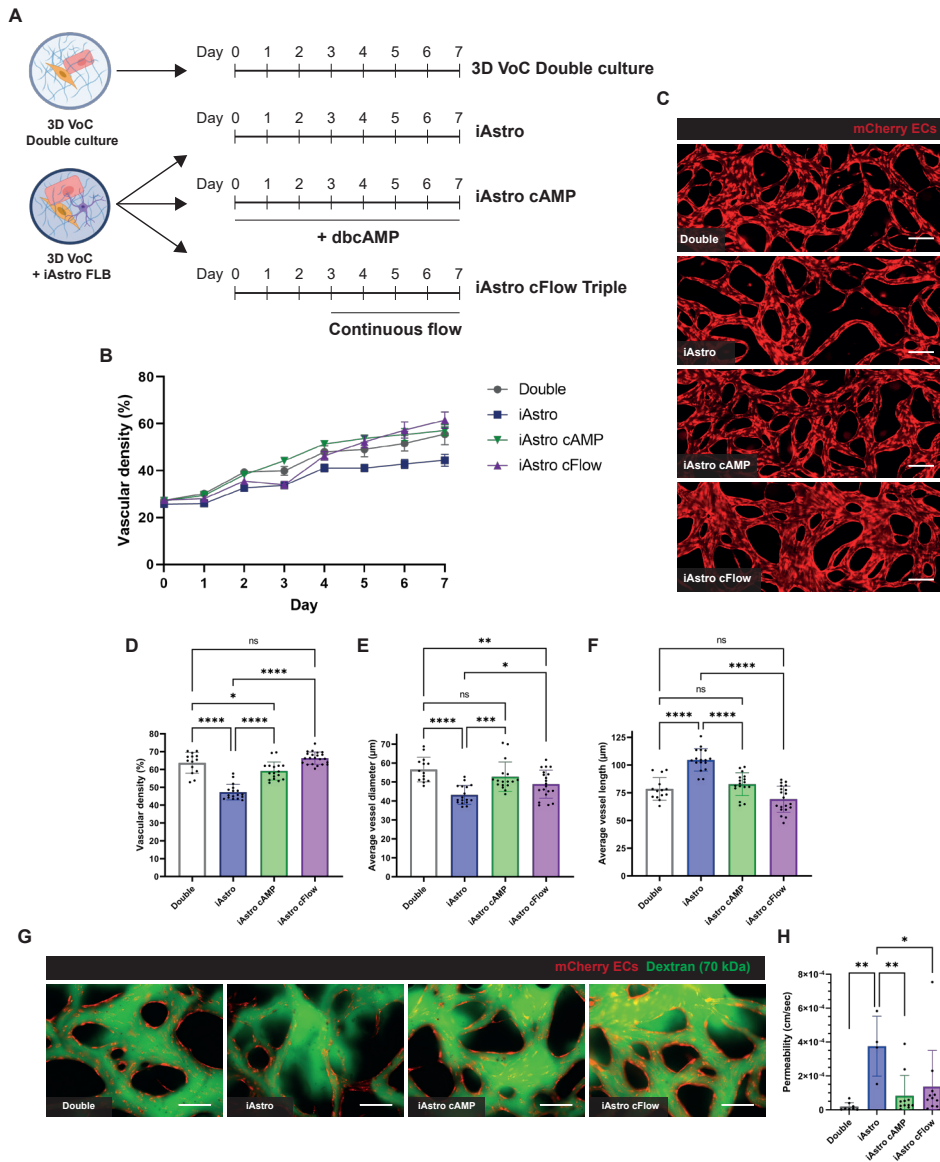


**Figure 4. Improved microvascular network of 3D VoC triple culture including hiPSC-Astros upon activation of cAMP signaling or application of continuous perfusion**

A) Schematic of experimental setup for improving microvascular network formation of VoC triple cultures containing hiPSC-ECs, HBVPs and iAstros from the FLB iPSC line. In the iAstro cAMP condition, the medium was daily supplemented with 250  $\mu\text{M}$  dbcAMP to activate cAMP signaling. In the iAstro continuous flow (cFlow) condition, the VoC triple culture was subjected to continuous flow from day 3 onwards. B) Quantification of vessel density over time from daily images of hiPSC-mCherry ECs for the four VoC culture conditions. C) Representative immunofluorescence images of microvascular networks from the four VoC culture conditions at day 7 showing hiPSC-mCherry ECs (red). iAstro conditions are triple cultures containing iAstros from the FLB hiPSC line. Scale bars: 200  $\mu\text{m}$ . (D-F) Quantification of

microvascular networks showing vascular density at end-point day 7 (D), average vessel diameter (E) and average vessel length (F). Data are shown as mean  $\pm$  SD. Data shown is N = 3-4, n = 14-22; three or four independent experiments with a minimum of 3 microfluidic channels per experiment. iAstro conditions are triple cultures containing iAstros from the FLB hiPSC line. Scale bars: 200  $\mu$ m. G) Representative immunofluorescence images of microvascular networks (red; hiPSC-mCherry ECs) perfused with 70 kDa FITC-Dextran (green) on day 7, 30 seconds after start of perfusion. Images show VoC double cultures (hiPSC-ECs with HBVPs) and VoC triple cultures also containing iAstros from the FLB hiPSC line. Scale bars: 200  $\mu$ m. H) Quantification of permeability coefficient for the four VoC culture conditions at end-point day 7 from N=3-4, n=4-11; three or four independent experiments with one to six microfluidic channels per experiment. In the iAstro conditions, data is pulled from triple cultures containing both iAstros from the FLB and the TUBA hiPSC lines. One-way ANOVA with Sidaks multiple comparison test. \* $p < 0.05$ , \*\* $p < 0.01$ , \*\*\* $p < 0.001$ , \*\*\*\* $p < 0.0001$ , ns, non-significant.

We subsequently investigated whether dbcAMP (the cell membrane permeable analog of cAMP) or continuous perfusion affected microvascular network formation through increased proliferation or through increased presence of matrix metalloproteinase-2 (MMP2), as was shown in a recent study of a VoC containing primary brain ECs, HBVPs and pAstros<sup>32</sup>. Proliferation was quantified by 5-ethynyl-2'-deoxyuridine (EdU) pulse experiments on day 4 of culture. Continuous flow in the VoC model with iAstros increased proliferation compared to the control VoC cultures with- or without (dbcAMP treated) iAstros (Figure S3B and S3C). Co-staining of microfluidic channels with the EC-specific transcription factor SOX17 revealed that most of proliferating cells were hiPSC-ECs (Figure S3D and S3E). Quantitative real-time PCR (qRT-PCR) of VoC cultures at end-point day 7 confirmed the increase in MMP2 in the iAstro VoC triple culture under continuous flow condition (Figure S3F).

We next perfused VoC cultures with FITC-Dextran (70 kDa) to investigate local vascular barrier integrity and quantified the permeability coefficient of the four VoC triple culture conditions (Figure 4G, H; cm/sec). Both addition of dbcAMP and application of continuous flow improved local vascular integrity and significantly decreased the permeability coefficient in iAstro VoC triple cultures (Figure S3G).

Finally, we explored the influence of the different VoC conditions on the expression of BBB-related markers. qRT-PCR of VoC culture conditions at end-point day 7 was somewhat variable between experiments, and did not show a significant increase in most of the investigated BBB-related genes in triple culture conditions (Figure S4A). Integration of astrocytes had no effect on the expression of adherens- and tight junction markers, such as VEC, ZO1 and CLDN5 by qRT-PCR (S4A) and by immunohistochemistry (S4B). Some upregulation of transport-related genes, such as SLC2A1 and PGP and ECM-related gene COL4A1 was observed by qRT-PCR (S4A) under continuous flow, but this was less evident by immunohistochemistry (S4C,D).

## Discussion

In this study, we described the generation of 3D microvascular networks containing hiPSC-ECs, HBVPs and hiPSC-Astros. We showed that these triple cultures develop interconnected,

lumenized, perfusable networks, with direct interaction between the incorporated cell-types. No apparent differences were observed in the morphology and expression of reactive markers in astrocytes, in any of the culture conditions tested in this study. Although the number of HBVPs and their interaction with the microvascular network was similar between culture conditions, the average volume and expression of the contractile marker SM22 did differ between HBVPs in double and triple cultures. This could indicate that both primary- and hiPSC-Astros affect the maturity and contractile phenotype of the HBVPs in our system. Interestingly, we observed decreased vascular density and diameter of the vessels upon adding pAstros or iAstros, similar to earlier studies also using primary astrocytes<sup>19,20</sup>. Decreased vascular density and diameter can be a consequence of “tightening” of the endothelium through astrocyte-induced paracrine signaling which has been well-established *in vivo*<sup>17,19</sup>, and has also been observed *in vitro*<sup>19</sup>. In addition, the sub-optimal microenvironment for ECs caused by the presence of astrocytes could have reduced vessel stabilization, evidenced by local vascular barrier disruptions and increased leakage of FITC-Dextran in our VoC triple cultures including iAstros. We also observed cell-line dependence of hiPSC-Astros on vessel parameters which will be important to note for those developing patient specific models. This was in agreement with other studies showing cell batch (i.e. donor) variability of primary astrocytes on microvascular network formation<sup>26</sup>. Additional studies will be needed to further define the impact of astrocytes on these self-assembling *in vitro* microvascular networks.

For *in vitro* models to be useful for disease modeling and drug screening, it is essential that these models are reproducible and robust<sup>33</sup> across independent technical experiments, as we demonstrated in the present study. In addition, we showed that appropriate culture medium and fluidic flow are important in the formation and stability of microvascular networks containing hiPSC-ECs, HBVPs and hiPSC-Astros. We demonstrated that the addition of dbcAMP improved microvascular network formation and organization and vascular permeability in the VoC model that included iAstros. This is in line with previous reports demonstrating the importance of cAMP signaling in astrocyte and EC function<sup>27,28,30,34,35</sup>. Interestingly, EC proliferation was not increased by adding dbcAMP, although we cannot exclude the possibility that timing of the EdU experiment was sub-optimal. Future studies will be needed to clarify the exact mechanism by which dbcAMP acts in this 3D model.

We also showed that continuous microfluidic flow promoted EC proliferation and improved stability of the triple culture microvascular networks. This is consistent with the general notion of improved stability and organization of ECs under flow conditions<sup>31</sup> and earlier studies using similar microvascular systems<sup>21,36,37</sup>. In addition, we observed increased MMP2 expression as shown previously<sup>32</sup>, even though this earlier study investigated the effect of interstitial flow in the first stages of vasculogenesis while we only applied flow when a lumenized microvascular network had already formed, primarily resulting in luminal

shear stress.

Co-culture of hiPSC-ECs with tissue-specific cells has previously been shown to enable the induction of a tissue-specific molecular identity for several organ systems<sup>38,39</sup>, including the brain<sup>19</sup>. While we see direct interaction between the multiple cell types in our system, we did not observe consistent increases in BBB-related markers in which iAstros were added to the VoC model. These results were independent of whether iAstros were from FLB or TUBA hiPSC lines. Additional optimization of the metabolic environment, adding other relevant small molecules or cytokines or altering the transcriptional regulation of hiPSC-ECs using transcription factors will be required for the model to closely recapitulate the BBB<sup>9</sup>.

In summary, we have established a 3D VoC model containing hiPSC-ECs, HBVPs and hiPSC-Astros mimicking the direct cell-cell interactions seen *in vivo*. We demonstrated that hiPSC-Astros perform similarly to pAstros and are thus an alternative source to primary brain tissue for this cell type. However, we noted that the extent to which hiPSC-Astros influence microvascular network formation can be hiPSC line dependent. Elevation of cAMP signaling or application of continuous flow improved microvascular networks containing hiPSC-Astros. For future studies it would be interesting to integrate hiPSC-derived smooth muscle cells<sup>23</sup> instead of HBVPs for a fully hiPSC-derived model suitable for investigating the cell type-specific contribution in disease phenotypes. Nevertheless, culture conditions will need further refinement before hiPSC can be implemented as next-generation BBB model systems for modeling neurodegenerative disorders and subsequent screening for new therapeutic interventions.

## Experimental Procedures

### hiPSC lines and maintenance

hiPSCs were maintained on recombinant vitronectin-coated plates in TeSR-E8, all from StemCell Technologies, according to the manufacturer's instructions. hiPSCs used for astrocyte differentiation were cultured on matrigel-coated (BD Biosciences, 354230) plates in TeSR<sup>TM</sup>1 medium (StemCell Technologies, 05850) and mechanically passaged once a week using dispase solution 1 mg/mL (Gibco, 17105-041). The following hiPSC lines were used: LUMC0020iCTRL (Described in this report as FLB and generated from skin fibroblasts, <https://hpscereg.eu/cell-line/LUMCi028-A>)<sup>40</sup>. NIH Center for Regenerative Medicine hiPSC line (NCRM-1, generated from CD34+ cord blood cells, <https://hpscereg.eu/cell-line/CRMi003-A>), obtained from RUDCR Infinite Biologicals at Rutgers University, was modified in-house with a mCherry expression cassette under the human cytomegalovirus (hCMV) early enhancer/chicken  $\beta$  actin (CAG) promoter using a previously established protocol<sup>41</sup>. The Allen Cell Collection line AICS-0012 (Described in this report as TUBA and generated from skin fibroblasts, <https://hpscereg.eu/cell-line/UCSFi001-A-2>) with mEGFP insertion site at TUBA1B.

### Cell preparation prior to VoC culture

hiPSC-ECs (P1) were thawed and cultured on gelatin-coated plates in complete EC growth medium composed of Human Endothelial-SFM (EC-SFM) with 1% platelet poor serum (PPS), VEGF (30 ng/mL) and bFGF (20 ng/mL) 4 days prior to VoC seeding. HBVPs (P4) were thawed and cultured on gelatin-coated plates in Pericyte Medium (ScienceCell, 1201) supplemented with 1% Pericyte Growth Supplement (ScienceCell, 1252), 2% FBS and 1% penicillin/streptomycin, 4 days prior to VoC seeding. pAstros were thawed and cultured in Astrocyte Medium (ScienceCell, 1801) supplemented with 1% Astrocyte Growth Supplement (AGS, Sciencell, 1852), 2% FBS and 1% penicillin/streptomycin, 4 days prior to VoC seeding. iAstros were thawed and cultured in NS medium supplemented with 20 ng/mL CNTF, 4 days prior to VoC seeding. iSCT-Astros were used directly after maturation at the end of the differentiation protocol. For an overview of the hiPSC lines and differentiation batches used for the different experiments, see Supplemental Table 1.

### VoC set up and culture

Microvascular networks inside microfluidic chips were generated as previously described<sup>23,42</sup> with minor modifications. Microfluidic chips with one middle gel channel flanked by two media channels (AIM Biotech, idenTx9 chip) were used. Cells were resuspended in EGM-2 medium supplemented with thrombin (4 U/mL, Sigma, T4648) at  $15 \times 10^6$  cells/mL for hiPSC-ECs,  $3 \times 10^6$  cells/mL for HBVPs and  $7.5 \times 10^6$  cells/mL for astrocytes (5:1:2.5 ratio respectively). Three astrocyte cell suspensions were tested in combination with hiPSC-ECs and HBVPs: (1) pAstros, (2) iAstros and (3) iSCT-Astros. The cell suspensions were mixed with an equal volume of fibrinogen solution (6 mg/mL, final concentration 3 mg/mL, Sigma, 8630) and immediately injected into the gel channel of the microfluidic chip (3 gel channels per cell/fibrin mix and 15  $\mu$ L per gel channel). Chips were incubated for 15 minutes at RT before adding EGM-2 supplemented with 50 ng/mL VEGF and 1% Astrocyte Growth Supplement (AGS; Sciencell, 1852) to the media channels. The microfluidic chips were refreshed every 24 hours with EGM-2 supplemented with VEGF (50 ng/mL) and 1% AGS. Refreshing was done by application of a hydrostatic pressure over the medium channel by adding 100  $\mu$ L medium to the right media ports and 50  $\mu$ L medium the left media ports. On day 1,  $\gamma$ -secretase inhibitor N-[N-(3,5-difluorophenacetyl)-l-alanyl]-s-phenylglycine-butyl ester (DAPT, 10  $\mu$ M, Sigma, D5942) was added for 24 hours. For cAMP condition, the media was additionally supplemented with 250  $\mu$ M dbcAMP (Sigma, D0627) for the entire duration of culture. For the continuous perfusion condition, the microfluidic chips were placed on an interval rocker platform (Perfusion rocker, MIMETAS) set at a 5-degree inclination and 8 minutes cycle time from day 3 onwards.

### Statistical Analysis

Statistical analyses were performed using GraphPad Prism 9 software. Normality of the data was evaluated by the Shapiro-wilk test. One-way ANOVA with Tukey's multiple comparison test or Sidak multiple comparison test was used for comparing multiple groups. Detailed statistics are indicated in each figure legend. The data are reported as mean  $\pm$  SD.

## **Acknowledgments**

We thank the LUMC human iPSC Hotel for the generation and characterization of hiPSC lines and the LUMC confocal imaging facility (Lennard Voortman, Annelies Boonzaier – van der Laan) for their help with imaging. Ruben van Helden is thanked for useful discussions and providing pipelines for analysis. Elga de Vries is thanked for providing aliquots of several antibodies. Laurent Roybon is thanked for the discussions and providing information on the astrocyte differentiation protocol. Ncardia is thanked for the use of the FDSS/ $\mu$ cell for the calcium experiments. The Allen Cell Collection, available from Coriell Institute for Medical Research, provided materials. Images were generated using Biorender.com. This work was supported by the Netherlands Organ-on-Chip Initiative, an NWO Gravitation project (024.003.001) funded by the Ministry of Education, Culture, and Science of the government of The Netherlands and The Novo Nordisk Foundation Center for Stem Cell Medicine supported by Novo Nordisk Foundation grants (NNF21CC0073729).

## **Author Contributions**

Conceptualization, V.V.O.; methodology, D.M.N., M.V.C. and V.V.O.; software, D.M.N.; investigation, D.N.M, M.V.C., M.H., F.E.v.d.H., T.d.K. and J.F.; visualisation, D.M.N.; resources, C.L.M. and V.V.O.; writing – original draft, D.M.N, C.L.M. and V.V.O.; writing – review & editing, D.M.N., C.L.M., and V.V.O.; supervision, C.L.M. and V.V.O.; project administration, V.V.O.; funding acquisition, A.M.J.M.M., C.L.M., and V.V.O.

## **Conflict of interests**

The authors declare no competing interests

## References

1. Daneman, R. & Prat, A. The Blood–Brain Barrier. *Cold Spring Harbor Laboratory Press* 7, 1–23 (2015).
2. Sweeney, M. D., Kisler, K., Montagne, A., Toga, A. W. & Zlokovic, B. V. The role of brain vasculature in neurodegenerative disorders. *Nat Neurosci* 21, 1318–1331 (2018).
3. Hajal, C., Roi, B. Le, Kamm, R. D. & Maoz, B. M. Biology and Models of the Blood-Brain barrier. *Annu Rev Biomed Eng* 23, 359–84 (2021).
4. Cecchelli, R. *et al.* A stable and reproducible human blood-brain barrier model derived from hematopoietic stem cells. *PLoS One* 9, (2014).
5. Boyer-Di Ponio, J. *et al.* Instruction of circulating endothelial progenitors in vitro towards specialized blood-brain barrier and arterial phenotypes. *PLoS One* 9, (2014).
6. Lippmann, E. S. *et al.* Derivation of blood-brain barrier endothelial cells from human pluripotent stem cells. *Nat Biotechnol* 30, 783–791 (2012).
7. Lippmann, E. S., Al-Ahmad, A., Azarin, S. M., Palecek, S. P. & Shusta, E. V. A retinoic acid-enhanced, multicellular human blood-brain barrier model derived from stem cell sources. *Sci Rep* 4, 1–10 (2014).
8. Qian, T. *et al.* Directed differentiation of human pluripotent stem cells to blood-brain barrier endothelial cells. *Sci Adv* 3, (2017).
9. Lu, T. M. *et al.* Human Induced Pluripotent Stem Cell-Derived Brain Endothelial Cells: Current Controversies. *Front Physiol* 12, (2021).
10. Lu, T. M. *et al.* Pluripotent stem cell-derived epithelium misidentified as brain microvascular endothelium requires ETS factors to acquire vascular fate. *Proc Natl Acad Sci U S A* 118, (2021).
11. Gastfriend, B. D. *et al.* Wnt signaling mediates acquisition of blood-brain barrier properties in naive endothelium derived from human pluripotent stem cells. *Elife* 10, 1–33 (2021).
12. Nishihara, H. *et al.* Advancing human induced pluripotent stem cell-derived blood-brain barrier models for studying immune cell interactions. *FASEB Journal* 34, 16693–16715 (2020).
13. Nishihara, H. *et al.* Intrinsic blood-brain barrier dysfunction contributes to multiple sclerosis pathogenesis. *Brain* 145, 4334–4348 (2022).
14. Mandrycky, C. J., Howard, C. C., Rayner, S. G., Shin, Y. J. & Zheng, Y. Organ-on-a-chip systems for vascular biology. *J Mol Cell Cardiol* 159, 1–13 (2021).
15. Vatine, G. D. *et al.* Human iPSC-Derived Blood-Brain Barrier Chips Enable Disease Modeling and Personalized Medicine Applications. *Cell Stem Cell* 24, 995–1005 (2019).
16. Maoz, B. M. *et al.* A linked organ-on-chip model of the human neurovascular unit reveals the metabolic coupling of endothelial and neuronal cells. *Nat Biotechnol* 36, 865–874 (2018).
17. Abbott, N. J., Rönnbäck, L. & Hansson, E. Astrocyte-endothelial interactions at the blood-brain barrier. *Nat Rev Neurosci* 7, 41–53 (2006).
18. Obermeier, B., Daneman, R. & Ransohoff, R. M. Development, maintenance and disruption of the blood-brain-barrier. *Nat Med* 19, 1584–1596 (2013).
19. Campisi, M. *et al.* 3D self-organized microvascular model of the human blood-brain barrier with endothelial cells, pericytes and astrocytes. *Biomaterials* 180, 117–129 (2018).
20. Lee, S., Chung, M., Lee, S. R. & Jeon, N. L. 3D brain angiogenesis model to reconstitute functional human blood–brain barrier in vitro. *Biotechnol Bioeng* 117, 748–762 (2020).
21. Winkelman, M. A. *et al.* Interstitial flow enhances the formation, connectivity, and function of 3D brain microvascular networks generated within a microfluidic device. *Lab Chip* 22, 170–192 (2022).
22. Orlova, V. V. *et al.* Generation, expansion and functional analysis of endothelial cells and pericytes derived from human pluripotent stem cells. *Nat Protoc* 9, 1514–1531 (2014).
23. Vila Cuenca, M. *et al.* Engineered 3D vessel-on-chip using hiPSC-derived endothelial- and vascular smooth muscle cells. *Stem Cell Reports* 16, (2021).
24. Peteri, U. *et al.* Generation of the Human Pluripotent Stem-Cell-Derived Astrocyte Model with Forebrain Identity. *Brain Sci* 11, (2021).
25. Roberts, B. *et al.* Systematic gene tagging using CRISPR/Cas9 in human stem cells to illuminate cell organization. *Mol Biol Cell* 28, 2854–2874 (2017).
26. Hajal, C. *et al.* Engineered human blood–brain barrier microfluidic model for vascular permeability analyses. *Nat Protoc* 17, 95–128 (2022).
27. Reuschlein, A. K., Jakobsen, E., Mertz, C. & Bak, L. K. Aspects of astrocytic cAMP signaling with an emphasis on the putative power of compartmentalized signals in health and disease. *Glia* 67, 1625–

- 1636 (2019).
28. Zhou, Z., Ikegaya, Y. & Koyama, R. The astrocytic cAMP pathway in health and disease. *Int J Mol Sci* 20, 1–27 (2019).
  29. Giacomelli, E. *et al.* Human-iPSC-Derived Cardiac Stromal Cells Enhance Maturation in 3D Cardiac Microtissues and Reveal Non-cardiomyocyte Contributions to Heart Disease. *Cell Stem Cell* 26, 862–879 (2020).
  30. Viña, D., Seoane, N., Vasquez, E. C. & Campos-Toimil, M. cAMP compartmentalization in cerebrovascular endothelial cells: New therapeutic opportunities in alzheimer’s disease. *Cells* 10, 1–23 (2021).
  31. Campinho, P., Vilfan, A. & Vermot, J. Blood Flow Forces in Shaping the Vascular System: A Focus on Endothelial Cell Behavior. *Frontiers in Physiology* vol. 11 Preprint at <https://doi.org/10.3389/fphys.2020.00552> (2020).
  32. Zhang, S. *et al.* Interstitial Flow Promotes the Formation of Functional Microvascular Networks In Vitro through Upregulation of Matrix Metalloproteinase-2. *Adv Funct Mater* (2022) doi:10.1002/adfm.202206767.
  33. Tronolone, J. J. & Jain, A. Engineering New Microvascular Networks On-Chip Ingredients Assembly and Best Practices. *Adv Funct Mater* 31, (2021).
  34. Ishizaki, T. *et al.* Cyclic AMP induces phosphorylation of claudin-5 immunoprecipitates and expression of claudin-5 gene in blood-brain-barrier endothelial cells via protein kinase A-dependent and -independent pathways. *Exp Cell Res* 290, 275–288 (2003).
  35. McRae, M. P. *et al.* Characterization of cell-cell junction changes associated with the formation of a strong endothelial barrier. *Tissue Barriers* 6, 1–9 (2018).
  36. Abe, Y. *et al.* Balance of interstitial flow magnitude and vascular endothelial growth factor concentration modulates three-dimensional microvascular network formation. *APL Bioeng* 3, 036102 (2019).
  37. Phan, D. T. T. *et al.* A vascularized and perfused organ-on-a-chip platform for large-scale drug screening applications. *Lab Chip* 17, 511–520 (2017).
  38. Cao, X. *et al.* Tissue microenvironment dictates the state of human induced pluripotent stem cell-derived endothelial cells of distinct developmental origin in 3D cardiac microtissues. *Biorxiv* (2022).
  39. Palikuqi, B. *et al.* Adaptable haemodynamic endothelial cells for organogenesis and tumorigenesis. *Nature* 585, (2020).
  40. Zhang, M. *et al.* Recessive cardiac phenotypes in induced pluripotent stem cell models of Jervell and Lange-Nielsen syndrome: Disease mechanisms and pharmacological rescue. *Proc Natl Acad Sci U S A* 111, E5383–E5392 (2014).
  41. Rostovskaya, M. *et al.* Transposon-mediated BAC transgenesis in human ES cells. *Nucleic Acids Res* 40, (2012).
  42. Orlova, V. *et al.* Vascular defects associated with hereditary hemorrhagic telangiectasia revealed in patient-derived isogenic iPSCs in 3D vessels on chip. *Stem Cell Reports* 17, 1536–1545 (2022).

## Supplementary material

### Content

#### Supplemental figures and legends:

**Figure S1. Related to Figure 1.** Characterization of hiPSC-astrocytes.

**Figure S2. Related to Figure 1.** iSCT Astros incorporated into 3D VoC model.

**Figure S3. Related to Figure 4.** Microvascular network integrity in VoC conditions and increased proliferation and increased expression of MMP2 upon continuous flow in 3D VoC triple cultures including astrocytes.

**Figure S4. Related to Figure 4.** Assessment of blood-brain barrier properties in 3D VoC cultures.

#### Supplemental Table:

**Supplemental Table 1.** List of hiPSC lines and batches used per experiment.

**Supplemental Table 2.** List of antibodies for immunofluorescence.

**Supplemental Table 3.** List of primers for qRT-PCR.

#### Supplementary Video:

**Supplementary Video 1:** 3D confocal reconstruction of EC-HBVP and EC-iAstro interactions

#### Supplemental Experimental Procedures

#### Supplemental References

# Supplementary figure 1

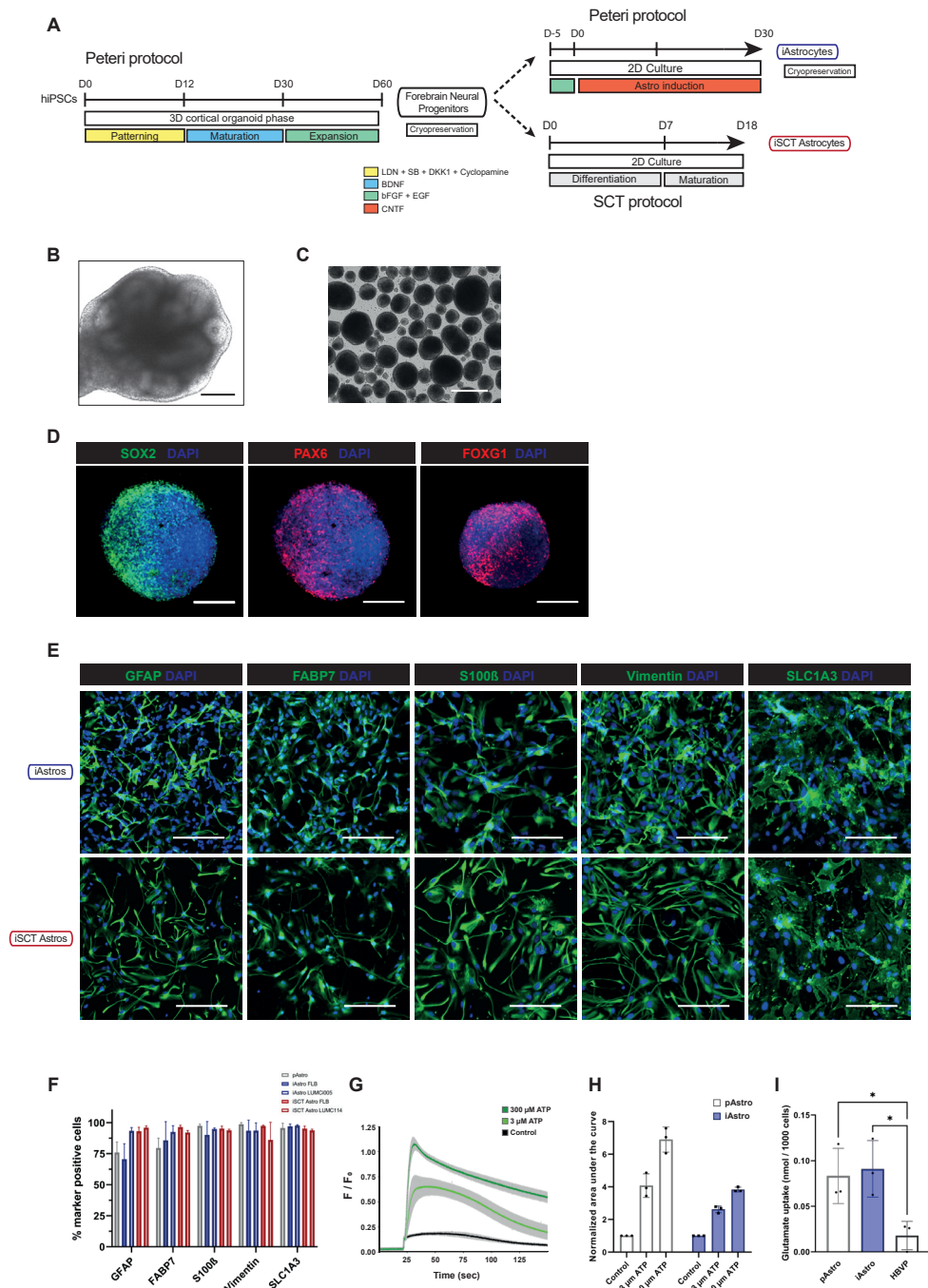


**Figure S1. Related to Figure 1. Characterization of hiPSC-astrocytes.**

A) Schematic of 'Peteri' protocol (iAstro) and 'SCT' protocol (iSCT Astro) to generate forebrain patterned astrocytes from hiPSCs. B) Representative brightfield image of a regionalized hiPSC-derived neural organoids on day 30. Scale bar: 250  $\mu\text{m}$ . C) Representative brightfield image of hiPSC-derived neural organoids on day 60. Scale bar: 500  $\mu\text{m}$ . D) Representative immunofluorescence images of hiPSC-derived neural organoids (day 72) differentiated from the FLB hiPSC line stained for SOX2, PAX6 or FOXP1. Scale bars: 100  $\mu\text{m}$ . E) Representative immunofluorescence images of iAstros and iSCT Astros stained for GFAP, FABP7, S100 $\beta$ , Vimentin and GLAST. Scale bars; 200  $\mu\text{m}$ . F) Image based quantification of the percentage of marker positive cells. Data are shown as mean  $\pm$  SD. pAstro, iAstro FLB and LUMCi005 are N = 3. iSCT Astro FLB and LUMC114 are N = 2. G) Assessment of intracellular  $\text{Ca}^{2+}$  release in iAstros. Representative traces of normalized average fluorescence intensity (F/F<sub>0</sub>) in iAstros. Astrocytes were either stimulated by automated addition of plain NS medium (black) or NS medium supplemented with 3  $\mu\text{M}$  (light green) or 300  $\mu\text{M}$  (dark green) ATP. Data are shown as mean  $\pm$  SD of N = 3; iAstros from one hiPSC line (FLB), one differentiation, in three independent experiments. H) Quantification of intracellular  $\text{Ca}^{2+}$  release; normalized area under the curve, for pAstros and iAstros. Data shown as mean  $\pm$  SD of N = 3; iAstros from one hiPSC line (FLB), three differentiations, in three independent experiments. (I) Quantified glutamate uptake normalized to the number of cells (nmol/1000 cells) for pAstros, iAstros and HBVP. Data shown as mean  $\pm$  SD of N = 3, n = 6; one batch of pAstros and HBVPs and iAstros from one hiPSC line (FLB), three differentiations, in three independent experiments. One-way ANOVA with Tukey's multiple comparison. \*p < 0.05; ns, non-significant.

## Supplementary figure 2

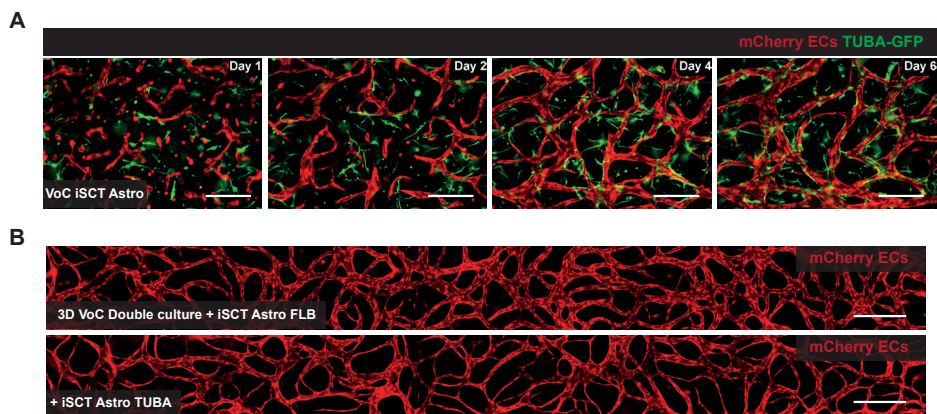


**Figure S2. Related to Figure 1. iSCT Astros incorporated into 3D VoC model.**

A) Representative immunofluorescence images from day 1, 2, 4 and 6 showing hiPSC-mCherry ECs (red) and hiPSC-TUBA astrocytes (green, TUBA-GFP) from the 'SCT' protocol (iSCT Astro) in VoC triple cultures. Scale bars: 250  $\mu$ m. B) Representative immunofluorescence images of microvascular networks in microfluidic chips on day 7 showing hiPSC-mCherry ECs (red). Images showing microvascular networks from 3D VoC triple cultures including iSCT Astros from two independent hiPSC lines (FLB or TUBA). Scale bars: 250  $\mu$ m.

### Supplementary figure 3

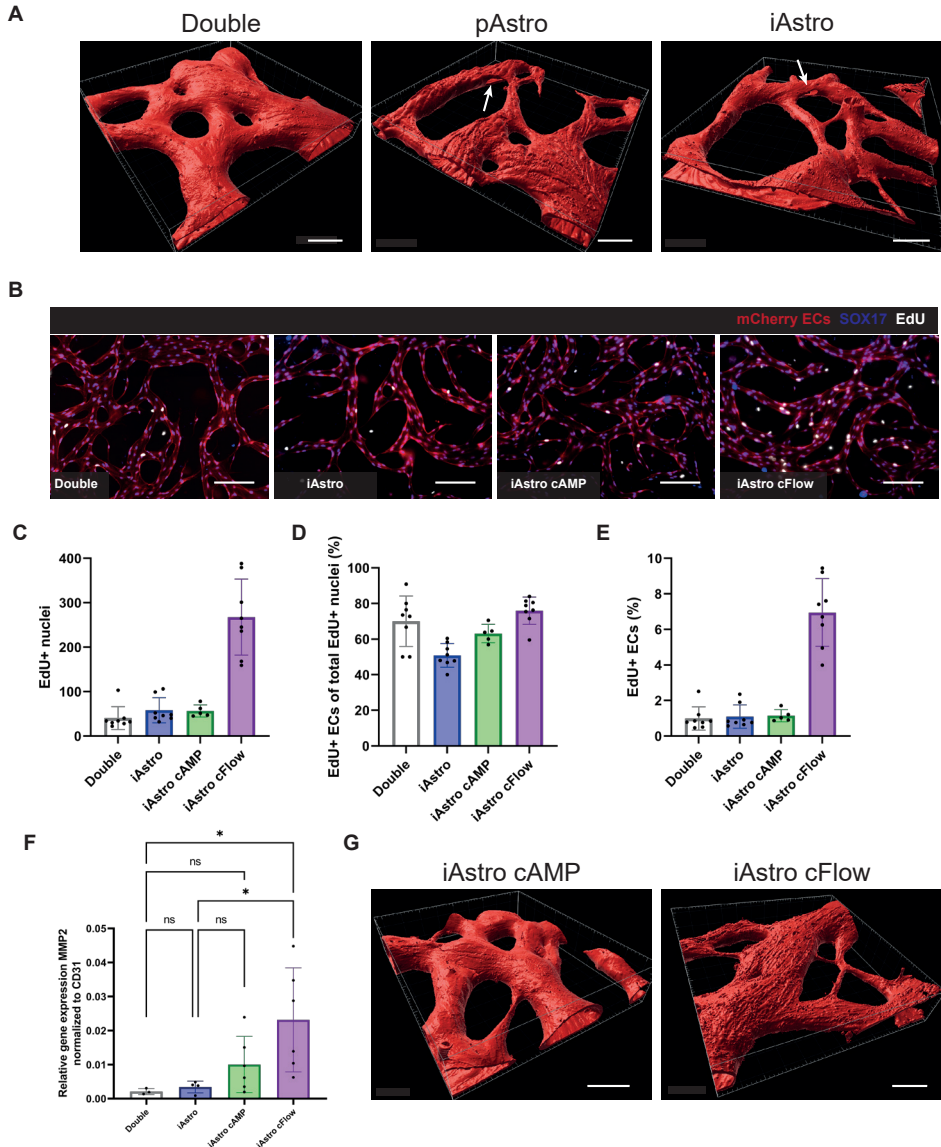


**Figure S3. Related to Figure 3. Microvascular network integrity in VoC conditions increased proliferation and increased MMP2 expression upon continuous flow in 3D VoC triple cultures with astrocytes.**

A) Representative immunofluorescence confocal surface rendered images of microvascular networks in microfluidic chips of VoC cultures on day 7 showing hiPSC-mCherry ECs (red). Scale bars: 100  $\mu$ m. B) Representative images showing proliferating cells (silver; EdU) and

ECs (red and green; mCherry-ECs and SOX17 respectively) in VoC double cultures (hiPSC-ECs with HBVPs) and VoC triple cultures with iAstros from the FLB hiPSC line. In the iAstro cAMP condition, medium was daily supplemented with 250  $\mu$ M dbcAMP and in iAstro continuous flow (cFlow) condition, microfluidic chips were continuously perfused from day 3 onwards. Microfluidic channels were fixed and stained at day 4. Scale bars: 200  $\mu$ m. (C-E) Quantification of proliferation showing the total number of EdU positive nuclei (C), percentage of proliferating cells which are ECs  $((\text{EdU}+ \text{SOX17}+)/(\text{EdU}+)*100)$  (D) and percentage of ECs which are proliferating  $((\text{EdU}+ \text{SOX17}+)/(\text{SOX17}+)*100)$  (E). Data shown as mean  $\pm$  SD of N = 2, n = 8; two independent experiment with a minimum of 3 microfluidic channels per experiment. Exception is iAstro cAMP with N = 1, n = 5; one independent experiment with 5 microfluidic channels. F) Relative expression of MMP2 normalized to CD31 as assessed with quantitative real-time PCR (qRT-PCR) for the four VoC culture conditions at end-point day 7. Data shown as mean  $\pm$  SD from N = 3-6 independent experiments. In the iAstro conditions, data shown is from triple cultures containing both iAstros from the FLB and the TUBA hiPSC line. One-way ANOVA with Sidaks multiple comparison test. \*p < 0.05 G) Representative immunofluorescence confocal surface rendered images of microvascular networks in microfluidic chips of VoC cultures on day 7 showing hiPSC-mCherry ECs (red). Scale bars: 100  $\mu$ m.

## Supplementary figure 4

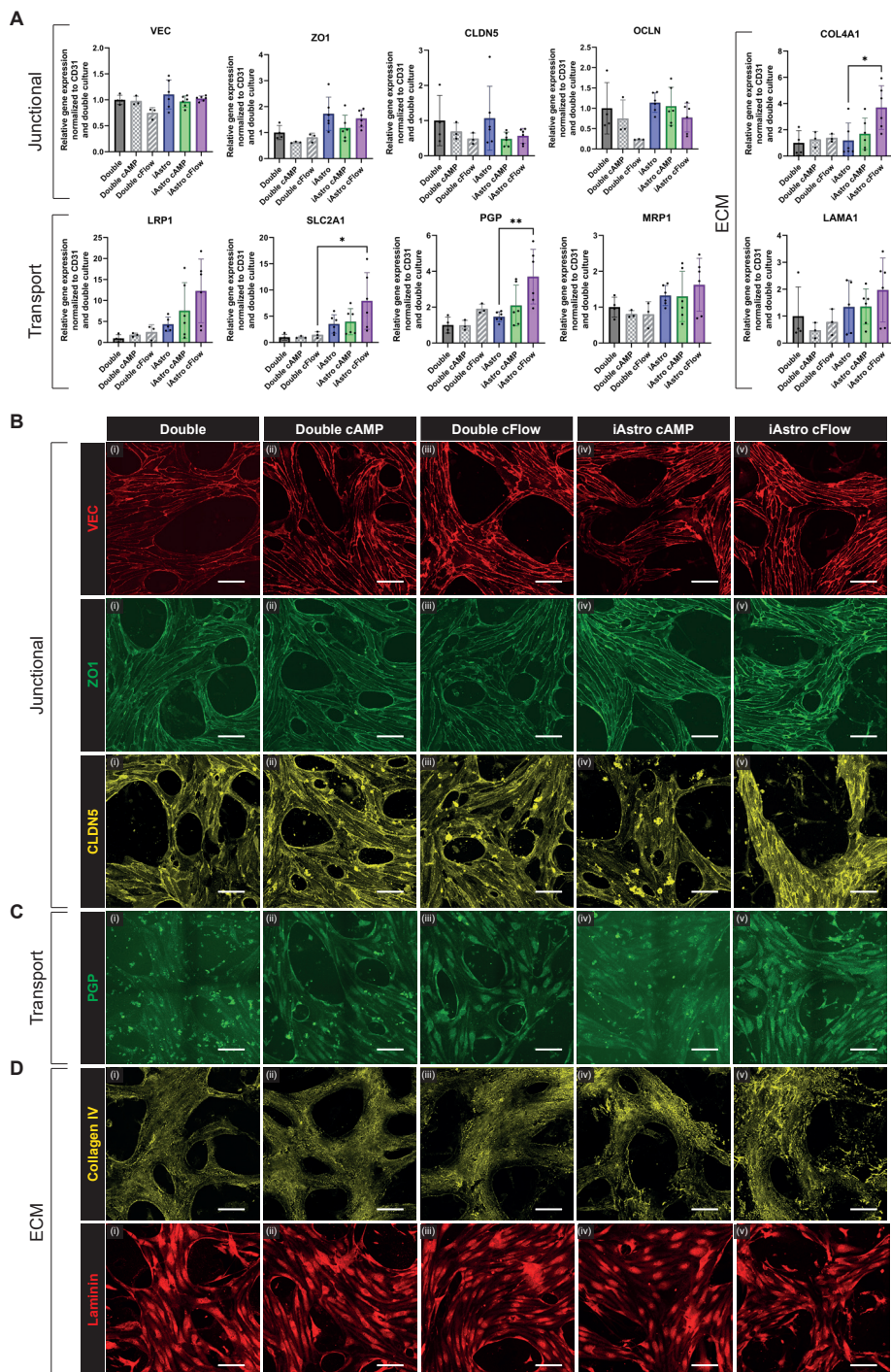


**Figure S4. Related to Figure 4. Assessment of blood-brain barrier properties in 3D VoC cultures.**

A) RNA expression of key BBB-genes for the different 3D VoC culture conditions. Values were obtained with qRT-PCR and were normalized to housekeeping gene hARP and to CD31. Individual repeats are plotted for the conditions indicated. B) Representative immunofluorescence confocal images for junctional proteins VE-Cadherin (VEC), Zonula occludens-1 (ZO1) and Claudin-5 (CLDN5). C) Representative immunofluorescence confocal images for transporter protein P-glycoprotein (PGP). D) Representative immunofluorescence confocal images for extracellular matrix (ECM) proteins Collagen IV and Laminin. Scale bars: 100  $\mu$ m. Data are shown as mean  $\pm$  SD. For N = 3-4, n = 3-6; three or four independent experiments with one pulled RNA sample per condition. In the iAstro conditions, data is pulled from triple cultures containing both iAstros from the FLB and the TUBA hiPSC lines. One-way ANOVA with Sidaks multiple comparison test. \*p < 0.05, \*\*p < 0.01; ns, non-significant.

**Supplemental Table 1. List of hiPSC lines and batches used per experiment**

Figure	hiPSC-ECs		hiPSC-Astros	
	Line	Number of batches	Line	Number of batches
Fig S1 F	-	-	iAstro: LUMC0020iCTRL	3
			iAstro: LUMCi005-A	1
			iSCT-Astro LUMC0020iCTRL	2
			iSCT-Astro LUMC114iCTRL01	2
Fig S1 H, I	-	-	LUMC0020iCTRL	3
Fig 1 D-F ; 2 B, D, E	NCRM-1	3	LUMC0020iCTRL	2
			AICS-0012	1
Fig 3 C-F	NCRM-1	3	AICS-0012	1
Fig 4 D-F ; S3 B-D	NCRM-1	3	LUMC0020iCTRL	2
Fig 4 G, I; S4 A	LUMC0054iCTRL02	1	LUMC0020iCTRL	1
			AICS-0012	1
Fig S4 C, E, G	LUMC0054iCTRL02	1	LUMC0020iCTRL	1

**Supplemental Table 2. List of antibodies for IF**

Antibody	Species	Source	Use	Dilution	Catalog #
SOX2	Rat	eBiosciences	2D	1:200	53-9811-80
PAX6	Rabbit	Cell Signaling	2D	1:200	60433S
FOXP1	Rabbit	Abcam	2D	1:200	ab18259
GFAP	Rabbit	DAKO	2D + 3D VoC	1:1500	Z033401
FABP7	Mouse	Santa Cruz	2D + 3D VoC	1:500	sc-374588
S100 $\beta$	Mouse	Sigma	2D	1:500	S2532
VIM	Mouse	Sigma	2D	1:300	V6630

SLC1A3/GLAST/ EAAT1	Mouse	Miltenyi	2D	1:100	130-095-822
Aqp4	Rabbit	Novus Bio	3D VoC	1:200	NBP1-87679
NG2	Mouse	Santa Cruz	3D VoC	1:200	sc-53389
SM22/TAGLN	Rabbit	Abcam	3D VoC	1:400	ab14106
SOX17	Goat	R&D systems	3D VoC	1:300	AF1924
PGP	Mouse	Invitrogen	3D VoC	1:100	MA1-26528
CollagenIV	Goat	Millipore	3D VoC	1:200	AB769
Laminin	Rabbit	Sigma	3D VoC	1:100	AB19012

### Supplemental Table 3. List of primers for qRT-PCR

Target	Forward primer (5' – 3')	Reverse primer (5' – 3')
VEC	GGCATCATCAAGCCCATGAA	TCATGTATCGGAGGTCGATGGT
CD31	GCATCGTGGTCAACATAACAGAA	GATGGAGCAGGACAGGTTCCAG
ZO1	CAACATACAGTGACGCTTCACA	CACTATTGACGTTTCCCCACTC
CLDN5	GCGTGCTCTACCTGTTTTGC	CAGCTCGTACTTCTGCGACA
OCLN	ACAAGCGGTTTTATCCAGAGTC	GTCATCCACAGGCGAAGTTAAT
SLC2A1	AACTCTCAGCCAGGGTCCAC	CACAGTGAAGATGATGAAGAC
PGP	TGACCCGCACTTCAGCTAC	GGGCTTCCCAGATGATGTCG
MRP1	TTACTCATTAGCTCGTCTTGTC	CAGGGATTAGGGTCGTGGAT
LRP1	CTATCGACGCCCTAAGACTT	CATCGCTGGGCCTTACTCT
COL4A1	CAAAAGGGTGATACTGGAGAACC	ATTCCTGCGAAACCAGGCA
LAMA1	GTGATGGCAACAGCGCAA	GACCCAGTGATATTCTCTCCCA
MMP2	CTACGATGGAGGCGCTAATGG	CTTGGGGCAGCCATAGAAGG

## Supplemental Experimental Procedures

### Differentiation of hiPSCs towards ECs

hiPSCs were maintained in mTeSR-E8 and differentiated towards ECs as previously described<sup>1,2</sup>. Briefly, mesoderm was induced by changing the media to B(P)EL medium supplemented with 8  $\mu$ M CHIR99021 (Tocris Bioscience, 4423). Cells were refreshed at day 3, 6 and 9 with B(P)EL with VEGF (50 ng/mL) and 10  $\mu$ M SB431542 (Tocris Bioscience, 1614).

hiPSC-ECs were isolated on day 10 using CD31-Dynabeads™ (Thermo Fisher Scientific) as previously described<sup>1,2</sup>. hiPSC-ECs were expanded in complete EC growth medium comprised of Human Endothelial-serum free medium (EC-SFM) with 1% Human platelet poor serum (P2918, Sigma), VEGF (30 ng/mL) and bFGF (20 ng/mL). hiPSC-ECs were expanded for additional 3-4 days post-isolation and cryopreserved using serum-free cryopreservation medium at passage number 1 (P1) (CryoStor®CS10) (StemCell Technologies, 100-1061).

### **Differentiation of hiPSCs towards neural progenitors**

Neural progenitor cells (NPCs) were generated through a regionalized neural organoid phase as described previously, with minor modifications<sup>3</sup>. Briefly, hiPSCs were dissociated using 0,5 mM Ethylenediaminetetraacetic acid (EDTA, Invitrogen, 15575020) and plated as small clumps 1:1 into ultra-low attachment 6-well plate (Corning, 3471) or ultra-low T75 (Corning, 3814) in mTESR-1 with 20 ng/mL bFGF (Miltenyi Biotec, 130-093-842) and RevitaCell (Life Technologies, 1:200). Following day an additional refreshment with mTESR-1, bFGF and Revitacell. The subsequent day neural induction and regional (forebrain) patterning was started by changing the medium to Neuronal Induction Medium (NIM) consisting of advanced DMEM/F12 (Life Technologies, 31331028), 2 mM L-glutamine (Life Technologies, 25030), 1% non-essential amino acids (NEAA; Life Technologies, 11140035), 1% N2 supplement (Life Technologies, 17502048), 1% Penicillin-Streptomycin (Life Technologies, 15070063 ) supplemented with 0.1 μM LDN-193189 (Axon Medchem), 10 μM SB-431542 (Tocris Bioscience, 1614), 0.5 μg/mL DKK-1 (PreproTech, 120-30B) and 1 μM cyclopamine (R&D systems, 1623/1). Patterning took place from day 0 until day 12 with medium changes every second day. NPCs were matured from day 12 to day 30 by refreshment every second day with NIM medium supplemented with 20 ng/mL brain-derived neurotrophic factor (BDNF; Peprotech, 450-02). NPCs were expanded from day 30 by switching to Neurosphere (NS) Medium consisting of advanced DMEM/F12, 2 mM L-glutamine, 1% NEAA, 2% B27 supplement (Life Technologies, 17504044), 2 μg/mL heparin (Leo Pharma BV, 14179857) and 1% Penicillin-Streptomycin supplemented with 20 ng/mL bFGF and 20 ng/mL epidermal growth factor (EGF; R&D systems, 236-EG-200). Medium was changed two times a week and NPC spheres were manually dissociated to small clumps approximately every one and a half week. At day 60, NPC spheres were manually dissociated to small clumps and cryopreserved in 50 % NS medium, 40 % FBS (Biowest, S1860) and 10 % dimethyl sulfoxide (DMSO; Sigma, D2650). NPCs were thawed and cultured on 6-well plates coated with 20 μg/mL poly-ornithine (PO; Sigma, P3655) and 5 μg/mL laminin (Sigma, L2020) and maintained for 5 days in NS medium supplemented with 20 ng/mL bFGF and 20 ng/mL EGF to recover. The first day the media was also supplemented with 1:200 Revitacell. The NPCs were subsequently used for differentiation towards astrocytes.

### **Differentiation of neural progenitors towards astrocytes**

NPCs were either differentiated using a previously published protocol<sup>3</sup> (iAstros) or using a commercially available kit (iSCT Astros). In the iAstro differentiation, astrocyte specification was started by changing the media to NS medium supplemented with 20 ng/mL CNTF (Peprotech, 450-13). When reaching 80-90% confluency, cultures were passaged 1:4 using accutase (Millipore, SCR005). At day 30, astrocytes were cryopreserved in CryoStor<sup>®</sup>CS10. For characterization and functional assays of astrocytes, cryopreserved iAstros were thawed and cultured for 3 days on PO/laminin-coated plates in NS medium supplemented with 20 ng/mL CNTF.

For iSCT Astro differentiation, NPCs were passaged to matrigel-coated plates and maintained in STEMdiff<sup>™</sup> Neural Progenitor Medium (StemCell Technologies, 05833) for 4-5 days to recover and expand. NPCs were subsequently differentiated using the STEMdiff<sup>™</sup> Forebrain Neuron Differentiation Kit (StemCell Technologies, 08600), following manufacturer's protocol. After completing the 7 days differentiation protocol, medium was changed to BrainPhys<sup>™</sup> Neuronal medium (StemCell Technologies, 05790) and cells were maintained for 11 more days before using in functional assays. Population of astrocytes was confirmed by positive staining for key astrocyte markers. Cells were passaged using accutase before use in microfluidic chips to enrich the astrocyte population.

#### **Primary human brain vascular pericyte and primary astrocyte culture**

Human brain vascular pericytes (HBVPs) and primary human cortical astrocytes (pAstros) were purchased from ScienceCell. HBVPs were cultured in Pericyte Medium (ScienceCell, 1201) supplemented with 1% Pericyte Growth Supplement (ScienceCell, 1252), 2% FBS and 1% penicillin/streptomycin. pAstros were cultured on poly-L-lysine coated (15 µg/mL, Sigma, P4707) plates in Astrocyte Medium (ScienceCell, 1801) supplemented with 1% Astrocyte Growth Supplement (AGS, Sciencell, 1852), 2% FBS and 1% penicillin/streptomycin. HBVPs and pAstros were cryopreserved at passage number 3 (P3) or 2 (P2) respectively, using serum-free cryopreservation medium (CryoStor<sup>®</sup>CS10) (StemCell Technologies, 100-1061).

#### **Immunostaining and microscopy of forebrain neural organoid**

Forebrain neural organoids were fixed with 4% paraformaldehyde (PFA, Sigma) for 30 minutes at 4 °C and washed with phosphate-buffered saline (PBS) before continuing for wholemount staining. Cell plasma membranes were permeabilized with 0.5% Triton X-100 for 15 minutes at RT and washed 3 times for 10 minutes with PBS. Blocking was performed by adding 2% BSA in PBS for 3 hours at RT. Primary antibodies (see Supplemental Table 1 for details) were diluted in 1% BSA in PBS and incubated O/N at 4 °C. After washing with PBS, secondary antibodies (1:300, Invitrogen) diluted in 1% BSA were added and incubated for 2 hours at RT. Stained organoids were mounted with ProLong Gold Antifade Mountant (ThermoFisher Scientific #P36930) on microscope slides. Images were taken using the EVOS M7000 using 20x magnification objective.

### **Immunostaining, microscopy and quantification of 2D astrocytes**

iAstros were seeded on PO/laminin coated 96-well black imaging plates (Corning) at a seeding density of 35000 cells/well in NS medium supplemented with 20 ng/mL CNTF. iSCT-Astros were seeded on PO/laminin coated 96-well black imaging plates at a seeding density of 35000 cells/well in BrainPhys™ Neuronal medium. Both were fixed 3 days later, using 4% PFA for 10 minutes at RT. Cell membranes were permeabilized with 0.1% Triton X-100 for 5 minutes at RT and washed with PBS before blocking with 1% BSA in PBS for 1 hour. Primary antibody diluted in 1% BSA were added and incubated O/N at 4 °C. For primary antibody overview see Supplemental table 1. Images were taken using EVOS M7000 using 10x magnification objective. Quantification of the percentage of marker positive astrocytes was performed using custom pipelines developed on the free open source CellProfiler software (<https://cellprofiler.org/>)<sup>4</sup>. In brief, both nuclei and marker objects were identified after pre-processing steps to reduce unspecific object identification. Nuclei and marker objects were subsequently overlapped for visual examination of proper identification and to calculate number of masked nuclei objects.

### **Immunostaining and microscopy of VoC**

Cells in VoCs were fixed *in situ* in 4% PFA for 30 minutes at RT. Cell plasma membranes were permeabilized with 0.5% Triton X-100 for 15 minutes at RT and washed 3 times for 10 minutes with PBS. Blocking was performed by adding 2% BSA in PBS for 3 hours at RT. Primary antibodies (see Supplemental Table 1 for details) were diluted in 1% BSA in PBS and incubated O/N at 4 °C. After washing with PBS, secondary antibodies (1:300, Invitrogen) diluted in 1% BSA were added and incubated for 2 hours at RT. Images of the full microfluidic channel of VoCs were taken with the EVOS M7000 using the 10x objective and automated stitching. 3D images were taken using the DragonFly spinning disk (Andor) microscope with 40x magnification objective, 2x2 tile scans with automated stitching and post-processing performed using Imaris 9.5 software (Bitplane, Oxford Instruments).

### **EdU assay for EC proliferation in 3D microfluidic chips**

Proliferation was measured using the EdU Click-iT kit Alexa-488 (ThermoFisher Scientific #C10337) according to manufacturer's protocol. Briefly, on day 4 of culture, microfluidic chips were refreshed with EGM-2 supplemented with 50 ng/mL VEGF and 1% AGS additionally supplemented with EdU (1:1000) for 6 hours. Cells were fixed with 4% PFA for 30 minutes, permeabilized with 0.5% TX-100 for 15 minutes at RT. Freshly prepared Click-iT reaction cocktail was added for 3 hours at RT. Microfluidic chips were washed three times with PBS and blocked in 2% BSA in PBS for 3 hours at RT, followed by co-staining with primary and secondary antibodies.

### **Characterization of vascular and perivascular parameters in 2D images**

Quantification of VoC vascular and perivascular parameters vessel density, average diameter, average vessel length, average astrocyte length and number, average HBVP length and number, EdU+ nuclei, EdU+ ECs of total EdU+ nuclei, EdU+ ECs, PGP intensity and CollagenIV and Laminin area from 2D images was performed as previously described<sup>5,6</sup>. Briefly, images of the whole microfluidic channel as acquired using EVOS M7000, were quantified using custom pipelines developed on the free open source CellProfiler software (<https://cellprofiler.org/>)<sup>4</sup>. Pre-processing steps were applied to all images to enhance image features and a gaussian filter to reduce unspecific object identification. A minimum cross-entropy thresholding method was used on vascular network images to produce a binarized image. The binarized images from the CellProfiler output were then analyzed using ImageJ software with the freely available plugin DiameterJ (<https://imagej.nih.gov/ij/>, <https://imagej.net/DiameterJ>)<sup>7</sup>. For quantification of CollagenIV and Laminin, a similar pipeline was used to generate binarized images. Quantification of PGP intensity was done by using a custom cell profiler pipeline with maximum projection images from 3D confocal images as input. Both intensity of PGP and area covered by either CollagenIV or Laminin staining was normalized by the area of the vessel, as determined by CD31 staining . EdU+ nuclei, EdU+ ECs of total EdU+ nuclei and EdU+ ECs were quantified with a custom-made pipeline in CellProfiler<sup>4</sup>.

### **Characterization of astrocyte and HBVP cell parameters in 3D**

Characterization and quantification of GFAP positive and SM22 positive objects and quantification of PGP intensity was performed by 3D quantitative analysis using images taken with the DragonFly spinning disk (Andor) and processed using Imaris 9.5 software (Bitplane, Oxford Instruments). Average HBVP SM22 object intensity and volume was obtained by first surface-rendering both individual SM22 positive objects and individual FABP7 or TUBA-GFP positive objects for the pAstro or iAstro conditions respectively. HBVP SM22 positive objects were obtained by filtering out the double positive objects. For quantification of the percentage of HBVP SM22 positive or GFAP positive objects touching the vessel, first an additional surface rendering of the microvascular network (mCherry positive) was performed. HBVP SM22 positive or GFAP positive objects touching the vessel was defined as a distance of 0  $\mu\text{m}$  between the surface-rendered objects and  $>0 \mu\text{m}$  distance was defined as no contact.

### **Perfusion assessment in VoC system**

Before the perfusion assessment and time-lapse imaging for permeability quantification, ECs were first stained using Ulex Europaeus Agglutinin I, DyLight594 (1:600, Vector Laboratories, DL-1067) by incubation of the microfluidic channels for 45 minutes in the incubator. Subsequently, time-lapse images were taken using the EVOS M7000 with on stage

incubator with the 10x objective at 20 fps for 30 seconds. 70  $\mu\text{L}$  of 70 kDa FITC-Dextran (1:1000, Sigma) in EGM-2 was added to one medium port and 50  $\mu\text{L}$  of EGM-2 to all other media ports to induce interstitial gravity driven flow. Agglutinin was imaged at the same location as the dextran perfusion was imaged to enable accurate assessment of fluorescent tracer leakage inside and outside the microvascular network. Calculation of permeability coefficient was based on previously established methods<sup>8</sup>. In short, the following formula was used:

$$P = 1/\Delta t * A_m/SP_v * \Delta I_m/\Delta I$$

With  $\Delta t = T_2 - T_1$  (30 seconds),  $A_m$  being the surface area of the matrix,  $SP_v$  being the surface perimeter of the vessel,  $\Delta I_m = (I_{m2} * (I_{v1}/I_{v2})) - I_{m1}$  being the difference in fluorescence intensity in the matrix corrected for potential changes in the dextran concentration in the vascular space during imaging and  $\Delta I = I_{v1} - I_{m1}$  being the difference in fluorescence intensity between the vasculature and matrix at the start of the measurement.

### Assessment of intracellular Ca<sup>2+</sup> release in astrocytes

Intracellular Ca<sup>2+</sup> release was assessed in astrocytes at day one post-seeding in a black, flat-bottomed 96-well plate coated with poly-L-lysine for pAstros and PO/laminin for iAstros. The calcium-6 dye (Molecular Devices) was dissolved in 10 mL HBSS buffer B and subsequently diluted 1:4 in Buffer B (Molecular Devices). The diluted dye solution was added 1:1 to the wells containing astrocytes in NS medium. Astrocytes were incubated for 2 hours at 37 °C with 5% CO<sub>2</sub> before being measured on the FDSS/ $\mu\text{cell}$  (Hamamatsu Photonics) at 37 °C with an exposure time of 0.017s. Response to ATP stimulus was performed by first preparing a compound plate including a medium control of NS medium, 30  $\mu\text{M}$  ATP (Sigma, A9187) in NS medium or 3 mM ATP in NS medium. Control and ATP stimulus from the compound plate were automatically mixed and injected into the assay plate, reaching final ATP concentrations of 3 and 300  $\mu\text{M}$ . Analysis was performed in R (4.0.3) and the induced change in Ca<sup>2+</sup> release was calculated by quantification of the area under the curve of the average fluorescence intensity normalized to the NS medium control.

### Glutamate uptake assay

A colorimetric glutamate assay kit (Sigma, MAK004) was used to determine the reduction of glutamate in the cell culture medium over time. Cells were plated 2 days before the assay in a 96 well plate. Before the assay, cells were washed with HBSS (Gibco) and then incubated with 100  $\mu\text{M}$  glutamate in HBSS. Samples were collected and analyzed according to the manufacturer's instructions. The uptake of glutamate was normalized to the number of cells per well. Cells were stained with 1  $\mu\text{g}/\text{mL}$  HOECHST 33342 (Thermo Fisher Scientific, 62249) for 20 minutes before washing with PBS. Whole wells were imaged using EVOS M7000 and

subsequent downstream identification and quantification of the number of nuclei was performed with ImageJ software (<https://imagej.nih.gov/ij/>).

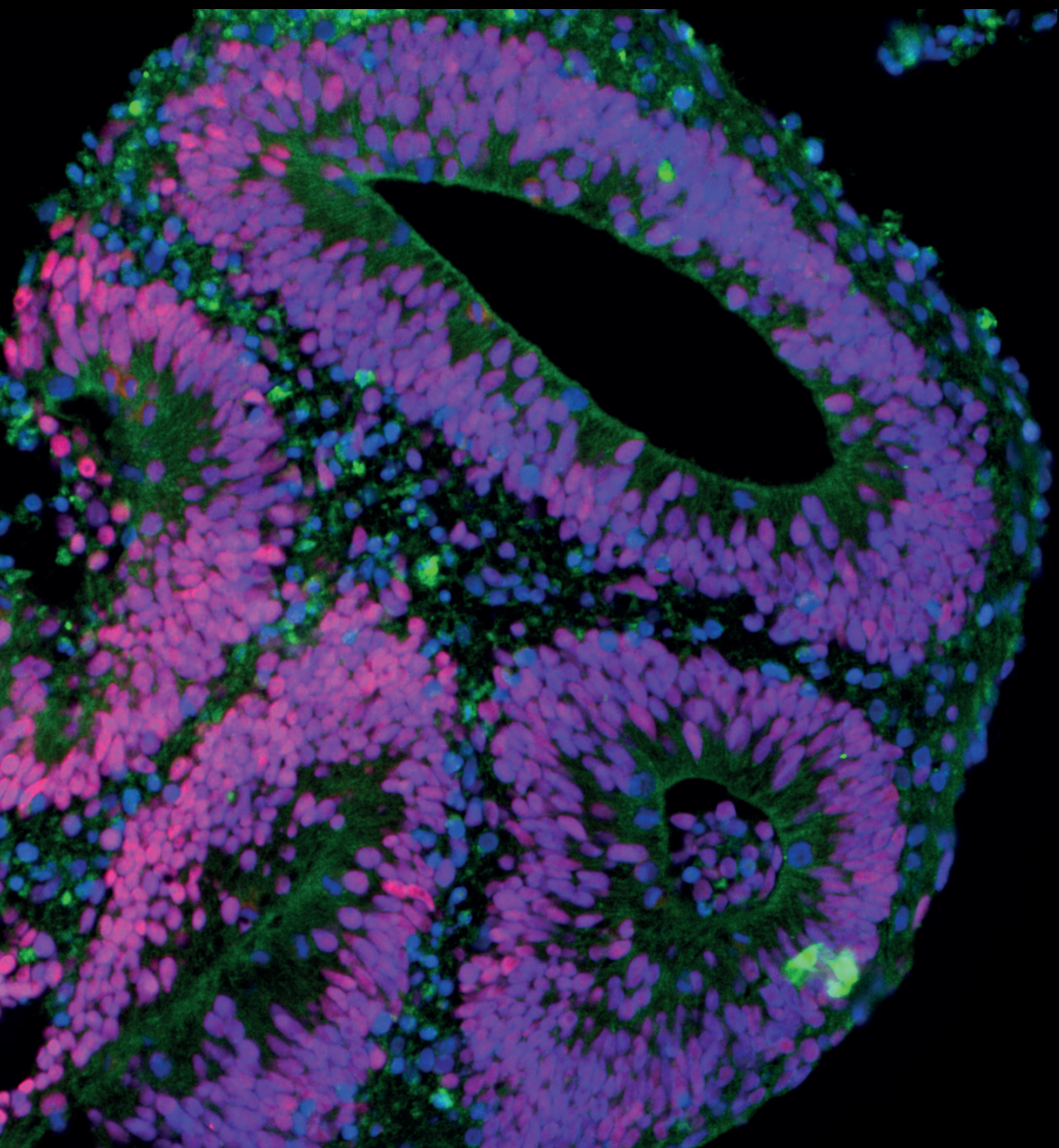
### **RNA isolation and quantitative RT-PCR**

Total RNA was isolated from the microfluidic devices at end-point day 7. Cells were extracted by dissolving the extracellular matrix / fibrin mix with Collagenase B (1 mg/ml, Roche, 11088815001) for half an hour at 37 degrees °C, while rocking. RNA was extracted using the NucleoSpin RNA XS kit (Macherey-Nagel) and cDNA was synthesized using an iScript-cDNA Synthesis kit (Bio-Rad). iTaq Universal SYBR Green Supermixes (Bio-Rad) and Bio-Rad CFX384 real-time system were used for the PCR reaction and detection. Primers used can be found in Supplemental Table 3. Relative gene expression was calculated using the delta Ct calculation and normalized to the housekeeping gene hARP and to CD31. Heatmap was generated using the freely available online tool <http://www.heatmapper.ca/expression/><sup>9</sup>.

### **Supplemental References**

1. Orlova, V. V. *et al.* Generation, expansion and functional analysis of endothelial cells and pericytes derived from human pluripotent stem cells. *Nat Protoc* **9**, 1514–1531 (2014).
2. Orlova, V. V. *et al.* Functionality of endothelial cells and pericytes from human pluripotent stem cells demonstrated in cultured vascular plexus and zebrafish xenografts. *Arterioscler Thromb Vasc Biol* **34**, 177–186 (2014).
3. Peterj, U. *et al.* Generation of the Human Pluripotent Stem-Cell-Derived Astrocyte Model with Forebrain Identity. *Brain Sci* **11**, (2021).
4. Carpenter, A. E. *et al.* CellProfiler: Image analysis software for identifying and quantifying cell phenotypes. *Genome Biol* **7**, (2006).
5. Vila Cuenca, M. *et al.* Engineered 3D vessel-on-chip using hiPSC-derived endothelial- and vascular smooth muscle cells. *Stem Cell Reports* **16**, (2021).
6. Orlova, V. v *et al.* Vascular defects associated with hereditary hemorrhagic telangiectasia revealed in patient-derived isogenic iPSCs in 3D vessels on chip. *Stem Cell Reports* **17**, 1536–1545 (2022).
7. Hotaling, N. A., Bharti, K., Kriel, H. & Simon, C. G. DiameterJ: A validated open source nanofiber diameter measurement tool. *Biomaterials* **61**, 327–338 (2015).
8. Hajal, C. *et al.* Engineered human blood–brain barrier microfluidic model for vascular permeability analyses. *Nat Protoc* **17**, 95–128 (2022).
9. Babicki, S. *et al.* Heatmapper: web-enabled heat mapping for all. *Nucleic Acids Res* **44**, W147–W153 (2016).





# **Chapter 7**

## **Discussion and future perspectives**

## Introduction

Organ-on-Chip (OoC) models have emerged in the recent years as possible solutions to the substantial hurdle faced in drug development, where only a small fraction of candidate drugs advances to clinical approval, largely due to the inability to predict responses (and effectivity) in humans. Simple models are adequate in most primary compound screens for drug discovery but for more complex (secondary) screens *in vitro* models are needed that faithfully recapitulate human physiology<sup>1</sup>. Cardiovascular diseases are an increasing burden on society and thus present a prime target for the development of advanced (secondary) *in vitro* models. In this thesis, several steps have been taken to enable modeling of vascular diseases. Firstly, multiple cellular tools were generated from human pluripotent stem cells (hPSCs): endothelial cells, vascular smooth muscle cells and astrocytes. Some of these cells were employed successfully to study vascular defects in traditional 2D vasculogenesis assays. Secondly, Vessel-on-Chip (VoC) systems were developed to increase complexity and provide the appropriate stimuli to uncover cellular defects as seen *in vivo*. Ultimately, these complex secondary screen could be used to determine the effectivity of drug treatments in patients. The foundation of disease modeling in this thesis lies in the utilization of human induced pluripotent stem cells (hiPSCs) and their derivatives.

## hiPSC-derived cells for disease modeling

hiPSCs have found applications across various model types for disease modeling and drug screening in traditional 2D cultures, microfluidic chips, tissue engineering or organoids<sup>2,3</sup>. While the pursuit for the most complex models may be academically intriguing, it is essential to adhere to the principle of seeking as much as simplicity as the research question allows. If a disease phenotype can be observed with a 2D assay, it offers a more cost-effective, potentially high throughput platform for future mechanistic and therapeutic studies. In this thesis, hiPSC lines and/or their isogenic controls were generated from patients with three distinct genetic vascular diseases in Chapter 3, Chapter 4 and Chapter 5. These studies yielded varying results in demonstrating disease phenotypes, some assays showing expected outcomes in relation to the patient phenotype, others being more challenging to interpret. This underscored the importance of several key considerations in hiPSC-based disease modeling.

Among the most basic issues, the first consideration regards the verification of the hiPSC lines and determination of the number of lines and clones to use when modeling diseases. hiPSC disease modeling often demands a large cohort size due to the greater genetic variability between lines compared to traditional inbred animal models or standard cell lines<sup>4</sup>. Recent studies have focused on understanding the statistical power and optimal study design for hiPSC-derived disease models. These studies have highlighted the increased power of using isogenic paired- over non-isogenic (familiarily related or independent) hiPSCs, particularly in modeling monogenic disorders, by minimizing the variation stemming

from individual genetic differences<sup>5</sup>. This aligns with the experimental design employed in the disease modeling in both Chapter 4 and Chapter 5. However, to further enhance the generalizability of findings to broader patient groups, inter-individual variation needs to be incorporated in the study. The most cost-effective way to achieve this is by including additional donors rather than increasing the number of hiPSC clones in the study design<sup>6</sup>. An innovative and potentially effective approach to do this is by combining different lines in a single dish, referred to as “village in a dish” model systems. These model systems have demonstrated the ability to significantly increase throughput while maintaining consistency in genetic, epigenetic or line-dependent effects underlying gene expression variation, comparable to cells cultured separately<sup>7</sup>.

The second consideration in hiPSC disease modeling is the potential influence of the X-chromosome inactivation status (XCI) when working with female lines. As discussed in Chapter 4, aberrant XCI status in female hiPSCs could lead to changes in the cellular protein content and differentiation potential<sup>8–10</sup>. While erosion of XCI is primarily seen in human embryonic stem cells (hESCs) and only to a lesser extent in hiPSCs<sup>11</sup>, significant variation remains between hiPSC lines. Interestingly, in Chapter 4, differences in XCI status between clones did not appear to directly correlate with hiPSC-ECs differentiation potential, as evidenced by variation in both gene and protein expression of EC-specific markers. This is consistent with some other reports demonstrating XCI status independent differentiation efficiencies into germ cells<sup>12</sup>. Future investigations should aim to elucidate the underlying mechanisms, potentially by exploring strategies to prevent aberrant XCI, as demonstrated with hESCs through changes in media composition using lithium chloride or inhibitors of GSK-3 proteins<sup>13</sup>.

The final consideration is the recognized immaturity of most hiPSC-derived cells, which can limit the *in vitro* replication of disease phenotypes observed *in vivo*<sup>3,14</sup>. Immaturity as a limitation may also explain the absence of EC-defects seen in RVCL patient-derived hiPSC-ECs, as demonstrated in Chapter 4. Several strategies could be employed to enhance the maturity of hiPSC-derived cells, ranging from manipulation and improvement of the extracellular matrix (ECM), metabolism (e.g. altering the energy substrate), 3D culture, or biochemical stimulation of the cell culture using a multiplicity of reagents<sup>15</sup>. OoCs, and specifically VoC devices used in this thesis, offer unique abilities to alter these aspects in a controlled fashion by including microfluidic flow for factor delivery as well as shear stress over the endothelial cells lining the vessel wall.

## Vessels-on-Chip

The potential of complex humanized models, such as VoCs, has been recognized for over a decade<sup>16</sup>. However, examples of studies actually demonstrating their true benefit over traditional models to uncover disease pathologies remained limited. In this thesis, we provided such an example in Chapter 5 by unveiling a disease phenotype within a VoC

device that was absent in standard 2D assays. Furthermore, we extended our VoC model towards a brain-specific variant in Chapter 6. The extensions to model these brain-specific interactions hold particular significance due to the urgent need for complex humanized models, specifically in the context of vascular pathologies of the human brain for which access to primary tissue (biopsies) is mostly not an option. Recent studies have emphasized this urgency, by clearly showing only minimal overlap between *in vivo* mouse and human transcriptomic changes induced by stroke in the brain microvasculature<sup>17</sup>.

The VoCs models in this thesis make use of the self-assembly ability of the vascular cells introduced into the chips. While they demonstrated their value, our work has also highlighted certain general considerations in future exploration of these models. For discussion of these considerations, it is helpful to regard the model as a concept of *designed* and *emergent* features which have to be compared to *in vivo* physiology as far as possible, this was described and considered at length in the review in Chapter 2. For an overview and distinction of designed versus emergent features, particularly relevant in self-assembling VoCs, see Figure 1.

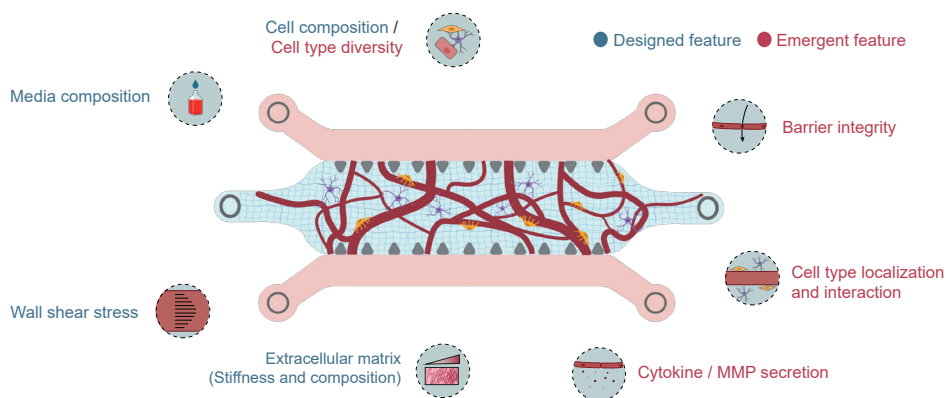


**Figure 1: Schematic of the essential designed and emergent features in self-assembling Vessel-on-Chip models.** MMP = matrix metalloproteinases. (Icons of the features were adapted from Nahon, Moerkens et al 2023, in press)

### Designed features in self-assembling VoCs

In Chapter 5, we successfully uncovered a disease phenotype using hiPSC-ECs derived from hereditary hemorrhagic telangiectasia (HHT) patients, using a commercially-available self-assembling VoC model. While this underscores the model's current utility, several facets offer room for refinement to achieve a closer resemblance to clinical manifestations. We were able to replicate the reduced mural cell – EC interactions as observed *in vivo*<sup>18</sup>; however, we simultaneously observed a decrease in the vessel diameter where in HHT patients, the average vessel diameter is increased, culminating in the formation of arteriovenous

malformations (AVMs). This occurs due to increased EC proliferation, EC enlargement and reduced EC migration<sup>19–22</sup>. One plausible explanation for this *in vivo/in vitro* difference is that the *in vivo* HHT phenotype is significantly influenced by secondary factors such as inflammation<sup>23</sup> and shear stress<sup>19,24–26</sup>. Consequently, incorporating inflammation as an additional trigger, either in the form of cellular source of inflammatory cells or via media supplementation with inflammatory cytokines, could be considered as a designed feature. Notably, we have proof-of-concept data illustrating an enhanced inflammatory response of HHT1 hiPSC-ECs when exposed to TNF $\alpha$  and BMP9 (Xu Cao, unpublished work). This was demonstrated at both a transcriptional level through RNA-sequencing and functionally via impaired barrier function. Future work could also include the inflammatory component in a cellular form by introducing HHT1 mutant and wildtype hiPSC-derived monocytes in the system. Previous reports have demonstrated that self-assembling models like these enable the functional characterization of immune cell recruitment, interaction and transmigration within the microvascular network<sup>27</sup>.

Shear stress is another secondary factor influencing HHT phenotypes *in vivo*<sup>28</sup>. Ways to modulate this could be introduced to the model as designed feature, specifically as fluid flow under controlled and variable flow rates. The most straight forward way, as implemented in Chapter 6, is to use a “rocker” platform that can induce continuous (albeit bidirectional) fluid flow in the microfluidic chips. This method is easy to scale for large numbers of samples; however, we estimate that it yields an average shear rate in the microvascular networks of  $\sim 0.01$  Pa, an order of magnitude lower than seen in the human body<sup>29</sup>. It is worth noting, that the use of a rocking platform induces bidirectional flow, which has been shown to induce distinct cellular behavior and transcriptional responses compared to the physiological unidirectional flow seen *in vivo*<sup>30–33</sup>. This divergence in behavior is likely influenced by the ECs’ known directional response to flow, inducing cellular rearrangements through cytoskeletal remodeling to migrate in the opposite direction of the flow<sup>34</sup>. To circumvent this, unidirectional flow in self-assembling systems has been established by use of large 3D printed reservoirs on the inlets allowing application of a substantial hydrostatic pressure<sup>35–37</sup>, or by connecting the microfluidic chip to a pressure pump<sup>38,39</sup>. Implementing similar strategies in our model could potentially enhance the physiological relevance and facilitate the exploration of additional disease mechanisms.

In Chapter 6 we established a self-assembling VoC model using hiPSC-ECs, human brain vascular pericytes (HBVPs) and hiPSC-derived astrocytes (iAstros), replicating cellular interactions that would occur in the blood brain barrier (BBB). iAstros and primary human astrocytes (pAstro) exhibited similar behavior within the VoC cultures and we subsequently demonstrated that we could further improve the culture by application of continuous flow or activation of the cAMP pathway. Nevertheless, the model did not consistently exhibit an upregulation of BBB-specific EC markers, so that even though the correct cell types were present, features seem to be still missing. To optimize the model further, exploration of

additional alterations in designed features, such as cell source, media composition and extracellular matrix (ECM), is needed.

The generation of hiPSC-ECs with BBB characteristics has been a dynamic and debated field over the past decade. As outlined in Chapter 1, one of the most used protocols to generate these cells, yields ECs with a strong resemblance to epithelial-like cells<sup>40</sup>. To enable establishment of genuine ECs with BBB characteristics, in Chapter 6 we chose to use hiPSC-ECs generated from a mesodermal state, aligning with known developmental pathways. While we previously demonstrated the capacity of hiPSC-ECs to acquire tissue-specific characteristics through co-culturing with tissue-specific cells<sup>41</sup>, the co-culture with iAstros did not consistently induce tissue-specific transcriptomic changes. *In vitro* studies have highlighted the role of astrocyte-secreted factors such as sonic hedgehog and angiotensin in supporting and inducing BBB function<sup>42–44</sup>. Future work should investigate whether our iAstros produce these proteins in the VoC model. Alternatively, supplementing the culture media with these factors could potentially enhance the BBB-phenotype in hiPSC-ECs.

Furthermore, the choice of matrix in the self-assembled model could be fine-tuned to enhance astrocyte culture and EC-brain specification. Currently, the OoC model uses a fibrin hydrogel for embedding the cells in the microfluidic device. Although hiPSC-ECs eventually deposit their own basement membrane, modifying the hydrogel to more closely mimic the brain's molecular composition and stiffness is a potential avenue for future research. Fibrin is favored for its ease of use, EC compatibility and relatively low batch-to-batch variability. However, it lacks similarity to the native brain ECM, which is composed of glycosaminoglycans (particularly hyaluronan), proteoglycans, glycoproteins, and small amounts of fibrous proteins (e.g. collagen, fibronectin, and vitronectin)<sup>45–47</sup>. Supplementing the fibrin hydrogel with some of these factors could increase the similarity with *in vivo* brain tissue, potentially inducing a more faithful EC-BBB phenotype. Alternatives are designed defined matrices, such as crosslinked networks of polyethylene glycol (PEG) linked to RDG peptides, which could target and adhere to integrins on cell surfaces, minimizing variability associated with biological matrices<sup>48</sup>.

### **Emergent features in self-assembling VoCs**

To accurately model a disease and relate *in vitro* to *in vivo* observations, a model system must enable accurate quantification of the relevant emergent features. In Chapter 5 and Chapter 6, three emergent features of interest were barrier integrity in the form of apparent permeability, cell type diversity and cytokine and matrix metalloproteinases (MMP) secretion.

In both Chapter 5 and Chapter 6, we evaluated barrier integrity by quantifying the apparent permeability of cells in the self-assembling VoC using a dextran permeability assay. The quantified apparent permeabilities for 70 kDa were in the range of  $10^{-4}$  cm/s. This

value is orders of magnitude lower than seen *in vivo* ( $\sim 10^{-7}$ )<sup>49</sup>. Interestingly, other similar *in vitro* self-assembling models, using primary astrocytes, have reported permeability values more in line with physiological norms<sup>35,39</sup>. The differences between these values could be attributed in part to the inherent variability in the technical challenges associated with conducting permeability measurements in self-assembling models: the ECs may not form an entirely intact monolayer or the junctions may be deficient. Fluid flow rates inside the microvascular networks directly influence the availability and passage of the fluorescent dextran across the vasculature. The published studies each employ varying hydrostatic pressure when conducting the permeability assay and investigate microvascular networks with different average diameters, both factors directly affecting the flow rate within the system. Additionally, the density of the microvascular network can influence the fluorescent signal of the dextran detected within the 'extracellular matrix compartment'. Therefore, to facilitate meaningful comparisons of EC permeability, it would be advantageous to use a more standardized system offering control over both the flow rate and the vessel diameter.

In the development of a novel models, such as in Chapter 6, a comprehensive understanding of the exact cell type diversity and identity is essential for assessing the similarity of cultured cells to their *in vivo* counterparts. Chapter 6 uses a co-culture approach to induce a BBB identity in the ECs. This is one of the many different identities that ECs can adopt, each associated with the tissue in which they reside<sup>50</sup>. Due to the challenges associated with collecting sufficient high-quality RNA from the microfluidic devices, our comparisons between conditions have been limited to a select list of key BBB-EC markers. While informative, a preferred and less biased approach would be to perform single cell RNA sequencing (scRNAseq) on the VoCs. This would allow comparison with recently established scRNA seq databases containing data from both mouse and human brain vasculature<sup>51-53</sup>.

Lastly, to gain a comprehensive understanding of cellular responses, particularly under diseased conditions, accurate analysis of secreted components within the VoC culture is of great importance. In Chapter 6 we investigated the secretion of the matrix metalloproteinase 2 (MMP2) by measuring its concentration in the conditioned media using a cytokine bead assay. This assay offered quantitative detection of several proteins in a multiplexed fashion, using media samples collected at specific time points. Implementation of real-time sensors inside the microfluidic devices would allow the monitoring of cell state throughout the experiment. In this thesis, commercially available AIM Biotech chips were used, limiting the ability to incorporate such technological advances where needed. Future research using in-house microfluidic chip production, particularly optimization chip design through methods such as maskless photolithography (e.g. Alvéole Lab PRIMO)<sup>54</sup>, could facilitate the development of advanced platforms tailored to specific needs.

## Future perspectives

VoCs are beginning to prove to be a powerful tools for modeling various aspects of vascular

biology that has long been promised. In particular, the self-assembling VoCs, as used in this thesis, have demonstrated their value in uncovering biological processes associated with diseases. However, like all OoC models, a single model cannot address all biological questions. Future disease modeling efforts will benefit from the integration and application of multiple VoC models, each suited for the study of specific physiological features. Among the most complementary models to self-assembling VoCs are single lumen models, which offer superior control of fluid flow rates due to their uniform diameter<sup>55,56</sup>. Alternatively, more complex approaches are emerging, enabling the generation of engineered vascular networks using methods such as laser ablation, laser cavitation or UV-hydrogel patterning<sup>57,58</sup>. These networks facilitate the standardization of fluid flow profiles and permeability analysis, while allowing for some self-organization of the vascular structures to establish relevant cell-cell interactions as seen *in vivo*.

OoC in general, particularly in combination with hiPSCs and their derivatives, have also gained significant interest from both academic and industrial perspectives, most notably during the duration of this thesis research. A prime example of this growing interest and confidence in the models is the approval of the FDA modernization act 2.0 in December 2022, which authorizes the use of alternatives to animal testing, such as OoC technology. However, to fully realize their potential and completely integrate in the workflows of end-users, such as major pharmaceutical companies, several considerations, as evidenced by the work in this thesis, must be addressed. Firstly, reproducibility should be more thoroughly accounted for and reported. When working with hiPSCs and their derivatives, understanding and reporting the line-to-line variation would enhance our comprehension of the model and ultimately contribute to confidence in their use. Well-characterized and widely distributed standard hiPSC lines could facilitate comparisons between and within models, i.e. including those related to lab-to-lab variability. Additionally, descriptions of OoC models should be provided in a more structural fashion, establishing connections between the implemented and measured physiological features and relevant *in vivo* data whenever possible. Lastly, increased utilization and integration of continuous monitoring, coupled to artificial intelligence, can enable more and direct improvements to cellular models.

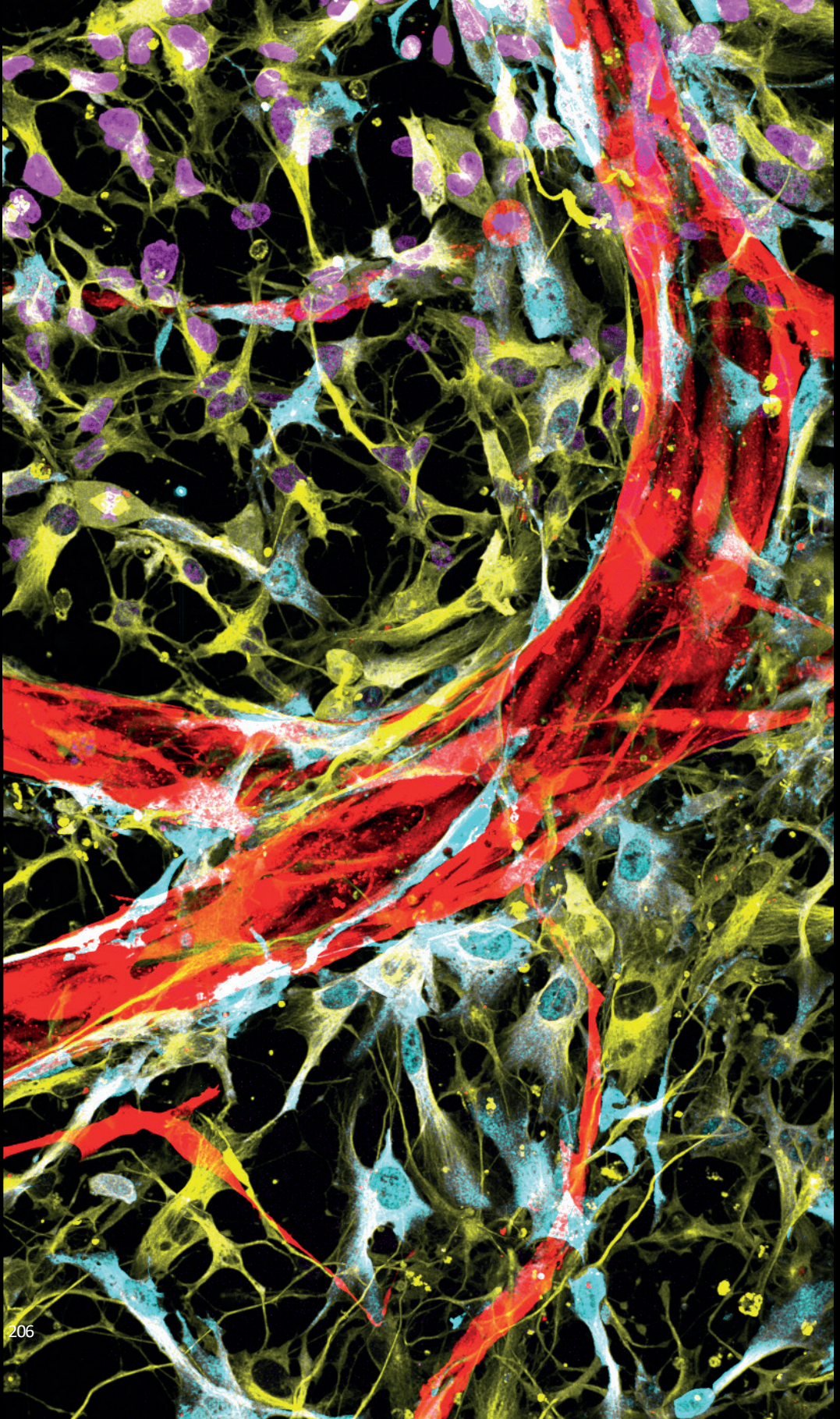
In conclusion, OoC technology as carried out in this thesis represents the convergence of cutting-edge stem cell biology and technical advancements. While the considerations mentioned are essential for achieving widespread application and adoption, there is an exciting future ahead for complex disease modeling using these innovative approaches.

## References

1. Ingber, D. E. Human organs-on-chips for disease modelling, drug development and personalized medicine. *Nat Rev Genet* (2022) doi:10.1038/s41576-022-00466-9.
2. Passier, R., Orlova, V. V. & Mummery, C. L. Complex Tissue and Disease Modeling using hiPSCs. *Cell Stem Cell* 18, 309–321 (2016).
3. Sharma, A., Sances, S., Workman, M. J. & Svendsen, C. N. Multi-lineage Human iPSC-Derived Platforms for Disease Modeling and Drug Discovery. *Cell Stem Cell* 26, 309–329 (2020).
4. Volpato, V. & Webber, C. Addressing variability in iPSC-derived models of human disease: Guidelines to promote reproducibility. *DMM Disease Models and Mechanisms* vol. 13 Preprint at <https://doi.org/10.1242/dmm.042317> (2020).
5. Brunner, J. W. *et al.* Power and optimal study design in iPSC-based brain disease modelling. *Mol Psychiatry* 28, 1545–1556 (2023).
6. Germain, P. L. & Testa, G. Taming Human Genetic Variability: Transcriptomic Meta-Analysis Guides the Experimental Design and Interpretation of iPSC-Based Disease Modeling. *Stem Cell Reports* 8, 1784–1796 (2017).
7. Neavin, D. R. *et al.* A village in a dish model system for population-scale hiPSC studies. *Nat Commun* 14, 3240 (2023).
8. Anguera, M. C. *et al.* Molecular signatures of human induced pluripotent stem cells highlight sex differences and cancer genes. *Cell Stem Cell* 11, 75–90 (2012).
9. Geens, M. & Chua De Sousa Lopes, S. M. X chromosome inactivation in human pluripotent stem cells as a model for human development: back to the drawing board? *Hum Reprod Update* 23, 520–532 (2017).
10. Brenes, A. J. *et al.* Erosion of human X chromosome inactivation causes major remodeling of the iPSC proteome. *Cell Rep* 35, (2021).
11. Bar, S., Seaton, L. R., Weissbein, U., Eldar-Geva, T. & Benvenisty, N. Global Characterization of X Chromosome Inactivation in Human Pluripotent Stem Cells. *Cell Rep* 27, 20–29.e3 (2019).
12. Chang, Y. W. *et al.* Tissue of origin, but not XCI state, influences germ cell differentiation from human pluripotent stem cells. *Cells* 10, (2021).
13. Cloutier, M. *et al.* Preventing erosion of X-chromosome inactivation in human embryonic stem cells. *Nat Commun* 13, (2022).
14. Camprostrini, G. *et al.* Maturation of hiPSC-derived cardiomyocytes promotes adult alternative splicing of SCN5A and reveals changes in sodium current associated with cardiac arrhythmia. *Cardiovasc Res* 119, 167–182 (2023).
15. Ottaviani, D., ter Huurne, M., Elliott, D. A., Bellin, M. & Mummery, C. L. Maturing differentiated human pluripotent stem cells in vitro: methods and challenges. *Development* 150, (2023).
16. Vunjak-Novakovic, G., Ronaldson-Bouchard, K. & Radisic, M. Organs-on-a-chip models for biological research. *Cell* 184, 4597–4611 (2021).
17. Callegari, K. *et al.* Molecular profiling of the stroke-induced alterations in the cerebral microvasculature reveals promising therapeutic candidates. *Proc Natl Acad Sci U S A* 120, (2023).
18. Lebrin, F. *et al.* Thalidomide stimulates vessel maturation and reduces epistaxis in individuals with hereditary hemorrhagic telangiectasia. *Nat Med* 16, 420–428 (2010).
19. Corti, P. *et al.* Interaction between alk1 and blood flow in the development of arteriovenous malformations. *Development* 138, 1573–1582 (2011).
20. Snodgrass, R. O., Chico, T. J. A. & Arthur, H. M. Hereditary haemorrhagic telangiectasia, an inherited vascular disorder in need of improved evidence-based pharmaceutical interventions. *Genes* vol. 12 Preprint at <https://doi.org/10.3390/genes12020174> (2021).
21. Campinho, P., Vilfan, A. & Vermot, J. Blood Flow Forces in Shaping the Vascular System: A Focus on Endothelial Cell Behavior. *Frontiers in Physiology* vol. 11 Preprint at <https://doi.org/10.3389/fphys.2020.00552> (2020).
22. Sugden, W. W. *et al.* Endoglin controls blood vessel diameter through endothelial cell shape changes in response to haemodynamic cues. *Nat Cell Biol* 19, 653–665 (2017).
23. Jerkic, M. & Letarte, M. Contribution of oxidative stress to endothelial dysfunction in hereditary hemorrhagic telangiectasia. *Frontiers in Genetics* vol. 5 Preprint at <https://doi.org/10.3389/fgene.2015.00034> (2015).

24. Jin, Y. *et al.* Endoglin prevents vascular malformation by regulating flow-induced cell migration and specification through VEGFR2 signalling. *Nat Cell Biol* 19, 639–652 (2017).
25. Park, H. *et al.* Defective Flow-Migration Coupling Causes Arteriovenous Malformations in Hereditary Hemorrhagic Telangiectasia. *Circulation* 144, 805–822 (2021).
26. Tual-Chalot, S., Oh, S. P. & Arthur, H. M. Mouse models of hereditary hemorrhagic telangiectasia: Recent advances and future challenges. *Frontiers in Genetics* vol. 5 Preprint at <https://doi.org/10.3389/fgene.2015.00025> (2015).
27. Boussoimmier-Calleja, A. *et al.* The effects of monocytes on tumor cell extravasation in a 3D vascularized microfluidic model. *Biomaterials* 198, 180–193 (2019).
28. Franco, C. A. & Gerhardt, H. Morph or Move? How Distinct Endothelial Cell Responses to Blood Flow Shape Vascular Networks. *Developmental Cell* vol. 41 Preprint at <https://doi.org/10.1038/cdd.2017.36> (2017).
29. Pollet, A. M. A. O. & den Toonder, J. M. J. Recapitulating the vasculature using Organ-on-Chip technology. *Bioengineering* 7, 1–18 (2020).
30. Yee, A., Bosworth, K. A., Conway, D. E., Eskin, S. G. & McIntire, L. V. Gene expression of endothelial cells under pulsatile non-reversing vs. steady shear stress; comparison of nitric oxide production. *Ann Biomed Eng* 36, 571–579 (2008).
31. Feaver, R. E., Gelfand, B. D. & Blackman, B. R. Human haemodynamic frequency harmonics regulate the inflammatory phenotype of vascular endothelial cells. *Nat Commun* 4, (2013).
32. Zheng, C., Zhang, X., Li, C., Pang, Y. & Huang, Y. Microfluidic Device for Studying Controllable Hydrodynamic Flow Induced Cellular Responses. *Anal Chem* 89, 3710–3715 (2017).
33. Xanthis, I. *et al.*  $\beta$ 1 integrin is a sensor of blood flow direction. *J Cell Sci* 132, (2019).
34. Franco, C. A. *et al.* Non-canonical Wnt signalling modulates the endothelial shear stress flow sensor in vascular remodelling. *Elife* 5, (2016).
35. Winkelman, M. A. *et al.* Interstitial flow enhances the formation, connectivity, and function of 3D brain microvascular networks generated within a microfluidic device. *Lab Chip* 22, 170–192 (2022).
36. Haase, K. *et al.* Physiologic flow-conditioning limits vascular dysfunction in engineered human capillaries. *Biomaterials* 280, (2022).
37. Zhang, S. *et al.* Interstitial Flow Promotes the Formation of Functional Microvascular Networks In Vitro through Upregulation of Matrix Metalloproteinase-2. *Adv Funct Mater* (2022) doi:10.1002/adfm.202206767.
38. Offeddu, G. S. *et al.* Application of Transmural Flow Across In Vitro Microvasculature Enables Direct Sampling of Interstitial Therapeutic Molecule Distribution. *Microcirculation-on-Chip* 1902393, (2019).
39. Hajal, C. *et al.* Engineered human blood–brain barrier microfluidic model for vascular permeability analyses. *Nat Protoc* 17, 95–128 (2022).
40. Lu, T. M. *et al.* Human Induced Pluripotent Stem Cell-Derived Brain Endothelial Cells: Current Controversies. *Front Physiol* 12, (2021).
41. Cao, X. *et al.* Tissue microenvironment dictates the state of human induced pluripotent stem cell-derived endothelial cells of distinct developmental origin in 3D cardiac microtissues. *Biorxiv* (2022).
42. Wosik, K. *et al.* Angiotensin II controls occludin function and is required for blood-brain barrier maintenance: Relevance to multiple sclerosis. *Journal of Neuroscience* 27, 9032–9042 (2007).
43. Wang, H. *et al.* Inactivation of Hedgehog signal transduction in adult astrocytes results in region-specific blood–brain barrier defects. *Proc Natl Acad Sci U S A* 118, 1–10 (2021).
44. Alvarez, J. I. *et al.* The hedgehog pathway promotes blood-brain barrier integrity and CNS immune quiescence. *Science* (1979) 334, 1727–1731 (2011).
45. Lau, L. W., Cua, R., Keough, M. B., Haylock-Jacobs, S. & Yong, V. W. Pathophysiology of the brain extracellular matrix: A new target for remyelination. *Nature Reviews Neuroscience* vol. 14 722–729 Preprint at <https://doi.org/10.1038/nrn3550> (2013).
46. Burnside, E. R. & Bradbury, E. J. Manipulating the extracellular matrix and its role in brain and spinal cord plasticity and repair. *Neuropathology and Applied Neurobiology* vol. 40 26–59 Preprint at <https://doi.org/10.1111/nan.12114> (2014).
47. Song, I. & Dityatev, A. Crosstalk between glia, extracellular matrix and neurons. *Brain Research*

48. *Bulletin* vol. 136 101–108 Preprint at <https://doi.org/10.1016/j.brainresbull.2017.03.003> (2018).  
de Mel, A., Jell, G., Stevens, M. M. & Seifalian, A. M. Biofunctionalization of biomaterials for accelerated in situ endothelialization: A review. *Biomacromolecules* vol. 9 2969–2979 Preprint at <https://doi.org/10.1021/bm800681k> (2008).
49. Hajal, C., Roi, B. Le, Kamm, R. D. & Maoz, B. M. Biology and Models of the Blood-Brain barrier. *Annu Rev Biomed Eng* 23, 359–84 (2021).
50. Jambusaria, A. *et al.* Endothelial heterogeneity across distinct vascular beds during homeostasis and inflammation. *Elife* 9, (2020).
51. Yang, A. C. *et al.* A human brain vascular atlas reveals diverse mediators of Alzheimer’s risk. *Nature* 603, 885–892 (2022).
52. Winkler, E. A. *et al.* A single-cell atlas of the normal and malformed human brain vasculature. *Science* (1979) 7377, (2022).
53. Zhang, Y. *et al.* Purification and Characterization of Progenitor and Mature Human Astrocytes Reveals Transcriptional and Functional Differences with Mouse. *Neuron* 89, 37–53 (2016).
54. Kasi, D. G. *et al.* Rapid Prototyping of Organ-on-a-Chip Devices Using Maskless Photolithography. *Micromachines (Basel)* 13, (2022).
55. Bulut, M. *et al.* Three-Dimensional Vessels-on-a-Chip Based on hiPSC-derived Vascular Endothelial and Smooth Muscle Cells. *Curr Protoc* 2, (2022).
56. de Graaf, M. N. S. *et al.* Scalable microphysiological system to model three-dimensional blood vessels. *APL Bioeng* 3, 026105 (2019).
57. Arakawa, C. *et al.* Biophysical and biomolecular interactions of malaria-infected erythrocytes in engineered human capillaries. *Sci Adv* 6, (2020).
58. Enrico, A. *et al.* Three Dimensional Microvascularized Tissue Models by Laser-Based Cavitation Molding of Collagen. *Advanced Materials* 34, (2022).



# Appendix

Summary

Nederlandse samenvatting

Curriculum Vitae

List of publications

Dankwoord

## Summary

A properly functioning vascular system is crucial for the overall health of our body. It transports the necessary oxygen, nutrients, and immune cells to all organs while removing harmful waste products. Blood vessels consist of a single layer of cells called endothelial cells (ECs) and are supported by smooth muscle cells or pericytes. The exact composition and functionality of these vessels vary from one organ to another, and they play a significant role in various medical conditions.

Vascular diseases impose a significant burden on society, mainly due to the lack of effective treatment methods. One major reason for this is the inadequacy of current pre-clinical modeling systems. Traditional models, such as mice or cultured cells in plastic petri dishes, often fail to accurately replicate human physiology. While mice come close in terms of complexity, ethical concerns and important human-specific aspects in many complex diseases remain significant challenges. Cultured cells in petri dishes may have a human origin but lack the complexity of a fully functional mature organ, including its 3D and multi-cellular structure.

Organs-on-Chip (OoC) is an innovative technology that uses microscopic culture environments to more realistically mimic organ functions. This is achieved by replicating one or more physiological stimuli, such as blood flow, tissue stretching, or 3D organ structure. While various cell sources can be used in these systems, human induced pluripotent stem cells (hiPSCs) are particularly attractive for future disease modeling and drug development. These hiPSCs can be generated in the lab by reprogramming normal human cells from any individual and have the ability to differentiate into nearly all cell types. Because these cells retain the genetic background of the donor, they are highly suitable for researching hereditary diseases. In this thesis, we differentiate hiPSCs from patients with neurovascular disorders into vascular cells, with the aim of using them in the development of so-called (blood) Vessels-on-Chip (VoC) models.

In chapters 1 and 2 of this thesis, we introduce OoC and hiPSCs, and we describe the current limitations in the field of OoC. Specifically, in Chapter 2, we emphasize that the (industrial) adoption of OoCs in drug development and disease modeling would be accelerated if researchers paid more attention to comparing experimental results with physiological human data when designing and interpreting experiments. We discuss which OoC data already align well with human data and highlight emerging technological developments that can contribute to a more accurate replication and measurement of other organ functions.

In Chapter 3, we utilize hiPSCs from a patient with a hereditary form of cerebral amyloid angiopathy (also known as D-CAA or HCHWA-D). This disease is characterized by the accumulation of amyloid- $\beta$  protein specifically in the brain's blood vessels, which can lead to cerebral hemorrhages. We correct the hereditary DNA mutation in the hiPSCs of this patient to enable further studies into the underlying disease mechanisms.

Similar to Chapter 3, in Chapter 4, we correct the causal DNA mutation in hiPSCs

from a patient suffering from Retinal Vasculopathy with Cerebral Leukoencephalopathy and Systemic Manifestations (RVCL-S). This rare disease causes unstable small blood vessels and results in symptoms in various organs, including the brain. To investigate the specific role of ECs in this disease, we differentiate the hiPSCs from the patient ('diseased' cells) and the hiPSCs with the corrected DNA ('healthy' cells) into ECs. Functionally, the differentiated ECs did not show significant differences. Further research with more complex models is needed to better understand the differences between these ECs.

In Chapter 5, we once again compare 'healthy' and 'diseased' ECs, this time differentiated from hiPSCs from a patient with the vascular disease Hereditary Hemorrhagic Telangiectasia (HHT). This condition leads to abnormal formation of small blood vessels, resulting in severe blood loss. While standard two-dimensional analyses of the ECs did not show significant differences, we identified differences after integrating the cells into a more complex VoC model. The ECs, together with supporting pericytes, formed a complex 3D microvascular network in the microfluidic chips. The 'healthy' ECs formed larger and more stable blood vessels with more direct interactions with the supporting pericytes than the 'diseased' ECs. This lack of stability and interaction aligns with patient data, highlighting the value of such complex VoC models.

As many of the diseases discussed in this thesis specifically affect blood vessels in the brain, we expand the VoC model further in Chapter 6 by adding brain-specific astrocytes. By, for the first time in the research field, adding astrocytes that are also differentiated from hiPSCs, future research into the influence of astrocytes on the formation of microvascular networks becomes possible. We successfully integrated these astrocytes into the VoC model and observed direct interactions between the cells that resemble what we observe in the human body. Additionally, we demonstrated that mimicking blood flow or adding specific components in the chip can enhance the development of these astrocyte containing VoC models.

Ultimately, in Chapter 7, we discuss the results of this thesis and its future perspectives. We emphasize that the generated patient-specific hiPSCs serve as essential tools for further research into these diseases. Moreover, the results underscore the potential of VoC models for understanding and studying vascular diseases. Finally, the research also highlights the need to further refine current models by integrating additional factors (such as immune cell integration or more precise regulation in mimicking blood flow) to more accurately replicate the disease's characteristics. Additionally, improvements in standardization, reproducibility, and enhanced continuous monitoring of conditions in cellular VoC models are necessary.

## Nederlandse samenvatting

Een goed functionerend bloedvaten systeem is essentieel voor de gezondheid van elk onderdeel van ons lichaam. Het transporteert de benodigde zuurstof, voedingsstoffen en immuuncellen naar alle organen en verwijdert de schadelijk afvalstoffen. Ze bestaan uit een enkele laag cellen, genaamd endotheel cellen (ECs), en worden ondersteund gladde spiercellen of pericyten. De precieze samenstelling en functionaliteit van de vaten verschilt per orgaan en is van grote invloed in een groot aantal ziektebeelden.

Vasculaire ziektes vormen een aanzienlijke last op de maatschappij, grotendeels vanwege het gebrek aan effectieve behandelingsmethode. Een belangrijke reden hiervoor is het tekortschieten van de huidige preklinische modelsystemen. Traditionele modellen, zoals muizen of gekweekte cellen in een plastic petrischaaltje, repliceren vaak niet nauwkeurig de menselijke fysiologie. Muizen komen qua complexiteit weliswaar in de buurt van mensen, maar naast de ethische bezwaren, zijn er vaak ook belangrijke mens-specifieke aspecten in veel complexe ziektes. Gekweekte cellen in petrischaaltjes hebben wel de menselijk achtergrond, maar missen de complexiteit van een functioneel volwassen orgaan, met zijn 3D en multi-cellulaire structuur. Organen-op-Chip (OoC), is een innovatie technologie die microscopische kweekomgevingen gebruikt om functies van organen realistischer na te bootsen. Dit wordt bereikt door een of meerdere fysiologische stimuli, zoals, bloedstroom, weefselrekking of 3D orgaanstructuur te reproduceren. In deze chips kunnen verschillende cellen gegroeid worden. Hoewel veel verschillende soorten cel bronnen hiervoor kunnen worden gebruikt, zijn humane geïnduceerde pluripotente stamcellen (hiPSCs) bijzonder aantrekkelijk met het oog op toekomstige ziektemodellen en medicijnontwikkeling. Deze hiPSCs kunnen in het lab worden gecreëerd door de herprogrammering van normale menselijk cellen van elk individu en hebben de capaciteit om te ontwikkelen ('differentiëren') tot bijna alle gespecialiseerde celtypes. Omdat deze cellen de genetische achtergrond van de donor behouden, zijn ze uitermate geschikt voor onderzoek naar erfelijke ziektes. In dit proefschrift differentiëren wij hiPSCs van patiënten met neuro-vasculaire aandoeningen tot vasculaire cellen, met als doel ze te gebruiken in de ontwikkeling van zogenaamde (bloed) Vaten-op-Chip (VoC) modellen.

In hoofdstuk 1 en 2 van dit proefschrift introduceren wij OoC en hiPSCs en beschrijven wij de huidige beperkingen in het veld van OoC. Specifiek benadrukken wij in hoofdstuk 2 dat de (industriële) adoptie van OoCs in ziektemodellering en medicijnontwikkeling versneld zou worden als onderzoekers meer aandacht besteden aan de vergelijking met fysiologische humane data bij het opzetten en interpreteren van experimenten. We bespreken welke OoC data al goed overeenkomen met humane gegevens en belichten opkomende technologische ontwikkelingen die kunnen bijdragen aan een nauwkeurigere nabootsing en meting van andere orgaanfuncties.

In hoofdstuk 3 maken we gebruik van hiPSCs van een patiënt met een erfelijke vorm van cerebrale amyloïdeangiopathie (ook wel D-CAA of HCHWA-D genoemd). Deze

ziekte wordt gekenmerkt door een ophoping van het amyloïde- $\beta$  eiwit specifiek in de bloedvaten in de hersenen, wat kan leiden tot hersenbloedingen. We corrigeren de erfelijke DNA-fout in de hiPSCs van deze patiënt om vervolgstudies naar de onderliggende ziekte mechanismes mogelijk te maken.

Vergelijkbaar als in hoofdstuk 3, corrigeren we in hoofdstuk 4 de causale DNA-mutatie in hiPSCs van een patiënt die leidt aan Retinale Vasculopathie met Cerebrale Leukoencefalopathie en Systemisch manifestaties (RVCL-S). Deze zeldzame ziekte veroorzaakt instabiele kleine bloedvaten wat leidt tot symptomen in verschillende organen, waaronder de hersenen. Om de specifieke invloed van ECs in deze ziekte te onderzoeken, differentiëren we de hiPSCs van de patiënt ('zieke' cellen) en de hiPSCs met het gecorrigeerde DNA ('gezonde' cellen) tot ECs. Functioneel vertoonden de gedifferentieerde ECs geen significante verschillen. Meer onderzoek met complexere modellen is nodig om het verschil tussen ECs in deze ziekte beter te begrijpen.

In hoofdstuk 5 vergelijken we wederom 'gezonde' en 'zieke' ECs, deze keer gedifferentieerd van hiPSCs van een patiënt met de vasculaire ziekte Hereditary hemorrhagic telangiectasia (HHT). Deze aandoening leidt tot abnormale vorming van kleine bloedvaten, wat ernstig bloedverlies kan veroorzaken. Terwijl standaard tweedimensionale analyses van de ECs geen significante verschillen aantoonde, identificeerden we wel verschillen nadat wij de cellen hadden geïntegreerd in een complexer VoC model. De ECs vormden samen met de ondersteunende pericyten een complex 3D microvasculair netwerk in de microfluidische chips. De 'gezonde' ECs vormden grotere en stabielere bloedvaten met meer directe interacties met de ondersteunende pericyten dan de 'zieke' ECs. Dit gebrek aan stabiliteit en interactie komen overeen met patiënt data en ondersteunen daarmee de meerwaarde van dergelijk complexe VoC modellen.

Aangezien veel van de ziektes die in dit proefschrift worden besproken, specifiek de bloedvaten in de hersenen beïnvloeden, breiden we in hoofdstuk 6 het VoC model verder uit door hersen-specifieke astrocyten toe te voegen. Door, als eerste in het onderzoeksveld, astrocyten toe te voegen die ook gedifferentieerd zijn vanuit hiPSCs, wordt toekomstig onderzoek naar de invloed van astrocyten in gezonde en zieke hersenbloedvaten mogelijk. We hebben succesvol deze astrocyten geïntegreerd in het VoC model en observeerde directe interacties tussen de cellen die vergelijkbaar zijn met wat we in het menselijk lichaam zien. Bovendien hebben we aangetoond dat het nabootsen van de bloedstroom of het toevoegen van specifieke componenten aan de 'bloedstroom' in de chip, de ontwikkeling van deze VoC modellen met astrocyten kan verbeteren.

Uiteindelijk bediscussiëren we in hoofdstuk 7 de resultaten uit dit proefschrift met een toekomstperspectief. We bespreken dat de gegenereerde patiënt-specifieke hiPSCs dienen als essentiële instrumenten voor vervolgonderzoek naar deze ziektebeelden. Daarnaast ondersteunen de resultaten de potentie van VoC modellen voor het begrijpen en bestuderen van vasculaire ziektes. Ten slotte benadrukt het onderzoek ook de noodzaak om

de huidige modellen verder te verfijnen door aanvullende factoren (bijvoorbeeld immuun cel integratie of nauwkeurigere regulatie in het nabootsen van bloedstroom) te kunnen integreren, om zo nog nauwkeuriger het ziektebeeld te kunnen nabootsen. Daarnaast zijn er nog verbeteringen vereist op het gebied van standaardisatie, reproduceerbaarheid en verbeterd continu monitoren van de omstandigheden in de cellulaire VoC modellen.



## Curriculum Vitae

Dennis Nahon was born on May 5th, 1993 in Voorburg, the Netherlands. After graduating from secondary school (Alfrink College, Zoetermeer), he started a bachelor Life Science & Technology focusing in detail on cellular biology by combining the molecular and biological expertise from the University of Leiden and the (bio)technological expertise from the University of Delft. During his bachelor he also participated in the Honours College track.

After his bachelor, Dennis pursued the biomedical research master Cancer, Stem cells & Developmental biology at the University of Utrecht. During his first major internship at the Cancer Biophysics group of prof. Jacco van Rheenen at the Hubrecht Institute he gained experience with organoid culturing and the mechanisms underlying epithelial to mesenchymal transition in cancer metastasis. In his second internship in the group of Developmental biology at the University of Utrecht in the group of prof. Sander van den Heuvel he focused on the development of a screening platform to study cell cycle entry and exit in differentiated cells in *c. elegans*.

Next, he started his PhD research under supervision of dr. Valeria Orlova and prof. dr. Christine Mummery in the department Anatomy and Embryology at the Leiden University Medical Center. During his PhD, he was awarded prizes for best abstract and poster (European Organ-on-Chip Society Conference), best presentation (European Vascular Biology Organization Summer school) and best PhD research pitch (human organ and Disease Model Technologies (hDMT) PhD Spotlight competition). He has been selected for several oral presentations at other scientific conferences. In addition, he presented his work at multiple public events to promote the understanding of stem cell biology and novel disease models by the general public.



## List of publications

### **Self-assembling 3D Vessel-on-Chip model with hiPSC-derived astrocytes**

Dennis M. Nahon, Marc Vila Cuenca, Francijna E. van den Hil, Michel Hu, Tessa de Korte, Jean-Philippe Frimat, Arn M.J.M. van den Maagdenberg, Christine L. Mummery, and Orlova VV. *Stem Cell Reports*. (2024) *In Press*

### **Standardizing designed and emergent quantitative features in microphysiological systems**

Dennis M. Nahon\*, Renée Moerkens\*, Hande Aydogmus, Bas Lendemeijer, Jeroen M. Stein, Adriana Martinez-Silgado, Milica Dostanić, Frimat JP, Cristina Gontan, Mees N.S. de Graaf, Michel Hu, Dhanesh G. Kasi, Lena S. Koch, Kieu T.T. Le, Sangho Lim, Heleen H.T. Middelkamp, Joram Mooiweer, Paul Motreuil-Ragot, Eva Niggli, Cayetano Pleguezuelos-Manzano, Jens Puschhof, Nele Revyn, José M. Rivera-Arbelaez, Jelle Slager, Laura M. Windt, Mariia Zakharova, Berend J. van Meer, Valeria V. Orlova, Femke M.S. de Vrij, Sebo Withoff, Massimo Mastrangeli, Andries van der Meer, and Christine L. Mummery. *Nature Biomedical Engineering*. (2024) *In Press*

### **Genetic repair of human induced pluripotent cell line from patient with Dutch-type cerebral amyloid angiopathy**

Dennis M. Nahon, Sravya Ganesh, Francijna E. van den Hil, Christian Freund, Christine L. Mummery, and Valeria V. Orlova. *Stem Cell Research*. Sep;71 (2023)

### **Vascularized hiPSC-derived 3D cardiac microtissue on chip**

Ulgu Arslan, Marcella Brescia, Viviana Meraviglia, Dennis M. Nahon, Ruben W.J. van Helden, Jeroen M. Stein, Francijna E. vanden Hil, Berend J. van Meer, Marc Vila Cuenca, Christine L. Mummery, and Valeria V. Orlova. *Stem Cell Reports*. 11;18 (2023)

### **Vascular defects associated with hereditary hemorrhagic telangiectasia revealed in patient-derived isogenic iPSCs in 3D vessels on chip**

Valeria V. Orlova, Dennis M. Nahon, Amy Cochrane, Xu Cao, Christian Freund, Francijna E. van den Hil, Cornelius J.J. Westermann, Repke J. Snijder, Johannes Kristian Ploos van Amstel, Peter ten Dijke, Franck Lebrin, Hans-Jurgen Mager, and Christine L. Mummery. *Stem Cell Reports*. 12;17 (2022)

### **Scanning mutagenesis in a yeast system delineates the role of the NPxxY(x)(5,6)F motif and helix 8 of the adenosine A(2B) receptor in G protein coupling**

Rongfang Liu, Dennis M. Nahon, Beau le Roy, Eelke B Lenselink, and Adriaan P IJzerman. *Biochem Pharmacol*. 15;94 (2015).



## Dankwoord

Deze intense tocht was nooit gelukt zonder de hulp en steun van zo veel mensen.

Valeria, thanks for the opportunity to experience the wide scale of your research. The amount of readily available knowledge you have never ceases to amaze me. Thanks for the freedom to explore my own projects and the support where needed.

Christine, your dedication, overview and ability to provide feedback without any delay has truly been inspiring. Thank you for sharing your enthusiasm and the trust you put in me in everything I did.

Lisa, in de vessel groep, toch echt het kloppende hart. Door jouw scherpe en onverzettelijke goed gesteldheid, de beste analist die iemand zich kan wensen. Marc, your straight to the point mentality and calmness have helped me through many times. Dhanesh, de PRIMO magiër, dankje voor de open samenwerking, het lachen, het schelden en de combinatie van de twee. Merve, for all the times together in the lab, for always being naïve and nice, even when I kept annoying you for your own good. Ulgu, Kendy, Theano, Sara, Sebastiaan, Mees, Amy, Xu, Oleh thanks for the input, support and great atmosphere in the group.

Big thank you to the whole anatomy department for all the help and the accompanying great time. Ruben, buurman, bedankt voor je hulp, energie, gezelligheid en fidget cube. Tessa, dankje voor je waardevolle suggesties en je enthousiasme met het onvergetelijke gala als eigenhandig georganiseerde beloning. Berend, bedankt voor de input en de kleine praktische push die ik soms nodig had. Jeroen bedankt voor alle snelle antwoorden en de thesis cover. Thanks for the (work)trips; Julieta, Axelle, Isabel, Benji my favorite couch and Señor Alberto. Also all others for the scientific discussion, volleyball and lunches; Laura, Milica, Dorien, Arend, Linda, Clara, Ouafa, Eline, Yolanda, Loukia, Marcella, James, Beatrice, Maury, Louise, Vivi, Giulia, Babette, Lettine, Karina, Sanne, Esmee, Nicola, Spiros, Veronika, Mervyn, Christiaan, Mehmet, Celine, Julia, Bert.

How lucky I feel to have shared this whole PhD experience with the entire NOCI-crew. Thanks to everyone for the open, friendly and curious environment in which we truly started to talk each other's languages. Life would have been boring without our intense bonding over countless apenkoppen, café-takeovers and subsequent hangover presentations. Specifiek grote dank voor mijn partner in crime Renée. Ik ben super blij en trots op het product van onze eindeloze gezellige zoom-sessies. Blijf, scherp, perfectionistisch en onvermoeibaar aardig.

Lennart en Annelies bedankt voor menig microscopie hulp. Nicolette bedankt voor de bijpraat lunches. Carla thanks for the amazing thesis lay-out inspiration. Mandy and Simone dank voor de leuke outreach mogelijkheden.

Alle vrienden van Chill leks voor de essentiële afleiding tijdens afgelopen jaren. Bram, bedankt voor het aanhoren van mijn oneindige overpeinzingen, je support waar nodig met een biertje en je constante eerlijkheid. Roos, bedankt voor het zijn van mijn

Leiden go-to en je aanstekelijke enthousiasme. Andrew en Anouk voor de goede gesprekken tijdens heerlijke etentjes. Chris en Marit voor de sport afleiding na een lange dag op het lab. Ook alle anderen; Dick en Sam, Mick en Fee, Sander en Fleur en Edwin enorm bedankt.

Avonturiers, nu eindelijk echt, Bas en Djoer, bedankt voor de avondjes couchgames, padellen, Cacaw, wandelen en de perfecte afsluiting in Zuid-Amerika.

Jasper en Twan, de Tony Haks, de combinatie van semi-intelligente gesprekken en nog minder intelligente activiteiten waren een welkome afwisseling van werk.

Joris bedankt voor de goede gesprekken. Joep voor de PhD drama besprekingen en de nodige goede muziek en feestjes. Eva, voor het luisterende oor of je nou dichtbij of ver weg was.

De familie Adrichem, al lang voor dit moment onderdeel van mijn reis hierheen. Jos, Sandra, Hessel, Rima, bedankt dat jullie er waren. Demi, bedankt voor wie je bent, voor alles wat je mij geleerd hebt en vooral dat je me altijd bent blijven steunen in de pieken en dalen van deze tocht, ook al was ik soms niet op mijn best in mijn PhD bubbel.

Ten slotte nog dank aan mijn familie voor het vormen van de essentiële stabiele basis. Kimberly en Joya, zusjes, alhoewel ik eerst heb geprobeerd om origineel te zijn, moest ik toch snel toegeven dat jullie ook mij onomkeerbaar hadden aangestoken met de biomedische passie. Dat wij dit tot zover kunnen delen blijft super bijzonder en ik ben dan ook super trots op ons samen. Casper, Joost, Lize, Wouter, Rosa, Leyla, ik weet dat ik altijd bij jullie terecht kan en ik ben heel blij dat jullie onderdeel waren van dit traject. Tot slot, Papa en Mama. Ondanks dat ik dingen soms wat anders aanpak dan jullie zouden doen, weet ik dat jullie mij onvoorwaardelijk steunen. Die basis van oneindige liefde en steun is de reden dat ik hier nu ben. Dank jullie.